Durham E-Theses

The molecular properties of zwitterionic, non-linear optical molecules and their evolution with molecular environment.

Thomas, Philip Robert

How to cite:

Use policy

THE MOLECULAR PROPERTIES OF
ZWITTERIONIC, NON-LINEAR OPTICAL
MOLECULES AND THEIR EVOLUTION
WITH MOLECULAR ENVIRONMENT.

Philip Robert Thomas

Thesis submitted in part fulfilment of the requirements for the

degree of

Doctor of Philosophy

at the

University of Durham

Department of Physics

February 1998.

Abstract.

The concepts involved with the experimental techniques of Electric Field Induced Second Harmonic generation (EFISH), dipole moment measurement, and solvatochromism, are introduced with particular application to the properties of organic molecules. A number of organic chromophores are introduced, but emphasis is applied to the study of tetracyanoquinodimethane (TCNQ) derivatives which are expected to possess large dipole moments (μ) and large hyperpolarisabilities (β). Furthermore, the behaviour of μ and β with respect to the local environment of the molecule is discussed where a novel evolution is predicted from theoretical calculations. The measurement of μ, is discussed with particular reference to the geometry of the local field factor and the size of the molecule. Consequently, the choice of local field is found to be critical when dipole moments are large, as is the case with the TCNQ derivatives.

The EFISH experimental technique is introduced where the calibration of the experiment is discussed. The measurement of the molecular figure of merit, $\mu\beta$ at 1.064 μm and 1.907 μm in chloroform and dichloromethane is presented for the TCNQ derivatives, again paying attention to the geometry of the local field factor. $\mu\beta$ is found to be moderate for most of the compounds, but β is found to be unexpectedly small. This is partly due to the fact that μ is large.

A novel evolution of the transition frequency with solvent polarity is found for three of the chromophores under study, where the solvatochromic shift reverses. Solvatochromism experiments are conducted with binary solvent mixtures to ascertain the position of the cyanine limit ($\beta = 0$) with respect to reaction field. It is found that the materials reside close to the cyanine limit in chloroform and dichloromethane. This is attributed as a reason for the low β measurements. Comparisons of μ and β are also made with Sum-Over-State calculations. A better correlation is found for ellipsoidal local field factors.

Declaration and Copyright.

I hereby declare that the work presented in this thesis has not been previously submitted for any degree and is not being currently submitted in candidature for any other degree.

Signed..

Candidate

The work reported in this thesis was carried out by the candidate. Any work not carried out by the candidate is acknowledged in the main text.

Signed..

Supervisor

Signed..

Candidate

To my parents

and

to Anna.

Contents.

Acknowledgements.

Firstly and foremost, I would like to thank Professor Jean-Luc Brédas, Dr. Massimo Malagoli, and Dr. Fabienne Meyers at the Service de Chimie des Materiaux Nouveaux, Université de Mons Hainaut, Mons, Belgium for providing the 40-state Sum-Over-State calculations conducted upon DEMI which are subsequently compared to the experimental results obtained for DEMI and discussed this thesis. I would also like to thank Jacqueline Cole and Judith Howard of the Chemistry Department at Durham University for providing crystal structure densities and dipole moments for the amino TCNQ derivatives. Furthermore, I thank Dr. Marek Szablewski who is in Dr. Graham Cross's group at the Physics department, Durham University for synthesising and providing the amino TCNQ derivatives which are primarily discussed in this thesis, and I also thank Professor David Allen of the Chemistry department at Sheffield Hallam University for providing the four "Sheffield" materials for dipole moment analysis.

Additionally, I would like to thank Dr. Graham H. Cross for allowing me to undertake studies for a Ph.D. His patience with me has been exemplary when I have not understood aspects of my studies, and his supervisory nature has allowed me to partake in discussions at the highest level.

Dr. Marek Szablewski has been a major influence for my work. Acting sometimes as co-supervisor and mentor rather than purely a postdoctoral colleague, I have welcomed his comments on my work and enjoyed numerous discussions about the materials under study. His patience and kindness has also been exemplary, for which I thank him.

In addition, I would like to thank Dr. Anna Thornton for a number of discussions concerning the material aspects of my work. I found her professional support and help during my studies extremely useful, and value any advice that was

given. I would also like to thank her for the personal support she has provided throughout the production of this thesis. She has listened tirelessly about the work (and number of pages) involved with the thesis, and without her help I would not have completed this thesis so quickly.

I would also like to thank the outgoing and incoming members of Graham's research group. Dr.'s Dave Gray, Dave Healy, Maria Farsari, and Marcus Swan as well as those above, welcomed me to the group so that I felt part of that group very quickly. I thank them for any initial discussions and help they provided in my first and second years. I also thank Yitao Ren, Yasuyuki Kagawa, Nancy-Ann Hackman and Christoph Renger for allowing the continuation of the group spirit and making the research labs an enjoyable place to work in. In addition, I would like to thank my other friends and colleagues who are members of other research groups in the Physics Department, for contributing to the enjoyable and workable atmosphere in the research labs. I also thank Professor David Bloor for many helpful discussions and the multitude of references he has passed on to me.

The help and support provided by the technical staff at the Physics Department has been invaluable, and I am sure I would not have completed my studies without it. Norman Thompson and Davey Patterson have always been kind and helpful and have almost shown a willingness to drop everything to aid me with a technical problem, for which I thank them. I would also like to thank the staff at the mechanical workshop who made several pieces of equipment for me, and the staff in the electrical workshop who tirelessly fixed broken electrical equipment for me. Also, I would like to thank the rest of the technical and secretarial staff at the Physics Department who have always been courteous and helpful when I have presented them with a problem.

Finally, I would like to thank my family and close friends for the support and assistance they have given me during, and in the years leading up to my time in Durham.

Glossary of Symbols.

a, b, c The lengths of the principal semi-axes for an ellipsoidal cavity in the z, y, and x directions, respectively.

a_n, b_n, c_n, d_n The nth order coefficients used for calculating the reaction field.

A_m^L The average magnitude of Maker fringes for a liquid.

A_m^Q The average magnitude of Maker fringes for quartz.

A_1 The Maker fringe amplitude.

A_2 The Maker fringe amplitude offset.

A_z The shape factor in the z direction.

B_1, B_2 The coefficients used in the anharmonic oscillator model.

$\mathbf{B}$ The magnetic flux.

c   The speed of light.

$c.c.$ The complex conjugate of a preceding term in any equation.

C_A The capacitance of a capacitor with air between the electrodes.

C_s The capacitance of a capacitor with a solution between the electrodes.

C The concentration of the solute in a two component solution.

d_q Charge separation.

d_{ijk} A tensorial representation of the effective second harmonic coefficient.

d_{IJKL}^{eff} The effective second harmonic coefficient for EFISH ($\equiv \Gamma_{IJKL} E_L^0$).

$d_{eff}(z)$ The effective second harmonic coefficient as a function of the propagation distance.

d The density.

$d_{x\text{-}ray}$ The density of a molecular crystal obtained via x-ray crystallography.

d_w The reflected ray separation found while measuring θ_w.

$\mathbf{D}$ The electric displacement vector (= $\varepsilon\mathbf{E}$).

e	The charge on the electron.
$|e\rangle$	The first excited state of a material system.
$\mathbf{E}$	An electric field vector.
$\mathbf{E}(t)$	The external field as a function of time.
$\mathbf{E}_{loc}(t)$	The local electric field as a function of time.
$\mathbf{E}_0$	The electric field amplitude.
E_0	The static electric field amplitude.
$E^{2\omega}(z)$	The total second harmonic electric field at frequency 2ω as a function of the propagation direction.
$E^{\omega}(z)$	The fundamental electric field at frequency ω as a function of propagation direction.
$E_f^{2\omega}$	The second harmonic free wave electric field amplitude at 2ω.
$E_b(z)$	The second harmonic bound wave electric field amplitude as a function of the propagation direction, z.
$E_f^{(n)}$	The free wave field amplitude in medium n either side of an interface.
$E_b^{(n)}$	The bound wave field amplitude in medium n either side of an interface.
$E_R^{(n)}$	The reflected wave field amplitude in medium n either side of an interface.
E_J^{ω}	The electric field at frequency ω in the Jth direction ($\omega = 0$ - static field).
$\mathbf{E}_d$	The directing electric field.
$\mathbf{E}_c$	The component of electric field inside a cavity.
$E_N^T(30)$	Reichardt's normalised scale of solvent polarity.
f	The spherical reaction field factor.
f'	The spherical reaction field factor replacing ε with n^2.
f_z	The reaction field factor in the z direction for an ellipsoidal cavity.
f^L	The Lorentz local field factor.

f_ω^L	The Lorentz-Lorenz local field factor at frequency ω.
f^ω	The local field factor at frequency ω ($\omega = 0$ - static factor).
f_{ell}^ω	The ellipsoidal local field factor at frequency ω ($\omega = 0$ - static factor).
f_k^*	The local field factor pertaining to dipole orientation only for k^{th} species.
f_k^0	f^0 for the kth species.
$[f_k]$	$f_k^0 \left(f_k^\omega \right)^2 f_k^{2\omega}$ for k^{th} species.
f_m	The spatial frequency of Maker fringes.
$f_{osc.}$	The oscillator strength of an energy transition.
$\mathbf{F}_\lambda$	A tensorial representation of the ellipsoidal reaction field factor in the λ direction.
$\mathbf{F}$	The force on an anharmonic oscillator.
$|g\rangle$	The ground state of a material system.
h	Planck's constant.
$\hbar$	$h/2\pi$.
$\mathbf{H}$	The magnetic field.
i	$\sqrt{-1}$.
i, j, k, l	The usual tensors applied to the polarisation or the tensor indices specifically for the molecular frame of axes.
I, J, K, L	The tensorial indices representing the laboratory frame of axes.
$\mathbf{I}$	The internal field experienced by a molecule.
$I_\alpha(\omega)$	The absorption intensity.
I^ω	The fundamental intensity at frequency ω.
$I^{2\omega}$	The second harmonic intensity at frequency 2ω.
$\mathbf{J}$	The free current density.
k_n	The nth wave vector of a plane wave at frequency ω_n.

k_f	The wave vector pertaining to the second harmonic free wave.
k_b	The wave vector pertaining to the second harmonic bound wave.
k_B	Boltzman's constant.
Δk	The wave vector mismatch parameter ($\Delta k = k_f - k_b$).
l	The interaction length for SHG.
l_t	The translation distance of the EFISH cell.
l_w	The distance from the pinhole used with the measurement of θ_w.
l_α	The absorption path length.
l_c	The coherence length.
l_c^0	The coherence length of the solvent.
l_c^G	The coherence length of BK7 glass.
l_c^Q	The coherence length of quartz.
l_c^L	The coherence length of a liquid.
m_e	The mass of an electron.
$\lvert m \rangle$, $\lvert n \rangle$	The representation of the virtual energy levels involved with SHG.
m_s	The mass of a solute.
M_k	The molecular weight of species k.
$n_{\omega,\,2\omega}$	The refractive index at frequency ω or 2ω.
$n_{\omega,2\omega}^G$	The refractive index of BK7 glass at frequency ω or 2ω.
$n_{\omega,2\omega}^L$	The refractive index of a liquid at frequency ω or 2ω.
$n_{\omega,2\omega}^Q$	The refractive index of quartz at frequency ω or 2ω.
n	The refractive index of a solvent ($\omega \to 0$).
n_k	The refractive index of the kth species ($\omega \to \infty$).
Δn	The difference in refractive indices at ω and 2ω $\left(n_{2\omega} - n_\omega\right)$.

n_{ell}	The value of n calculated through the ellipsoidal version of the Clausius-Mossotti equation.
ND	The optical density of neutral density filters.
N	The number density.
N_k	The number density for the kth species.
N_a	Avogadro's number.
$\mathbf{p}(t)$	The microscopic polarisation as a function of time.
p_I	A tensorial representation of the microscopic polarisation.
$p(\theta)$	The probability of orientation.
$\bar{\mathbf{p}}_d$	The average component of the polarisation due to the directing field.
$\bar{\mathbf{p}}_R$	The average component of the polarisation due to the reaction field.
$\mathbf{P}(t)$	The macroscopic polarisation as a function of time.
P_I	A tensorial representation of the macroscopic polarisation.
$P_I^{2\omega}$	The second harmonic polarisation in the Ith direction.
$\mathbf{P}_0$	The macroscopic polarisation of a system with no applied field.
$\mathbf{P}^{NL}$	The non-linear part of the macroscopic polarisation.
$\mathbf{P}_\mu$	The polarisation due to the dipole moment only.
$\mathbf{P}_\alpha$	The polarisation due to the polarisability only.
$p_n(\cos\theta)$	The nth order Legendre polynomial.
$\wp_F$	The full permutation symmetry operator.
q	The charge difference pertaining to a dipole.
Q_1, Q_2	Transmission factors.
Q	Charge.
r	The radius of a spherical cavity.
$\bar{r}$	The average radius of an ellipsoidal cavity.
$\bar{r}_{x-ray}$	The average radius of a cavity obtained using d_{x-ray}.
R_s	Ratio of box-car sensitivities.

$\mathbf{R}$	The reaction field.
R_{sph}	The reaction field calculated using a spherical cavity
R_{ell}	The reaction field calculated using an ellipsoidal cavity.
$\overline{\mathbf{R}}$	The average reaction field.
t	Time.
t_A^{ω}	The Fresnel transmission factor for an air-glass interface at frequency ω.
$t_A^{2\omega}$	The Fresnel transmission factor for a glass-air interface at frequency ω.
$t_G^{\omega,2\omega}$	The Fresnel transmission factor for a glass-liquid interface at frequencies ω or 2ω.
$t_L^{\omega,2\omega}$	The Fresnel transmission factor for a liquid-glass interface at frequencies ω or 2ω.
T_0	The time at which the laser lamp triggers.
T_G	A transmission factor for glass
T_L	A transmission factor for a liquid.
T	Temperature.
v	The specific volume.
V	Voltage.
V_T	The total volume of a solution.
V_{tol}	The volume of toluene.
V_{MeCN}	The volume of acetonitrile.
V_{MeCN}^f	The volume fraction of acetonitrile.
$V(x)$	The potential of an anharmonic oscillator.
w	The weight fraction of solute in a two component system.
W	The energy of a dipole in an applied field.
x_e	The electron co-ordinate.
$x_e^{(n)}$	The displacement amplitude associated with the nth term of the Taylor expansion for the potential.

x_1	The path length between the front "pot" window and the front glass wedge.
x_2	The path length between the two glass wedges.
x_3	The path length between the back "pot" window and the back glass wedge.
x, y, z	The Cartesian axes (sometimes used to represent the molecular frame of axes).
X, Y, Z	The Cartesian axes representing the laboratory frame.
y_l	Gaussian and Lorentzian summed lineshape.
z_0	The position of an interface at $z=0$.
α_{ij}	A tensorial representation of the polarisability.
α_z	The polarisability in the z direction.
α_e	The polarisability in the excited state.
α_g	The polarisability in the ground state.
$\alpha_{\omega,2\omega}$	The absorption coefficient at ω or 2ω.
$\alpha_k, \overline{\alpha}_k$	The average polarisability for species k.
α	The symbol pertaining to the α-scale of hydrogen bonding acceptor basicities.
β	The second polarisability or first hyperpolarisability.
β_{ijk}	A tensorial representation of the second polarisability.
β_{CT}	The contribution to β due to charge-transfer (CT) interactions only (π-electrons)
$\beta(0)$	The static frequency component of β.
$\beta(\omega)$	A resonantly enhanced value of β.
β_{sph}	The value of β which is calculated using spherical local fields.
β_{ell}	The value of β which is calculated using ellipsoidal local fields.
β_Z	The orientation average value of β in the Z direction.

$\beta(0)_{EFISH}$	The value of β obtained form EFISH measurements.
$\beta(0)_{SCI}$	The value of β obtained from 40-state SOS SCI calculations.
$\beta(0)_{SDCI}$	The value of β obtained from 40-state SOS SD-CI calculations.
β_{zzz}	A tensorial component of β entirely in the z direction.
$\beta_{dip.}$	The component of β in the direction of the dipole moment.
$\beta_{vec.}$	The magnitude of the vector component of β.
β	The symbol pertaining to the β-scale of hydrogen bonding donor acidities.
$\chi^{(1)}$	The linear susceptibility.
$\chi^{(n)}, (n \neq 1)$	The non-linear susceptibilities.
$\chi^{(2)}_{ijk}, \chi^{(3)}_{ijkl}$	Tensorial representations of the second and third susceptibilities.
ε	The low frequency dielectric constant.
ε_0	The permittivity of free space.
$\varepsilon^{(1)}(\omega)$	The frequency dependent linear dielectric tensor.
ϕ	An angle of transformation between Cartesian axes.
ϕ_1, ϕ_2	The potential outside and inside a dielectric cavity.
γ_d	The damping coefficient of an anharmonic oscillator.
γ	The third polarisability or second hyperpolarisability.
γ_{ijkl}	A tensorial representation of the third polarisability.
γ'	The total γ pertaining to EFISH in a microscopic system $\left(= \bar{\gamma}_z + \mu\beta_{zzz}/5k_BT\right)$.
$\bar{\gamma}_z$	The average component of γ in the Z direction.
Γ_{IJKL}	$\equiv \chi^{(3)}_{IJKL}$.
Γ_L	The third susceptibility of a two component solution.
Γ_G	The third susceptibility of BK7 glass.

λ Wavelength.

λ_{max} The wavelength of the longest wavelength absorption band maximum.

μ_{gn}^{i} The transition dipole moment in the ith direction between the energy levels g and n.

$\mu_{i}^{E=0}$ The dipole moment of a molecule under to application of no electric field.

μ^{e} The dipole moment of a molecule in the excited state.

μ^{0} The dipole moment of a molecule in the ground state.

$\mu_{g}^{Sph.,ell.}$ The dipole moment at the cyanine limit, calculated using spherical or ellipsoidal local fields.

μ_{x-ray} The dipole moment obtained from crystallographic studies.

$\Delta\mu_{Sph,ell}$ The difference between the excited and ground state dipole moments $\left(=\mu^{e}-\mu^{0}\right)$, calculated using either spherical or ellipsoidal local fields.

μ_{eg} The transition dipole pertaining to a two level system.

μ The molecular dipole moment vector.

$\overline{\mu}$ The orientation averaged dipole moment vector.

$\mu_{s}^{sph,ell}$ The solution state dipole moment obtained using spherical or ellipsoidal local fields.

$\mu_{g}^{sph,ell}$ The gas phase dipole moment obtained using spherical or ellipsoidal local fields.

v_{eg} The frequency of a two level transition.

v_{max} The frequency of the longest wavelength absorption band maximum.

v^{sol} The frequency of a transition in the solution state.

v^{0} The frequency of a transition in the gas phase.

$\Delta v_{eg}^{sol.}$ The difference between the gas and solution phase transition frequencies $\left(v_{eg}^{sol}-v_{eg}^{0}\right)$.

π The numerical constant pi.

π^* The symbol pertaining to the π^*-scale of solvent polarity.

π The symbol pertaining to the π-electrons of organic molecules.

θ An angle of transformation between Cartesian axes.

θ_f An electric field phase term pertaining to the free wave.

θ_b An electric field phase term pertaining to the bound wave.

θ_w The angle of the Maker wedge.

ρ The free charge density.

σ The symbol pertaining to the σ-electrons of organic molecules.

ω Angular frequency.

$\omega_\sigma, \omega_p, \omega_q, \omega_n$ The nth (σ, p, q) angular frequency involved with any equation.

ω_{eg} The angular frequency for transitions between the excited state and ground state.

ω_{ng}, ω_{mg} The frequencies of the transitions between the virtual states, m and n and the ground state, g.

$\xi(\omega)$ The extinction coefficient of a molecule as a function of ω.

∇ The nabla operator $\left(= \dfrac{\partial}{\partial x} + \dfrac{\partial}{\partial y} + \dfrac{\partial}{\partial z} \right)$.

Glossary of Tables and Figures.

xvii

Chapter 1

Non-Linear Optics and the Application to Organic Materials.

§1.1 Introduction.

To study non-linear optics (NLO) is to study the extension of linear optics where the interaction of light with a medium in which it propagates induces a change in the properties of the medium, or a change in the properties of the incident radiation. Such studies, which are dependent on the production of intense pulses of electro-magnetic radiation, have only been largely attainable with the advent of the laser [1], which as a result has allowed the demonstration of second harmonic generation (SHG) [2] and a number of other non-linear optical phenomina [3, 4].

Non-linear optical devices which are made principally from inorganic materials, such as gallium arsenide (GaAs), lithium niobate (LiNbO$_3$), and potassium dihydrogen phosphate (KDP), are now evident in a number of industrial and research environments. Crystals are used to double, triple, and combine the frequencies of light so that previously unattainable frequencies using lasers may be now be achieved in optical experiments or systems [5, 6]. Phase conjugation and optical bistability have been demonstrated in a number of applications [7, 8], and electro-optic modulators are commonly used in fibre optical systems applicable for today's telecommunication industry [9]. However, future requirements for the telecommunication industry include the need for high speed and high capacity systems, long system life times, and more efficient active devices [9, 10]. NLO polymers and organic materials have potential advantages over inorganic materials. Lower dielectric loss at microwave frequencies is

an inherent advantage of organic materials, as is a potential greater mechanical robustness, and ability to "tune" the non-linear response of an active device in a polymeric system, so that a more efficient device is possible [6, 11, 12, 13, 14]. Indeed, relatively simple chromophores, as will be subsequently seen, possess a non-linearity greater than 45 times than that of $LiNbO_3$ [11, 15, 16]. Organic materials have already had an increasing role in conventional semiconductor electronics, and have aided in the advancement of such technologies [17]. Examples of organic applications that are used today are photoresistive masks [17], multi-chip dielectrics [17], polymer optical fibres (POFs) [12, 17], and thermo-optic switches [18], and there are non-linear optical organic devices which are well on their way to becoming applicable to a number of systems [19, 20, 21, 22].

Even though a number of active chromophores have been incorporated into polymer structures, there is still a need develop chromophores that possess higher non-linearities, but are equally as robust and stable in a working environment [15, 23, 24, 25]. To do this, the molecular properties of an NLO chromophore in a working environment must be well understood. The effect of varying the composition, length or the extent of conjugation of the chromophore, and the involvement of intermolecular interactions on the linear and non-linear properties of a molecule have been well documented, both theoretically [26, 27, 28, 29, 30] and experimentally, where large molecules with high non-linear coefficients have been developed [11, 12, 15, 31, 32, 33, 34]. However, as the dielectric properties, non-linear optical properties, and size of a molecule increase, conceptual difficulties arise in the measurement and interpretation of the linear and non-linear properties of NLO chromophores. The validity of standard local field approximations is brought into question [35, 36, 37], and static electric fields for the purpose of poling are increasingly difficult to apply reliably to highly polar molecules [12]. The variation of molecular properties with the local environment is a process which is yet to be fully understood, even though there have been a number of investigations on the subject [28, 36, 38, 39].

The aim of this thesis is therefore to aid in the understanding of the behaviour of a particular class of organic materials, where the molecular linear and non-linear properties of the materials are expected to be large. Theoretical calculations on these and similar classes of material have predicted, not only large linear and non-linear responses, but also a novel evolution of such properties with the environment in which the molecule resides [40]. This study attempts to ascertain if the behaviour and size of the NLO properties of the materials are close to that predicted, by determining the dipole moment, first hyperpolarisability, and the transition energy of the materials as a function of the electric field experienced by them in solution.

In the next few sections an introduction to the basic concepts of non-linear optics will be given, before moving onto Chapter 2 where the theoretical aspects of the experiments discussed in this thesis are presented. This includes an analysis of the choice of local field involved with such calculations. Chapter 3 presents the materials under study with an overview of the work that has previously been conducted. Such work will be useful as a comparison to the results presented in this thesis. The results of experiments to measure the molecular dipole moment are presented in Chapter 4, where it is hoped to ascertain whether an ellipsoidal or spherical local field provides a better estimate of the dipole moment. Chapter 5 presents the method and results used to obtain the molecular hyperpolarisability using both spherical and ellipsoidal local fields in accordance with Chapter 4. In Chapter 6, the evolution of the energies of the optical absorption bands for the materials with the molecular environment are presented, where such behaviour is a convenient manifestation of changes to the linear and non-linear optical properties with environment. This leads finally to Chapter 7 where a comparison will be made between the experimental data obtained in this study and theoretical data obtained elsewhere.

§1.2 Non-Linear Optics.

It is stated in §1.1 that non-linear optics is the extension of linear optics under the application of intense pulses of light, where light interacts with or induces a change in the media in which light propagates. In the linear regime, the time dependent

induced polarisation of a material, $\mathbf{P}(t)$ is proportional to the applied electric field, $\mathbf{E}(t)$, such that [5, 6, 41]

$$\mathbf{P}(t) = \chi^{(1)}\mathbf{E}(t),$$

(1.2-1)

where $\chi^{(1)}$ is the linear susceptibility. For a lossless, dispersionless medium, the non-linear regime may be included by the expansion of (1.2-1) to a Taylor power series of electric field strength, [5, 6, 11, 42, 43]

$$\mathbf{P}(t) = \chi^{(1)}\mathbf{E}(t) + \chi^{(2)}\mathbf{E}^2(t) + \chi^{(3)}\mathbf{E}^3(t) + \ldots,$$

(1.2-2)

where $\chi^{(2)}$ and $\chi^{(3)}$ are the quadratic and cubic non-linear susceptibilities respectively. The electric field may be expressed in terms of sinusoidal components such that $\mathbf{E}(t) = \mathbf{E}_0 \cos(\omega t)$, where ω is the angular frequency, and $\mathbf{E}_0$ is the amplitude at $t = 0$. Applying this to (1.2-2) yields the expression

$$\mathbf{P}(t) = \chi^{(1)}\mathbf{E}_0 \cos(\omega t) + \chi^{(2)}\mathbf{E}_0^2 \cos^2(\omega t) + \chi^{(3)}\mathbf{E}_0^3 \cos^3(\omega t) + \ldots$$

(1.2-3)

which can be re-written as

$$\mathbf{P}(t) = \chi^{(1)}\mathbf{E}_0 \cos(\omega t) + \frac{1}{2}\chi^{(2)}\mathbf{E}_0^2\{1 + \cos(2\omega t)\} + \frac{1}{4}\chi^{(3)}\mathbf{E}_0^3\{3\cos(\omega t) + \cos(3\omega t)\} + \ldots$$

(1.2-4)

The inclusion of the non-linear terms in the description of the polarisation has given rise to components of the fundamental frequency at 2ω and 3ω, the processes of which are thus defined as second and third harmonic generation, respectively. A number of other effects, such as sum and difference frequency generation, and Pockel's effect may be realised by developing (1.2-2) in a similar manner to that above.

If anisotropic media are to be considered, then the application of an electric field in a particular direction will result in polarisations in other directions as well as the

principal direction of the applied field. The polarisation, electric fields and susceptibilities are therefore described by tensorial relationships (dropping the time dependency (t) for neatness)

$$P_i = \chi_{ij}^{(1)}E_j + \chi_{ijk}^{(2)}E_jE_k + \chi_{ijkl}^{(3)}E_jE_kE_l$$

<div align="right">(1.2-5)</div>

where i, j, k, and l are the tensorial indices for the crystal directions x, y, and z. It is also necessary to consider the frequency of each electric field applied to the medium. If the second order polarisation, for example under the application of sum frequency generation, is expressed considering the fundamental and resulting frequencies such that

$$P_i^{(2)}(\omega_3 = \omega_1 + \omega_2) = \chi_{ijk}^{(2)}(\omega_3 = \omega_1 + \omega_2)E_j(\omega_1)E_k(\omega_2)$$

<div align="right">(1.2-6)</div>

it is possible to see, by permutation of all the frequencies and tensorial indices, that a large number of complex numbers are needed to describe any one interaction for $\chi^{(2)}$. However, a number of permutation symmetries and conditions may be applied to (1.2-5) so that these combinations are reduced. x, y and z are often represented by the numbers 1, 2, and 3 respectively, and a common shorthand notation is given for combinations of j and k in the form of yz, xz, and xy, which are represented by the numbers 4, 5, and 6 respectively. For these relations to be valid, intrinsic permutation symmetry must be applicable, i.e. $\chi_{ijk}^{(2)} = \chi_{ikj}^{(2)} = \chi_{kji}^{(2)}$ etc., where it can be shown that $\chi^{(2)}$ remains unchanged under such permutations [6, 44, 45]. The susceptibility may then be expressed as $\chi_{xyz}^{(2)} \equiv \chi_{14}^{(2)}$ for example.

Since the polarisation is a physical and measurable quantity, it is therefore real. Furthermore, since the electric field is described by a complex number, it can be shown for second harmonic generation that $\chi^{(2)}$ must also be real, as similarly for third harmonic generation, it may be shown that $\chi^{(3)}$ is complex. Full permutation symmetry may be applied to (1.2-5) for a lossless medium where the components of

$\chi^{(2)}$ (i.e. the frequencies) are real, and the indices of the frequencies are permuted with respect to the tensorial indices [6]. In addition, Kleinman's [46] symmetry may be invoked under the conditions where the fundamental and resulting frequencies are far from resonance, thus $\chi^{(2)}$ is essentially independent of the frequency of interaction and all indices may be permuted independently [6, 46].

Analysis of the tensorial nature of the polarisation also gives rise to the conclusion that second order effects (i.e. those dependent on $\chi^{(2)}$) are only present in anisotropic or non-centrosymmetric media. In centrosymmetric media, inversion symmetry must be evident, i.e. upon inversion the polarisation, $P \rightarrow -P$, and the electric field, $E \rightarrow -E$. Equating the second order polarisation only, upon inversion

$$-P_i^{(2)} = \chi_{ijk}^{(2)}\left(-E_j\right)\left(-E_k\right) = \chi_{ijk}^{(2)} E_j E_k .$$

(1.2-7)

This condition is only possible if $\chi_{ijk}^{(2)} = 0$, therefore in centrosymmetric media, in addition to linear effects ($\chi^{(1)}$), only odd order non-linear effects (i.e. $\chi^{(3)}$, $\chi^{(5)}$ etc.) will be observed.

The application of these conditions to (1.2-5) for second harmonic generation may reduce the number of independent elements of $\chi^{(2)}$ to 10 [5, 6, 11]. Any additional, crystalline or molecular symmetries may reduce this number further so that in many cases only one or two independent coefficients remain.

§1.3 The Anharmonic Oscillator Model.

An atom or collection of atoms under the influence of a low intensity alternating electric field will oscillate in a manner which can be described in the linear regime by the harmonic oscillator model [5, 6, 41]. To consider NLO effects, the potential energy, $V(x)$ and restoring force, $F(x)$ of an electron may be written as a Taylor expansion of the co-ordinate of the electron, x_e. For the inclusion of $\chi^{(2)}$ effects however, the anharmonic oscillator model should be considered where the

6

potential energy of an electron should fulfill the condition $V(x) \neq V(-x)$ for moderate electric field strengths in non-centrosymmetric media [5, 6]. This condition is fulfilled by the inclusion of the second term for the potential in equation (1.3-1), where

$$\mathbf{F} = -\frac{\partial V(x)}{\partial x_e} = -\left(m_e \omega_0^2 x_e + m_e B_1 x_e^2 + m_e B_2 x_e^3 + \ldots\ldots\right)$$

$$V(x) = \frac{m_e \omega_0^2}{2} x_e^2 + \frac{m_e}{3} B_1 x_e^3 + \frac{m_e}{4} B_2 x_e^4 + \ldots\ldots$$

$$(1.3\text{-}1)$$

Here, B_1 and B_2 are constants of proportionality, m_e is the mass of an electron and ω_0 is the natural frequency of the resonator. Allowing for an asymmetric potential results in a larger restoring force in one polarisation direction than the other, and the asymmetry of the polarisation gives rise to the production of harmonic frequencies, as previously discussed in §1.1.

To relate the non-linear polarisation to the applied field, the equation of motion for an electron is solved with the inclusion of the restoring force

$$\frac{\partial^2 x_e}{\partial t^2} + 2\gamma_d \frac{\partial x_e}{\partial t} + \omega_0^2 x_e + B_1 x_e^2 + B_2 x_e^3 = -\frac{e\mathbf{E}(t)}{m_e},$$

$$(1.3\text{-}2)$$

where e is the charge of an electron, and γ_d is the damping constant. In the linear regime, the solution of (1.3-2) results in the displacement amplitude, $x^{(1)}(\omega)$ which is found to be [5, 6, 41]

$$x^{(1)}(\omega) = -\frac{e}{m_e} \frac{\mathbf{E}(\omega)}{\left(\omega_0^2 - 2i\gamma_d \omega - \omega^2\right)}.$$

$$(1.3\text{-}3)$$

Since the polarisation may be expressed as $\mathbf{P} = -Nex$, where N is the electron density, and since both the electron co-ordinate and electric field are sinusoidal, this suggests that the polarisation is also sinusoidal and increases in magnitude as the frequency

approaches resonance, at ω_0. In addition, since $P^{(1)}(\omega) = \chi^{(1)}(\omega)E(\omega)$, an expression for the linear susceptibility may be found

$$\chi^{(1)}(\omega) = \frac{Ne^2}{m_e} \frac{1}{\left(\omega_0^2 - 2i\gamma_d\omega - \omega^2\right)}$$

(1.3-4)

which also increases as the interaction frequency approaches resonance.

For the second order non-linear case, solutions for (1.3-2) may be found for specific frequencies, providing the anharmonic term is much smaller than the linear term which is usually the case with NLO coefficients. Considering second harmonic generation at frequency 2ω, the harmonic displacement amplitude, $x_e^{(2)}(2\omega)$ is found to be [5, 6]

$$x_e^{(2)}(2\omega) = -\frac{B_1(e/m_e)^2 E^2(\omega)}{\left(\omega_0^2 - 4i\gamma_d\omega - 4\omega^2\right)\left(\omega_0^2 - 2i\gamma_d\omega - \omega^2\right)^2} .$$

(1.3-5)

As with (1.3-4), an expression for the second order susceptibility may be found. With the addition of (1.3-4) to (1.3-5) this is found to be

$$\chi^{(2)}(2\omega) = \frac{B_1 m_e}{N^2 e^3} \chi^{(1)}(2\omega)\left[\chi^{(1)}(\omega)\right]^2 ,$$

(1.3-6)

and thus the second order susceptibility at 2ω is related to the linear susceptibility at both ω and 2ω. Furthermore, the dispersion of $\chi^{(2)}$ is adequately demonstrated with (1.3-6) which suggests that $\chi^{(2)}$ increases in magnitude when either frequency (ω or 2ω) approaches the resonance frequency. Similar, more complicated expressions may be developed for higher order susceptibilities where the NLO coefficients become increasingly dependent upon the interaction frequencies.

Though this model works well in a few real systems, such as with semiconductors, and it provides an insight into the basic physical processes involved, the main inadequacy of the model is that it cannot describe the complete resonance nature of complex systems, such as organic molecules, since it uses only one natural frequency. Other models therefore need to be employed.

§1.4 Propagation of Second Harmonic Light.

Before considering further the non-linear properties of a single molecule, it is necessary to consider the propagation of a harmonic wave through a medium which consists of a series of oscillating dipoles. For this, Maxwell's equations are utilised to develop the non-linear wave equation. For a medium that is non-magnetic, and contains no free charges (ρ) and no free currents (J), the Maxwellian and associated equations, expressed in Gaussian units[1] are [5, 6, 11]

$$\nabla \cdot \mathbf{D} = 4\pi\rho, \qquad \nabla \cdot \mathbf{B} = 0,$$

$$\nabla \times \mathbf{E} = -\frac{1}{c}\frac{\partial \mathbf{B}}{\partial t}, \qquad \nabla \times \mathbf{H} = \frac{1}{c}\frac{\partial \mathbf{D}}{\partial t} + \frac{4\pi}{c}\mathbf{J},$$

$$\rho = 0, \quad \mathbf{B} = \mathbf{H}, \qquad \mathbf{J} = 0, \quad \mathbf{D} = \mathbf{E} + 4\pi\mathbf{P},$$

(1.4-1)

where c is the speed of light, **D** is the displacement, and **B** is the magnetic flux. The wave equation is thus developed by taking the curl of the curl of **E** in the usual manner, where for a dispersive and non-dissipative medium the following equation is derived [6]

$$\nabla^2 \mathbf{E}_n = \frac{\varepsilon^{(1)}(\omega_n)}{c^2} \cdot \frac{\partial^2 \mathbf{E}_n}{\partial t^2} + \frac{4\pi\omega_n^2}{c^2}\mathbf{P}_n^{NL}$$

(1.4-2)

---

[1] There is often confusion over units. In this study, most molecular properties are presented in electrostatic units (esu) or the cgs system. Conversion factors to the MKS system can be found in Appendix III.

where ω_n is the nth specific angular frequency, $\varepsilon^{(1)}$ is the frequency dependent linear dielectric tensor, and $\mathbf{P}_n^{NL}$ is the non-linear part of the polarisation given by (1.2-5). For simplicity the direction of propagation is taken to be the z-direction, thus the second derivatives with respect to x and y associated with ∇^2 reduce to zero.

With the specific case of second harmonic generation, an analysis of $\chi^{(2)}$ requires the analysis of the interaction of three travelling waves, two for the fundamental frequency and one for the harmonic. These are of the form

$$E_1(z,t) = E_1(z)e^{i(\omega_1 t - k_1 z)} + c.c.$$
$$E_2(z,t) = E_2(z)e^{i(\omega_2 t - k_2 z)} + c.c.$$
$$E_3(z,t) = E_3(z)e^{i(\omega_3 t - k_3 z)} + c.c.$$

$$(1.4\text{-}3)$$

where $k_n = n_n \omega_n / c$ (subscript n = 1, 2, 3), $n_n = \left[\varepsilon^{(1)}(\omega_n)\right]^{1/2}$, c.c. stands for the complex conjugate of the first terms in (1.4-3), and $\omega_3 = \omega_2 + \omega_1 = 2\omega$. Thus, $\mathbf{E}_1$ and $\mathbf{E}_2$ are identical, and the total electric field at any point is the sum of these waves. The non-linear polarisation, according to (1.2-5), for each wave is [5, 6, 11, 42, 47]

$$P_1(z,t) = 2\chi^{(2)} E_2^*(z)E_3(z)e^{i[(\omega_3 - \omega_2)t - (k_3 - k_2)z]}$$
$$P_2(z,t) = 2\chi^{(2)} E_3(z)E_1^*(z)e^{i[(\omega_3 - \omega_1)t - (k_3 - k_1)z]}$$
$$P_3(z,t) = 2\chi^{(2)} E_2(z)E_1(z)e^{i[(\omega_1 + \omega_2)t - (k_1 + k_2)z]}$$

$$(1.4\text{-}4)$$

where, again $\mathbf{P}_1$ and $\mathbf{P}_2$ are in effect identical for second harmonic generation. Providing the fundamental is not depleted while generating the second harmonic and $\chi^{(2)}$ is treated as a slowly varying function of z, then the three equations may be reduced to one for the second harmonic and substituted into (1.4-1) to obtain the following equation [6, 11, 15, 47, 48]

$$E^{2\omega}(z) = E^{2\omega}e^{ik_{2\omega}z} - \frac{8\pi\omega^2}{c^2\left(k_{2\omega}^2 - k_\omega^2\right)}\chi^{(2)}(z)\left[E^\omega(z)\right]^2 e^{ik_\omega z},$$

<div align="right">(1.4-5)</div>

where $k_{2\omega} = 2n_{2\omega}\omega/c$, $k_\omega = 2n_\omega\omega/c$. $E^{2\omega}$ is often defined as the second harmonic free wave amplitude which is generated at the surface of a non-linear medium. The second term of (1.4-5) represents the second harmonic bound wave which is, as subsequently shown, coupled to the fundamental wave. A more detailed derivation of (1.4-5) is given in Appendix II.

Squaring the field amplitudes yields second harmonic intensity, [5]

$$I^{2\omega} \propto 16\pi^2\left(\frac{2\omega}{c}\right)^4\left(I^\omega\right)^2\left(\chi^{2\omega}\right)^2 l^2 \frac{\sin^2\left(\Delta kl/2\right)}{\left(\Delta kl/2\right)^2}$$

<div align="right">(1.4-6)</div>

which is proportional to the fundamental intensity, I^ω, the interaction length squared (l^2), and a sinc^2 $\left(\left(\sin(x)/x\right)^2\right)$ function of the phase mismatch between the fundamental and second harmonic waves, $\Delta k = k_{2\omega} - k_\omega$. As the harmonic wave propagates through a non-linear medium, light is coupled from the fundamental wave to the second harmonic wave, resulting in a build up of second harmonic intensity. This coupled wave is often known as the second harmonic bound wave. The coherence length may be defined as $l_c = \pi/\Delta k$ which is the length over which the fields at ω and 2ω dephase by π. Thus, a well phase matched material system possesses a large coherence length. When $\Delta k = 0$, i.e. $k_\omega = k_{2\omega}$ and a material is completely phase matched, the sinc^2 function approaches unity, and the intensity is only dependent upon $\left(\chi^{(2)}\right)^2$ and the squares of the fundamental intensity and propagation distance. At this point the coherence length is infinite. Furthermore, by eliminating the phase matching conditions, it is possible to obtain an unknown value of $\chi^{(2)}$ by comparison to a material of known $\chi^{(2)}$. This is the basic premise of many second order non-linear optical experiments.

§1.5 Quantum Mechanical Approach.

Quantum mechanics can be used to calculate explicitly the expressions for the non-linear optical susceptibilities. Furthermore, such expressions can show the dependence of the susceptibility on the numerous transition moments and natural frequencies of material systems.

The calculation of the first, second and third susceptibilities involves the perturbation solution to Schrödinger's equation where a similar power series to that of (1.2-5) is involved. In the case of sum frequency generation, the second order susceptibility may be approximated, for the non-resonant case, to [6]

$$\chi_{ijk}^{(2)}\left(-\omega_{\sigma};\omega_{p},\omega_{q}\right) = \frac{N}{\hbar^2} \wp_F \sum_{nm} \frac{\mu_{gn}^i \mu_{nm}^j \mu_{mg}^k}{\left(\omega_{ng} - \omega_{\sigma}\right)\left(\omega_{mg} - \omega_{p}\right)}$$

(1.5-1)

where $\omega_{\sigma} = \omega_{p} + \omega_{q}$, i, j, and k are the usual tensorial indices, μ is the transition dipole for transitions between the ground state, g and the excited states, n and m, and $\wp_F$ is the full permutation operator which is defined so that the expression is summed over all permutations of the frequencies, $-\omega_{\sigma}$, ω_{p} and ω_{q}, and all permutations of tensorial indices. The expression allows for the summation over all excitation states, thus allowing for more than one resonant frequency. The negative sign for ω_{σ} refers to
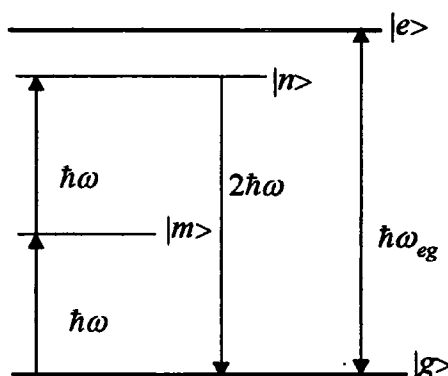
Figure 1.5-1: Quantum-level picture describing second harmonic generation.

12

the fact that a photon is emitted rather than absorbed.

Considering purely the two state case, the summation sign can be removed and the process involved with second harmonic generation investigated (Figure 1.5-1). Two photons of fundamental frequency ω are absorbed, exciting a molecule in the ground state first to a virtual level, $|m\rangle$ then to a second virtual level, $|n\rangle$. Since the lifetime of these virtual energy levels is extremely short, the molecule then relaxes back to the ground state quickly, emitting a photon of twice the energy of the fundamental photons. Thus, the frequency of the fundamental beam has been doubled. The resonant case is obtained when the virtual levels lie close to a natural energy level of a material system, $|e\rangle$, with a transition energy $\hbar\omega_{eg}$. Since full permutation symmetry is no longer valid under such situations, the expression for $\chi^{(2)}$ must be replaced by a function which allows for the ordering of the frequencies and states involved with such interactions [6].

§1.6 Microscopic Approach.

To describe the polarisation of individual molecules in solution, the dipole approximation is often used in an analogous manner to that of the macroscopic description of the polarisation. It is possible to see by comparison to the general form of the Taylor series, that the total polarisation, p of a molecule is given as [11, 49, 50, 51]

$$p_i = \mu_i^{E=0} + \frac{\partial \mu_{ij}}{\partial E_j}\bigg|_{E=0} E_j + \frac{1}{2!}\frac{\partial^2 \mu_{ijk}}{\partial E_j \partial E_k}\bigg|_{E=0} E_j E_k + \frac{1}{3!}\frac{\partial \mu_{ijkl}}{\partial E_j \partial E_k \partial E_l}\bigg|_{E=0} E_j E_k E_l + \ldots\ldots$$
$$= \mu_i^{E=0} + \alpha_{ij} E_j + \beta_{ijk} E_j E_k + \gamma_{ijkl} E_j E_k E_l + \ldots\ldots$$

(1.6-1)

where i, j, k, and l are the usual tensorial indices, and E is the local or microscopic field applied to the molecule. $\mu^{E=0}$ is the molecular dipole moment under the influence of no internal field, defined by $\mu = qd_q$ [35], where q is the charge and d_q is the charge-separation. α is the polarisability, defined by the rate of change of the dipole moment

with respect to applied field, and similarly, β and γ are the second and third polarisabilities, defined by the second and third differentials with respect to the internal field, multiplied by numerical factors. Using the definition for the polarisability and ignoring the tensor properties of each parameter, it is possible to show that

$$\beta = \frac{1}{2}\frac{\partial \alpha}{\partial E}, \text{ and } \gamma = \frac{1}{6}\frac{\partial^2 \alpha}{\partial E^2} = \frac{1}{3}\frac{\partial \beta}{\partial E}.$$

(1.6-2)

It is also possible to relate the polarisability to the linear susceptibility, via the equation [35]

$$\chi_{ij}^{(1)}(\omega) = Nf^{\omega}\alpha_{ij}(\omega)$$

(1.6-3)

where f^{ω} is the local field factor relating the macroscopic or external electric field to the microscopic electric field. β and γ may be related to the second and third susceptibilities in a similar manner, depending on the process involved. For example, with second and third harmonic generation respectively [6, 11],

$$\chi_{ijk}^{(2)}(2\omega) = Nf^{2\omega}\left(f^{\omega}\right)^2\beta_{ijk}(2\omega)$$
$$\chi_{ijkl}^{(3)}(3\omega) = Nf^{3\omega}\left(f^{\omega}\right)^3\gamma_{ijkl}(3\omega)$$

(1.6-4)

where the local field factors are included for all fundamental and harmonic fields. A description of the local field factors involved with these equations will be provided in Chapter 2.

§1.7 The Two-Level Model.

It has already been shown that a quantum mechanical description may be applied to a macroscopic system. In a similar manner, the first hyperpolarisability may be described as [6, 11]

$$\beta_{ijk}(-2\omega;\omega,\omega) = \frac{e^3}{2\hbar^2} \wp_F \sum_{nm} \frac{\mu^i_{gn}\mu^j_{nm}\mu^k_{mg}}{(\omega_{ng} - 2\omega)(\omega_{mg} - \omega)}$$

(1.7-1)

where μ is the molecular transition dipole for transitions between the ground state, g and the excited states n and m, and e is the charge on an electron. By considering the specific case where only transitions involving two levels are involved, and that the transition dipole moments lie parallel to each other, of which only a single diagonal matrix element dominates the contribution to β (in the *zzz* direction for example), β may then be approximated to [6, 11, 52, 53,]

$$\beta_{zz}(-2\omega;\omega,\omega) \approx \frac{3e^2\hbar^2}{2m} \frac{\omega_{eg} f_{osc.} \Delta\mu}{(\omega_{eg}^2 - \omega^2)(\omega_{eg}^2 - 4\omega^2)}$$

(1.7-2)

where ω_{eg} is the angular frequency of an energy transition and $\Delta\mu$ is the difference between the ground and excited state dipole moments of the molecule $(\mu^e - \mu^0)$. The oscillator strength, $f_{osc.}$ is related to the transition dipole, μ_{eg} via the equation [52, 54]

$$f_{osc} = \frac{8\pi^2}{3} \frac{m_e\omega_{eg}}{\hbar e^2} \mu_{eg}^2 ,$$

(1.7-3)

and is found by estimating the area under the absorption band, such that

$$\int_{Band} \xi(\omega) d\omega = \frac{N_a e^2}{4m_e \ln 10\varepsilon_0 c} f_{osc.}$$

(1.7-4)

where $\xi(\omega)$ is the extinction coefficient as a function of angular frequency.

The expression for β, given by (1.7-2), may be divided into two parts with the aid of (1.7-3); a frequency independent term, $\beta(0)$ which is directly related to the properties of the molecule, and a dispersion term, $F(\omega)$ which is dependent on the

15

fundamental and second harmonic frequencies in relation to the transition frequency, ω_{eg}

$$\beta_{zzz}(-2\omega;\omega,\omega) = \beta(0)F(\omega) = \frac{3\mu_{eg}^2 \Delta\mu}{2\varepsilon_0 \hbar \omega_{eg}^2} \frac{1}{\left(1-\left(\omega^2/\omega_{eg}^2\right)\right)\left(1-\left(4\omega^2/\omega_{eg}^2\right)\right)}.$$

(1.7-5)

Often equation (1.7-5) is used account for the frequency used to measure β, where the extrapolation of the measurement of $\beta(\omega)$ to the zero frequency component, $\beta(0)$ allows for relatively easy comparisons between different molecules.

By assuming two levels, a similar problem arises to that of the anharmonic oscillator model when more than one transition is evident, and it is often desirable to invoke a number of excited states. However, the two-level approximation has been proven on a number of occasions to be a good enough approximation for a number of applications [11], though one must be aware that for new and novel compounds this is not always the case.

§1.8 Applications to Molecular Systems.

The general form of an organic molecule consists of a number of carbon and hydrogen atoms that are bonded to each other in various ways by the covalent "sharing" of electrons in the upper electronic orbitals of the atoms. Other elements, such as nitrogen, sulphur and phosphorous, may also be included. The types of bonding and subsequent arrangement of atoms depends upon the degree of orbital overlap between them. With carbon - carbon bonds, three types of bond are possible of which two are discussed here. σ-bonds (denoted by a single bond (see Figure 1.8-1)) are formed by "sharing" one electron in the outer shell of each atom. These are highly localised thus only slightly perturb under the application of an electric field, but nonetheless contribute significantly to the properties of a molecule. π-bonds (represented by double bonds), are formed in addition to σ-bonds by "sharing" an additional electron from each carbon atom. π-electrons are highly delocalised and perturb a great deal under the influence of an electric field. Molecules that possess

16
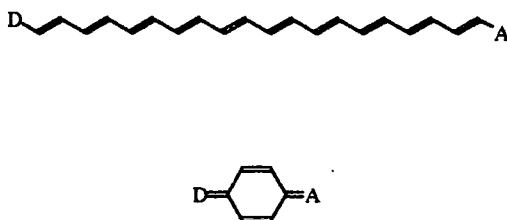
Figure 1.8-1: Examples of a donor - acceptor molecules.

combinations of double and single bonds are often defined as conjugated molecules (see Figure 1.8-1). The delocalisation of π-electrons allows charge to "move" along the conjugated structure under the influence of an electric field, allowing larger dipole moments, polarisabilities, and hyperpolarisabilities to be obtained than is usual with purely σ-bonded molecules. The polarisability of such molecules can be further enhanced by the addition of electron donors and acceptors bonded to either end of the molecule. This also allows for a degree of non-centrosymmetry to be introduced to the molecule, which is necessary for second order non-linear optics. With a number of molecules, the combination of a conjugated system with strong electron donating and withdrawing groups allows a large amount of charge (in comparison to most molecules) to transfer from one end of the molecule to the other. These can be classed in various ways, but they are often termed charge-transfer (CT) molecules and occasionally as zwitterionions (i.e. partially-ionic). As mentioned earlier, it is usual for these to posses large dipole moments, polarisabilities, and hyperpolarisabilities.

The properties of a molecule in any one direction can be considered as the vectorial sum of the properties of the individual bonds of the molecule. Furthermore, the contibution to the dipole moment, polarisability, and hyperpolarisability due to σ-bonds and π-bonds are often considered seperately. So for example, σ-contributions to the dipole moment and hyperpolarisability are thus termed as $\mu_{add.}$ and $\beta_{add.}$ respectively where they are summed over all contributing σ-bonds. In addition, π-contributions for CT molecules are often defined as μ_{CT} and β_{CT}, but this time, such contributions are usually only along the direction of the conjugation since this is the most polarisable direction. The total dipole moment and hyperpolarisability in the direction of the conjugation is thus defined as

$$\mu = \mu_{add.} + \mu_{CT}, \text{ and } \beta = \beta_{add.} + \beta_{CT}$$

where $\mu_{add.}$ and $\beta_{add.}$ are in the direction of charge-transfer only. Since CT contributions to the total dipole moment, polarisability, and hyperpolarisability are large, μ_{CT} and β_{CT} are usually dominant over $\mu_{add.}$ and $\beta_{add.}$. Thus, the total dipole moment and hyperpolarisability can be considered sometimes as resulting purely from CT contributions.

Since in most experimental situations the macroscopic non-linearity is probed, conceptual difficulties arise when attempting to obtain molecular properties. Due to symmetry conditions, the non-centrosymmetric molecules must lie in a non-centrosymmetric envorinment to obtain a macroscopic non-linearity. If for example, two molecules lie anti-parallel to each other, the second harmonic contribution from each molecule would cancel and no second harmonic signal would be observed. Unfortunately, many molecular crystals tend to be centrosymmetric structures rendering such crystals useless for second order NLO applications. The random orientation of molecules doped into polymers or in solution allows the formation of centrosymmetric systems also. However with these situations, the centrosymmetry of the macroscopic system can be broken by utilisng the polar nature of individual molecules and applying static electric fields such that the molecules lie in the same direction. The technique of Electric Field Induced Second Harmonic generation (EFISH) is a process that does precisely this, and this is utilised in this study to measure the hyperpolarisability of various molecules.

In Chapter 2, some of the theoretical aspects with respect to the measurement of the transition frequency, the dipole moment, and the hyperpolarisability of a molecule, will be discussed bearing in mind the above considerations.

[1] T. H. Maiman., *Nature*, **187**, 493, (1960).

[2] P. A. Franken, A. E. Hill, C. W. Peters, G. Weinriech, *Phys. Rev. Lett.*, **7**, 118, (1961).

[3] F. S. Chen, *J. Appl. Phys.*, **38**, 3418, (1967).

B. F. Levine, C. G. Bethea, *Appl. Phys. Lett.*, **24**, 445, (1974).

G. Mayer, *R. Acad. Sci.*, **B267**, 54, (1968).

P. D. Maker, R. W. Terhune, M. Nissenoff, C. M. Savage, *Phys. Rev. Lett.*, **8 (1)**, 21, (1962).

R. W. Terhune, P. D. Maker, C. M. Savage, *Phys. Rev. Lett.*, **14**, 681, (1965).

J. A. Armstrong, N. Bloembergen, J. Ducuing, P. S. Pershan, *Phys. Rev.*, **127 (6)**, 1918, (1962).

D. L. Weinberg, J. Chem. Phys., 47, 1307, (1967).

[4] K. Clays, A. Persoons, *Phys. Rev. Lett.*, **66**, 2980, (1982).

M. Evans, S. Kielich, *Modern NLO, (3)*, Chemical Physics Series, **LXXXV**; K. Clays, A. Persoons, L. De Maeyer, *Hyper-Rayleigh Scattering in Solution*, 455, (1994).

[5] A. Yariv, *Optical Electronics*, 3rd Ed., Holt Rinehart and Winston, London, (1985).

[6] R. W. Boyd, *Non-Linear Optics*, Academic Press Inc., London, (1992).

[7] D. H Houston, A. A. Ballman, P. Bhattacharya, G. J. Bjorklund *et al*, *Appl. Optics*, **26 (2)**, 211, (1987).

[8] A. C. Walker, *Opt. Comp. and Processing*, **1 (1)**, 91, (1991).

[9] J. M. Senior, *Optical Fibre Communications; Principles and Practice.*, **Second Ed.**, Prentice Hall, London, (1992).

[10] M. N. Islam, *Ultrafast Fibre Switching Devices and Systems*; Cambridge Studies in Modern Optics, **12**, Cambridge University Press, Cambridge, (1992).

[11] D. S. Chemla, J. Zyss, *Non-Linear Optical Properties of Organic Molecules and Crystals.*, **1 & 2**, Academic Press Ltd., London, (1987).

[12] L. A. Hornak, *Polymers for Lightwave and Integrated Optics; Technology and Applications*, Marcel Dekker Inc., (1992).

[13] J. Zyss, *J. Mol. Elec.*, **1**, 25, (1985).

[14] G. A. Lindsay, *Second order Non-Linear Optical Polymers; An Overview.*, **Chapter 1**, 1: *ACS Symposium Series*, **601**, (1995).

[15] J. Messier, F. Kajzar, P. Prasad, *Organic Molecules for Non-Linear Optics*, NATO ASI Series, *Series E: Applied Sciences*, **194**, Kluwer Academic Publishers, London, (1991).

[16] M. Barzoukas, D. Josse, P. Fremaux, J. Zyss, J. F. Nicoud, J. O. Morley, *J. Opt. Soc. Am. B*, **4 (6)**, 977, (1987).

[17] C. P. Wong, *Polymers for Electronic and Photonic Applications*, Academic Press Inc., (1993).

[18] "Polymers Muscle in on Switching Technology", *Fibre Systems News*, November, **1 (6)**, 24, (1997).

[19] S. Allen, R. T. Murray, *Physica Scripta*, **T23**, 275, (1988).

R. Dagani, *Chemical and Engineering News*, **March 4th**, 22, (1994).

S. R. Marder, J. W. Perry, *Science*, **263**, 1706, (1994).

J. Zyss., *Scientific American*, **October Ed.**, 33, (1990).

[20] G. C. Bjorklund, S. Ducharme, W. Fleming, D. Jungbauer, W. E. Moerner, J. D. Swalen, R. J. Tweig, C. G. Wilson, D. Y. Yoon, *Applications of Organic Second-Order NLO Materials*, **Chapter 13**, 216: ACS Symposium Series, **455**, *Materials for NLO; Chemical Perspectives*, Edited by S. R. Marder, J. E. Sohn, G. D. Stucky, American Chemical Society, Washington, (1991).

[21] L. W. Shacklette, R. A. Norwood, L. Eldada, C. Glass, D. Nguyen, C. Paga, B. Xu, S. Yin, J. T. Yardley, *Proc. SPIE*, **3147**, 222, (1997).

A. Knoesen, S. A. Hamilton, D. R. Yankelevich, R. T Weverka, R. A. Hill, G. C. Bjorklund, *Proc. SPIE*, **3147**, 233, (1997).

Y. Shi, W. Wang, D. J. Olsen, W. Lin, J. H. Bechtel, *Proc. SPIE*, **3147**, 259, (1997).

[22] M. G. Kuzyk, *Proc. POF Conf.*, Hawaii, 86, (1997).

N. Keil, H. Yao, C. Zawadzki, *Proc. POF Conf.*, Hawaii, 115, (1997).

[23] K. M. White, P. K. Kitipichai, C. V. Francis, *Appl. Phys. Lett.*, **66 (23)**, 3099, (1995).

D. Burland, R. D. Miller, C. A. Walsh, *Chem. Rev.*, **94**, 31, (1994).

A. Garito, R. F. Shi, M. Wu, *Physics Today*, **May Ed.**, 51, (1994).

W. E. Moerner, S. M. Silence, Chem. Rev., 94, 127, (1994).

[24] *Nato Advanced Research Workshop*, La Rochelle, August 27 - 31, (1990), Published in Reference [14].

[25] G. J. Bjorklund, R. W. Boyd, G. Garter, A. F. Garito, R. S. Lytel, G. R. Meredith, P. Prasad, J. Stamatoff, M. Thakur, *Organic and Polymeric Materials*, Published in Reference [15], 227.

[26] D. N. Bertran, *Electronic Hyperpolarisability and Chemical Structure*, **Chapter 5**, 89, D. F Eaton, *Non-Linear Optical Materials; The Great and Near Great.*, **Chapter 8**, 129: ACS Symposium Series, **455**, *Materials for NLO; Chemical Perspectives*, Edited by S. R. Marder, J. E. Sohn, G. D. Stucky, American Chemical Society, Washington, (1991).

[27] J. L. Brédas, C. Adant, P. Tackx, A. Persoons, P. M. Pierce, *Chem. Rev.*, **94**, 243, (1994).

D. R. Kanis, M. A. Ratner, T. J. Marks, Chem. Rev., 94, 195, (1994).

G. Bourhill, J. L. Brédas, L.-T. Cheng, S. R. Marder, F. Meyers, J. W. Perry, B. G. Tiemann, *J. Am. Chem. Soc.*, **116**, 2619, (1994).

F. Meyers, S. R. Marder, B. M. Pierce, J. L. Brédas, *Chem. Phys. Lett.*, **228**, 171, (1994).

F. Meyers, S. R. Marder, B. M. Pierce, J. L. Brédas, *J. Am. Chem. Soc.*, **116**, 10703, (1994).

[28] J. L. Brédas, Science, 363, 487, (1994).

S. R. Marder, J. W. Perry, G. Bourhill, C. B. Gorman, B. G. Tiemann, K. Mansour, *Science*, **261**, 186, (1993).

S. R. Marder, D. N. Bertran, L.-T. Cheng, *Science*, **252**, 103, (1991).

K. Clays, E. Hendrickx, M. Triest, T. Verbiest, A. Persoons, C. Dehu, J. L. Brédas, *Science*, **262**, 1419, (1993).

S. R. Marder, L.-T. Cheng, B. G. Tiemann, A. C. Friedli, , M. Blanchard-Desce, J. W. Perry, J. Skindhøj, *Science*, **263**, 511, (1994).

S. R. Marder, C. B. Gorman, F. Meyers, J. W. Perry, G. Bourhill, J. L. Brédas, B. M. Pierce, *Science*, **265**, 632, (1994).

I. D. L. Albert, T. J. Marks, M. A. Ratner, *J. Phys. Chem.*, **100**, 9714, (1996).

[29] T. Kogej, F. Meyers, S. R. Marder, R. Silbey, J. L. Brédas, Proceedings of the International Conference on Synthetic Metals, 1996. To be Published in Synth. Met..

[30] A. A. Hasanein, *AB Initio Computations of Polarisabilities and Hyperpolarisabilities of Atoms and Molecules.*, 415, Modern NLO., Part 2, Edited by M. Evans, S. Keilich, *Advances in Chemical Physics Series*, **LXXXV**, (1993).

[31] C. A. van Walree, O. Franssen, A. W. Marsman, M. C. Flipse, L. W. Jenneskens, *J. Chem. Soc., Perkin Trans. 2*, 799, (1997).

M. Stähelin, B. Zysset, M. Ahlheim, S. R. Marder, P. V. Bedworth, C. Runser, M. Barzoukas, A. Fort, *J. Opt. Soc. Am. B*, **13 (11)**, 2401, (1996).

R. A. Huijts, G. L. J. Hesselink, *Chem. Phys. Lett.*, **156 (2-3)**, 209, (1989).

[32] L.-T. Cheng, W. Tam, S. H. Stevenson, G. R. Meridith, G. Rikken, S. R. Marder, *J. Chem. Phys.*, **95**, 10631, (1991).

L.-T. Cheng, W. Tam, S. R. Marder, A. E. Stiegman, G. Rikken, C. W. Spangler, *J. Chem. Phys.*, **95**, 10643, (1991).

J. Zyss, *J. Chem. Phys.*, **71 (2)**, 909, (1979).

[33] S. R. Marder, B. Kippelen, A. K. Y. Jen, N. Peyghambarian, *Nature*, **388**, 845, (1997).

[34] T. Brotin, C. Andraud, I. Ledoux, S. Brasselet, J. Zyss, M. Perrin, A. Thozet, A. Collet, *Chem. Mater.*, **8**, 890, (1996).

L. R. Dalton, A. W. Harper, R. Ghosen, W. H. Stier, M. Ziari, H. Fetterman, Y. Shi, R. V. Mustacich, A. K.-Y. Yen, K. J. Shea, *Chem. Mater.*, **7**, 1060, (1995).

R. G. Denning, *J. Mater. Chem.*, **5 (3)**, 365, (1995).

Y. Kawabe, H. Ikeda, T. Sakai, K. Kawasaki, *J. Mater. Chem.*, **2 (10)**, 1025, (1992).

M. Barzoukas, M. Blanchard-Desce, D. Josse, J.-M. Lehn, J. Zyss, *Chem. Phys.*, **133**, 323, (1989).

[35] C. J. F. Böttcher, *Theory of Electric Polarisation.*, **2nd ed.**; O. C. Van Belle, P. Bordewick, A. Rip., Volume **1**; *Dielectrics in Static Fields.*, Elsevier, London, (1993).

[36] C. Dehu, F. Meyers, E. Hendrickx, K. Clays, A. Persoons, S. R. Marder, J. L. Brédas, *J. Am. Chem. Soc.*, **117**, 10127, (1995).

[37] J. J. Makosz, *J. Mol. Liq.*, **59**, 103, (1994).

J. J. Makosz, *J. Chem. Phys.*, **87 (10)**, 6053, (1987).

A. B. Meyers, R. R. Birge, *J. Chem. Phys.*, **74**, 3514, (1981).

H. Block, S. M. Walker, *Chem Phys. Lett.*, **19 (3)**, 363, (1973).

[38] I. D. L. Albert, S. di Bella, D. R. Kanis, T. J. Marks, M. A. Ratner, *Solvent Effects on the Molecular Quadratic Hyperpolarisabilities.*, **Chapter 4**, 57; *ACS Symposium Series*, **601**, (1995).

[39] S. B. Allin, T. M. Leslie, R. S. Lumpkin, *Chem. Mater.*, **8**, 428, (1996).

M. Barzoukas, A. Fort, P. Boy, C. Combellas, A. Thiebault, *Non-Linear Optics*, **7**, 41, (1994).

Ch. Bosshard, G. Knöpfle, P. Prêtre, P. Günter, *J. Appl. Phys.*, **71 (4)**, 1594, (1992).

M. S. Paley, J. M. Haris, H. Looser, J. C. Baumert, G. C. Bjorklund, D. Jundt, R. J. Tweig, *J. Org. Chem.*, **54**, 3774, (1989).

I. Ledoux, J. Zyss, *Chem. Phys.*, **73**, 203, (1983).

B. F. Levine, C. G. Bethea, *J. Chem. Phys.*, **65 (6)**, 2429, (1976).

[40] T. Kogej, M. Malagoli, J.-L. Brédas, G. H. Cross, Private Communications, (1995 - 1997).

[41] E. Hecht, *Optics*, **2nd Ed.**, Addison-Wesley Publishing, Wokingham, (1987)

[42] P. A. Franken, J. F. Ward, *Rev. Mod. Phys.*, **53 (1)**, 23, (1963).

[43] D. L. Andrews, *Molecular Theory of Harmonic Generation*, in *Modern Non-Linear Optics*, Edited by M. Evans, S. Kielich, , *Chem. Phys. Series*, Volume **LXXXV**, Part 2, John Wiley and Sons Inc., (1993).

[44] C. Flytzianis, *Quantum Electronics, a Treatise*, **1 A**, Academic Press, New York, (1975).

[45] P. N. Butcher, *Non-Linear Optical Phenomena*, Ohio State University, (1965).

[46] D. A. Kleinman, *Phys. Rev.*, **126**, 1977, (1962).

[47] J. A. Armstrong, N. Bloembergen, J. Ducuing, P. S. Pershan, *Phys. Rev.*, **127 (6)**, 1918, (1962).

[48] J. L. Oudar, *J. Chem. Phys.*, **67 (2)**, 446, (1977).

[49] H. A. Kurtz, J. J. P. Stewart, K. M. Dieter, *J. Comp. Chem.*, **11 (1)**, 82, (1990).

[50] S. B. Allin, T. M. Leslie, R. S. Lumpkin, Chem. Mater., 8, 428, (1996).

[51] I. D. L. Albert, T. J. Marks, M. A. Ratner, J. Chem. Phys., 100, 9714, (1996).

[52] Ch. Bosshard, G. Knöpfle, P. Prêtre, P. Günter, *J. Appl. Phys.*, **71 (4)**, 1594, (1992).

[53] J. Zyss, *J. Chem. Phys.*, **71 (2)**, 909, (1975).

[54] P. W. Atkins, *Physical Chemistry*, **3rd Ed.**, Oxford University press, Oxford, (1986).

Chapter 2

Theoretical Considerations for EFISH and Dipole Moment Characterisation.

§2.1 Obtaining the First Hyperpolarisability from Measurements of Macroscopic Non-Linearities using EFISH.

It has already been indicated in Chapter 1, that the orientation of a molecule in solution will be in a random direction with respect to the electric field at any moment in time. A number of molecules will have a distribution of orientations with respect to any direction, which will fluctuate as time progresses. As a result, the macroscopic properties of a material system will be averaged with respect to these fluctuations. With the case of non-linear optics, such averaging reduces $\chi^{(2)}$ to zero since the average of any random fluctuations is inherently centrosymmetric. Thus with non-centrosymmetric molecules, a degree of alignment is required to break the centrosymmetry of the macroscopic medium. One way of doing this is to apply a static electric field to the macroscopic system, which allows the molecules to align. This process is conducted with the experimental technique of electric field induced second harmonic generation (EFISH). The use of a static electric field, in addition to the two optical fields, means that $\chi^{(3)}$ must be considered rather than $\chi^{(2)}$, since three electric fields are acting upon the system. Equating the third term of the polarisation given by (1.2-5) as

$$P_I^{(3)} \equiv \chi_{IJKL}^{(3)} E_J^\omega E_K^\omega E_L^0 \equiv \Gamma_{IJKL} E_J^\omega E_K^\omega E_L^0 \equiv d_{IJK}^{eff} E_J^\omega E_K^\omega,$$

<div align="right">(2.1-1)</div>

it is possible to see that the inclusion of the static field produces an effective second harmonic coefficient, d_{IJK}^{eff} which can be used to describe second harmonic generation.

The tensorial indices, I, J, K, and L are capitalised so as to represent the macroscopic laboratory frame with axes, X, Y, and Z. Assuming the direction of propagation is in the X direction and that the optical and static electric fields are polarised in the Z direction, only one component of Γ is available, namely $\Gamma_{ZZZZ}(=\Gamma_L)$. This, now has to be related to the molecular frame of axes to obtain the hyperpolarisability.

The second harmonic microscopic polarisation, $p^{2\omega}$ of a molecule under the influence of static and optical electric fields is given by (1.6-1) in Chapter 1 as

$$p_i^{2\omega} = \beta_{ijk}^{2\omega} E_j^\omega E_k^\omega + \gamma_{ijkl}^{2\omega} E_j^\omega E_k^\omega E_l^0 = \left(\frac{\beta_{ijk}^{2\omega}}{E_l^0} + \gamma_{ijkl}^{2\omega} \right) E_j^\omega E_k^\omega E_l^0$$

<div align="right">(2.1-2)</div>

where i, j, k, and l refer to the indices for the molecular axes x, y and z, and β and γ are the second and third polarisabilities of a molecule, respectively. The second order polarisability is non-zero for non-centrosymmetric molecules and thus contributes to the final polarisation, in addition to the third order polarisability.

The transformation of the molecular frame to the laboratory frame involves a projection cosine for each tensorial component due to the presence of an electric field [55]. For example, to find the component of β_{ijk} along the Z laboratory axis,

$$\beta_Z = \sum_{ijk} \cos\theta_{Zi} \cos\theta_{Zj} \cos\theta_{Zk} \beta_{ijk}$$

<div align="right">(2.1-3)</div>

<div align="center">25</div>

The figure shows coordinate transformations with:
$$X = z \sin\theta \cos\phi$$
$$Y = z \sin\theta \sin\phi$$
$$Z = z \cos\theta$$
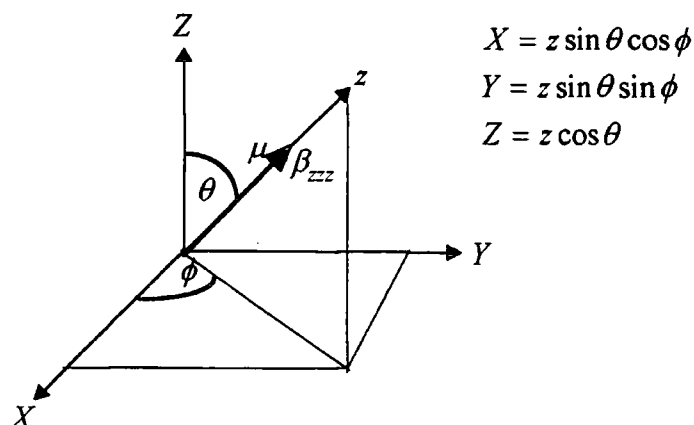
Figure 2.1-1: Transformations of Cartesian co-ordinates.

as is visualised in Figure 2.1-1. Thus, for the component of β in the z direction, i.e. β_{zzz}, β_Z becomes $\beta_Z = \beta_{zzz} \cos^3\theta$.

The magnitude of the vectorial components of μ and β are found to be [55]

$$\mu_{vec.} = \left(\mu_x^2 + \mu_y^2 + \mu_z^2\right)^{1/2},$$

(2.1-4)

and

$$\beta_{vec.} = \left(\beta_{xxx}^2 + \beta_{yyy}^2 + \beta_{zzz}^2\right)^{1/2}.$$

(2.1-5)

If the conjugation axis of a CT molecule lies in the z-direction, it is often the case that the largest component of μ and β also lies in the z-direction, since contributions to μ and β are dominated by CT interactions (see Chapter 1). If this is the case, it is also usual that the contributions to μ and β in the x and y-directions are small compared to the z-direction, so that $\mu_{vec.}$ and $\beta_{vec.}$ lie in the z-direction parallel to each other. As will be shown subsequently, the application of the static electric field in EFISH experiments, orients dipoles so that an average macroscopic dipole moment lies in the direction of the external field. If $\mu_{vec.}$ and $\beta_{vec.}$ lie parallel to each other and lie in the z-direction, an average component of $\beta_{vec.}$ is thus measured through EFISH

experiments. Experiments and calculations have often shown that $\beta_{vec.}$ and β in the direction of the dipole moment ($\beta_{dip.}$) are similar for a number of CT molecules [55], though it should be remembered this is not necessarily the case for all situations.

§2.2 Molecular Orientation.

With a large number of molecules, a molecular property measured in any macroscopic direction, will be the microscopic properties of all the molecules, averaged over all directions of the molecules. Thus, μ and β need to be averaged over all molecular orientations before any relation to the macroscopic non-linearity can be made. The energy of a dipole, μ in an external, low intensity directing field, $\mathbf{E}_d$ is found to be [56, 57]

$$W = -\mu \cdot \mathbf{E}_d = -\mu E \cos\theta$$

(2.2-1)

where θ is the angle between the directing field and dipole moment at any moment in time.

First considering the case when no directing field is applied, $W = 0$ and all directions of the dipole are equally probable. The probability, $p(\theta)d\theta$ of a dipole
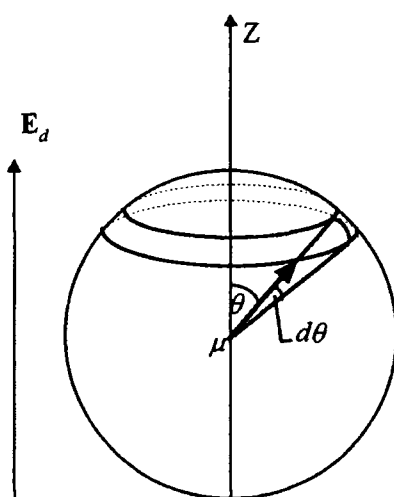
Figure 2.2-1: Schematic of the orientation of a dipole under the influence of a directing field.

27

occupying an angle between θ and $d\theta$ to the Z-axis (see Figure 2.2-1) is such that

$$p(\theta)d\theta = \frac{2\pi r \sin\theta r d\theta}{4\pi r^2} = \frac{1}{2}\sin\theta d\theta$$

(2.2-2)

where r is the radius the sphere prescribed by the dipole. When a directing field is applied, the probability of a dipole lying in a particular direction is balanced by the Boltzman factor, $e^{-W/k_BT} = e^{\mu E_d \cos\theta/k_BT}$, where k_B is Boltzman's constant and T is the temperature. To determine the extent to which the directing field orients a dipole, the average value $\overline{\cos\theta}$ is used where $\overline{\cos\theta} = 0$ for a random distribution of dipoles, and $\overline{\cos\theta} = 1$ for a completely aligned system. Introducing the normalised distribution,

$$\overline{\cos\theta} = \frac{\int_0^\pi \cos\theta e^{\mu E_d \cos\theta/k_bT} \frac{1}{2}\sin\theta d\theta}{\int_0^\pi e^{\mu E_d \cos\theta/k_bT} \frac{1}{2}\sin\theta d\theta}$$

(2.2-3)

and using the abbreviations $x = \frac{\mu E_d \cos\theta}{k_B T}$ and $a = \frac{\mu E_d}{k_B T}$, the average orientation is thus found to be

$$\overline{\cos\theta} = \frac{1}{a}\frac{\int_{-a}^a e^x x dx}{\int_{-a}^a e^x dx} = \frac{1}{a}\frac{[xe^x - e^x]_{-a}^{+a}}{[e^x]_{-a}^{+a}},$$

(2.2-4)

or

$$\overline{\cos\theta} = \frac{e^a + e^{-a}}{e^a - e^{-a}} - \frac{1}{a} = \coth a - \frac{1}{a} = L_1(a)$$

(2.2-5)

where $L_1(a)$ is the first order Langevin function, first developed for magnetic moments in a magnetic directing field [58, 59]. $L_1(a)$ may be developed as a power series of a [56], so that for small values of a

$$\overline{\cos\theta} = \frac{1}{3}a = \frac{\mu E_d}{3k_B T}$$

and the average dipolar orientation of an assembly of molecules can be determined.

As indicated in §2.1, to obtain the average value of β_z, $\overline{\cos^3\theta}$ must be considered. Thus, (2.2-3) becomes

$$\overline{\cos^3\theta} = \frac{\int_0^\pi \cos^3\theta \, e^{\mu E_d \cos\theta/k_B T} \frac{1}{2}\sin\theta d\theta}{\int_0^\pi e^{\mu E_d \cos\theta/k_B T} \frac{1}{2}\sin\theta d\theta}.$$

Equation (2.2-7) may be solved by using x and a as defined above and by using the relationship $x^3 = a^3 \cos^3\theta$ so that, through integration by parts,

$$\overline{\cos^3\theta} = \frac{1}{a}\frac{\int_{-a}^a e^x x^3 dx}{\int_{-a}^a e^x dx} = \left(1 + \frac{6}{a^2}\right)\coth a - \frac{3}{a} - \frac{6}{a^3} = L_3(a).$$

where $L_3(a)$ is the third order Langevin function. This equation may be expanded in a similar manner to that of (2.2-5) so that for small values of a, [55]

$$\overline{\cos^3\theta} = \frac{1}{5}a = \frac{\mu E_d}{5k_B T}.$$

Substituting $\beta_z = \beta_{zzz} \overline{\cos^3 \theta}$ into (2.1-2) we see that the second harmonic polarisation becomes [55, 60, 61, 62, 63]

$$p_z^{2\omega} = \left(\frac{\mu \beta_{zzz}}{5 k_B T} + \bar{\gamma}_z \right) E_z^\omega E_z^\omega E_z^0,$$

(2.2-10)

where $\bar{\gamma}_z$ is the average component of γ in the Z-direction, and it is now possible to relate the microscopic polarisation to the macroscopic polarisation. In a similar manner to equations (1.6-2) and (1.6-3), the third order susceptibility, Γ_L can be related to the microscopic polarisation. This is found to be [55, 60, 61, 62, 63, 64]

$$\Gamma_L = \Gamma_{ZZZZ} = N f^{2\omega} \left(f^\omega \right)^2 f^0 \gamma' = N f^{2\omega} \left(f^\omega \right)^2 f^0 \left(\frac{\mu \beta_{zzz}}{5 k_B T} + \bar{\gamma}_z \right)$$

(2.2-11)

where f^ω and $f^{2\omega}$ are the local field factors at frequency ω and 2ω respectively, f^0 is the local static field factor, and N is the number density. Usually, in accordance with other experiments [60, 61, 62, 63, 64, 65], $\bar{\gamma}_z$ is assumed to be far smaller than $\mu \beta / 5 k_B T$, and is approximated to zero, but it may be developed in a similar manner to β_z to obtain γ_{zzz}. Thus, measurements of β can now be made by measuring the third order susceptibility of a liquid, Γ_L, and the dipole moment, μ of the molecule assuming $\bar{\gamma}_z$ is small.

§2.3 Determination of the Dipole Moment and Local Field Factors.

The dipole moment may be determined by using linear continuum theory [56, 57]. As described by (1.2-2) and (1.6-1) in Chapter 1, for low intensity electric fields the induced macroscopic polarisation may be split into contributions from the orientation of the permanent dipole moment, $\mathbf{P}_\mu$ and the polarisability, $\mathbf{P}_\alpha$ such that (shown here in Gaussian units)

$$\frac{\varepsilon - 1}{4\pi} \mathbf{E} = \mathbf{P}_\mu + \mathbf{P}_\alpha$$

(2.3-1)

where $\mathbf{E}$ is the external electric field, and ε is the low frequency dielectric constant. $\mathbf{P}_\mu$ and $\mathbf{P}_\alpha$ may be written in terms of the molecular dipole moment and polarisability, such that

$$\mathbf{P}_\mu = \sum_k N_k \overline{\mu}_k$$

$$\mathbf{P}_\alpha = \sum_k N_k \alpha_k \mathbf{I}_k$$

(2.3-2)

where the polarisations are summed over the total number of dipoles, N_k for each species k, $\overline{\mu}_k$ is the orientation averaged dipole moment under the influence of a directing field, $\mathbf{E}_d$, and $\mathbf{I}_k$ is the internal field experienced by the molecule. The influence of a directing field on the average value of the dipole moment has already been demonstrated in §2.2. Therefore, substituting $\overline{\mu} = \overline{\mu \cos \theta}$ and using (2.2-6), equation (2.3-1) becomes

$$\frac{\varepsilon - 1}{4\pi} \mathbf{E} = \sum_k N_k \left[\alpha_k \mathbf{I}_k + \frac{\mu_k^2 (\mathbf{E}_d)_k}{3k_B T} \right].$$

(2.3-3)

Debye [66, 67] assumed that the internal and directing fields were equal and related to the external field via the Lorentz local field factor, $\mathbf{E} = [(\varepsilon + 2)/3] \mathbf{I} = f^L \mathbf{I}$ [68], which results in the well known Debye equation [56, 66, 67, 69]. Guggenheim extended Debye's work by developing a method of measuring the dipole moment by measuring the dielectric constant of a solution for a number of solute concentrations, C and relating the gradient $\partial \varepsilon / \partial C$ to the dipole moment, such that [70]

$$\mu_s = \sqrt{\frac{10^{36}}{N_a} \cdot \frac{9k_B T}{4\pi} \cdot \frac{3}{(\varepsilon + 2)(n^2 + 2)} \cdot \frac{\partial \varepsilon}{\partial C}\Big|_0}$$

(2.3-4)

where μ_s is the solution state dipole moment, expressed in Debyes, N_a is Avogadro's number, and n is the refractive index of the solvent. Onsager soon realised that to obtain a gas phase dipole moment from measurements in solution, the directing and internal fields for a molecule must be treated separately [56, 69]. Thus in the next few sections, Onsager local field formalisms will be developed so that gas phase dipole moments are attainable. Consequently, it is also possible to obtain the local field factors used to relate the macroscopic polarisation to the microscopic polarisation.

§2.3.1 Spherical Local Fields.

The case of non-polar dielectrics shall first be considered, where the contribution from any permanent dipole is zero and only induced dipole moments are considered. Onsager showed that in this case the internal field is equal to the Lorentz local field by assuming that the internal field, $\mathbf{I}$ is split into two parts, the cavity field, $\mathbf{E}_c$ and the reaction field, $\mathbf{R}$, i.e. [56, 69]

$$\mathbf{I} = \mathbf{E}_c + \mathbf{R}.$$

(2.3-5)

The reaction field is essentially the electric field experienced by a dipole due to the presence of itself. Thus, $\mathbf{R}$ is always in the direction of the dipole moment, and is defined for non-polar dielectrics as

$$\mathbf{R} = f\alpha\mathbf{I} = f\alpha(\mathbf{E}_c + \mathbf{R}) \rightarrow \mathbf{R} = \mathbf{E}_c \frac{f\alpha}{(1 - f\alpha)}$$

(2.3-6)

where f is the reaction field factor. Thus, the internal field becomes

$$\mathbf{I} = \mathbf{E}_c \frac{1}{(1 - f\alpha)}.$$

(2.3-7)

For the calculation of the reaction and cavity fields, it is necessary to consider a dipole surrounded by an arbitrary shaped cavity. Assuming Onsager's model of a

spherical vacuum cavity of radius r, surrounded by a dielectric, ε, where a dipole is situated at the centre of the cavity and is aligned in the z-direction (see Figure 2.3-1), the potentials, ϕ_1 and ϕ_2, outside and inside the cavity respectively, may be found with the aid of the solutions to Laplace's equation (see Appendix VI) [56, 57]. The resulting equations for the reaction field factor and cavity field are thus [56, 69]

$$f = \frac{1}{r^3} \frac{2(\varepsilon - 1)}{2\varepsilon + 1}$$

$$\mathbf{E}_c = \frac{3\varepsilon}{2\varepsilon + 1} \mathbf{E}$$

(2.3-8)

which may be substituted into (2.3-7) to obtain an expression for the internal field. Further substitution of the internal field into $\mathbf{P}_\alpha$ yields the well known Clausius-Mossotti equation [56, 57, 71, 72]

$$\frac{\varepsilon - 1}{\varepsilon + 2} = \frac{4\pi}{3} N\alpha$$

(2.3-9)

or

$$P_\alpha = \frac{\varepsilon + 2}{3} N\alpha = N f^L \alpha \, .$$

(2.3-10)
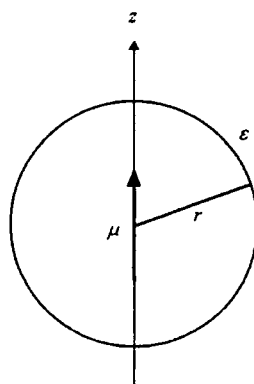
Figure 2.3-1: Onsager's spherical cavity surrounding a dipole in a dielectric continuum.

33

For the case of optical fields, the Lorentz local field factor, f^L may then be applied under the assumption, $\varepsilon \approx n^2$ in the low frequency limit, and the Lorentz-Lorenz local field factor, f_ω^L at a frequency ω is thus obtained [73]

$$f_\omega^L = \frac{n_\omega^2 + 2}{3}.$$

(2.3-11)

The presence of a permanent dipole however changes the value of the internal field. Onsager recognised that the reaction field of a permanent dipole, **R** will not contribute to the directing field since **R** is, for a spherical cavity, always in the same direction as the dipole moment [56, 69]. However, the reaction field does contribute to the internal field. Therefore, the difference between the internal field and the directing field is given by an average of the reaction field over all directions of permanent dipoles, i.e.

$$\mathbf{I} - \mathbf{E}_d = \overline{\mathbf{R}}.$$

(2.3-12)

The directing field is calculated by assuming the case where the permanent dipole moment is removed (since the contribution from the reaction field is removed). Thus, the situation is similar to the case of a non-polar dielectric, except that this time equation (2.3-5) becomes

$$\mathbf{E}_d = \mathbf{E}_c + f\alpha\mathbf{E}_d = \frac{1}{1 - f\alpha}\mathbf{E}_c = \frac{1}{(1 - f\alpha)}\frac{3\varepsilon}{(2\varepsilon + 1)}\mathbf{E}$$

(2.3-13)

where f is given by (2.3-8). Using (2.3-12) and

$$\overline{\mathbf{R}} = \frac{f}{1 - f\alpha}\overline{\mu},$$

(2.3-14)

where $\overline{\mu} = \mu\overline{\cos\theta}$, Onsager's equation for the polarisation of a polar dielectric is found, by substituting these into (2.3-3), to be [69]

$$\frac{\varepsilon-1}{4\pi} = \sum_k N_k \frac{3\varepsilon}{(2\varepsilon+1)} \frac{1}{(1-f_k\alpha_k)}\left[\alpha_k + \frac{1}{(1-f_k\alpha_k)}\frac{\mu_k^2}{3k_BT}\right]$$

(2.3-15)

for a kth species. Assuming the Onsager approximation $\left(4\pi Nr_k^3/3 = 1\right)$ and using the Clausius-Mossotti equation given by (2.3-9), equation (2.3-15) therefore becomes

$$\frac{\varepsilon-1}{4\pi} = \sum_k \frac{\varepsilon\left(n_k^2+2\right)}{2\varepsilon+n_k^2}\left[\alpha_k + \frac{\left(n_k^2+2\right)\left(2\varepsilon+1\right)}{3\left(2\varepsilon+n_k^2\right)}\frac{\mu_k^2}{3k_BT}\right]$$

(2.3-16)

where n_k is the refractive index of the solute which is measured at infinite frequency.

It is interesting to note that the pre-factor of (2.3-16) represents the often used and so called "Onsager local field factor", i.e. [55, 60, 61, 62, 63, 64, 65]

$$f_k^0 = \frac{\varepsilon\left(n_k^2+2\right)}{2\varepsilon+n_k^2}$$

(2.3-17)

for a species, k. With optical fields, the relation $\varepsilon \approx n^2$ may again be applied to the dielectric constant of the solvent, and if $n^2 \approx n_k^2$, the Lorentz-Lorenz local field formula, given by equation (2.3-11) is found. This has often been used in place of equation (2.3-17), where an error of less than 5 % has been found between the two local field formulas [55, 61, 63, 65].

§2.3.2 Ellipsoidal Local Fields.

Onsager's equation may be developed in a similar manner to that above for the case of an ellipsoidal cavity [56, 74, 75, 76, 77, 78]. This is done by splitting the polarisation into contributions due to oriented permanent dipoles and the polarisability of the molecules under the influence of an internal field, as is given by (2.3-1) [56]. However, there are some very important differences in the derivation of the ellipsoidal Onsager equation. The calculation of the reaction field, by finding the solution to Laplace's equation, is much more intricate than with the spherical case [56, 79, 80, 81, 82, 83]. In addition, the principal components of the polarisability tensor are not equal, thus a uniform dipole density does not form within the cavity [56, 74, 84]. Reproducing Figure 2.3-1 for an ellipsoidal cavity, the principal axis of the cavity may be defined in Figure 2.3-2 such that the polarisability tensor and direction of the dipole moment coincide. The dipole moment and cavity then resides at an angle θ with the applied field, **E**. Under these conditions, the average reaction field over all dipolar orientations is given by [56],
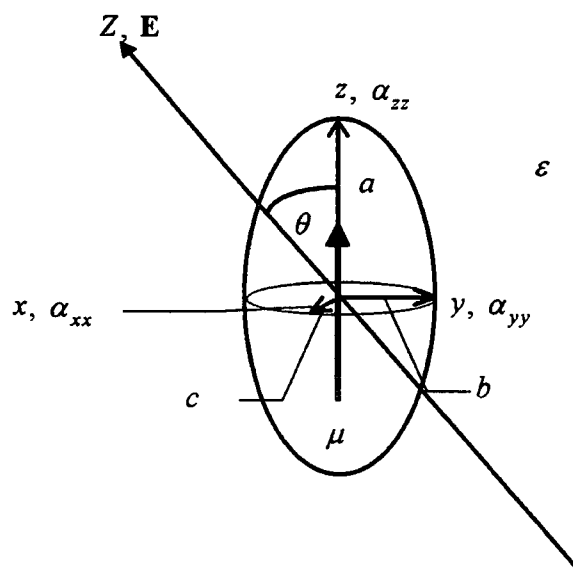
Figure 2.3-2: Definition of an ellipsoidal cavity and polarisability tensor components under the influence of a directing field in a dielectric continuum.

$$\overline{R} = \frac{f_z \overline{\mu}}{1 - f_z \alpha_z}$$

<div align="right">(2.3-18)</div>

where α_z is the polarisability in the z-direction, f_z is the reaction field factor for the z-direction given by

$$f_z = \frac{3}{abc} \frac{A_z(1 - A_z)(\varepsilon - 1)}{\varepsilon + (1 - \varepsilon)A_z},$$

<div align="right">(2.3-19)</div>

and A_z is the ellipsoidal shape factor for the z-direction which is calculated by means of the equation

$$A_z = \frac{abc}{2} \int_0^\infty \frac{ds}{\left(s + a^2\right)^{3/2}\left(s + b^2\right)^{1/2}\left(s + c^2\right)^{1/2}},$$

<div align="right">(2.3-20)</div>

where a, b and c are the ellipsoidal principal semi-axes [56, 57, 76, 77, 78, 86]. Here, the average radius of an ellipsoid is given by $\bar{r}^3 = abc$. It should be noted that if $a = b = c$, then $A_z = 1/3$ and all ellipsoidal equations revert to their spherical counterparts. The cavity field in the z-direction, $(E_c)_z$ may be related to the external field in the z-direction, E_z via the equation [56]

$$\left(E_c\right)_z = \frac{\varepsilon}{\varepsilon + (1 - \varepsilon)A_z} E_z = \frac{\varepsilon}{\varepsilon + (1 - \varepsilon)A_z} E \cos\theta_z.$$

<div align="right">(2.3-21)</div>

By using an equation analogous to (2.3-13), the directing field in the z-direction, $(E_d)_z$ is found to be [56, 57]

$$\left(E_d\right)_z = \frac{\varepsilon E \cos\theta}{(1 - f_z\alpha_z)(\varepsilon + (1 - \varepsilon)A_z)}.$$

<div align="right">(2.3-22)</div>

The directing field may then be used in conjunction with (2.2-1) to obtain the energy of an oriented dipole and the average dipole moment in the direction of the external field, where a similar relationship to (2.2-6) is found. The polarisation due to a permanent dipole is, thus,

$$\mathbf{P}_{\mu} = \sum_k \frac{N_k \mu_k^2}{3k_B T} \frac{\varepsilon}{\left\{1 - (f_z)_k (\alpha_z)_k\right\}\left\{\varepsilon + (1-\varepsilon)(A_z)_k\right\}} \mathbf{E}.$$

(2.3-23)

To obtain $\mathbf{P}_{\alpha}$, the internal field is developed using (2.3-12) which defines the internal field as the sum of the directing and reaction fields. The contributions to the polarisation due purely to the directing and reaction fields, $\mathbf{p}_d$ and $\mathbf{p}_R$ respectively, are considered separately. $\bar{\mathbf{p}}_R$, averaged over all directions, is found to be [56, 57]

$$\bar{\mathbf{p}}_R = \frac{f_z \alpha_z}{1 - f_z \alpha_z} \bar{\mu}$$

(2.3-24)

where $\bar{\mu}$ is the average dipole moment in the direction of the external field. $\mathbf{p}_d$ along any principal axis, λ, is defined partly by (2.3-22) such that [56, 85]

$$(\mathbf{p}_d)_{\lambda} = \alpha_{\lambda} (\mathbf{E}_d)_{\lambda} = \frac{\alpha_{\lambda}}{1 - f_{\lambda} \alpha_{\lambda}} (\mathbf{E}_c) = \frac{\alpha_{\lambda}}{(1 - f_{\lambda} \alpha_{\lambda})} \frac{\varepsilon}{(\varepsilon + (1-\varepsilon)A_{\lambda})} E \cos\theta_{\lambda}.$$

(2.3-25)

The component in the direction of the external field utilises a further $\cos\theta$ term which must be averaged for all molecular orientations. The average of $\cos^2\theta$ is 1/3, and the average of the prefactor of (2.3-25), for not too eccentric ellipsoids, differs only slightly from the spherical case. Thus, the spherical equivalent for $\mathbf{p}_d$ is used. Using the average of (2.3-25) and (2.3-24), (2.3-23) and (2.3-3), the ellipsoidal Onsager equation is thus defined as [56, 57, 78, 85]

$$\frac{\varepsilon-1}{4\pi} = \sum_k N_k \left[\frac{3\varepsilon}{(2\varepsilon+1)} \frac{\overline{\alpha}_k}{(1-f_k\overline{\alpha}_k)} + \frac{\varepsilon}{(\varepsilon+(1-\varepsilon)(A_z)_k)} \frac{\mu_k^2}{3k_BT\{1-(f_z)_k(\alpha_z)\}^2} \right],$$

<div align="right">(2.3-26)</div>

where $\overline{\alpha}$, is the average polarisability.

Once again it is of interest to introduce the Clausius-Mossotti formula for spherical cavities, given by (2.3-9), and for ellipsoidal cavities, given by [56, 57, 86]

$$\alpha_z = \frac{n^2-1}{3\{1+(n^2-1)A_z\}} abc,$$

<div align="right">(2.3-27)</div>

where the density of ellipsoidal particles are such that $4\pi Nabc/3 = 1$. Equation (2.3-26) may then be written with the aid of (2.3-19) and (2.3-16) so that [56, 57]

$$\frac{\varepsilon-1}{4\pi} = \sum_k N_k \left[\frac{\varepsilon(n_k^2+2)}{2\varepsilon+n_k^2} \overline{\alpha}_k + \frac{\varepsilon\{\varepsilon+(1-\varepsilon)(A_z)_k\}\{1+(n_k^2-1)(A_z)_k\}^2}{(\varepsilon+(n_k^2-\varepsilon)(A_z)_k)^2} \frac{\mu_k^2}{3k_BT} \right],$$

<div align="right">(2.3-28)</div>

and an equation analogous to (2.3-16) is obtained.

For optical fields in the linear regime, the first term of (2.3-28) is identical to (2.3-17), thus only spherical formalisms need to be used for calculations of the polarisabilities. For the spherical case, the local field factors for β are also identical to (2.3-17) [55]. However for ellipsoidal cavities, the static local field factor becomes [87]

$$f_{ell}^0 = \frac{\varepsilon(1+(n^2-1)A_z)}{(\varepsilon+(n^2-\varepsilon)A_z)}.$$

<div align="right">(2.3-29)</div>

When $\varepsilon \approx n_0^2$, for optical fields, and $n_0 \approx n_k$,

$$f_{ell}^{\omega} = \left(1 + \left(n_{\omega}^2 - 1\right)A_z\right)$$

which may be approximated to (2.3-11) with only a small error for values of A_z greater than 0.1.

Ellipsoidal local field factors associated with the measurement of the dipole moment have been used previously with some success [56, 76, 77, 78, 82, 85, 86, 88, 89, 90, 91]. However, one must be aware that a number of other geometrical shapes are applicable since the cavity is defined purely as an arbitrary shape [56, 92]. One must also be aware of the uncertainty involved with the estimate of the cavity radius [56, 56, 69, 85, 86, 92]. Since the cavity is an arbitrary shape, it is possible to choose a radius which reflects the experimental conditions and the choice of cavity shape. However, the error on such a choice is large and, as will be seen in Chapter 4, this can result in large changes in the estimated dipole moment. As a result, a careful consideration of the cavity radius is presented in Chapter 4.

Additional cavity corrections may be applied for dipoles not at the centre of the cavity [56, 57, 93], non ideal dipoles [93], and dipolar solute-solute and solute-solvent interactions for polar solutes in polar solvents, [56, 57, 93, 94, 95]. Also, the very nature of the Onsager cavity, in that it represents a discontinuous step function between the vacuum and the dielectric, may be brought into question [96]. Reaction fields have been calculated and applied to experimental results for the case where the function between the dielectric and the vacuum is an exponential, dependent on the distance, r from the centre of the cavity [97, 97, 98, 99, 100]. Such a modification is, indeed applicable to ellipsoidal reaction fields [99], but in view of the uncertainty involved with the estimate of the cavity radius, it would be difficult to apply such modifications.

With the above considerations in mind, it is now possible to estimate μ and β utilising the two sets of local field factors which have just been derived (see equations

(2.2-11), (2.3-16), and (2.3-28)). These equations may now be developed further for the case of a solution of polar molecules in a moderately polar solvent.

§2.4 Concentration Dependent Measurements of μ and β.

The static dielectric constant for a two component system, consisting of a solvent (1) and a solute (2), using (2.3-16) or (2.3-28), may be written as [56, 62]

$$\frac{\varepsilon - 1}{4\pi} = N_1 \alpha_1 f_1^0 + \frac{N_1 \mu_1^2 f_1^*}{3 k_B T} + N_2 \alpha_2 f_2^0 + \frac{N_2 \mu_2^2 f_2^*}{3 k_B T}$$

$$(2.4\text{-}1)$$

where f_k^0 is given by equation (2.3-17) for spherical local fields and $f_k^* = f_k^0 / (1 - f_k \alpha_k)$. Letting w represent the solute weight fraction, v the specific volume, and M_k the molecular weight of species k, in the infinite dilution limit equation (2.4-1) may be re-written as

$$\left. \frac{\partial \varepsilon}{\partial w} \right|_0 + \left(\frac{\varepsilon - 1}{v_1} \right) \left. \frac{\partial v}{\partial w} \right|_0 + (\varepsilon - 1) - \left(\frac{n^2 - 1}{f_1^0} \right) \left. \frac{\partial f_1^0}{\partial w} \right|_0 - \left(\frac{\varepsilon - n^2}{f_1^*} \right) \left. \frac{\partial f_1^*}{\partial w} \right|_0 = \frac{4\pi N_a}{M_2 v_1} \left(\alpha_2 f_2^0 + \frac{\mu_2^2 f_2^*}{3 k_B T} \right)$$

$$(2.4\text{-}2)$$

where ε and n are the dielectric constant and refractive index of the solvent respectively, and N_a is Avogadro's number. Assuming, at low concentrations, that changes in local field, specific volume, and refractive index with respect to weight fraction are small compared to changes in dielectric constant, equation (2.4-2) thus becomes

$$\left. \frac{M_2 v_1}{N_a} \frac{\partial \varepsilon}{\partial w} \right|_0 \approx \left. \frac{1}{N_a} \frac{\partial \varepsilon}{\partial C} \right| \approx 4\pi \left(\alpha_2 f_2^0 + \frac{\mu_2^2 f_2^*}{3 k_B T} \right)$$

$$(2.4\text{-}3)$$

41

where C is the concentration of the solute (2). This may be rearranged to obtain the solution state dipole moment [101],

$$\mu_s = \sqrt{\left(\frac{1}{4\pi N_a}\frac{\partial \varepsilon}{\partial C}\bigg|_0 - f_2^0\alpha\right)\frac{3k_BT}{f_2^0}}.$$

(2.4-4)

The gas phase dipole moment may then be obtained via the equation

$$\mu_g = \frac{\mu_s}{1 - f\alpha}$$

(2.4-5)

for spherical local fields. Similar equations may also be reproduced using ellipsoidal local fields.

Similarly with the non-linear polarisation, for a two component solution consisting of a solvent (1) and a solute (2), the non-linear susceptibility of the liquid, [62, 102]

$$\Gamma_L = N_1 f_1^0\left(f_1^\omega\right)^2 f_1^{2\omega}\gamma_1' + N_2 f_2^0\left(f_2^\omega\right)^2 f_2^{2\omega}\gamma_2'$$

(2.4-6)

where $\gamma_k' = \left(\mu\beta_{zzz}/5k_BT + \bar{\gamma}_z\right)$ for material k. In the infinite dilution limit

$$\frac{\partial \Gamma_L}{\partial w}\bigg|_0 + \frac{\Gamma_1}{v_1}\frac{\partial v}{\partial w}\bigg|_0 + \Gamma_1 - \frac{\Gamma_1}{[f_1]}\frac{\partial[f_1]}{\partial w}\bigg|_0 = \frac{N_a}{M_2}[f_2]\gamma_2'$$

(2.4-7)

where $[f_k] = f_k^0\left(f_k^\omega\right)^2 f_k^{2\omega}$. Assuming Lorentz-Lorenz field factors for optical fields and Onsager spherical field factors for the static field, if $n_\omega \approx n_{2\omega} \approx n$, equation (2.4-7) becomes upon rearrangement [62, 63]

$$\gamma' = \frac{27M_2(n^2 + 2\varepsilon)}{N_a\varepsilon(n^2 + 2)^3(n_2^2 + 2)}\left[v_1\frac{\partial\Gamma}{\partial w}\bigg|_0 + \Gamma_1\frac{\partial v}{\partial w}\bigg|_0 + v_1\Gamma_1 - \right.$$

$$\left. v_1\Gamma_1\left\{\left(\frac{1}{\varepsilon} - \frac{2}{2\varepsilon + n^2}\right)\frac{\partial\varepsilon}{\partial w}\bigg|_0 + \frac{3}{n^2 + 2}\frac{\partial n^2}{\partial w}\bigg|_0\right\}\right]$$

where n_2 is the refractive index of the solute measured at infinite frequency. This is often found by using the approximate relationship $n_\infty \approx 1.05 n_D$ where n_D is the refractive index measured at the sodium-D line. If ellipsoidal local fields are used for the solute and spherical local fields for the solvent, then (2.4-7) becomes

$$\gamma' = \frac{M_2(\varepsilon + (n_2^2 - \varepsilon)A_a)}{N_a\varepsilon(1 + (n^2 - 1)A_a)^3(1 + (n_2^2 - 1)A_a)}\left[v_1\frac{\partial\Gamma}{\partial w}\bigg|_0 + \Gamma_1\frac{\partial v}{\partial w}\bigg|_0 + v_1\Gamma_1 - \right.$$

$$\left. v_1\Gamma_1\left\{\left(\frac{1}{\varepsilon} - \frac{2}{2\varepsilon + n^2}\right)\frac{\partial\varepsilon}{\partial w}\bigg|_0 + \frac{3}{n^2 + 2}\frac{\partial n^2}{\partial w}\bigg|_0\right\}\right]$$

Once again, it is sometimes preferable to assume that changes on volume and refractive index with respect to volume fraction are minimal when compared to changes in dielectric constant and Γ. In cases where n_2 is unavailable, the refractive index of the solvent at 2ω may be used with only a small error on the final result.

Using these equations and (2.4-4), it is now possible to obtain μ and β for a number of materials. This will be discussed in chapters 4 and 5.

§2.5 The Effect of the Local Environment on the Molecular Properties of a Molecule.

The effect of the environment on molecular properties, such as μ, α and β, has already been intuitively exhibited through the calculation of the local fields and their dependence on the dielectric constant and refractive index of a medium. Increases in the dielectric constant of a medium enhances the dipole moment, and as is shown by

inspection of (1.6-1), also affects the values of α and β which are the first and second derivatives of μ with respect to the local field. The behaviour of μ, α, and β will be discussed in Chapter 3 for the materials under study. In much the same manner, the transition energy of a molecule is dependent upon the dielectric constant and refractive index of the environment, resulting in an effect known as solvatochromism which is commonly observed with many materials [103, 104].

Theoretical considerations of the degree of shift of the transition frequency of a chromophore with respect to changes in the molecular environment have long been a subject of discussion [104, 105, 105, 106, 107, 108, 109, 110]. Generally, assuming two levels, the difference between the transition frequencies of a molecule in the solution state, v_{eg}^{sol} and the gas phase, v_{eg}^{0} is defined by the relationship (in units of cm^{-1}) [105, 104, 109, 111]

$$10^2 hc \Delta v_{eg}^{sol} = 10^2 hc \left(v_{eg}^{sol} - v_{eg}^0 \right) \approx \frac{1}{2} \Delta \mu^2 \frac{f'}{\left(1 - f'\alpha_e\right)} - \mu^0 \Delta \mu \frac{f}{\left(1 - f\alpha_g\right)}$$
$$- \frac{\mu^0}{\left(1 - f'\alpha_e\right)} \frac{f}{\left(1 - f\alpha_g\right)^2} \left(\alpha_e - \alpha_g \right) \left[\frac{1}{2} \frac{f\mu^0}{\left(1 - f\alpha_g\right)} + \frac{f\Delta\mu}{\left(1 - f\alpha_g\right)} \right]$$

(2.5-1)

where $\Delta\mu$ is the difference between the excited state and ground state dipole moments, $\mu^e - \mu^0$, α is the polarisability in the ground (*g*) and excited (*e*) states, *h* is Planck's constant, and c is the speed of light. It is easy to see, by comparing (2.3-14) with (2.5-1), that the terms involving *f* and *f'* are related to the reaction field of a dipole, where, for spherical cavities, *f* is defined by (2.3-8) and *f'* is defined by the same equation using the relationship $\varepsilon \approx n^2$. The first and second terms on the right hand side of (2.5-1) represent the differences in energy of a dipole in the excited state compared to the ground state, and the last term represents changes of energy due to the polarisability [104]. Additional terms may be included for higher orders of the polarisation, dispersion interactions, and the difference in the energy of formation of the cavities in the ground and excited states [105, 108, 109, 110].

44

Substituting (2.3-8) into (2.5-1), to a second approximation, the frequency shift between the gas phase and solution phase may be written as [111]

$$hc\left(v_{eg}^{sol} - v_{eg}^{0}\right) = -\frac{1}{4\pi\varepsilon_0 \bar{r}^3}\left[2\left(\mu^e - \mu^0\right)\mu^0\left\{\frac{\varepsilon-1}{\varepsilon+2} - \frac{n^2-1}{n^2+2}\right\} + \left[\left(\mu^e\right)^2 - \left(\mu^0\right)^2\right]\left\{\frac{n^2-1}{n^2+2}\right\}\right]$$

(2.5-2)

If the degree of shift is known with respect to the functions in the curly brackets, then it is possible to obtain a value of the excited state dipole moment, μ_e, provided the ground state dipole moment, μ^0 and cavity radius have been determined. Furthermore, if the oscillator strength is estimated (see (1.7-3)) then it is possible to estimate a value of β by means of (1.7-2) in Chapter 1. Comparisons can then be made to that of EFISH experiments. Measurements of this kind will be discussed in Chapter 6.

References to Chapter 2.

[55] D. S. Chemla, J. Zyss, *Non-Linear Optical Properties of Organic Molecules and Crystals.*, 1 & 2, Academic Press Ltd., London, (1987).

[56] C. J. F. Böttcher, *Theory of Electric Polarisation.*, 2nd ed.; O. C. Van Belle, P. Bordewick, A. Rip., Volume 1; *Dielectrics in Static Fields.*, Elsevier, London, (1993).

[57] B. K. P. Scaife, *Principles of Dielectrics*, Clarendon Press, Oxford, (1989).

[58] P. Langevin, *J. Phys.*, 4 (4), 678, (1905).

[59] P. Langevin, *Ann. Chim. Phys.*, 5 (8), 70, (1905).

[60] F. Kajzar, J. Messier, *Phys. Rev. A*, 32 (4), 2352, (1985).

[61] B. F. Levine, C. G. Bethea, *J. Chem. Phys.*, 65 (6), 2429, (1976).

[62] K. D. Singer, A. F. Garito, *J. Chem. Phys.*, 75 (7), 3572, (1981).

[63] C. C. Teng, A. F. Garito, *Phys. Rev. B.*, 28 (12), 6766, (1983).

[64] R. W. Boyd, *Non-Linear Optics*, Academic Press Inc., London, (1992).

[65] J. L. Oudar, *J. Chem. Phys.*, 67 (2), 446, (1977).

[66] P. Debye, *Phys. Z.*, 13, 97, (1912).

[67] P. Debye, *Collected Papers*, Interscience, New York, (1954); *Polar Molecules.*, Dover, New York, p173.

[68] H. A. Lorentz, *Ann. Phys.*, 9, 641, (1880).

[69] L. Onsager, *J. Am. Chem. Soc.*, **58**, 1486, (1936).

[70] E. A. Guggenheim, *Trans. Farad. Soc.*, **45**, 714, (1949).

[71] O. F. Mossotti, *Bibl. Univ. Modena*, **6**, 193, (1847).

[72] R. Clausius, *Die Mechanische Wärmetheorie*, **II**, Braunschweig, (1879).

[73] L. V. Lorenz, *Ann. Phys.*, **11**, 70 (1880)

[74] Th. G. Scholte, *Recueil*, **70**, 50, (1951)

[75] J. R. Weaver, R. W. Parry, Inorganic Chem., 5 (5), 703, (1966).

[76] Th. G. Scholte, *Physica*, **15**, 437, (1949).

[77] R. J. W. E. Le Fèvre, D. A. A. S. Narayana Rao, *Aust. J. Chem.*, **8**, 330, (1955).

[78] J. J. Makosz, E. Trenda, *Acta Physica Polonica*, **A70 (5)**, 615, (1986).

[79] W. Schröer, C. Rybarsch, *Chem. Phys. Lett.*, **126 (3-4)**, 342, (1986).

[80] C. E. Felder, *J. Chem. Phys.*, **75 (9)**, 4679, (1981).

[81] J. A. Abbott, H. C. Bolton, *Trans. Farad. Soc.*, **48**, 422, (1952).

[82] S. W. Harrison, H.-J. Nolte, D. Beveridge, *J. Phys. Chem.*, **80 (23)**, 2580, (1976).

[83] P. G. Kusalik, M. E. Mandy, I M. Svishchev, J. Chem. Phys., 100 (10), 7654, (1994).

[84] A. D. Buckingham, *Aus. J. Chem.*, 93, (1952).

[85] A. B. Myers, R. R. Birge, *J. Chem. Phys.*, **74**, 3514, (1981).

[86] Th. G. Scholte, *Physica*, **XV (5-6)**, 450, (1949).

[87] D. M. Burland, R. D. Miller, C. A. Walsh, *Chem. Rev.*, **94**, 31, (1994).

[88] J. J. Makosz, *J. Chem Phys.*, **87 (10)**, 6053, (1987).

[89] J. J. Makosz, *J. Mol. Liq.*, **59**, 103, (1994).

[90] R. Finsay, R. Van Loon, *J. Phys. Chem.*, **80 (25)**, 2783, (1976).

[91] C. Dehu, F. Meyers, E. Hendrickx, K. Clays, A. Persoons, S. R. Marder, J.-L. Brédas, *J. Am. Chem. Soc.*, **117**, 10127, (1995).

[92] M. Bucher, *J. Quan. Chem. Solids*, **51 (11)**, 1241, (1990).

[93] L. Došen-Micovich, V. Zigman, *J. Chem. Soc., Perkin Trans. II*, 625, (1985).

[94] L. C. Rosenthal, *J. Chem. Phys.*, **79 (10)**, 4788, (1983).

[95] J. Kirkwood, *J. Chem Phys.*, **7**, 911, (1939).

[96] H. Block, S. M. Walker, *Chem. Phys. Lett.*, **19 (3)**, 363, (1973).

[97] T. Abe, Bull. *Chem. Soc. Jpn.*, **67**, 2913, (1994).

[98] S. Ehrenson, *J. Am. Chem. Soc.*, **104**, 4793, (1982).

[99] S. Ehrenson, *J. Comp. Chem.*, **2 (1)**, 41, (1981).

[100] S. A. Tyurin, M. V. Hatschina, Yu. D. Feldman, *Acta Physica Polonica*, **A70 (6)**, 697, (1976).

[101] M. Szablewski, P. R. Thomas, A. Thornton, D. Bloor, G. H. Cross, J. M. Cole, J. A. K. Howard, M. Malagoli, F. Meyers, J.-L. Brédas, W Wenseleers, E. Goovaerts, *J. Am. Chem. Soc.*, **119 (13)**, 3144, (1997).

[102] K. D. Singer, Ph.D. Thesis, **University of Pennsylvania**; *Experimental Studies of Second Order Non-Linear Optical Susceptibilities in Organic Systems.*, (1981).

[103] C. Reichardt, *Solvents and Solvent Effects in Organic Chemistry.*, **2nd Ed.**, VCH (UK) Ltd., Cambridge, (1990).

[104] N. Mataga, T. Kubota, *Molecular Interactions and Electronic Spectra.*, Marcel Dekker Inc., New York, (1970).

[105] B. Koutek, *Coll. Czech. Chem. Comm.*, **49**, 1680, (1984).

[106] P. Suppan, *Spectrochimica Acta*, **24A**, 1161, (1968).

[107] E. G. Mcrea, *J. Am. Chem. Soc.*, **61**, 562, (1956).

[108] W. Liptay, *Z. Naturforch.*, **20a**, 1441, (1965).

[109] T. Abe, *Bull. Chem. Soc. Jpn.*, **38 (8)**, 1314, (1964).

[110] O. Sinunogiu, *Modern Quantum Chemistry, Part II; Interactions*, Academic Press, London, (1965).

[111] Ch. Bosshard, G. Knöpfle, P. Prêtre, P. Günter, *J. Appl. Phys.*, **71 (4)**, 1594, (1992).

Chapter 3

Material Systems.

§3.1 Introduction.

The materials studied in this thesis are presented in Figure 3.1-1 where two main classes of organic molecule are shown. Firstly, there are those based upon the reaction of secondary and tertiary amine derivatives with tetracyanoquinodimethane (TCNQ) [112, 113]. The first three, DEMI, DCH, and ULTRA, are able to form zwitterionic structures in environments where the electric field experienced by them is large. The absorption spectra of these (which will be discussed at greater length in Chapter 6) consists of large absorption bands positioned around 700 nm and an optical "window" in the region between 400 and 500 nm (concentration $\approx 10^{-5}$ mol l^{-1}) allowing a blue colouration in solution. This previously prompted the description "blue window materials" [114]. DED however exhibits a yellow colouration in solution which is due to the presence of a single absorption band with $\lambda_{max.}$ residing around 490 nm.

The second class of materials presented are betaine and phosphonium derivatives, developed at Sheffield Hallam University [115, 116, 117], which are also zwitterionic compounds. These materials exhibit a high degree of solvatochromism and are also expected to have high dipole moments [117, 118].

Finally, NPP is also presented in Figure 3.1-1. This material is well known and has been documented many times with respect to its non-linear optical properties (see for example reference [119]). As a result it seems appropriate to use this molecule for the purpose of comparing the molecular properties to those of unknown materials.
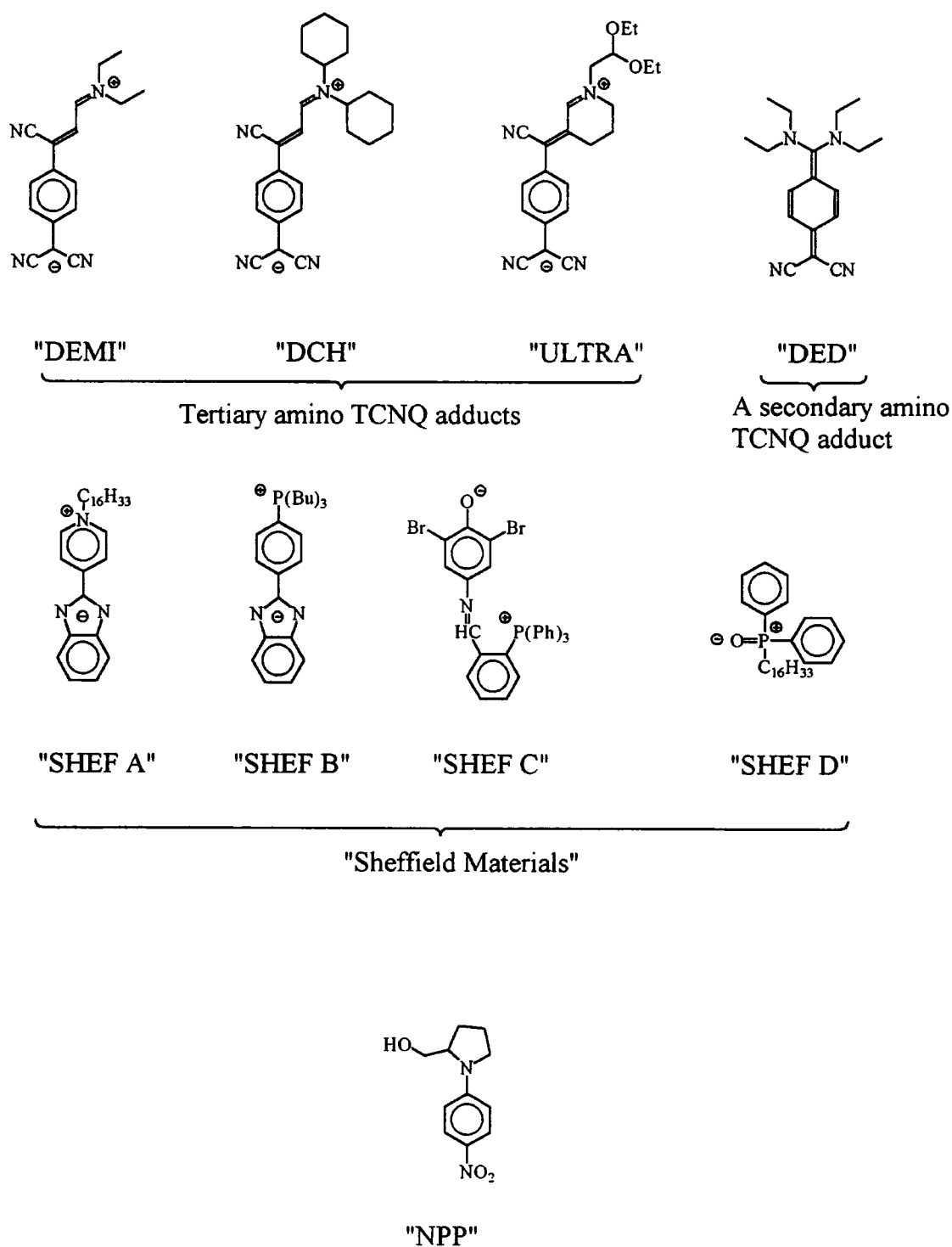
Figure 3.1-1: Structural representations of the materials discussed in this thesis.

In the following passages a review of work previously conducted on these materials is given, with indications how the present work can be related to such studies.

§3.2 NPP.

N-(4-nitrophenyl)-(L)-prolinol, more commonly known as NPP, was initially synthesised in 1984 exhibiting remarkably high powder SHG signals, up to 3,500 times the strength of urea at 1.064 μm [120]. NPP is moderately polarisable since it is a D-π-A molecule which is conjugated and possesses moderate strength donor and acceptor moieties [119, 121]. The presence of the chiral centre on the pyrolidine ring allows the formation of a non-centrosymmetric crystal structure, thus SHG in the crystal phase is possible [119, 120, 126]. Furthermore, the similar refractive indices of the crystal at ω and 2ω allow the enhancement of the second harmonic intensity through a degree of phase matching. Therefore, the extremely high non-linear optical response was attributed to the summation of phase matched components of the hyperpolarisability [119, 120]. The d_{21} coefficient for an NPP crystal was found to be 200×10^{-9} esu [119], nearly 200 times that of quartz and 45 times that of KDP. A plethora of non-linear optical experiments, measurements and demonstrations have since been conducted on NPP [119, 122, 123, 124]. Most notably and most applicable to the present studies, are the estimates of the molecular hyperpolarisability and dipole moment by various means.

EFISH experiments have been conducted on solutions of NPP in acetone, where $\beta(0)$ was found to be 42×10^{-30} esu [121]. This agrees well with the results of finite field calculations to obtain $\beta(0)$, presented in the same study and also found to be 42×10^{-30} esu . Additional EFISH measurements have been conducted where $\beta(0)$ was found to be 12×10^{-30} esu in 1,4-dioxane [125]. The lower value found in 1,4-dioxane can possibly be attributed to the effect of the lower reaction field on the hyperpolarisability of NPP. In addition, the same study estimates the dipole moment to

be 6.7 D in 1,4-dioxane which agrees well with theoretical MOPAC calculations (7.5 D) [121, 126, 127].

More recently, x-ray *and* neutron[1] diffraction techniques have been utilised to estimate the dipole moment and hyperpolarisability of NPP in the crystal phase [126, 127]. The dipole moment is shown in Table 3.2-2 alongside the density of the crystal. This value also agrees well with theoretical calculations presented in the same study [126, 127]. Two values of $\beta(0)$ are also estimated from this study. Firstly, the magnitude of the hyperpolarisability vector, β_{vec} is found to be 42.9 × 10^{-30} esu which is once again in agreement with theoretical calculations obtained in the literature. More applicable to EFISH however, is the value of the hyperpolarisability along the molecular dipole moment, $\beta_{dip.}$. This was found to be slightly smaller, 39.2 × 10^{-30} esu in the crystal phase [126, 127].

In addition, this study utilises MOPAC calculations [128, 129, 130] which have been conducted on NPP by the author of this thesis. Geometries are optimised and dipole moments are calculated in the gas phase using either AM1 or PM3 Hamiltonians to the Self Consistent Field (SCF) level, and the polarisabilities, α and β, are calculated, using the two level Sum Over States (SOS) model [131, 132]. It is acknowledged that the two level SOS model is somewhat inadequate for large polar molecules. However, surprisingly accurate results have been obtained in the literature for NPP [126]. The usefulness of such calculations is justified in the fact that parameters such as μ, α, and β can be obtained relatively easily. The results of the MOPAC calculations on NPP are presented in Table 3.2-2 for both methodologies. The dipole moments and polarisabilities obtained for NPP using the PM3 methodology are slightly lower than the AM1 calculations, though it is noticed that α and β do not vary by more than 10 %. Finally, it is noted that the PM3 dipole moment agrees well

---

[1] Both x-ray and neutron scattering techniques must be utilised to obtain an accurate analysis of the charge density and distribution of a molecule, and ultimately the dipole moment. This has found to be especially critical if analysis extends to the inclusion of higher order moments and the calculation of α, β, and γ. For more information on the technique, please refer to references [126, 161].

Material	$d_{x\text{-}ray}$ / g cm^{-3}	$\mu_{x\text{-}ray}$ / D
NPP [a]	1.41	8.1
DED [b]	1.17	26.4
DEMI	1.252	—
DCH	1.195	—
ULTRA	1.294	—

Table 3.2-1: Densities and dipole moments estimated through x-ray crystallographic analysis. a: References [126, 127]. b: Reference [161].

Material	AM1 Methodology			PM3 Methodology		
	μ_g D	$\overline{\alpha}$ Å^3	$\beta_{dip.}$ × 10^{-30} esu	μ_g D	$\overline{\alpha}$ Å^3	$\beta_{dip.}$ × 10^{-30} esu
NPP	9.2	19.1	10.8	7.9	17.2	9.0
DED	10.9	37.3	13.7	9.7	35.5	19.2
DEMI	10.1	45.4	77.2	8.6	43.4	71.0
DCH	10.5	56.4	97	7.6	51.4	74.2
ULTRA	9.0	46.4	54.5	7.9	44.3	35.4

Table 3.2-2: Dipole moments and polarisabilities for molecules presented in this thesis calculated using MOPAC.

with literature estimates and furthermore, the EFISH results conducted in 1,4-dioxane are in good agreement with the MOPAC calculations.

These calculations and the estimates presented above will be used as comparisons to the results obtained in Chapters 4 -6.

§3.3 The Tertiary Amino TCNQ Adducts.

As already stated, the three materials, DEMI, DCH and ULTRA, classed here as tertiary amino TCNQ adducts, arise thus from the reaction of TCNQ with various tertiary amines [112, 113]. They all have similar structures and are expected to be highly polarisable due to the presence of the conjugated system. Furthermore, the strong electron donating and withdrawing moieties introduce a high degree of asymmetry to conjugated system which allows positive charge to stabilise on the amino moieties and negative charge to stabilise on the dicyanomethanide groups. The tertiary amino TCNQ adducts are thus expected to possess high dipole moments and hyperpolarisabilities.

D-π-A conjugated polyenes have been studied extensively, both theoretically and experimentally [133, 134, 135, 136]. Under the influence of an electric field, the evolution of the geometry of the molecules is such that they may be described by two limiting canonical resonance forms [137] where the state of the molecule is determined by the polarisation of the environment and the molecular reaction field [138, 139] (see Figure 3.3-1). The molecule resides in a predominately quinoidal form close to the gas
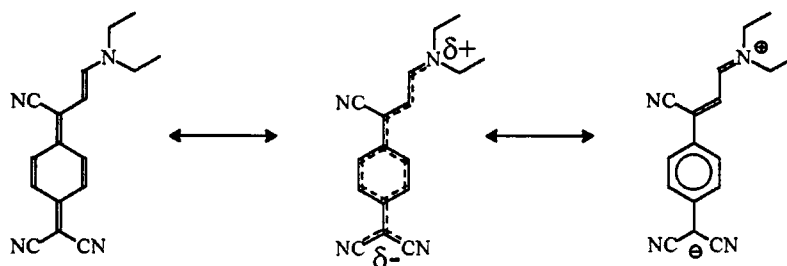
Figure 3.3-1: Structural representations of DEMI showing possible resonance forms.

phase, and a predominately aromatic form in a polar environment, such as the crystal phase. An intermediate of the two resonance structures is usually found in solution.

The geometrical state of a molecule can be defined in terms of the Bond Length Alternation (BLA) or Bond Order Alternation (BOA) parameters, where the BLA is defined as the differences in the total lengths of the double and single bonds in a conjugated system [137]. The evolution of the BLA and the resulting linear and non-linear properties of ideal polyenes [133, 137] and numerous other materials [139, 140, 141, 142, 143] under the influence of an arbitrary electric field has been modelled. When such a field is applied to a polar polyene structure, the geometry of the molecule undergoes a "cross-over" from a neutral state to a charge-separated, zwitterionic structure [137]. Similar calculations have been applied to the tertiary amino TCNQ adducts, though the majority of the work has concentrated on DEMI [113]. We can thus follow the evolution of the molecular parameters of the tertiary amino TCNQ adducts and similar D-π-A molecules with respect to applied field, by considering the evolution of the properties of DEMI. Molecular geometries in the presence of an electric field were optimised at the SCF level and calculations of the polarisabilities, α and β were performed by means of the SOS formalism (40 states) on the basis of state energies, state dipole moments and transition moments computed with a Single excitation Configuration Interaction (SCI) calculation [113, 144]. The electric fields ranged between 10^7 and 10^8 V cm^{-1} which are typical fields experienced by molecules in an organic liquid, such as a solvent.

The molecular dipole moment increases in a near linear fashion with applied field (and BLA [137]), as would be expected due to the linear dependence of the dipole moment on the reaction field (see Chapter 2, §2.3). Thus increasing the electric field strength transforms the geometry of DEMI from an initial charge-separated structure with a dipole moment of 14 D to a highly charge-separated zwitterionic form, as is shown in Figure 3.3-2 (top graph). One should note that the dipole moment is predicted to be extremely large in this state, close to 50 D. This is massive in comparison to the typical dipole moments possessed by small organic asymmetric molecules (0.5 - 4 D).
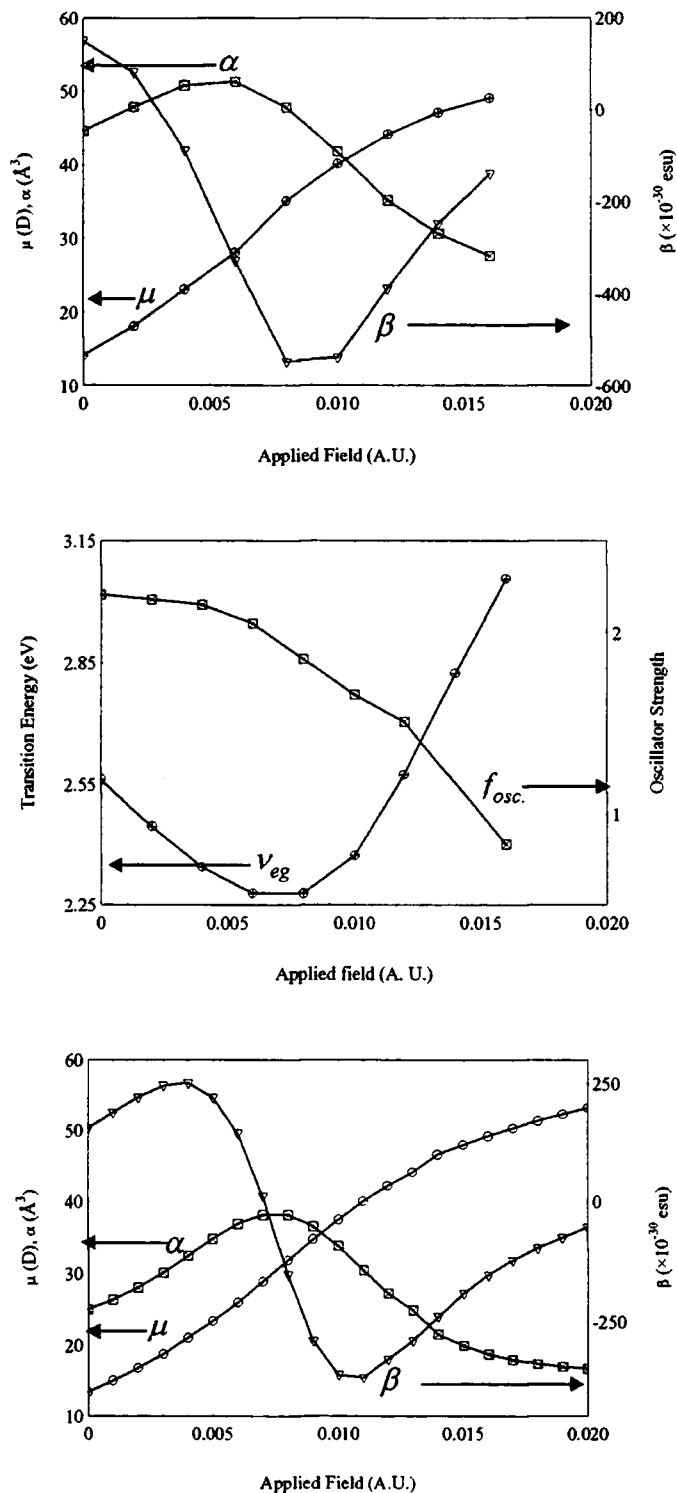
Figure 3.3-2: Three graphs showing the theoretical evolution of the linear and non-linear properties of DEMI. Top graph: evolution of the dipole moment (circles), polarisability (squares) and first hyperpolarisability (triangles) and middle graph: evolution of the transition energy (circles) and transition dipole computed using a 40-state, SOS, SCI formalism. Bottom graph: reproduction of the top graph accounting for a SD-CI formalism.

The polarisabilities, α and β undergo a more complicated evolution which is essentially due to the first and second derivatives of the evolution of the dipole moment, respectively (see Chapter 1, §1.6, and see Figure 3.3-2). The linear polarisability, α initially increases until the cyanine limit is reached (the point where the π-electron delocalisation is maximised and the BLA falls to zero), where it is maximum. This then decreases as the molecule evolves to a more charge-separated state. The value of α for DEMI in the gas phase, calculated by the SCI-SOS method is found to be 45 Å^3. The maximum occurs when an electric field of 0.07 au[2] is applied, and this is predicted to be around 51 Å^3. The polarisability is then predicted to decrease to around 30 Å^3 when DEMI is highly aromatic.

Furthermore, the evolution of α (and, for that matter β) results also from the evolution of the electronic transition energy and transition moment of the lowest energy state. The transition moment exhibits a similar evolution with BLA to the polarisability, since the two parameters are related [137], and the transition energy exhibits an inverse relationship where the energy first decreases to a minimum at the cyanine limit and then increases. At this point it is worth noting that the behaviour of the transition energy is not unlike the solvatochromic behaviour of merocyanine dyes where a reversal in the shift of the transition energy with solvent polarity is observed in low polarity solvents [145, 146, 147, 148, 149]. In fact the above SOS theory is partly based upon such experimental results.

Figure 3.3-2 also shows the theoretical evolution of the transition energy and oscillator strength for DEMI with applied field (middle graph). Here, the oscillator strength decreases as the molecule moves to a zwitterionic state. However, the transition energy initially decreases until a minimum is reached, then increases as the molecule becomes zwitterionic. The minimum transition energy is predicted to occur when a reaction field of 0.007 au is applied to DEMI which coincides with the maxima for the polarisability. The solvatochromic behaviour of DEMI, DCH and ULTRA will

---

[2] 1 au (atomic unit) = 5.14192 V m^{-1}. Please see Appendix III for further definitions of atomic units.

be discussed in conjunction with these results in Chapter 6 to ascertain whether they exhibit such behaviour.

The evolution of the transition energy is a manifestation of the evolution of the difference between the ground and excited state dipole moments, $\Delta\mu$ (see Chapter 2, §2.6) [137, 142]. The initial decrease in energy therefore suggests that the ground state dipole moment is less than the excited state dipole moment. However, the ground state dipole moment increases faster with an applied field than the excited state dipole moment, due to a difference of the polarisabilities in the ground and excited state. Therefore, $\Delta\mu$ soon reaches zero, at the point of minimum transition energy, and also at the cyanine limit. After this point the ground state dipole moment becomes larger than the excited state dipole moment and $\Delta\mu$ is thus negative. Since the first hyperpolarisability, β is related to $\Delta\mu$, β follows its evolution closely (see Figure 3.3-2). First, a maximum is reached quickly, followed by a reduction in β, which falls to zero at the cyanine limit. This is due to the dependence of β upon $\Delta\mu$ (see Chapter 1, (1.7-2)). Since $\Delta\mu$ becomes negative, β also reduces further, changing sign from positive to negative until a minimum is reached when the molecule is in the zwitterionic state.

For DEMI in the gas phase as calculated by the SCI-SOS method, the first maximum of β has been passed and the geometry lies close to the cyanine limit (Figure 3.3-2, top graph). The value of β in gas phase, calculated by this method is found to be 150×10^{-30} esu. The point where β falls to zero is reached when a field of 0.003 au is applied and the molecule possesses a dipole moment and polarisability of 20.5 D and 49 Å^3 respectively. However it is noted that this point does not coincide with the polarisability maxima or the transition energy minima estimated from the same calculations. The largest negative value of β for DEMI is -550×10^{-30} esu, which is reached when a field of 0.008 au is applied, and the corresponding values of the dipole moment and polarisability are 35.2 D and 47.7 Å^3 respectively.

More recently, additional calculations have been conducted which take into account the effect of Single *and* Double Configuration Interactions (SD-CI, see

57

Figure 3.3-2, bottom graph) [150]. With these calculations the magnitude of the dipole moment remains approximately the same as with the SCI calculations. However, the magnitude of the polarisability is lower as a result, and larger fields have to be applied to the molecule to obtain the maximum value (38 Å^3) which occurs at 0.007 au. Similarly, this is the point where β falls to zero. Fields of this strength yield a dipole moment of 28.9 D. To obtain the largest negative value of β (-360 × 10^{-30} esu), a field of 0.011 au is this time required, corresponding to a dipole moment of 40.1 D and a polarisability of 30.5 Å^3. The gas phase values for μ, α and β are 13.4 D, 25.0 Å^3, and 153 × 10^{-30} esu respectively.

It is beyond the scope of this thesis to attempt to evaluate the relative merits of the two sets of calculations described above. However, a degree of inconsistency is noted between the two sets of calculations. Since, with the SD-CI calculations, the polarisability is lower than the SCI polarisability, the evolution of the dipole moment is expected to be less sensitive to the applied field (as will be shown in Chapter 7, and see equation (2.3-6), Chapter 2), thus the gradient of the curve with respect to reaction field should be less. This is evidently not the case. Furthermore, additional inconsistencies are noted with the SCI calculations since the point where β = 0 does not coincide with the transition energy minima. A number of comparisons can be made between these calculations and the experimental results, which are obtained in the following chapters, to ascertain which model gives results closest to experimental values. This will be discussed fully in the Chapter 7.

Two level calculations have also been conducted (by the author of this thesis) on the tertiary amino TCNQ adducts using MOPAC, which are presented in Table 3.2-2. The usefulness of such calculations is justified in the fact that parameters such as μ, α, and β can be obtained relatively easily. As a result, these can be used for interpreting data on molecules where the 40-state calculations have not been conducted, as is the case with DCH and ULTRA. In comparison to the 40-state calculations, the dipole moment for DEMI in the gas phase is slightly lower. However, the average polarisabilities calculated using both methodologies are comparable to that

calculated via the SCI method. Since MOPAC uses the two-level model however, it might be expected that there would be a disagreement between the polarisabilities estimated using MOPAC and the 40-state calculations. This is clearly the case with β. Nonetheless, as already indicated these estimates are useful for comparisons to experimental results.

Comparisons can be made between the MOPAC values of the tertiary amino TCNQ adducts to facilitate general trends between them. Similar trends are exhibited with both methodologies. The dipole moment of DCH is similar to that of DEMI since there is relatively little change in the donor acceptor strengths. With the AM1 methodology, the dipole moment for ULTRA is lower than the others, which might be attributed to a reduction in planarity of the molecule induced by the addition of the piperidyl ring and results in a loss in aromaticity in the gas phase. Similar trends are exhibited with α and β. Once again, these results will be used with, and compared to, experimental results in future chapters.

Although the non-linear and linear properties calculated for DEMI are favourable in view of applications, there are several significant difficulties which have to be overcome in order to make such materials viable options for use in non-linear optical devices. The planarity and high dipole moment encourages aggregation, thus the solubility is often low. The presence of ethylenic bonds and a strong optical transition allows photo-oxidation to occur [151], and the presence of water in many polar solvents allows hydration of some TCNQ derivatives, resulting in a change in solution colour from blue to purple. However, the addition of the piperidyl ring on ULTRA appears to remove this problem while enhancing the solubility of the material by reducing the planarity. The presence of the diethylether terminal groups is considered to be a significant factor contributing to the observed enhanced solubility of ULTRA. A slight improvement in solubility is also obtained with DCH, probably due

Material	acetonitrile	chlorobenzene
DEMI	2×10^{-4}	5×10^{-5}
DCH	9×10^{-4}	2×10^{-4}
ULTRA	9×10^{-3}	2×10^{-3}

Table 3.3-1: Limiting solubilities (mol l^{-1}) determined by adherence to Beer - Lambert Law behaviour for the tertiary amino TCNQ adducts.

to the addition of the cyclohexyl terminal groups. This is adequately demonstrated by the solubilities shown in Table 3.3-1 [113].

A large amount of experimental data on the tertiary amino TCNQ adducts is now being collected, most of which has been conducted on DEMI. The materials form centrosymmetric crystals in the form of anti-parallel stacks of dimer pairs, rendering them useless for crystal non-linear optics [113, 152]. However, the charge-separated ground state of secondary and tertiary amino TCNQ adducts in the crystal phase has been confirmed through crystallographic analysis [152]. Though the aromatic ring system for DEMI was found to possess a predominately quinoidal character, charge could be assigned to the dicyanomethanide and tertiary amino moieties, thus confirming the charge-separated state of DEMI. More recently, studies have confirmed the reduction of planarity of ULTRA due to the addition of the piperidyl ring which confirms the conclusion made with the MOPAC calculations [153]. The densities of the tertiary amino TCNQ adducts in the crystal phase have also been estimated and are presented in Table 3.2-1 [154]. These are slightly lower than that of NPP. Unfortunately the dipole moments in the crystal phase for the tertiary amino TCNQ adducts are as yet unobtainable.

Dipole moment measurements have been conducted on DEMI. The dipole moment was found to be 45 D (calculated using Guggenheim's equation [155]) in dimethylformamide (DMF) [125], and 34 D (calculated using spherical local fields [156]) when measured in a polymethylmethacrylate (PMMA), DEMI (1 %) doped thin film [157, 158].

Various non-linear optical experiments have also been conducted. Among those, $|\mu\beta(0)|$ for DEMI has been measured through EFISH experiments in DMF and found to be $3,825 \times 10^{-48}$ esu (using mixed Lorentz and Onsager spherical local field factors) [125]. This corresponds to a $|\beta(0)|$ around 85×10^{-30} esu, using a dipole moment of 45 D. If the dipole moment is compared to Figure 3.3-2, we see for the SCI calculations that 45 D corresponds to a field of 0.0126 au and correspondingly $\beta(0)$ is -340×10^{-30} esu. With the SD-CI calculations, a dipole moment of 45 D corresponds to a field of 0.0133 au and thus $\beta(0)$ is -275×10^{-30} esu. Assuming that β in DMF is negative, the EFISH results are far smaller than the predicted values. $|\beta(0)|$ has also been measured for DEMI (1 %) doped in a PMMA thin film [157]. This was found to be 150×10^{-30} esu, which is a significantly larger value than the one found in solution. Once again using the measured dipole moment (34 D) we see from the SCI calculations that this represents a field of 0.0076 au and $\beta(0)$ is thus -519×10^{-30} esu. Similarly with the SD-CI calculations we obtain a field of 0.0086 au and $\beta(0) = -246 \times 10^{-30}$ esu. Clearly the experimental results neither agree with each other nor with the theoretical results. The solution state measurements produce a higher dipole than the corresponding solid solution measurements, yet the measured $\beta(0)$ values are vice-versa. There may be many reasons for this, such as differences in local field approximations, dimerisation in solution, reduced alignment of the chromophore etc. It is hoped that the experimental results obtained in Chapters 4, 5 and 6 will help resolve these matters to some extent.

Finally, the hyperpolarisability of DEMI has been measured in chloroform by means of hyper-Rayleigh scattering experiments [113, 159]. The magnitude of the hyperpolarisability, $|\beta(0)|$ was found to be 350×10^{-30} esu. Once again looking at the theoretical results and assuming that $\beta(0)$ is negative, there are two possible values of reaction field which will reproduce the experimental value. With the SCI calculations these are 0.0062 au and 0.0125 which correspond to dipole moments around 29 D and 45 D respectively. With the SD-CI calculations, the fields are 0.0098 au and 0.0113 au, and the dipole moments are 36 D and 41 D. Note that with these calculations, this nearly corresponds to the largest value of $|\beta(0)|$. Once again, the

estimates presented here will be compared to the experimental values obtained in Chapters 4 - 6.

§3.4 DED.

More recently, as a result of similar reactions with TCNQ, a range of "yellow" materials have been synthesised [160]. Like the tertiary amino TCNQ adducts, DED possesses an aromatic ring system with a dicyanomethanide acceptor group, but this time two diethylamine donor moieties are situated *para* to the dicyanomethanide unit. A limited amount of experimental or theoretical information is available on DED and no high level SOS calculations have been conducted. The results of MOPAC calculations however are presented in Table 3.2-2. This predicts dipole moments and average polarisabilities which are similar to that of the tertiary amino TCNQ adducts, but $\beta_{dip.}$ is estimated to be smaller. The crystal structure of DED has been determined, indicating that the molecule resides in a highly aromatic charge-separated state. The resulting density and dipole moment estimated from x-ray and neutron diffraction experiments (26.4 D) are presented in Table 3.2-1 [161, 162]. As would be expected for a molecule in the crystal phase, the dipole moment is greater than the gas phase dipole moment predicted by MOPAC calculations. These will be compared to the experimental results obtained in Chapter 4.

§3.5 The "Sheffield" Materials.

As stated earlier, results of dipole moment measurements will only be presented for the "Sheffield" materials. All of the materials are zwitterionic and are thus expected to possess high dipole moments. Previous dipole measurements and calculations have been conducted on similar molecules where the dipole moments were found to lie between 7 and 10 D in the gas phase [118, 163]. With the first two materials, negative charge is stabilised on the amino-heterocyclic moiety and positive charge on the pyridinium terminating groups. With SHEF C, negative charge is assigned to the oxygen and positive charge to the phosphorous, and as a result these are all expected to possess similar dipole moments since there are similar degrees of

charge-separation. The charge-separation for SHEF D however, only extends between the oxygen and phosphorous double bond. Thus the lower charge-separation distance implies that the dipole moment for this material should be lower.

Unfortunately these molecules are too large to conduct MOPAC calculations on. Small modifications have to be made to the molecular structure, such as the removal of long alkyl chains and phenol rings, so that calculations can be conducted. As a result, such calculations are generally confusing. The molecular dipole moments were found to be anomalously large (>20 D) using either AM1 or PM3 methodologies, so these will not be presented here. However, despite varying the structure several times, it was found, once again, that the average polarisabilities did not vary more than 10 %. Estimates of the polarisability calculated by MOPAC for the "Sheffield" materials and are presented in Table 3.5-1. It was found that similar polarisabilities to that of the tertiary amino TCNQ adducts are obtained for SHEF A, B, and C, the largest pertaining to SHEF C. SHEF D as expected, has a far lower polarisability.

	AM1 Methodology	PM3 Methodology
Material	$\overline{\alpha}$ / Å³	$\overline{\alpha}$ / Å³
SHEF A[a]	32.9	31.9
SHEF B[b]	37.1	36.1
SHEF C[c]	43.8	43.7
SHEF D	21.0	20.9

Table 3.5-1: *The average polarisabilities for the "Sheffield" materials calculated by MOPAC using AM1 and PM3 methodologies. The molecules are too large for MOPAC to calculate the polarisabilities of the full structures. Therefore the polarisabilities have been calculated by:-*
a: Exchanging the $C_{16}H_{33}$ chain with C_2H_5,
b: Exchanging the three C_4H_{11} chains with C_2H_5,
c: Exchanging the three phenol groups with C_2H_5.

References to Chapter 3.

[112] M. Szablewski, *J. Org. Chem.*, **59 (5)**, 954, (1994).

[113] M. Szablewski, P. R. Thomas, A. Thornton, D. Bloor, G. H. Cross, J. M. Cole, J. A. K. Howard, M. Malagoli, F. Meyers, J.-L. Brédas, W. Wenseleers, E. Goovaerts, *J. Am. Chem. Soc.*, **119 (13)**, 3144, (1997).

[114] G. H. Cross, D. Bloor, M. Szablewski, *Non-Linear Opt.*, **14**, 219, (1995).

[115] D. W. Allen, J. Hawkrigg, S. M. Tracey, A. K. Ray, A. Hassan, *Synth. Met.*, **87**, 89, (1987).

[116] D. W. Allen, P. Benke, *J. Chem. Soc. Perkin Trans. 1*, 2789, (1995).

[117] D. W. Allen, X. Li, *J. Chem. Soc. Perkin Trans. 2*, 1099, (1997).

[118] J. Abe, Y. Shirai, *J. Am. Chem. Soc.*, **118**, 4705, (1996).

[119] D. S. Chemla, J. Zyss, *Non-Linear Optical Properties of Organic Molecules and Crystals.*, **2**, Academic Press Ltd., London, (1987).

[120] J. Zyss, J. F. Nicoud, M. Coquillay, *J. Chem. Phys.*, **81 (9)**, 4160, (1984).

[121] M. Barzoukas, D. Josse, P. Fremaux, J. Zyss, J.-F. Nicoud, J. O. Morley, *J. Opt. Soc. Am. B*, **4 (6)**, 977, (1987).

[122] J. Zyss, J.-F. Nicoud, *Current Opinion in Solid State and Materials Science.*, **1**, 533, (1996).

[123] J. Zyss, *J. Mol. Electronics.*, **1**, 25, (1985).

[124] I. Ledoux, J. Badan, J. Zyss, A. Migus, D. Hulin, J. Etchepare, G. Grillon, A. Antonelli, *J. Opt. Soc. Am. B*, **4 (6)**, 987, (1987).

[125] D. Gray, Ph.D. Thesis, **University of Durham.**; *Molecular Organic Photonics.*, (1994).

[126] A. Fkyerat, A. Guelzim, F. Baert, W. Paulus, G. Heger, J. Zyss, A. Périgaud, *Acta Cryst. B*, **B51**, 197, (1995).

[127] A. Fkyerat, A. Guelzim, F. Baert, J. Zyss, A Périgaud, *Phys. Rev. B*, **53 (24)**, 16236, (1996).

[128] MOPAC, Version **6.0**, Shareware Ed.

[129] H. A. Kurtz, J. J. P. Stewart, K. M. Dieter, *J. Comp. Chem.*, **11 (1)**, 82, (1990).

[130] M. J. S. Dewer, *J. Am. Chem. Soc.*, **107**, 3902, (1985).

[131] R. W. Boyd, *Non-Linear Optics.*, Academic Press Inc., London, (1992).

[132] D. S. Chemla, J. Zyss, *Non-Linear Optical Properties of Organic Molecules and Crystals.*, **1**, Academic Press Ltd., London, (1987).

[133] S. R. Marder, L. T. Cheng, A. C. Tienmann, A. C. Friedli, M. Blanchard-Desce, J. W. Perry, J. Skindhøj, *Science*, **263**, 511, (1994).

[134] W. M. Laidlaw, R. G. Denning, T. Verbiest, E. Chauchard, A. Persoons, *Nature*, **363**, 58, (1993).

[135] C. Dhenaut, I. Ledoux, I. D. W. Samuel, J. Zyss, M. Bourgault, H. LeBozec, *Nature*, **374**, 339, (1995).

[136] S. R. Marder, J. E. Sohn, G. D. Stucky, *Materials for Non-Linear Optics.*, ACS Symposium Series, Washington D.C., (1991); D. N. Beratan, *Electronic Hyperpolarisability and Chemical Structure.*, **Chapter 5**, 89.

[137] F. Meyers, S. R. Marder, B. M. Pierce, J. L. Brédas., *J. Am. Chem. Soc.*, **116**, 10703, (1994).

[138] C. J. F. Böttcher, *Theory of Electric Polarisation.*, **2nd ed.**; O. C. Van Belle, P. Bordewick, A. Rip., Volume 1; *Dielectrics in Static Fields.*, Elsevier, London, (1993).

[139] A. Broo, M. C. Zerner, *Chem. Phys.*, **196**, 407, (1995).

[140] S. R. Marder, B. Kippelen, A. K.-Y. Jen, N. Peyghambarian, *Nature*, **388**, 845, (1997).

[141] S. R. Marder, C. B. Gorman, F. Meyers, J. W. Perry, G. Bourhill, J.-L. Brédas, B. M. Pierce, *Science*, **265**, 632, (1994).

[142] F. Meyers, S. R. Marder, B. M. Pierce, J.-L. Brédas, *Chem. Phys. Lett.*, **228**, 171, (1994).

[143] I. D. L. Albert, T. J. Marks, M. A. Ratner, *J. Phys. Chem.*, **100**, 9714, (1996).

[144] S. Ramasesha, Z. Shuai, J.-L. Brédas, *Chem. Phys. Lett.*, **245**, 224, (1995).

[145] P. Jacques, *J. Phys. Chem.*, **90**, 5535, (1986).

[146] H. G. Benson, J. N. Murrell, *J. Chem. Soc. Farad. Trans. 2*, **68 (1)**, 137, (1972).

[147] E. Buncel, S. Rajagopal, *J. Org. Chem.*, **54**, 798, (1989).

[148] L. G. S. Brooker, A. C. Craig, D. W. Hesaltine, P. W. Jenkins, L. L. Lincoln, J. Am. Chem. Soc., 87 (11), 2443, 2443, (1965).

[149] A. Botrel, A. Le Beuze, P. Jacques, H. Strub, *J. Chem. Soc. Farad. Trans. 2*, **80**, 1235, (1984).

[150] T. Kogej, J.-L. Brédas, Private communication, (1997).

[151] M. Prein,; W. Adam, *Angew. Chem. Int. Ed. Engl.*, **35**, 477, (1996).

[152] J. C. Cole, J. A. K. Howard, G. H. Cross, M. Szablewski, *Acta. Crystallographer Sect. C*, **C51**, 715, (1995).

[153] J. C. Cole, J. A. K. Howard, G. H. Cross, M. Szablewski, Private Communication (1996).

[154] J. Cole, J. A. K. Howard, Private Communication, (1997).

[155] E. A. Guggenheim, *Trans. Farad. Soc.*, **45**, 714, (1949).

[156] K. D. Singer, Ph.D. Thesis, **University of Pennsylvania.**; *Experimental Studies of Second Order Non-Linear Optical Susceptibilities in Organic Systems.*, (1981).

[157] D. Healy, Ph.D. Thesis, **University of Durham.**; *Solid Solution Studies of the Molecular Non-Linear Optical Properties of Organic Chromophores.*, (1996).

[158] D. Healy, P. R. Thomas, M. Szablewski, G. H. Cross, *Proc. SPIE.*, **2527**, 32, (1995).

[159] K. Clays, A. Persoons, *Phys. Rev. Lett.*, **66**, 2980, (1991).

[160] M. Szablewski, Private Communication, (1996).

[161] J. M. Cole, Ph.D. Thesis, **University of Durham.**; *Structural Studies of Organic and Organometallic Compounds Using X-Ray and Neutron Techniques.*, (1997). P. Coppens, T. N. Guru, P. Leng, E. D. Stevens, P. J. Becker, Y. W. Yang, *Acta Cryst. A*, **A35**, 63, (1979).

[162] J. C. Cole, J. M. Cole, G. H. Cross, M. Farsari, J. A. K. Howard, M. Szablewski, *Acta Crystallographer B*, **B53**, 812, (1997).

[163] E. Alcade, I. Dinarés, J. Frigola, C. Jaime, J.-P. Fayat, M.-C. Vertut, C. Miravitlles, J. Rius, *J. Org. Chem.*, **56 (13)**, 4223, (1991).

Chapter 4

Dipole Moments of Highly Dipolar, Anisotropic, Non-Linear Optical Chromophores.

§4.1 Introduction.

As already indicated in Chapter 2, to extract the first hyperpolarisability, β from EFISH measurements it is necessary to evaluate the dipole moment, μ of a molecule. One of the simplest methods used to measure the dipole moment is to measure the dielectric constant of a solution containing the unknown material. The equations needed to extract the dipole moment from an analysis of the dielectric constant were discussed in Chapter 2, and will be re-iterated in §4.4 for the analysis of experimental results.

Presented in this chapter are the results obtained from the measurement of the dielectric constant of solutions of the materials discussed in Chapter 3. The experimental apparatus and procedure used with such experiments are described, followed by a detailed analysis of the calculation of the dipole moment for these molecules. In addition, a comparison is made between the various local field formalisms used in such calculations (as discussed in Chapter 2), where attention is paid to the anisotropy of such molecules.

§4.2 Experimental Apparatus and Procedure.

There are numerous methods which can be utilised to measure the dielectric constant of a solution [164, 165, 166, 167]. Invariably, these involve the measurement of the capacitance of a solution filled cell. Variations on this theme may be adopted [164, 166, 167, 168] however, with the following experiments one of the simplest types of cell has been designed and used.

The three terminal, solution capacitor used for experimentation is shown in Figure 4.2-1 with its associated circuit diagram. It consists of a rod of stainless steel placed in the centre of a stainless steel tube, such that a concentric cylindrical capacitor is formed. The centre rod forms the high potential electrode and the outer tube, the low potential electrode. The electrode separation is 3 mm and the total diameter of the cell is approximately 65 mm, thus, the large electrode area and small electrode separation yields a large capacitance for the cell. This allowed fairly accurate determination of the dielectric constant. On top of the centre electrode is a guard ring which is earthed. The purpose of the guard ring is to remove any fringing of the electric field that may occur at the edge of the centre electrode. Thus, the field remains perpendicular to the surface of the electrodes along the entire electrode surface. The guard ring also ensures that the same volume of solution is measured each time. The distance between the guard ring and the centre electrode is also 3 mm. Finally, the entire arrangement is encased in a PTFE case so that the apparatus is electrically isolated. The electrodes are connected to the LCR meter via four BNC coaxial cable sockets, two for the centre electrode and two for the outer electrode. As is shown in the circuit diagram, the outer conductors for the sockets are connected to earth, and the centre conductors are connected to the high or low potential and current circuits of the LCR meter, respectively for the centre and outer electrodes.

The LCR meter (Hewlett Packard, HP4278a) used to measure the capacitance of the cell was operated at 1 MHz which is well away from any resonance points. To confirm this, in addition to the measurement of the capacitance, the

L_c L_p H_p

H_c

BNC sockets
leading to
LCR meter.

Outer polypropalene
insulating jacket.

Guard ring.

Solution between
electrodes, here.

Stainless steel inner
electrode: High
current / potential

Stainless steel outer
electrode: Low
current / potential.

H = High.
L = Low.
p = potential.
c = current.

Electronic Circuit

H_p H_c L_p L_c

To LCR
meter.

To inner
electrode.

To guard
ring.

To outer
electrode.
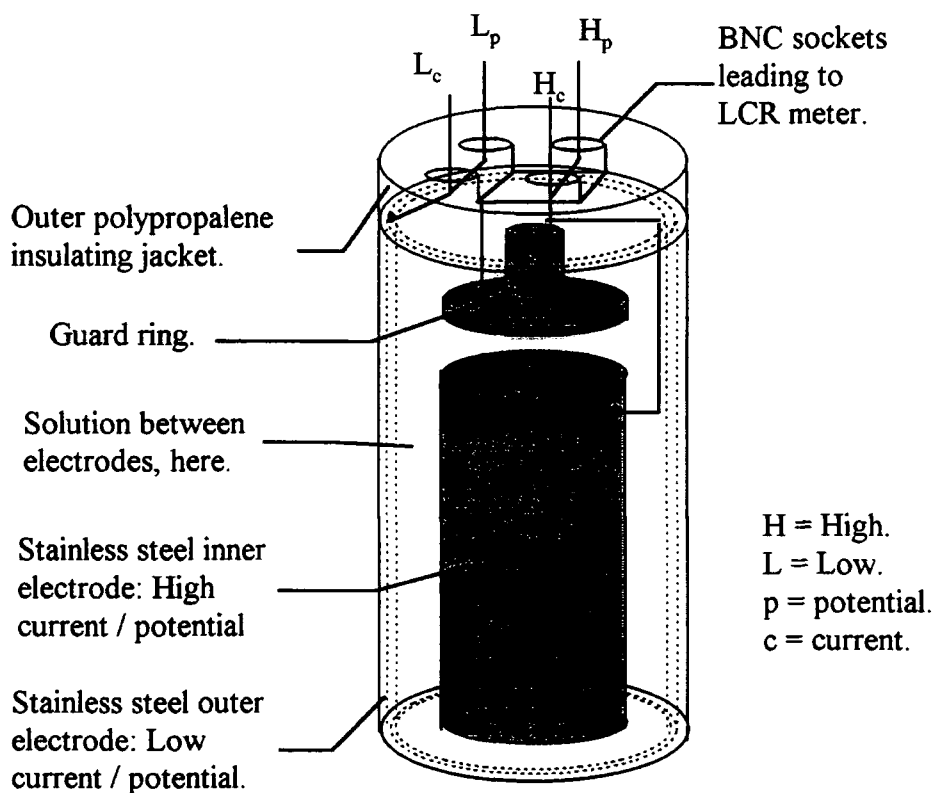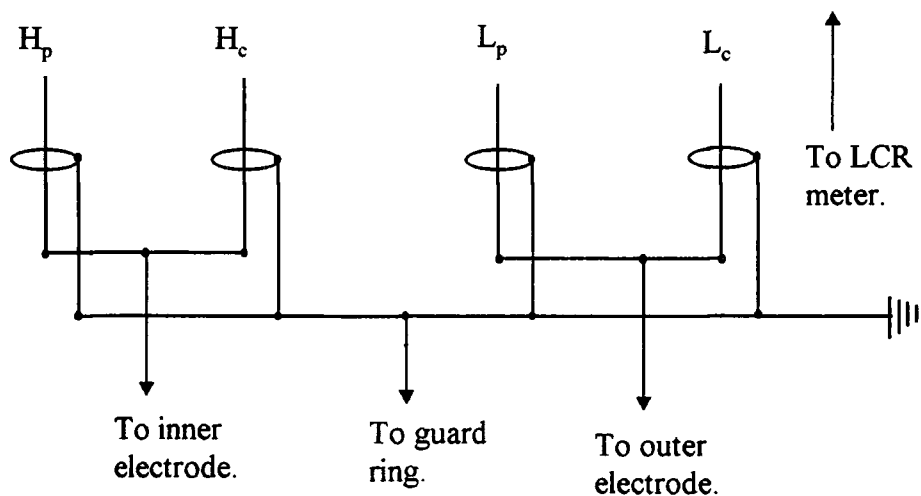
Figure 4.2-1: The capacitor and electronic circuit used in the measurement of the dielectric constant of solutions.

dielectric loss was also measured for each material in solution. The loss was found to be very low for all of the materials.

A typical experiment was conducted as follows. Firstly, the capacitance of the empty cell was measured. This was found to be approximately 14.43 ± 0.05 pF. Accuracy could be obtained to the fourth decimal place, but this was dependent on the temperature, humidity and conditions of the experiment at the time of measurement. Thus, measurements of the capacitance of the empty cell were conducted immediately before an experiment.

The dielectric constant, ε for each solution was calculated via the equation

$$\varepsilon = \frac{C_S}{C_A},$$

(4.2-1)

where C_S and C_A are the capacitances of the solution filled and empty cell respectively. To ensure that the cell provided accurate and sensible results, the dielectric constant of several solvents was measured and compared to that reported in the literature [169]. It was found that, for solvents that have a dielectric constant between 2 and 45, the measured dielectric constants of the solvents were within 10% of the literature values. This is an acceptable error when temperature and composition variations are considered. However, more accurate results could be obtained for solutions by measuring the variation in dielectric constant with concentration. It was found that repeated measurements of the same solvent resulted in an accuracy of 1 %, and for strongly concentrated solutions, the error on $\partial\varepsilon/\partial C$ could be as small as 5 %.

A stock solution of a material of concentration around 10^{-4} - 10^{-3} mol l^{-1}, was dissolved in the appropriate solvent, to a volume of 50 ml (using a 50 ml volumetric flask). The solution was then successively diluted (also using 50 ml volumetric flasks), such that two orders of magnitude in concentration were traversed during the experiment. The cell was then filled with each solution, the capacitance measured, and the solution returned to its flask. The order in which the experiment was conducted is

important as the temperature of each solution may vary and thus effect the value of the dielectric constant measured. Therefore, experiments were conducted from low to high and high to low concentrations in an attempt to eliminate any variation in temperature during the process of the experiment. A graph of the dielectric constant of each solution was then plotted versus the concentration of the solution, and an average gradient of the two experimental curves was taken. Experiments for each material were conducted three or four times to ensure that the experiment was repeatable and to obtain an average $\partial \varepsilon / \partial C$. All solvents used were HPLC grade (Aldrich - Sigma Co.) and the solutions were filtered using a 0.5 μm disposable filter before use.

§4.3 Experimental Results.

Experiments were conducted on NPP, DED and the "Sheffield" materials in chloroform. Chloroform was initially chosen as a solvent because its dielectric constant is low, allowing for more accurate readings of the dielectric increment. In addition, it was found that the solubility of NPP and the "Sheffield" materials was relatively high in chloroform, thus enabling experiments to be easily conducted. However, the solubility of DED in chloroform was fairly low and measurements were found to be difficult at low concentrations. Similar problems arose with the tertiary amino TCNQ adducts and as a result of this, experiments on the tertiary amino TCNQ adducts were conducted in dichloromethane (DCM). This has a higher dielectric constant, thus experiments may be less accurate. However, the solubility of the tertiary amino TCNQ adducts was found to be slightly better in DCM, thus allowing the gradient to be obtained at stronger concentrations. Despite this, it was found that due to the general low concentration of the solutions, the error on the experimental gradient for the tertiary amino TCNQ adducts and DED remained large, ≈ 30 %. The experiment gradients for the other materials have smaller errors.

The graphs obtained from the experiments described in §4.2 are presented in Figure 4.3-1 and Figure 4.3-2. The error bars show the possible deviation of the dielectric constant due to fluctuations in the temperature of the solutions. This was
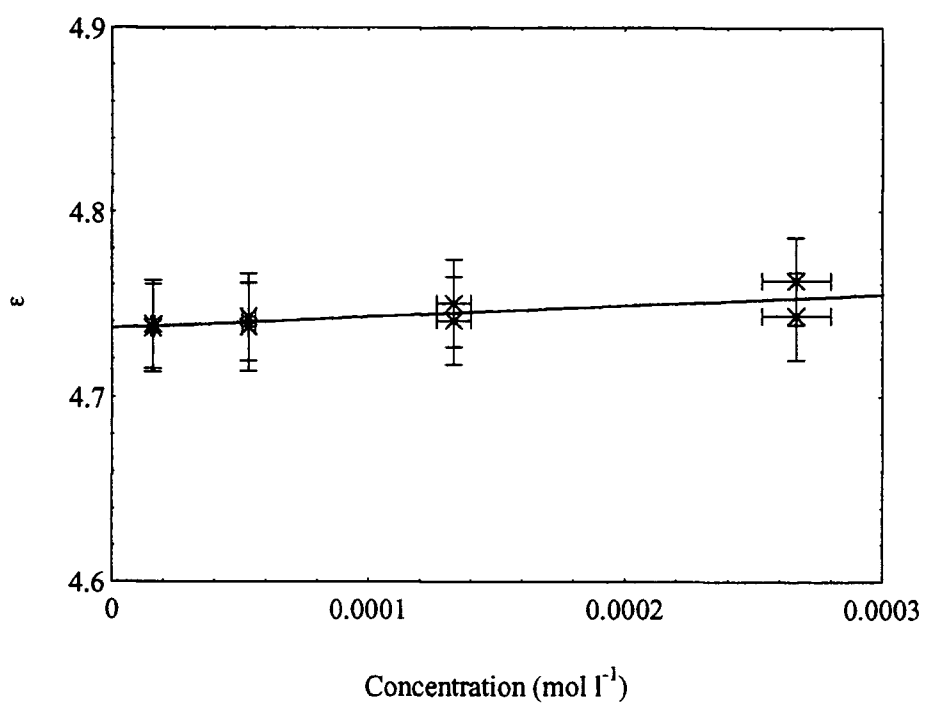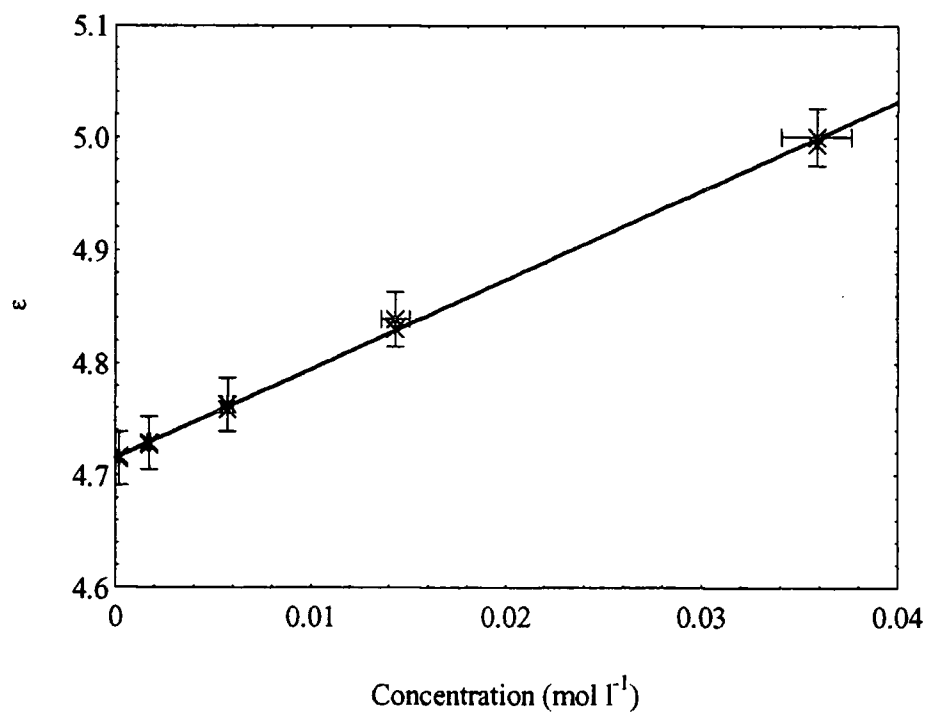
Figure 4.3-1: Typical graphs showing the dielectric constant obtained for solutions of increasing concentration of NPP (top) and DED (bottom). The straight lines are fits to the data.
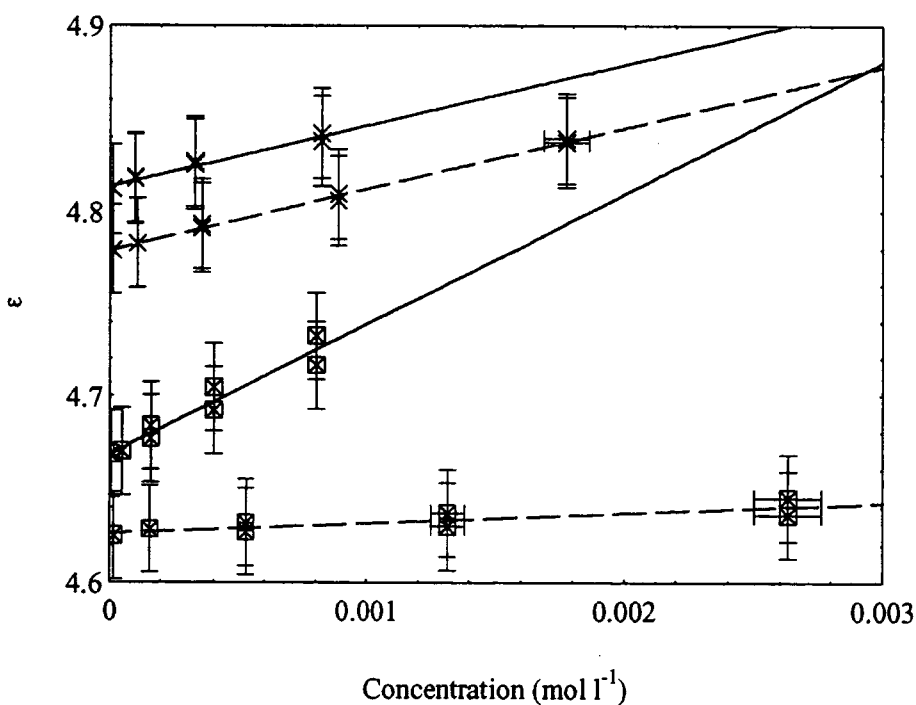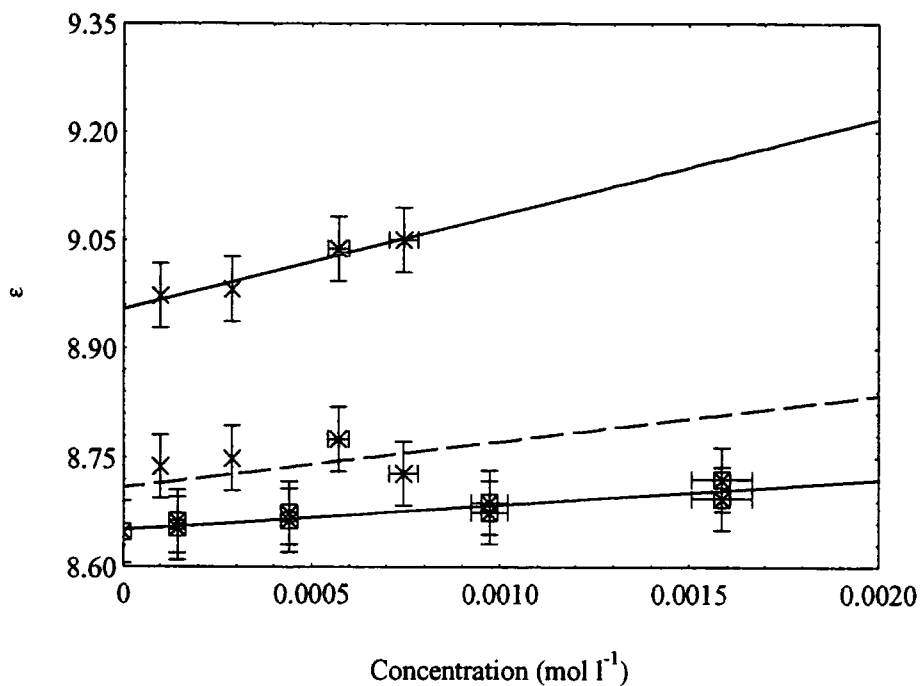
Figure 4.3-2: Typical graphs showing the dielectric constant obtained for solutions of increasing concentration. Top graph: For DEMI (crosses and solid line), DCH (crosses and dashed line), and ULTRA (squares and solid line). Bottom graph: For SHEF A (crosses and solid line), SHEF B (crosses and dashed line), SHEF C (squares and solid line), and SHEF D (squares and dashed line). The straight lines are fits to the data.

found to be a problem, thus the experimental cell may have to be modified for future experiments. All of the experiments yield a linear increase in dielectric constant with increasing concentration. This is best demonstrated with the results for NPP which are obtained using concentrations up to 100 times that used for DEMI and DED.

The data points are fitted to a straight line using a least squares fitting program, and the average gradients, obtained from analysis of several experiments for each material, are presented in Table 4.4-1. As is clearly evident, the gradients obtained for the tertiary amino TCNQ adducts, DED, and the first three "Sheffield" materials are large when compared to NPP or SHEF D as might be expected for these materials. With the tertiary amino TCNQ adducts, DEMI produces the largest gradient followed by DCH, and ULTRA respectively. With the "Sheffield" materials, SHEF C produces the largest gradient. Further analysis of these trends will be conducted in §4.5.

§4.4 The Interpretation of the Analysis used for the Determination of Dipole Moments.

We recall from Chapter 2, that there are many equations which can be used to measure the dipole moment, depending on the local field factors required for the analysis. Debye local field factors have already been found to be inadequate for measuring the gas phase dipole moment from solution measurements [166, 170]. However, Guggenheim's equation, as given previously by equation (2.3-4), may be used to calculate the dipole moment in the solution of measurement [166, 171, 172, 173]

$$\mu_s = \sqrt{\frac{10^{36}}{N_a} \cdot \frac{9k_B T}{4\pi} \cdot \frac{3}{(\varepsilon+2)(n^2+2)} \cdot \frac{\partial \varepsilon}{\partial C}\bigg|_0}$$

(4.4-1)

where N_a is Avogadro's number, ε and n are the dielectric constant and refractive index of the solvent respectively, $\partial \varepsilon / \partial C|_0$ is the experimental gradient at zero concentration,

Material	$\partial\varepsilon/\partial C$ / l mol^{-1}	$\bar{\alpha}$ / Å^3	α_z / Å^3
NPP[a]	7.0 ± 0.4	19.1	30.5
DED[a]	64.1 ± 19.2	37.3	70.4
DEMI[b]	145.0 ± 43.5	45.4	99.0
DCH[b]	67.6 ± 20.3	56.4	112.5
ULTRA[b]	33.7 ± 10.1	46.4	65.0
SHEF A[a]	20.8 ± 4.2	32.9[c]	71.7[c]
SHEF B[a]	39.2 ± 7.8	37.1[c]	70.5[c]
SHEF C[a]	71.0 ± 14.2	43.8[c]	88.7[c]
SHEF D[a]	5.1 ± 1.0	21.0	23

Table 4.4-1: Average gradients obtained from the measurement of the dielectric constant of solutions of the materials mentioned in the text, with increasing concentration. In addition, the average polarisability, $\bar{\alpha}$ and the polarisability along the principal axis, α_z are presented. These are obtained through MOPAC calculations using an AM1 Hamiltonian and SCF methodology.
a: Conducted in chloroform.
b: Conducted in DCM
c: See Table 3.5-1 for additional information.

k_B is Boltzman's constant and T is the temperature. k_B and $\partial\varepsilon/\partial C|_0$ are in cgs units, and the dipole moment, μ_s has units of Debyes.

As discussed in Chapter 2, the presence of a reaction field results in the enhancement of the dipole moment in solution, thus to obtain the gas phase dipole moment, Onsager's equation may be utilised [170]. The dipole moment in the solution of measurement, μ_s is calculated through equation (2.4-4),

$$\mu_s = \sqrt{\left(\frac{1}{4\pi N_a}\frac{\partial\varepsilon}{\partial C}\Bigg|_0 - f_2^0\alpha\right)\frac{3k_BT}{f_2^0}}$$

(4.4-2)

where f_2^0 arises from an analysis of the local field (see Chapter 2, §2.3). We recall, for Onsager's spherical local field factors [166, 170], f_2^0 is found to be

$$\left(f_2^0\right)^{Sph.} = \frac{1}{(1-f\alpha)}\frac{3\varepsilon}{(2\varepsilon+1)},$$

(4.4-3)

where α is the average polarisability of the molecule, and f is the reaction field factor and is defined by (2.3-8) in Chapter 2.

Since highly anisotropic molecules are considered, it may be inappropriate to use spherical local field factors. Once again we recall from Chapter 2 that ellipsoidal local field factors may be used for anisotropic molecules [166, 174, 175, 176]. In conjunction with (4.4-2), f_2^0 becomes

$$\left(f_2^0\right)^{ell} = \frac{\varepsilon}{\left(\varepsilon+(1-\varepsilon)A_z\right)}\frac{1}{\left(1-f_z\alpha_z\right)},$$

(4.4-4)

where α_z is the polarisability along the z-axis of the cavity and the parameters f_z and A_z are given by (2.3-19) and (2.3-20) respectively. The gas phase dipole moment may

be calculated through equation (2.4-5), replacing f and $\bar{\alpha}$ with f_z and α_z respectively when using ellipsoidal local fields.

The above equations are used to calculate the dipole moments of the materials discussed in Chapter 3 from the experimental gradients and polarisabilities presented in Table 4.4-1. As is evident from the analysis, several additional parameters are needed to calculate the dipole moment. For (4.4-1) this is simply the dielectric constant and refractive index of the solvent which is obtained either from experiment or the literature [169]. With the other equations, the polarisabilities, cavity radii, and shape factor need to be determined.

The polarisabilities may be obtained through various experimental methods [166, 177], and may be related to the refractive index and cavity radius via the Clausius-Mossotti equation (see equation (2.3-9)) [166]

$$\frac{n^2-1}{n^2+2}\bar{r}^3 = \bar{\alpha}$$

(4.4-5)

where n is the internal refractive index of the solute evaluated at infinite frequency and may be approximated to the refractive index at the sodium-D line ($\lambda = 589$ nm) by the relationship $n_\infty^2 \approx 1.05 n_D^2$. Insertion of (4.4-5) into (4.4-2) results in a simple calculation provided the cavity radius is known. However, the low solubility of the materials coupled with an appreciable absorption of the tertiary amino TCNQ adducts at the sodium-D line, inhibits considerably the measurement of the polarisability. Therefore, theoretical calculations of the polarisability have to be relied upon. α_z and $\bar{\alpha}$ are calculated using MOPAC [178] which is discussed in Chapter 3, and are, in addition, presented in Table 4.4-1. It is possible that the theoretical calculation of the polarisability may induce an error into the calculations especially where the structure of the molecule has been modified. As mentioned earlier, several molecular geometries were tried and the method of calculation (i.e. AM1 or PM3 Hamiltonians) also varied when calculating the polarisabilities, but it was found that the magnitudes of α_z and $\bar{\alpha}$ did not vary by more than 10 %.

The cavity radius may be estimated by several methods [166, 179, 180]. It has been found that a valid approximation of the cavity radius is the volume available to a solute molecule in a particular medium, i.e. the average radius of a molecule plus any unoccupied "space" [166]. The density of a solute, d is often used to obtain the radius via the equation [166, 170]

$$\bar{r} = \left(\frac{3M}{4\pi d N_A} \right)^{\frac{1}{3}},$$

<div align="right">(4.4-6)</div>

where M is the molecular weight, and N_A is Avogadro's number. The density may be obtained either by experimentally determining the density of solutions of varying concentration, or by using x-ray crystallography and using the density of the unit cell. The low solubility of the materials studied here means that the former method is impossible, as solution concentrations are too weak. The density has been estimated from the crystal structure, as is reported in Chapter 3 and the cavity radii calculated via the crystal densities for the first five materials are presented in Table 4.4-2.

A different method can be used [181, 182] which enables the average radius, $\bar{r}$ and the shape factor, A_z to be estimated. Commercial molecular modelling software [183] is used to calculate the solvent accessible surface (SAS) around a molecule, using a solvent probe of radius 3 Å based on the radius of chloroform or DCM. The SAS is then approximated to an ellipsoid with the semi-axes z, y, and x collinear with the length, width and breadth of the molecule respectively. An example of this is shown in Figure 4.2-1 for DED. The systematic errors involved with the measurement of a, b, and c can be as large as $\pm$ 0.5 Å which means that an error of $\pm$ 25 % is possible on A_z and $\pm$ 15 % is possible on $\bar{r}$. However, in addition a refinement can be made to the estimate of $\bar{r}$ and A_z by introducing a degree of self consistency to the calculations. The polarisability along the z-axis of the molecule, α_z may be related to the average polarisability, $\bar{\alpha}$ by [166, 175]

$$\alpha_z = \frac{\bar{\alpha}(abc)}{abc + (3A_z - 1)\bar{\alpha}} .$$

<div align="right">*(4.4-7)*</div>

Equation (4.4-7) is used to ensure that the theoretical value of α_z calculated in MOPAC can be obtained from $\bar{\alpha}$ and the estimated values of the shape factor and average radius. If this is not the case, then the values of a, b, and c are adjusted within the estimation error so that α_z is returned. Though this does not reduce the systematic errors on A_z and $\bar{r}$ significantly, it does ensure that there is at least a degree of consistency between the estimated shape of the cavity calculated by this method and the polarisability tensor estimated by MOPAC calculations.

In the following passages the calculation of the cavity radius is discussed in a little more detail for each molecule. The lengths of the cavity semi-axes, average radii and cavity shape factor are presented in Table 4.4-2. The molecular axes are defined generally such that the axes, z, y and x reside along the length, width and breadth of the molecules respectively. This is shown in Figure 4.4-1 for DED. (Please also refer to Figure 3.1-1 in Chapter 3.)

NPP is approximately twice as long as it is wide. The length (a) is essentially defined as the distance between the oxygens pertaining to the nitro-group and the terminal part of the pyrrole ring plus the van-der-waals radii of the nitrogen and oxygen on each terminal group, respectively. Similarly, the width (b) is defined by the distance between the hydrogens on the aromatic ring plus two van-der-waals radii. In addition, since NPP is quite planar, the breadth (c) is defined purely by the van-der-waals surface of the carbon atoms.

The cavity for DED is a little harder to define due to the presence of the diethylamine groups which enlarge one side of the SAS. The cavity is usually chosen to reside around the centre of the molecule, with the lengths of the axes defined as an average of the SAS, as shown in Figure 4.4-1. Consequently it is possible that the cavity radius can be under or over-estimated by a significant margin, and as a result,

<div align="center">79</div>
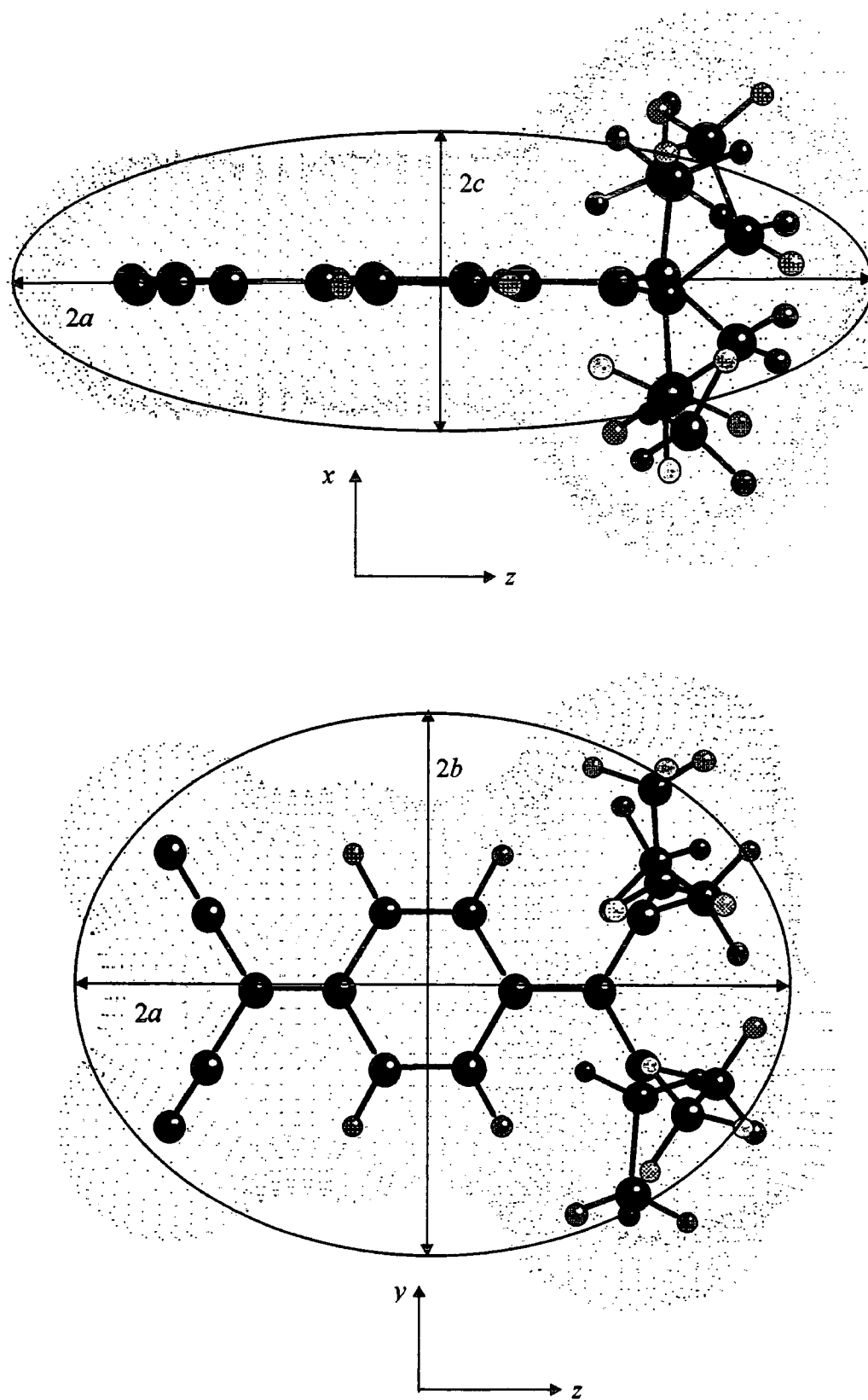
Figure 4.4-1: Two projections of DED with corresponding representations of the Solvent Accessible Surface surrounding the molecule. The ellipse surrounding each projection shows the approximation of the cavity from the SAS.

we see the origin of the estimation error. The width of the molecule is now dominated by the dicyanomethanide acceptor group, resulting in a significant increase in the cavity width with respect to NPP. However, it is estimated here that the length and breadth of DED are similar to that of NPP.

Like NPP and DED, DEMI is planar, thus the breadth of the cavity (c) is estimated to be approximately the same. The conjugated chain, *para* to the dicyanomethanide acceptor group on the aromatic ring-system, not only increases the length of the molecule and the cavity, but also brings the dipole moment slightly off axis. To circumvent this problem, the cavity axes are re-defined so that the z-axis lies along the dipole moment vector as is required by the above analysis (see Chapter 2, [166]). The average width of the cavity is consequently slightly smaller than that estimated for DED.

DCH is very similar to DEMI, in that it is planar and has approximately the same width and breadth. The presence of the large cyclohexyl groups on the amino end of the molecule results in a slight increase in the length of the cavity.

With ULTRA, the length of the molecule is larger than DCH or DEMI due to the addition of the diethylether groups to the amino end. There has also been the addition of a piperidyl ring to the conjugated chain which twists the molecule out of its planar configuration. As a result, the cavity becomes increasingly hard to define logically. The average length of the cavity (a) is only slightly larger than that of DCH or DEMI due to the lack of planarity in ULTRA. The average width is also estimated to be slightly larger. However, the breadth of the cavity is chosen to remain the same as DCH. This a somewhat arbitrary choice admittedly and c could be as much as 1.5 Å larger. However the refinement to the analysis using (4.4-7) allows at least consistent values to be used.

Material	a / Å	b / Å	c / Å	$\bar{r}$ / Å	A_z	$\bar{r}_{x-ray}$ / Å
NPP	5.7	2.9	1.9	3.2	0.1377	3.96
DED	5.9	4.0	2.0	3.6	0.1592	4.64
DEMI	8.0	3.6	1.9	3.8	0.1027	4.44
DCH	8.4	3.6	2.3	4.1	0.1105	5.03
ULTRA	8.5	3.8	2.3	4.2	0.1121	4.86
SHEF A	8.0(+)	3.2	1.9	3.7	0.0965(-)	—
SHEF B	8.0(+)	3.2	1.9	3.6	0.1010(-)	—
SHEF C	7.0	3.6(±)	2.0	3.7	0.1249	—
SHEF D	2.8	2.8(+)	2.8	2.8	0.3333(-)	—

Table 4.4-2: Table showing the lengths of the cavity semi-axes, a, b, and c, and the average radii and shape factor obtained from those estimates. Data with a (+) indicates that this value may be larger. Similarly, data with a (-) indicates the shape factor may reduce.

Problems in analysing the cavity through this method arise further when considering the "Sheffield" materials. Like the tertiary amino TCNQ adducts and DED, SHEF A is a planar molecule, where the width and breadth of the cavity may be easily defined. However, the addition of the alkyl chain at one end of the molecule gives rise to the question; what is the length of the cavity? The length could conceivably be up to 15 Å. Since the polarisabilities and dipole moments of long alkyl chains are usually low and that the dipole moment of SHEF A extends mainly between the positively charged pyridinium group and the negatively charged heterocyclic moiety (see Figure 3.1-1, Chapter 3), the alkyl chain on SHEF A could be treated in effect as "part of the solvent". The difference in dipole moments between similar molecules with and without such alkyl chains would only be small. Consequently the alkyl chains can be excluded from the cavity. Then for SHEF A, the distance between the pyridinium group and the negatively charged heterocyclic moiety, plus two van-der-waals radii can be defined as the length of the cavity. However one acknowledges that the cavity length could be considerably larger than estimated in Table 4.4-2.

With SHEF B, essentially the same problem arises with the length of the cavity as with SHEF A, except this time the three butyl groups are the cause. As a result there is a slight enlargement of the SAS at the appropriate end of the molecule. However, the same arguments applied to SHEF A can be applied here, thus for the moment the cavity axes are the same.

With SHEF C, there is considerable difficulty defining the cavity radius and it is increasingly difficult to approximate the SAS to a sphere or and ellipsoid. The presence of the three phenyl rings introduce large SAS lobes that stick out of the plane of the molecule. These can be treated as "part of the solvent" as with SHEF A and SHEF B, however it is unclear whether the exclusion of the phenol rings affects the dipole moment of SHEF C to a large extent. The length and breadth shown in Table 4.4-2 for SHEF C are those estimated when the phenyl rings are removed. Furthermore the dipole moment, which extends from the positively charged phosphorous to the negatively charged oxygen moiety, does not lie along the length of the molecule. The cavity axes may be re-defined so that the dipole moment lies along

the z-axis, but the molecule subsequently lies off axis and so that the dipole moment is not in the centre of the cavity. As a result it is extremely difficult to define the width of the cavity for SHEF C, nonetheless it is taken as an average of the SAS either side of the dipole moment vector. Once again, this means that the cavity radius and shape factor could be over or under-estimated.

Finally with SHEF D, it is noticed that, contrary to the previous molecules, the dipole moment is perpendicular to the length of the molecule. Thus the dipole does not lie along the z-axis, but this time the y-axis, from the positively charged phosphorus to the negatively charged oxygen, nearly parallel to the double bond. Since the charge separation distance is small, the dipole moment is expected to be additionally small. Again the axes can be transformed so that the dipole lies along the z-axis. The situation for SHEF D is then similar to that of an oblate spheroid where the y-axis may vary considerably due to the presence of the alkyl chain and phenol rings. Once again these may be excluded from the estimate of the cavity. The resultant SAS is thus the van-der-waals surface surrounding the oxygen and phosphorous atoms which is close to a sphere. The shape factor, A_z is then close to 1/3 and all ellipsoidal equations revert to the spherical counterparts. Furthermore, the estimated polarisability along the dipole moment, as calculated by MOPAC, is very close to the average polarisability, further suggesting that the molecule resides in a uniformly polarisable sphere and not an ellipsoid. Thus the values of a, b, and c presented in Table 4.4-2 are identical.

It is interesting to note the value of refractive index that is obtained using the Clausius-Mossotti equations for spherical and ellipsoidal local fields (see equations (2.3-9) and (2.3-26)), when inserting the polarisabilities, cavity radii, and shape factor estimated above. These are shown in Table 4.4-3. From the definition of the two equations [166, 175], the refractive indices obtained from either equation should be the same, providing consistent values of the radius, polarisability and shape factor are used. As a degree of self consistency is introduced through (4.4-7), this should be the case. Inspection of Table 4.4-3 shows this to be true within the error of measurement. It is noted, however that the refractive indices of all of the materials are quite high and

appear to be over-estimates in comparison to the refractive indices of crystals for example [184]. This indicates through inspection of the Clausius-Mossotti equations that the estimate of the cavity radius is too low. The Clausius-Mossotti equations are extremely sensitive to the value of the cavity radius, such that changes of the radius within the error of measurement may change the refractive index by as much as 40%. Thus, only small increases in cavity radius are needed to produce reasonable values of the refractive index. This is clearly evident when the refractive indices are re-calculated using the crystal structure cavity radius, as present in Table 4.4-4.

The dependence of the spherical and ellipsoidal gas phase dipole moments on the cavity radius (while the shape factor remains constant) is shown for DEMI in Figure 4.4-1. The radius increases between two limiting values; the cube root of the average polarisability, $\sqrt[3]{\bar{\alpha}}$ and approximately half the length of the molecule. We see that the gas phase dipole moment which is obtained from the experimental gradient, increases dramatically with $\bar{r}$ so if the SAS radius is an under-estimate of the cavity radius as is indicated by the refractive index estimates, the dipole moment will increase accordingly. Of course the over-estimation of the refractive indices could also mean that the polarisability is over-estimated. This only highlights the necessity of measuring refractive indices in conjunction with dipole moment measurements, especially for highly polar molecules such as those under study. Nonetheless, as stated earlier this is extremely difficult with the TCNQ materials, so theoretical estimates of the polarisability have to be relied upon.

The dipole moments for the materials discussed in this thesis are calculated utilising the estimates of the cavity radii and polarisabilities in combination with the experimental data, using a computer program which has been developed in Mathematica [185]. This is shown in Appendix I. The results are discussed in the following section.

Material	n	n_{ell}	$\bar{r}$ / Å
NPP	2.4	2.4	3.2
DED	3.5	4.1	3.6
DEMI	3.9	3.7	3.9
DCH	3.7	3.4	4.1
ULTRA	2.5	2.2	4.2

Table 4.4-3: Refractive indices for NPP and TCNQ derivatives obtained using spherical and ellipsoidal Clausius-Mossotti equations, estimated by using SAS cavity radii.

Material	n	n_{ell}	$\bar{r}$ / Å
NPP	1.5	1.7	4.0
DED	1.7	2.0	4.6
DEMI	2.1	2.6	4.4
DCH	1.8	2.2	4.9
ULTRA	1.7	1.8	5.0

Table 4.4-4: The refractive index of NPP and various TCNQ derivatives calculated using spherical and ellipsoidal Clausius-Mossotti equations, utilising crystal structure cavity radii.
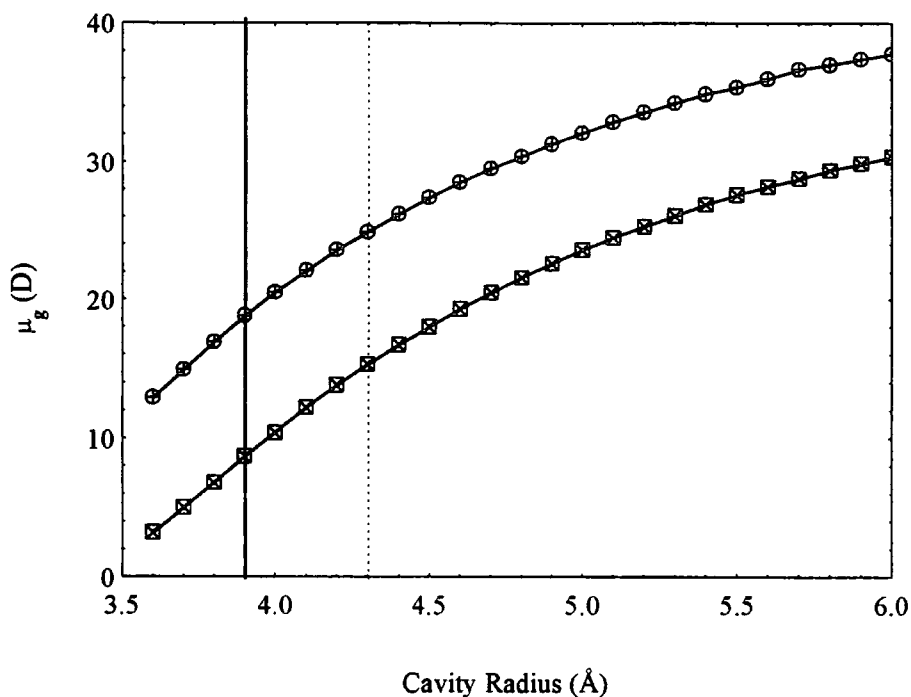
Figure 4.4-1: Evolution of the gas phase dipole moment, calculated using the spherical (squares) and ellipsoidal (circles) local field formalisms for DEMI with cavity radius. The solid and dotted lines represent the SAS and crystal structure radii, respectively.

§4.5 Discussion of Results.

The results of the dipole moment calculations are presented in Table 4.5-1. The percentage error on the dipole moments is half the percentage error on the gradients presented in Table 4.4-1, since the dipole moment is proportional to the square root of the gradient. It is estimated that and additional 5 % error on the dipole moment is incurred due to the uncertainty of the cavity radius, shape factor and polarisabilities.

The trends observed with the experimental gradients $\left(\partial \varepsilon / \partial C\right)$ are reflected directly by the dipole moments for the materials. The calculated solution state and gas phase dipole moments are extremely large for the tertiary amino TCNQ adducts and the first three "Sheffield" materials. In comparison to NPP (which still has a high dipole moment in comparison to a solvent molecule) the dipole moment for DEMI is

about three to four times larger, which is a particularly large value and serves to demonstrate that a high degree of charge-transfer is possible with the TCNQ materials.

Of the tertiary amino TCNQ adducts, DEMI has a larger dipole moment than DCH or ULTRA. The lower dipole moments can be attributed as a result of the loss of planarity in the molecules, resulting in shorter charge-separation distances, and slightly weaker electron donating moieties.

DED also has an extremely large dipole moment. One must be careful when comparing dipole moments of DED to the tertiary amino TCNQ adducts as experiments were conducted in different solvents. However, it is noted that though the charge-separation distance across DED is smaller, the dipole moment is comparable to that of the tertiary amino TCNQ adducts. This may indicate a considerable increase in the donor - acceptor strengths and an increase in the aromaticity of the DED. This is possibly confirmed by similar observations of DED in the crystal phase [186, 187]. One must be aware however, that the high dipole moment may also be due to an over-estimate of the cavity radius or an under-estimate of the polarisability for DED.

Of the "Sheffield" materials, SHEF C has the largest dipole moment. It is noted, once again, that the charge-separation for SHEF C is slightly smaller than that of SHEF A or SHEF B, but SHEF A and SHEF B possess smaller dipole moments than SHEF C. Such differences can be attributed to differing donor and acceptor strengths, and it also may indicate that SHEF C resides in a more zwitterionic state than SHEF A or SHEF B. Possible confirmation lies with solvatochromic evidence [188, 189] where an extremely large hypsochromic (negative) shift is exhibited for SHEF C in comparison to SHEF A or SHEF B. This indicates that the ground state dipole moment is significantly larger than the excited state dipole moment near the gas phase, and the molecule thus resides in a predominately zwitterionic state. Since lower negative shifts are observed for SHEF A and B [188, 190], it is possible that they are less aromatic near the gas phase than SHEF C and this appears to agree with the dipole moment results. SHEF D has a small dipole moment in comparison (smaller than NPP) as might be expected since the charge-separation is quite small. However, in

Material	μ_s^{Gugg} / D	μ_s^{Sph} / D	μ_g^{Sph} / D	μ_s^{ell} / D	μ_g^{ell} / D
NPP	6.1 ± 0.3	6.9 ± 0.6	3.9 ± 0.3	8.3 ± 0.8	5.8 ± 0.5
DED	18.4 ± 2.8	18.2 ± 3.6	7.9 ± 1.6	20.3 ± 4.1	9.3 ± 1.9
DEMI	21.9 ± 3.3	22.4 ± 4.5	6.8 ± 0.9	33.0 ± 6.6	15.2 ± 3.4
DCH	15.0 ± 2.3	15.6 ± 3.1	5.0 ± 1.0	22.8 ± 4.6	13.1 ± 2.6
ULTRA	10.6 ± 1.6	13.5 ± 2.7	6.4 ± 1.3	19.0 ± 3.8	14.1 ± 2.8
SHEF A	10.5 ± 1.1	11.3 ± 1.7	5.8 ± 0.9	14.4 ± 2.2	9.6 ± 1.4
SHEF B	14.4 ± 1.4	14.2 ± 2.1	6.3 ± 0.9	19.4 ± 2.9	12.5 ± 1.9
SHEF C	19.3 ± 1.9	17.9 ± 2.7	6.8 ± 1.0	22.5 ± 3.4	11.1 ± 1.7
SHEF D	5.2 ± 0.5	4.4 ± 0.7	1.4 ± 0.2	4.4 ± 0.7	1.4 ± 0.2

Table 4.5-1: Table showing the dipole moments obtained from experiment using Guggenheim's equation (superscript: Gugg.), and the spherical (superscript: Sph.) and ellipsoidal (superscript: ell.) local field formalisms. The subscripts s and g stand for the dipole moment in the solution and gas phases respectively.

89

comparison to the dipole moments of solvents (1.01 D for chloroform [166]) it is quite large. Considering the charge-separation distance for SHEF D is similar to that of solvents, the comparatively large dipole moment adequately demonstrates the zwitterionic nature of the molecule.

In comparison to the other estimates of the dipole moment, discussed in Chapter 3, we see for NPP that the spherical solution phase dipole moments presented in Table 4.5-1 agrees well with literature values obtained in the crystal phase (8.1 D [191, 192]) and solution phase (6.7 D [167]). Furthermore it may appear that the solution phase ellipsoidal dipole moments are over-estimated. However one must also consider the local fields used with the literature dipole moments which are all spherical, so it is likely that a disagreement is found here. Both ellipsoidal and spherical gas phase dipole moments for NPP, estimated here, do not agree with the MOPAC calculations conducted upon NPP which are discussed in Chapter 3 (9.2 D and 7.9 D for AM1 and PM3 methodologies respectively). It is possible that the MOPAC calculations over-estimate the value of the dipole moment for NPP, since it is unlikely that similar dipole moments are found in the gas phase as well as the crystal phase, as is evident from comparisons to literature values [191, 192]. Over-estimation of the gas phase dipole moment for large molecules is often a problem associated with MOPAC calculations, especially the AM1 methodology [193, 194]. Again this is evident through comparisons of AM1 dipole moments to PM3 dipole moments.

The gas phase dipole moment, estimated this time for DED, is also lower than that calculated via MOPAC. However, both spherical and ellipsoidal estimates fall just within experimental error of either dipole moment estimated using the AM1 (10.9 D) or PM3 (9.7 D) methodologies. The results are encouraging when the dipole moment for DED is compared to the dipole moment measured in the crystal phase (26.4 D [186]). The crystal phase dipole moment is larger than that measured here since it can be postulated that the molecule resides in a higher polarity environment in the crystal phase than the solution phase. The electric field experienced by DED in the crystal phase is therefore larger and the dipole moment is also larger than that in the solution phase.

Poor correlations are again found with the dipole moments of the tertiary amino TCNQ adducts and that calculated by MOPAC. The spherical gas phase dipole moments estimated here are generally lower than the MOPAC dipole moments and the ellipsoidal moments higher. Since MOPAC often erroneously estimates dipole moments for large molecules [193, 194] as explained above, emphasis will be placed on comparisons with 40-state calculations rather than these. There is also a strong disagreement between the solution phase dipole moment of DEMI and that previously measured (45 D in DMF [167]). This is to be expected, since the two measurements are conducted in different solvents. The neglect of specific solvent interactions and the use of different measurement techniques, hampers the comparison between the two results. Nonetheless, it is observed from the present study that the dipole moment of DEMI in DCM is extremely large and that a larger dipole moment of DEMI in DMF is not unlikely, since DMF possesses a higher dielectric constant. Thus the dipole moments obtained in this study appear to be consistent with those obtained in previous studies.

Dipole moments for the "Sheffield" materials estimated in this study cannot be compared to the MOPAC calculations, discussed in Chapter 3, since modifications to the structure of the molecules for the purpose of MOPAC calculations results in erroneous estimates of the dipole moment. In comparison to literature values however, similar compounds to SHEF A and SHEF B possess gas phase dipole moments around 7 - 10 D [188, 189]. The spherical gas phase dipole moments for the first three "Sheffield" materials are all slightly lower than this range. It is possible to perform MOPAC calculations on SHEF D and the dipole moment is estimated to be 4.3 D. This is in excellent agreement with the solution phase dipole moment for SHEF D presented in Table 4.5-1, though the estimated gas phase dipole moment is a little lower. It is possible that the cavity radius is slightly under-estimated, nonetheless the dipole moments generally agree well.

We have seen in §4.4 that larger dipole moments are possible if the crystal structure radius is used. Using the crystal structure radii (but maintaining the same shape factor), the spherical and ellipsoidal solution and gas phase dipole moments for

NPP, DED and the tertiary amino TCNQ adducts are re-calculated and presented in Table 4.5-2. With NPP, there is a better agreement with the MOPAC calculations and the spherical gas phase dipole moment and a very good agreement between the spherical solution phase dipole moment and that obtained in the crystal phase (8.1 D). Here, the ellipsoidal dipole moments are possibly over-estimated, but once again we can only compare dipole moments that have been estimated using similar local field formalisms. With the TCNQ materials the resulting dipole moments, both in the gas phase and solution phase estimated using the spherical and ellipsoidal equations, are extremely large. One must also be aware that the reaction field reduces as the cavity radius increases, thus there will be less change in dipole moment with changes in dielectric constant. This may have consequences with the evolution of the dipole moment and other molecular properties as will be seen in Chapter 7. It might be assumed that with these results, the cavity radius is over-estimated. However, it is only possible to say that the cavity radius will lie somewhere between the SAS radius and the crystal structure radius. Such a conclusion only emphasises the need to estimate the refractive index and polarisability through solution state measurements.

Material	NPP	DED	DEMI	DCH	ULTRA
μ_s^{sph} / D	8.0 ± 0.4	23.7 ± 4.8	30.6 ± 6.1	22.2 ± 4.4	15.9 ± 3.2
μ_g^{sph} / D	6.3 ± 0.3	17.3 ± 3.4	17.3 ± 3.4	13.8 ± 2.8	10.5 ± 2.1
μ_s^{ell} / D	9.2 ± 0.5	25.9 ± 5.2	38.1 ± 7.4	27.0 ± 5.4	20.1 ± 4.0
μ_g^{ell} / D	7.8 ± 0.4	19.3 ± 3.8	26.0 ± 5.2	20.1 ± 4.0	16.8 ± 3.4
$\bar{r}$ / Å	4.0	4.6	4.4	4.9	5.0

Table 4.5-2: Dipole moments of NPP, and TCNQ derivatives, estimated using crystal structure cavity radii.

When comparing the spherical and ellipsoidal local field formalisms, it is easy to see that the dipole moments obtained using the ellipsoidal equations are generally higher. This results from the increase in reaction field due to the anisotropy of the molecule. For materials with moderate or low polarisabilities as with NPP and SHEF D, there is only a small difference between the estimated spherical and ellipsoidal dipole moments. Indeed, given the uncertainty surrounding the cavity radius and polarisability it could be said that the spherical and ellipsoidal dipole moments lie within experimental error of each other. For such molecules, whose dipole moments are small, there is no real advantage in using the ellipsoidal equation. This is a conclusion that has been re-iterated many times **[165, 166, 174, 176, 195]**. However, with highly anisotropic molecules that have large dipole moments such as the TCNQ materials discussed here, the difference is now significant. In Chapter 7, a comparison of dipole moments estimated for DEMI in this chapter to that of 40-state SOS calculations will be made. It is hoped to ascertain from this, which local field formalism provides a better correlation with theoretical calculations.

§4.6 Conclusions.

The dielectric constants of solutions of highly anisotropic materials have been measured and plotted as a function of the solute concentration. The gradients obtained from these graphs have been used to calculate the dipole moments of these materials using equations that incorporate different local field factors. Also required for these calculations are estimates of the cavity radii and local fields, where the parameters chosen and method of calculation used has been described in detail for each molecule. The dipole moments for all of the molecules (with the exception of NPP and SHEF D) are high, reflecting the zwitterionic nature of the materials. Detailed analysis of the cavity radius highlights the many problems associated with its calculation. A comparison of the equations used to calculate the dipole moments and refractive indices reveals that the estimates of the polarisabilities and cavity radii appear to be fairly good, and there is an indication that the "real" value of the cavity radius lies somewhere between estimates obtained using SAS methods and crystal structure densities. In addition, estimates of the dipole moment appear to agree reasonably well

with similar estimates obtained elsewhere. Furthermore, the dipole moments obtained using the ellipsoidal local field factors produce higher dipole moments than that of the spherical local field equations. It is further postulated that for highly polar molecules, the use of an ellipsoidal cavity in the calculation of dipole moment becomes critical.

The results presented in this chapter will now be used in conjunction with the results obtained in Chapter 5 to extract a value of $\beta(0)$ for these materials.

References to Chapter 4.

[164] N. Hill, W. E. Vaughan, A. H. Price, M. Davies, *Dielectric Properties and Molecular Behaviour.*, Van Nostrand Reinhold Co. Ltd., London, (1969).

[165] B. K. P. Scaife, *Principles of Dielectrics.*, Oxford University Press., (1989).

[166] C. J. F. Böttcher, *Theory of Electric Polarisation.*, 2nd ed.; O. C. Van Belle, P. Bordewick, A. Rip., Volume 1; *Dielectrics in Static Fields.*, Elsevier, London, (1993).

[167] D. Gray, Ph.D. Thesis, University of Durham; *Molecular Organic Photonics.*, (1994).

[168] M. Farsari, Ph.D. Thesis, University of Durham, *Dielectric and Optical Properties of Organic Photorefractive Materials.*, (1996).

[169] A. J. Riddick, W. B. Bunger, T. K. Sakano, *Organic Solvents, Physical Properties and Methods of Purification.*, 4th ed., John Wiley and Son Inc., New York, (1986).

[170] L. Onsager, *J. Am. Chem. Soc.*, 58, 1486, (1936).

[171] P. Debye, *Phys. Z.*, 13, 97, (1912).

[172] P. Debye, *Collected Papers*, Interscience, New York, (1954); *Polar Molecules.*, Dover, New York, p173.

[173] E. A. Guggenheim, *Trans. Farad. Soc.*, 45, 714, (1949).

[174] A. B. Myers, R. R. Birge, *J. Chem. Phys.*, 74, 3514, (1981).

[175] Th. G. Scholte, *Recueil*, 70, 50, (1951).

[176] J. J. Makosz, *J. Mol. Liq.*, 59, 103, (1994).

[177] K. D. Singer, Ph.D. Thesis, University of Pennsylvania; *Experimental Studies of Second Order Non-Linear Optical Susceptibilities in Organic Systems.*, (1981).

[178] M. J. S. Dewer, *J. Am. Chem. Soc.*, 107, 3902, (1985).

[179] M. S. Paley, J. M. Harris, H. Looser, J. C. Baumert, G. C. Bjorklund, D. Jundt, R. J. Tweig, *J. Org. Chem.*, 54, 3774, (1989).

[180] Ch. Bosshard, G. Knöpfle, P. Prêtre, P. Günter, *J. Appl. Phys.*, 71, 1594, (1992).

[181] M. Szablewski, P. R. Thomas, A. Thornton, D. Bloor, G. H. Cross, J. M. Cole, J. A. K. Howard, M. Malagoli, F. Meyers, J.-L. Brédas, W Wenseleers, E. Goovaerts, *J. Am. Chem. Soc.*, 119 (13), 3144, (1997).

[182] P. R. Thomas, G. H. Cross, *Proc. SPIE.*, 3147, 30, (1997)

[183] *Nemesis*, Version 2.0, Oxford Molecular Ltd., (1990 - 1994).

[184] See for example E. Hecht, *Optics*, Addison-Wesley Publishing, Wokingham, England, (1987), p56, *n* for Diamond = 2.419, *n* for fused silica = 1.458.

[185] *Mathematica*, Version 2.2, Wolfram Research Inc., 1993.

[186] J. M. Cole, Ph. D. Thesis, **University of Durham.**; *Structural Studies of Organic and Organometallic Compounds Using X-Ray and Neutron Techniques.*, (1997).

[187] J. C. Cole, J. M. Cole, G. H. Cross, M. Farsari, J. A. K. Howard, M. Szablewski, *Acta Cryst. B*, B53, 812, (1997).

[188] D. W. Allen, X. Li, *J. Chem. Soc. Perkin Trans. 2*, 1099, (1997).

[189] J. Abe, Y. Shirai, *J. Am. Chem. Soc.*, 118, 4705, (1996).

[190] P. Thomas, G. H. Cross, W. Allen, Private Communications, (1996).

[191] A. Fkyerat, A. Guelzim, F. Baert, W. Paulus, G. Heger, J. Zyss, A. Périgaud, *Acta Cryst. B*, B51, 197, (1995).

[192] A. Fkyerat, A. Guelzim, F. Baert, J. Zyss, A Périgaud, *Phys. Rev. B*, 53 (24), 16236, (1996).

[193] H. A. Kurtz, J. J. P. Stewart, K. M. Dieter, *J. Comp. Chem.*, 11 (1), 82, (1990).

[194] M. J. S. Dewer, *J. Am. Chem. Soc.*, 107, 3902, (1985).

[195] J. R. Weaver, R. W. Parry, *Inorganic Chem.*, 5 (5), 703, (1966).

Chapter 5

First Hyperpolarisabilities from EFISH
Measurements.

§5.1 Introduction.

The theoretical basis needed for determining the first hyperpolarisability, β is described in Chapter 2. In this chapter, the equipment used with the experimental technique of electric field induced second harmonic generation (EFISH) is described, and the results of calibration measurements on the experimental system are provided which are used as a basis for measurements on unknown materials.

Results of EFISH experiments and the corresponding first hyperpolarisabilities of the four TCNQ derivatives and NPP are also presented in this chapter. These experiments have been conducted at 1.064 μm and 1.907 μm. Experiments are also conducted in two different solvent systems to determine the effect of the solvent on the value of β.

§5.2 Experimental Set-up.

EFISH, as explained in Chapter 2, utilises a static electric field to break the symmetry of a homogeneous, isotropic medium and induce a macroscopic, third order non-linearity, Γ_L of a solution. The method used to measure Γ_L when subjected to such an electric field, is the Maker fringe technique [196, 197, 198, 199, 200]. This technique utilises the difference in phase velocities of the bound and free second harmonic waves, so that when a wedge of material is translated normal to the incident

optical radiation, an interference pattern arises due to the differing optical path lengths of these waves. For the case of solutions, glass windows are placed between two electrodes such that a wedge shaped cavity is formed for the liquid to fill. Previous EFISH experiments [201] have incurred experimental difficulties such as accidental movement of the wedge and solution leakage from the cell. Thus, a considerable amount of effort was required to refine the design of the experimental cell so that such experimental difficulties are removed. The experimental technique and set-up are described here in detail.

The solution wedge is defined by two BK7, 20 × 8 × 2 mm glass windows (supplied by Multilab Ltd., Newcastle Upon Tyne.) which are polished along the long faces and placed between two electrodes, such that a cavity for the solution is formed. The angle of the wedge is chosen such that an acceptable amount of fringes are observed over a translation distance of 2 - 5 mm. This angle is typically about 2 - 5°, as shown in Figure 5.2-1. To ensure that the electric field is zero at one face of each window [200, 202], the windows occupy the majority of the cell, allowing the solution cavity to be approximately 2 mm wide. These are held in place between the electrodes by a PTFE spacer which also serves to separate the top and bottom of the cell. Two holes are left either side of the cell to allow the solution to flow in and out. The electrodes are approximately 10 × 15 mm and the positive electrode at the top of the cell is encased in PTFE for isolation purposes, as are the two clamping rods at either end of the cell. The bottom of the cell, which serves as the negative electrode, is made from stainless steel and has two positioning holes drilled in the underside. This ensures that the inner cell does not move when placed in the outer cell which is shown in Figure 5.2-2.

The outer cell or "pot" is also made from stainless steel and has approximate dimensions of 50 mm × 50 mm × 30 mm. Optical windows (24 mm diameter), made from BK7 glass (also supplied by Multilab Ltd.) are clamped to the front and back of the cell to allow incident radiation to pass through. These windows are large so that the translation distance along the inner cell is maximised, and are sealed so that the pot will not leak. A total translation distance of about 10 mm is allowed using this set-up.

The cavity of the outer cell is designed so that a minimal amount of solution is needed for each experiment. It was found that a minimum of 6 ml of liquid was required to sufficiently immerse the inner windows and cell, and the pot is capable of holding 21 ml of liquid when the inner cell is inside. In addition, the optical path length between the outer and inner glass windows is minimised. If the solution absorbs at the fundamental or second harmonic wavelengths then it is possible that the signal may not be detected over long path lengths. The distance between these windows is typically about 3 mm either side of the cell which is small enough to be able to conduct experiments when a small absorptive loss is involved. The positive electrode is connected to the positive high voltage (HV) supply via an isolated stainless steel rod. This also serves to help position the inner cell in the pot by being held in place by an electrically isolated clamped lid. The negative electrode of the inner cell is in contact with the entire body of the outer cell and this forms the negative electrode contact. The whole arrangement is then placed on an electrically isolated translation stage (Ealing Electro-Optics), which is capable of translating in 1 μm steps, and clamped into place.

The source of the experiment employs an Nd-YAG, Q - switched laser (Spectra-Physics Inc., DCR - 11) to provide ~80 mJ, 7 ns, 1.064 μm pulses at a repetition rate of 3 - 10 Hz. This can either be used as a fundamental wavelength source, producing second harmonic light at 532 nm, or to pump a Raman shifter as shown in Figure 5.2-3, producing a fundamental of 1.907 μm and second harmonic of 954 nm. The incident radiation is polarised vertically with respect to the electrodes ("s-polarised") with the aid of a BK7 glass cube polariser (Ealing Electro-Optics). A similar polariser is used to provide control of the beam intensity which typically reduces the incident energy to around 30 mJ when the polarisers are uncrossed and ~0.1 mJ when crossed.

Fluctuations in the energy of the fundamental beam are removed by normalising the signal with respect to a fundamental beam reference. A plate beam splitter is placed just after the polarisers to provide a reference arm which remains at a shallow
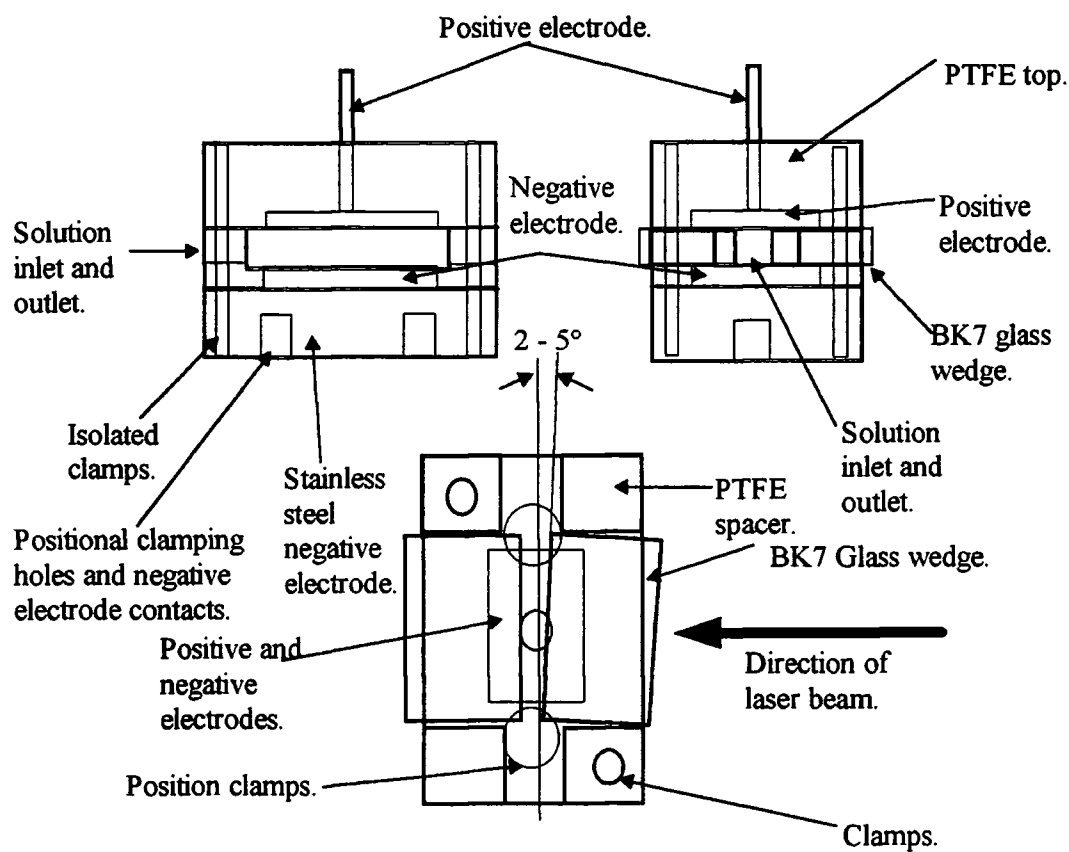
Figure 5.2-1: The inner EFISH cell.
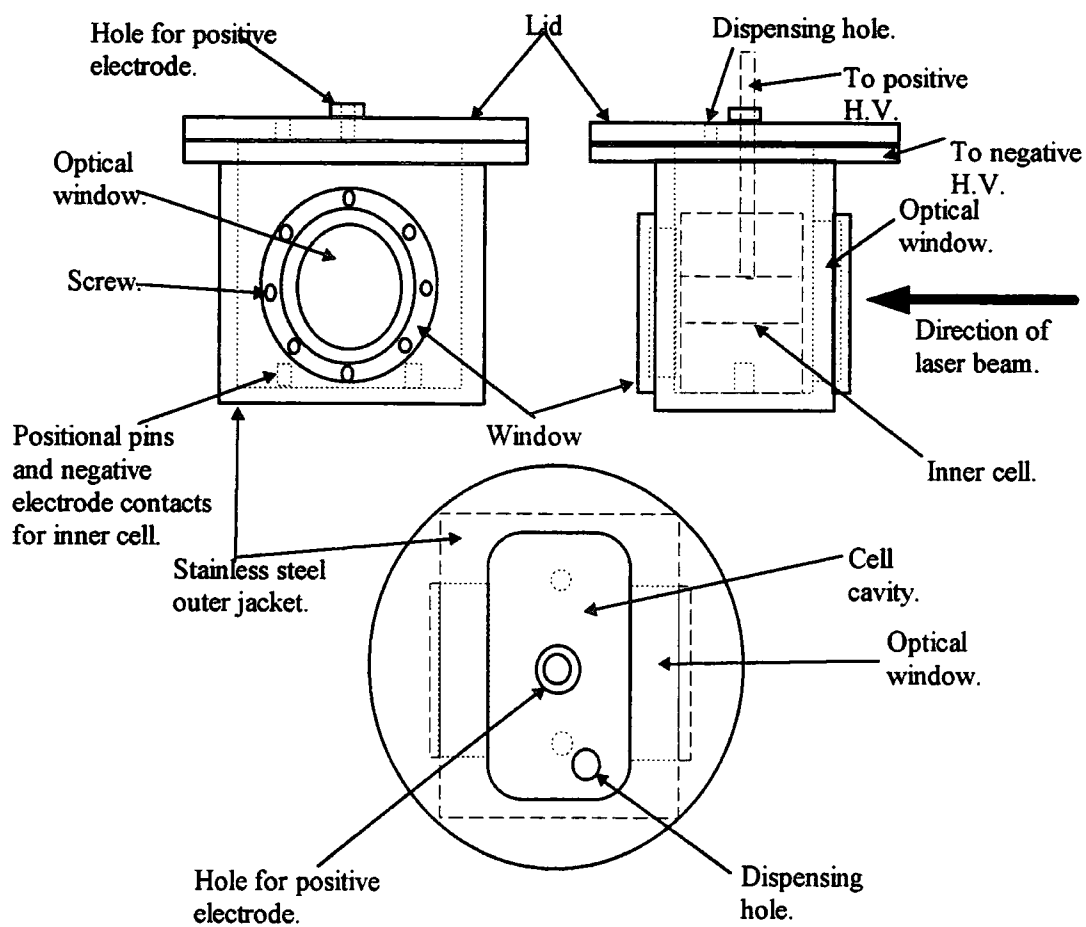
Figure 5.2-2: The outer EFISH cell or pot.

Nd:YAG Laser, λ = 1064 nm.

Raman Tube.

BS

M_1

M_2

M_1

M_2

D

A

P

P

DF

PD

V

ND

NPP Sample

1,907 nm Only

BPF_2

BS

NF

$\lambda/2$

L_1

L_4

ND

PMT_2

M_1

L_2/L_3

T

P

PMT$_1$

Cell

KG3

ND

BPF_1/BPF_2
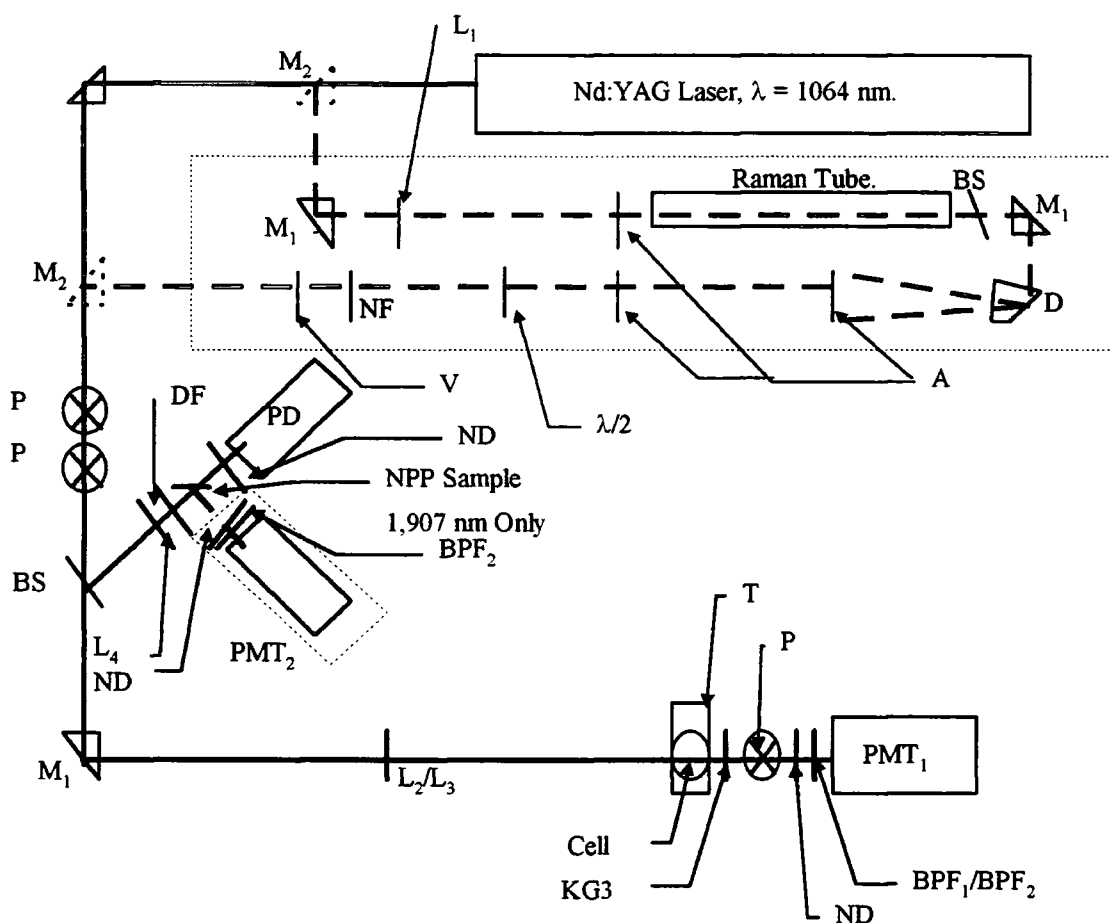
Key

A: Aperture	**BS:** Beam Splitter.
ND: Neutral Density Filters.	**DF:** Diffusion Screen.
D: Dispersing Prism.	**T:** Translation Stage
KG3: KG3 Blocking Filter.	**V:** Visible Blocking Filter
PD: Photodiode.	**P:** Polariser.
M$_1$: Prism mirror.	**M$_2$:** Prism Mirror, 1,907 nm
L$_1$: 150 cm lens.	Only.
L$_2$: 80 cm lens, 1064 nm Only.	**L$_3$:** 10 cm lens, 1,907 nm Only.
PMT$_1$: Photo Multiplier Tube.	**L$_4$:** 5 cm lens 1,907 cm Only.
PMT$_2$: Photo Multiplier Tube,	**BPF$_1$:** 532 nm Band Pass Filter.
1,907 nm Only.	**BPF$_2$:** 954 nm Band Pass Filter,
$\lambda/2$: Half Wave Plate, 1,907nm	1,907 nm Only.
Only.	

Figure 5.2-3: The laser set-up for 1.064 μm and 1.907 μm.

angle such that the reflectance of the two orthogonal polarisation's are the same [203]; around 5°.

A computer controls the majority of the experiment including the translation stage via a standard IEEE 488 interface and stage controller (Ealing Electro-Optics). Connected to the computer by the interface is a gated integrator and boxcar averager (Stanford Research Systems Ltd.) which provides two electronic detection gates each centred over the reference and signal. This eliminates unwanted noise which may occur in a different temporal position to that of the signal and sends the data, integrated over the gate width, to the computer. Further to this, shot-to-shot averaging is conducted and the data is stored on computer. An internally clocked digital delay generator is used to control the timing of the laser pulse, applied electric field and detection electronics. A schematic of the timing sequence is shown in Figure 5.2-4. The delay generator initiates a trigger at T_0 which starts the laser flash lamp current and allows lasing to occur. About 200 - 250 μs after T_0, the generator initiates
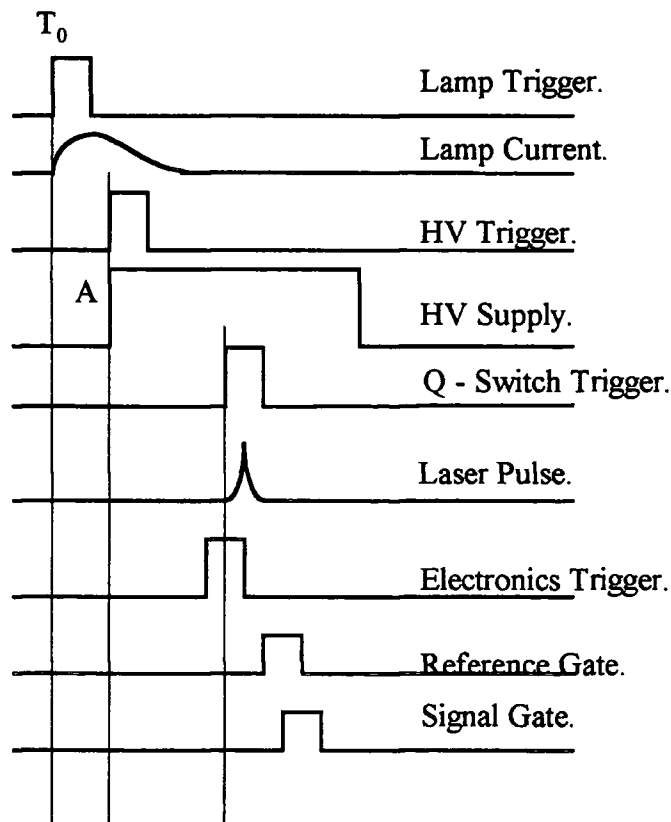
Figure 5.2-4: A schematic of the timing of the EFISH experiment.

102

the HV supply trigger (via output A) which also turns on the HV. The d.c. supply (Hartley Measurements Ltd.) provides a 6 μs pulse ranging between 0.4 and 10 kV. The trigger is timed such that the laser pulse is in the centre of the electric field pulse when the beam passes through the cell. This ensures an essentially static electric field for the duration of the laser pulse. The Q-switch is controlled by the internal delay generator of the laser which is in turn triggered at T_0. This also pre-triggers the boxcar electronics such that the signal and reference may be detected by adjusting the appropriate delays on the box car.

The optical set-up for each wavelength is slightly different, thus each shall be treated separately.

§5.2.1 Experiments Utilising 1.064 μm Radiation.

The incident radiation is focused at the centre of the cell ensuring that the solution cavity resides within the confocal region of the beam [202]. A 100 cm focal length lens is used for this purpose at 1.064 μm.

The second harmonic radiation is detected using an S1 response photomultiplier tube (PMT) (Thorn EMI) which is pre-filtered using a 532 nm bandpass filter and a KG3 near infra-red blocking filter. The PMT is powered using a HV power supply (Thorn EMI, Electron Tubes Division, PM28B) and operates in a linear regime when 1.1 - 1.3 kV is applied, though usually 1.1 kV is sufficient to detect the second harmonic. Another polariser is placed between the cell and the detector so that only "s-polarised" light is detected. Appropriate neutral density (ND) filters are used to reduce the intensity of the detected signal if necessary.

The reference beam is detected by a fast S1 response silicon photodiode (Instrument Technology Ltd. (UK), $\tau \approx 500$ ps) which is pre-filtered by appropriate value ND filters (ND = 0.0 - 1.0) and a diffusion screen such that the detector operates in a linear regime. This is also operated by a standard HV supply, operating at 3.0 kV (Thorn EMI, PM28A). The reference is detected, averaged by the boxcar and collected by the computer which also collects the corresponding second harmonic

signal. This is then normalised by dividing the second harmonic by the square of the reference.

§5.2.2 Experiments Utilising 1.907 μm Radiation.

For experiments using 1.907 μm radiation, as previously mentioned, the 1.064 μm laser beam can be used to pump a Raman shifter. The laser beam is focused using a 350 cm focal length lens into a 1.5 m long tube, filled with hydrogen gas (H_2) to a pressure of 15 lb./ in^2 (250 Bar). The majority of incident radiation is then removed with a dielectric mirror which only reflects 1.064 μm radiation and directs the reflected beam into a beam dump. Any residual radiation and the emitted Stokes and anti-Stokes Raman lines, are then directed through a dispersing prism and removed through a series of small apertures along the table, until the first Stokes line at 1.907 μm remains. This resulting fundamental beam provides approximately 5 mJ of radiation over 4 ns pulses. The polarisation of the beam is horizontal or "p-polarised" which is orthogonal to the required polarisation for the experiment. Thus, a quartz multiple order (Melles Griot) half waveplate is used to rotate the plane of polarisation by 90° to the "s-polarised" state. A 954 nm dielectric filter is used to remove any second harmonic which may be produced by the Raman tube or the quartz waveplate. In addition, a visible blocking filter (RG850) removes some visible light which is produced by the Raman tube. The beam is then directed back along the same experimental line as the 1.064 μm beam. A polariser oriented for "s-polarised" light is used to ensure any residual "p-polarised" light is removed.

The incident radiation is focused at the centre of the cell this time using a 20 cm focal length lens. The second harmonic is detected using an extended range S1-PMT, pre-filtered using only a 954 nm band pass filter. Since the incident and second harmonic intensity is less, it is usual for the PMT to be operated at 1.3 kV.

An appropriate detector for 1.907 μm is unavailable, therefore the reference beam is detected by placing a powder sample of NPP in the reference arm at 45° to the incident radiation. The light is focused onto the sample using a 10 cm focal length lens

and the second harmonic generated by the sample is collected by another extended range S1 response PMT, pre-filtered with a 954 nm band pass filter. Again appropriate ND filters are employed to obtain a usable signal (typically ND = 0.0 - 1.0). Since the light detected in the reference arm is now the second harmonic, the signal is thus normalised directly to the reference power and not the square of the reference as with 1.064 μm. A separate computer program is utilised to collect the normalised signal data at 1.907 μm.

To allow for a quantitative analysis of the resulting fringes produced at either wavelength, the entire experiment is referenced to quartz [197, 198, 199, 202]. A crystal of α-quartz is cut to an angle of 1° along the (011) plane [197], such that the d_{11} tensorial component is accessed when the incident light upon the crystal is polarised along this direction. Maker fringes are produced when the crystal is translated horizontally and irradiated with "p-polarised" light. The second harmonic, which is also "p-polarised" is detected in the usual manner for each experiment. Typically, the signal strength for quartz is 10^4 - 10^5 times larger than the EFISH signal, thus appropriate ND filters are employed to obtain a usable signal.

§5.3 Analysis of Signal.

The experimental set-up described in § 5.2 differs slightly to that described by Oudar [200] and others [201, 207, 211, 212], in that the EFISH cell resides in a solution filled pot. Consequently, the equations describing the propagation of the fundamental and second harmonic waves through the cell need to be revised. The second harmonic is analysed by following Oudar's method [200] allowing for the extra boundaries involved with the pot and any absorption due to the liquid. This involves the solution of the non-linear wave equation in each homogeneous medium and the calculation of the amplitudes of the fundamental and second harmonic waves with the aid of boundary conditions. The additional effect of each boundary shall be considered only in this section. The derivations of equations (5.3-6), (5.3-7), and (5.3-8) can subsequently be found in Appendix II.

Consider a fundamental beam with electric field, $E^\omega(z)$ propagating in the z-direction, normal to each interface as shown in Figure 5.3-1. The addition of the first two boundaries have the effect of reducing the initial electric field strength by the Fresnel transmission coefficients for normal incidence [203], such that

$$E^\omega(2) = t_G^\omega t_A^\omega E^\omega(0),$$

<div align="right">(5.3-1)</div>

where

$$t_A^\omega = \frac{2}{1+n_\omega^G}$$

<div align="right">(5.3-2)</div>

and

$$t_G^\omega = \frac{2n_\omega^G}{n_\omega^G + n_\omega^L},$$

<div align="right">(5.3-3)</div>

where n_ω^G and n_ω^L are the refractive indices at angular frequency ω for BK7 glass, G and the liquid, L. $E^\omega(2)$ represents the optical field strength just after the position 2 in Figure 5.3-1, $E^\omega(0)$ represents it immediately before the interface.

The situation where the solution absorbs the fundamental radiation must also be considered. The field strength is reduced by a factor induced by the absorption coefficient of the liquid medium at frequency ω, α_ω, and then again reduced by the
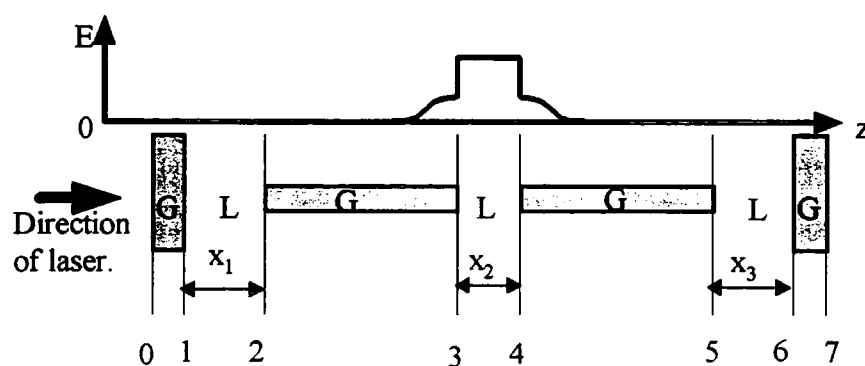
Figure 5.3-1: A schematic diagram showing the boundaries and static electric field variation in the EFISH cell.

transmission factor for the liquid-glass interface at position 3. The field strength thus becomes

$$E^{\omega}(3) = t_L^{\omega} t_G^{\omega} t_A^{\omega} e^{-\alpha_{\omega} x_1 / 2} E^{\omega}(0),$$

(5.3-4)

where

$$t_L^{\omega} = \frac{2 n_{\omega}^L}{n_{\omega}^G + n_{\omega}^L}$$

(5.3-5)

and x_1 is the distance travelled between the two interfaces at positions 2 and 3.

From this point the analysis is exactly that of Oudar's with the fundamental field amplitude represented by (5.3-4) [200]. Approximately half way through the first glass wedge the static electric field turns on and so does the quadratic non-linearity. This is assumed to be slowly spatially varying (as described in Appendix II) due to the fringing effects of the electrodes and thus only contributes to the second harmonic bound wave at interface 4, where the static electric field is now constant. Equation (5.3-6) describes the relationship between the bound wave, $E_b(z)$ produced and the fundamental field strength, $E^{\omega}(z)$:

$$E_b(z) = \frac{-4\pi}{n_{2\omega}^2 - n_{\omega}^2} d_{eff}(z) \left[E^{\omega}(z) \right]^2,$$

(5.3-6)

where $d_{eff}(z)$ is the effective quadratic non-linearity and n_{ω} and $n_{2\omega}$ are the refractive indices of a medium at frequencies ω and 2ω respectively.

By considering the boundary conditions for the second harmonic electric and magnetic field amplitudes, $E_{2\omega}$ and $H_{2\omega}$ (see Appendix II), the transmitted free wave amplitude may be calculated between two media with an interface at z_0:

$$E_f^{(2)} e^{i\theta_f} = t_{2\omega} E_f^{(1)} e^{i\theta_f} + \left[T_1 E_b^{(1)}(z_0) - T_2 E_b^{(2)}(z_0) \right] e^{i\theta_b},$$

(5.3-7)

where

$$\theta_f = \left(k_f + \frac{i\alpha_{2\omega}}{2}\right)z_0, \qquad \theta_b = \left(k_b + i\alpha_\omega\right)z_0,$$

$$t_{2\omega} = \frac{2n_{2\omega}^{(1)}}{n_{2\omega}^{(1)} + n_{2\omega}^{(2)}}, \qquad T_1 = \frac{n_\omega^{(1)} + n_{2\omega}^{(1)}}{n_{2\omega}^{(2)} + n_{2\omega}^{(1)}}, \qquad T_2 = \frac{n_\omega^{(2)} + n_{2\omega}^{(1)}}{n_{2\omega}^{(2)} + n_{2\omega}^{(1)}}.$$

$$(5.3\text{-}8)$$

The superscripts (1) and (2) represent the medium in which each parameter is measured. The first term in (5.3-7) represents the transmitted free wave and the second represents the mismatch between the two bound waves in their respective media. Thus, (5.3-7) may be successively applied in combination with (5.3-4) and (5.3-6) to obtain the final field strengths.

At position 5 in Figure 5.3-1 the transmitted free wave amplitude is

$$E_f^{2\omega} = t_G^{2\omega}\left[T_G E_b^{G'} - T_L E_b^{L'}\right]\left(e^{i\theta_f} + e^{i\theta_b}\right),$$

$$(5.3\text{-}9)$$

where

$$t_G^{2\omega} = \frac{2n_{2\omega}^G}{n_{2\omega}^G + n_{2\omega}^L}, \qquad T_L = \frac{n_\omega^L + n_{2\omega}^L}{n_{2\omega}^G + n_{2\omega}^L}, \qquad T_G = \frac{n_\omega^G + n_{2\omega}^L}{n_{2\omega}^G + n_{2\omega}^L},$$

$$E_b^{G'} = \frac{4\pi}{\left(n_{2\omega}^G\right)^2 - \left(n_\omega^G\right)^2}\Gamma_G E_0\left[E^\omega(3)\right]^2 = \left(t_L^\omega\right)^2\left(t_G^\omega\right)^2 e^{-\alpha_\omega x_1} E_b^G,$$

and

$$E_b^{L'} = \frac{4\pi}{\left(n_{2\omega}^L\right)^2 - \left(n_\omega^L\right)^2}\Gamma_L E_0\left[t_G^\omega E^\omega(3)\right]^2 = \left(t_L^\omega\right)^2\left(t_G^\omega\right)^2 e^{-\alpha_\omega x_1} E_b^L,$$

$$(5.3\text{-}10)$$

where E_b^G and E_b^L are the bound wave electric field amplitudes described by Oudar's method [204].

The free wave is then transmitted through two additional boundaries and another liquid medium which have the effect of reducing the second harmonic in much

the same way as with the fundamental. The final transmitted free wave amplitude is thus

$$E_f^{2\omega} = \left\{ \left(t_L^\omega\right)^2 \left(t_G^\omega\right)^2 t_L^{2\omega} t_G^{2\omega} e^{-(\alpha_\omega x_1 + \alpha_{2\omega} x_3/2)} \right\} \left\{ t_A^{2\omega} \left[T_G E_b^G - T_L E_b^L \right] \left(e^{i\theta_f} + e^{i\theta_b} \right) \right\},$$

(5.3-11)

where

$$t_A^{2\omega} = \frac{2n_{2\omega}^G}{1 + n_{2\omega}^G},$$

(5.3-12)

$t_G^{2\omega}$ and $t_L^{2\omega}$ are the transmission coefficients at frequency 2ω, described by (5.3-2) and (5.3-3) respectively (replacing ω with 2ω), $\alpha_{2\omega}$ is the second harmonic absorption coefficient, and x_3 is the propagation distance between positions 5 and 6 in Figure 5.3-1. In comparison to the expression obtained by Oudar [205], five extra terms are involved which are given by the prefactor of (5.3-11). A simplification can be made to this term since the product of the transmission factors $t_L t_G$ at either frequency is close to unity. Therefore, these terms can be removed with a negligible error (<0.05%) and, thus only the extra absorption term remains.

It follows that the expression for the intensity of the second harmonic, $I_{2\omega}$ which is obtained by squaring the field amplitudes is [198]

$$I_{2\omega} = \frac{8\pi}{c} \left(\frac{8\omega}{c}\right)^2 E_0^2 I_\omega^2 \left(T_1 \Gamma_G l_c^G - T_2 \Gamma_L l_c^L\right)^2 f(l),$$

(5.3-13)

where

$$f(l) = 2e^{-(\alpha_\omega + \alpha_{2\omega}/2)l} \left[\cosh\left(\left(\alpha_\omega - \frac{\alpha_{2\omega}}{2}\right)l\right) - \cos\left(\frac{\pi l}{l_c}\right) \right] e^{-(2\alpha_\omega x_1 + \alpha_{2\omega} x_3)},$$

(5.3-14)

$$T_1 = t_A^{2\omega}\left(t_A^{\omega}\right)^2 \frac{T_G}{n_{2\omega}^G + n_{\omega}^G},$$

<div align="right">(5.3-15)</div>

$$T_2 = t_A^{2\omega}\left(t_A^{\omega}\right)^2 \left(t_G^{\omega}\right)^2 \frac{T_L}{n_{2\omega}^L + n_{2\omega}^L},$$

<div align="right">(5.3-16)</div>

with $t_A^{2\omega}$, t_A^{ω}, t_G^{ω}, T_G and T_L given by (5.3-12), (5.3-2), (5.3-3), and (5.3-10) respectively. E_0 is the applied electric field, I^{ω} is the fundamental intensity, c is the speed of light, Γ is the third order non-linearity of the liquid and glass media, l_c is the coherence length, and l is the path length in the wedge.

Taking the average path length over the translation distance to be x_2, equation (5.3-13) may be used to obtain an expression for the average second harmonic intensity, $A_m{}^L$ when the wedge is translated over several Maker fringes [198]. A similar expression to (5.3-13) may be used for the average second harmonic intensity produced by a quartz wedge, $A_m{}^Q$ which may be used as a reference for the entire experiment. The final expression is thus:

$$\frac{A_m^L}{A_m^Q} = \frac{E_0^2\left(T_1\Gamma_G l_c^G - T_2\Gamma_L l_{c\,1}^L\right)^2\left(e^{-2\alpha_\omega x_2} + e^{-\alpha_{2\omega}x_2}\right)e^{-\left(2\alpha_\omega x_1 + \alpha_{2\omega}x_3\right)}}{\left(Q_1^2 + Q_2^2\right)d_{11}^2\left(l_c^Q\right)^2}$$

<div align="right">(5.3-17)</div>

where

$$Q_1 = \left(\frac{2n_{2\omega}^Q}{1+n_{2\omega}^Q}\right)\left(\frac{n_{\omega}^Q+1}{n_{2\omega}^Q+1}\right)\left(\frac{1}{n_{2\omega}^Q+n_{\omega}^Q}\right)\left[\frac{2}{1+n_{\omega}^Q}\right]^2,$$

<div align="right">(5.3-18)</div>

$$Q_2 = \left(\frac{n_{2\omega}^Q+n_{\omega}^Q}{1+n_{2\omega}^Q}\right)\left(\frac{1}{n_{2\omega}^Q+n_{\omega}^Q}\right)\left[\frac{2}{1+n_{\omega}^Q}\right]^2,$$

<div align="right">(5.3-19)</div>

and l_c^Q and d_{11} are the coherence length and effective quadratic non-linear optic coefficient (11 direction) of quartz, respectively. Thus upon rearranging (5.3-17), Γ_L may be obtained from the average intensity of a set of experimental fringes when compared to that of quartz, provided that Γ_G, l_c^G, l_c^L, l_c^Q, the appropriate refractive indices, and any absorption parameters are known.

A computer program has been developed using Mathematica [206] to calculate Γ_L. This can be found in Appendix I.

§5.4 Calibration Measurements.

As is indicated in §5.3, before measurements of unknown materials can be made, various optical and electrical constants must be measured or obtained from the literature. Table 5.4-1 shows the refractive index values for quartz, BK7 glass, and the solvents used in the following experiments [197, 198, 200, 207, 208, 209, 210]. These are used in conjunction with the following calibration measurements to calculate Γ_L for solutions of unknown materials.

§5.4.1 Quartz Referencing.

In §5.2 the experimental set-up to obtain a quartz reference signal is described. Typical sets of fringes produced by this wedge at 1.064 μm and 1.907 μm are shown in Figure 5.4-1. A translation distance of 3 - 5 mm is sufficient to produce enough fringes for accurate analysis. The experimental data is fitted using a non-linear regressional analysis program (see Appendix I) to the function [198]

$$y = A_1 \sin^2\left[f_m l_t + \phi\right] + A_2,$$

(5.4-1)

where A_1 is the fringe amplitude, A_2 is the amplitude offset, ϕ is the phase offset, and l_t is the translation distance. f_m is the spatial frequency of the Maker fringes and can be related to the coherence length by the relation

Wavelength	1.064 μm		1.907 μm	
Material	n_ω	$n_{2\omega}$	n_ω	$n_{2\omega}$
BK7 Glass[a]	1.507	1.519	1.496	1.508
Quartz[b]	1.53413	1.54702	1.5224	1.5358
Chloroform	1.435[g]	1.447[c]	1.427[g]	1.432[d]
Dichloromethane	1.409[g]	1.42[f]	1.408[g]	1.4123[e]

Table 5.4-1: Refractive indices for the materials used in EFISH.

a: Reference [208];

b: References [197, 200, 208];

c: Reference [200, 212];

d: Reference [207];

e: Reference [209];

f: Reference [210].

g: Calculated through measurements of the coherence length, error $\approx \pm 0.005$*.*
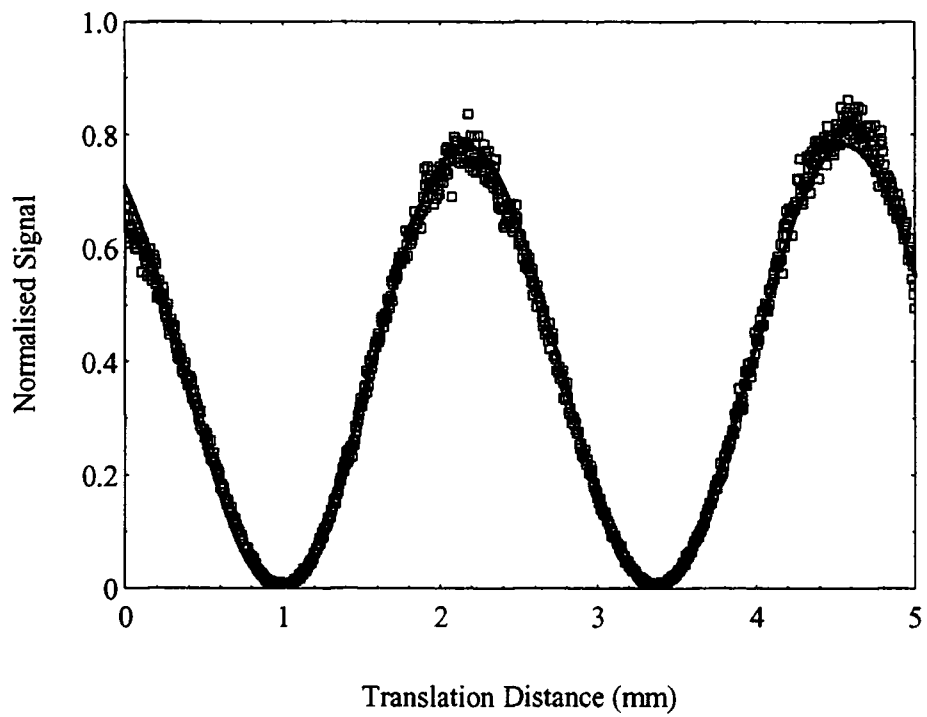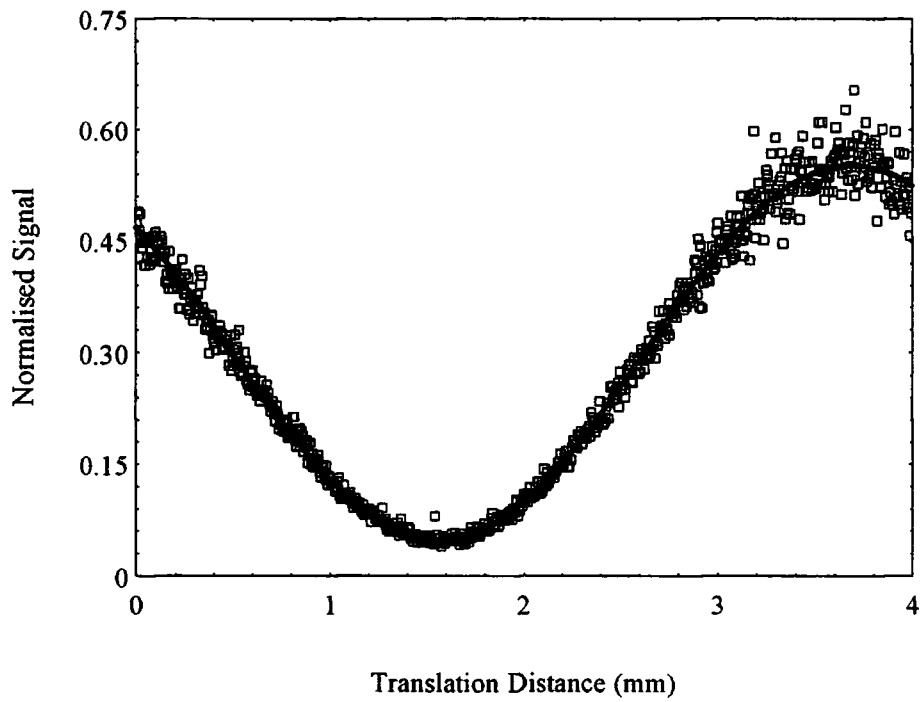
Figure 5.4-1: Graph showing the Maker fringes obtained for quartz using 1.907 μm (top) and 1.064 μm (bottom) radiation. The squares are data points and the solid lines are fits to the data using the function described by (5.4-1).

$$f_m = \frac{\pi \tan[\theta_w]}{2l_c}$$

(5.4-2)

where θ_w is the angle of the wedge. The average height of the fringes is calculated using the following expression:

$$A_m = \left(\frac{A_1}{2} + A_2\right) 10^{ND} R_s,$$

(5.4-3)

where ND is the value of the neutral density filters placed before the signal detector and R_s is the ratio of signal sensitivities on the boxcar averager between a solution experiment and a quartz experiment.

Average values of the coherence length obtained from several quartz experiments were found to be 20.9 ± 0.5 μm at 1.064 μm and 35.7 ± 0.5 μm at 1.907 μm, which agree well with literature values [197, 198, 200]. A^2_m varies from experiment to experiment as it is dependent on the specific experimental set-up. Thus, a quartz reference is conducted after each individual experimental run to allow for changes in set-up and any slow fluctuations in beam intensity.

The d_{11} value for quartz was obtained from the literature and found to be 1.2×10^{-9} esu for both 1.064 μm and 1.907 μm radiation [197].

§5.4.2 Electric Field Calibration.

To enable measurements of Γ_L and Γ_G to be made, the size of the static electric field applied across the wedge must be known. The d.c. high voltage supply allows the measurement of the voltage across the electrodes via an output circuit which reduces the signal by 10. A 1 MΩ voltage probe is connected to this output, and in turn, to an oscilloscope (Tektronix 2467B (400 MHz)). Thus, the actual electric field across the electrodes can be measured and related to the front dial readings through a calibration

graph, as shown in Figure 5.4-2. A linear relationship is exhibited between 1 and 10 kV on the front dial. The slight deviation from linearity for small voltages is due to the HV supply possessing a turn-on voltage of 400V. Voltages of 6 - 8 kV on the front dial may be applied while the cell is filled with solution without risk of electrical breakdown. This corresponds to 2.5 - 3.4 kV applied across the electrodes. The electrode separation was found to be approximately 2 mm, thus electric fields ranging between 1.25 - 1.7 MV m^{-1} are typical.

§5.4.3 BK7 Glass.

For the measurement of Γ_G, a single glass wedge, cut to an angle of 2° (supplied by Multilab inc.) is placed between the electrodes such that the electrodes completely overlap the edges of the wedge. A small voltage (about 5 kV on the dial) is applied so that a non-linearity is induced, being careful not to cause breakdown across the electrodes. The resulting Maker fringes, upon translation of the wedge are shown in Figure 5.4-3 for 1.064 μm radiation.

Γ_G may be calculated by modifying (5.3-17) for air - glass interfaces only, such that

$$\frac{A_m^G}{A_m^Q} = \frac{E_0^2 \left(G_1^2 + G_2^2 \right) \Gamma_G^2 \left(l_c^G \right)^2}{\left(Q_1^2 + Q_2^2 \right) d_{11}^2 \left(l_c^Q \right)^2}$$

(5.4-4)

where G_1 and G_2 are similar to that Q_1 and Q_2 given by (5.3-18) except that the refractive index for BK7 glass is to be used. From the average height of the Maker fringes obtained, Γ_G was found to be $3.8 \pm 0.4 \times 10^{-14}$ esu at 1.064 μm which agrees well with literature values [200, 211]. The average coherence length, measured by analysis of several sets of fringes was found to be 20.5 ± 0.5 μm. Again, this agrees well with literature values.
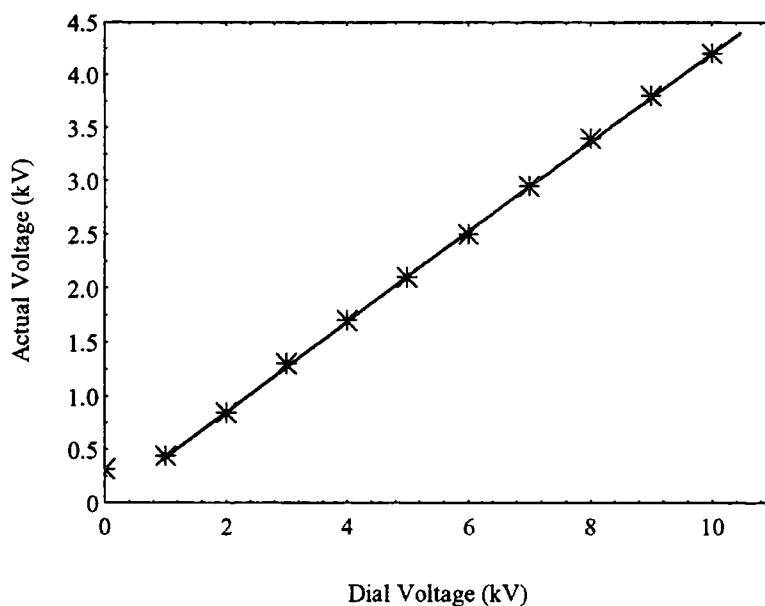
Figure 5.4-2: The electric field calibration graph. Stars are data points and the solid line is a straight line fit to the data above the 1 kV mark on the x axis.
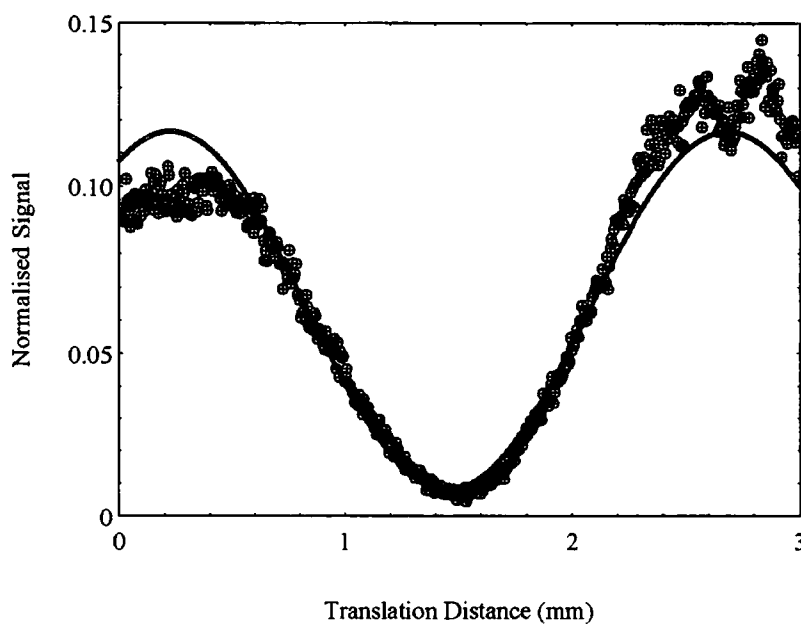
Figure 5.4-3: The Maker fringes obtained from BK7 glass using 1.064 μm radiation. Circles are data points and the solid line is a fit to the data.

116

Unfortunately at 1.907 μm the incident radiation was not sufficiently intense to observe any non-linearity from the glass wedge. Thus, we are reliant on values obtained from the literature which are found to be 3.45×10^{-14} esu [198].

§5.4.4 Solvent Measurements.

As previously indicated, experiments were conducted in two solvents; chloroform and dichloromethane (DCM). These were chosen principally for the reason that the TCNQ derivatives are fairly soluble in these solvents, and that they were the solvents used for dipole moment measurements allowing for easy comparisons of molecular properties.

Measurements were conducted on chloroform and DCM to obtain Γ_1 and l_c at both 1.064 μm and 1.907 μm. Figure 5.4-4 and Figure 5.4-5 show the typical Maker fringes that are obtained using both wavelengths. Analysis of the fringes yields the magnitude of the non-linearity, $|\Gamma_1|$ for the solvent and the sign is either obtained from the literature [200] or from additional experiments using a known standard. By analysing several sets of results, $|\Gamma_1|$ for chloroform was found to be $6.0 \pm 1.4 \times 10^{-14}$ esu at 1.604 μm and $7.5 \pm 1.6 \times 10^{-14}$ esu at 1.907 μm. For DCM, $|\Gamma_1|$ was found to be $6.2 \pm 1.2 \times 10^{-14}$ esu at 1.604 μm and $5.5 \pm 1.0 \times 10^{-14}$ esu at 1.907 μm.

In addition, the solution wedge angle is required to obtain the coherence length. The angle is measured by shining a helium neon (HeNe) laser beam through a pinhole onto the front face of the glass windows which are at a distance l_w from the pinhole, as shown in Figure 5.4-6. The reflected rays are separated by a distance, d_w defined by the wedge angle, θ_w such that

$$\theta_w = \frac{1}{2}\tan^{-1}\left(\frac{d_w}{l_w}\right).$$

(5.4-5)

117
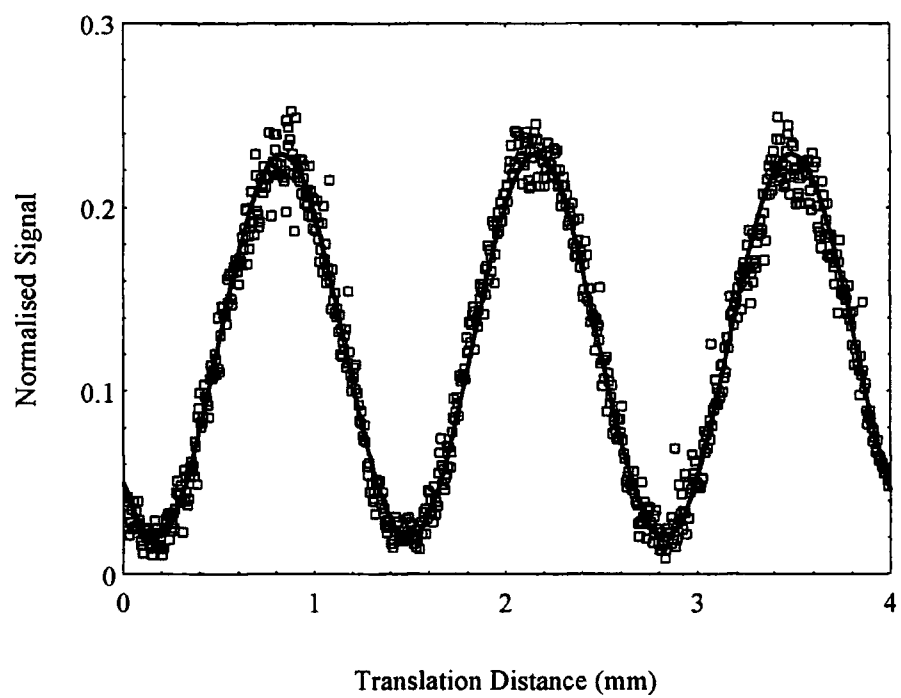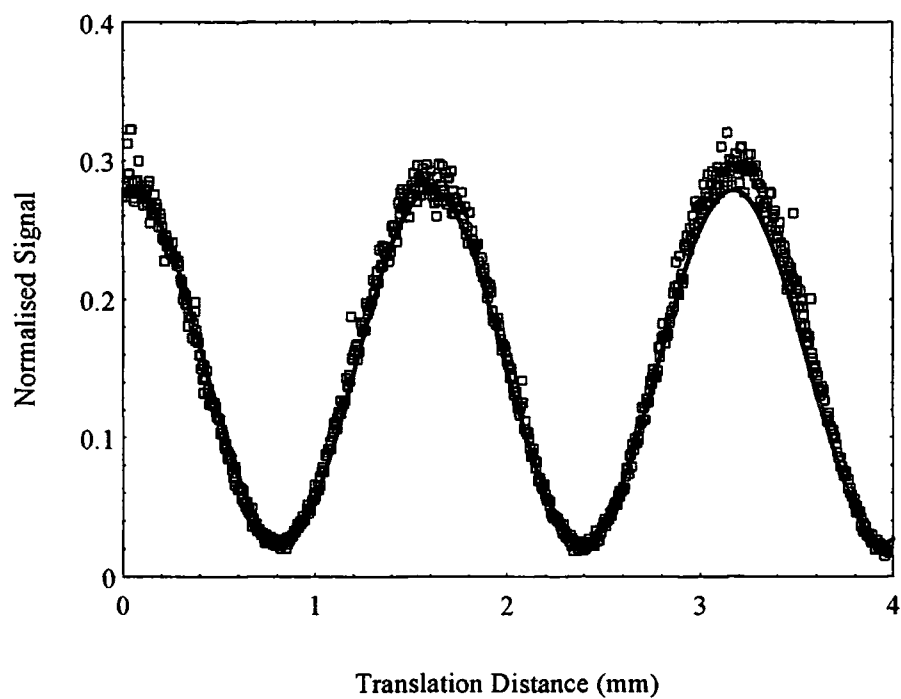
Figure 5.4-4: The Maker fringes obtained for chloroform at 1.064 μm (top, θ_w = 1.76°) and 1.907 μm (bottom, θ_w = 8.8°). The squares are data points and the solid lines are fits to the data.
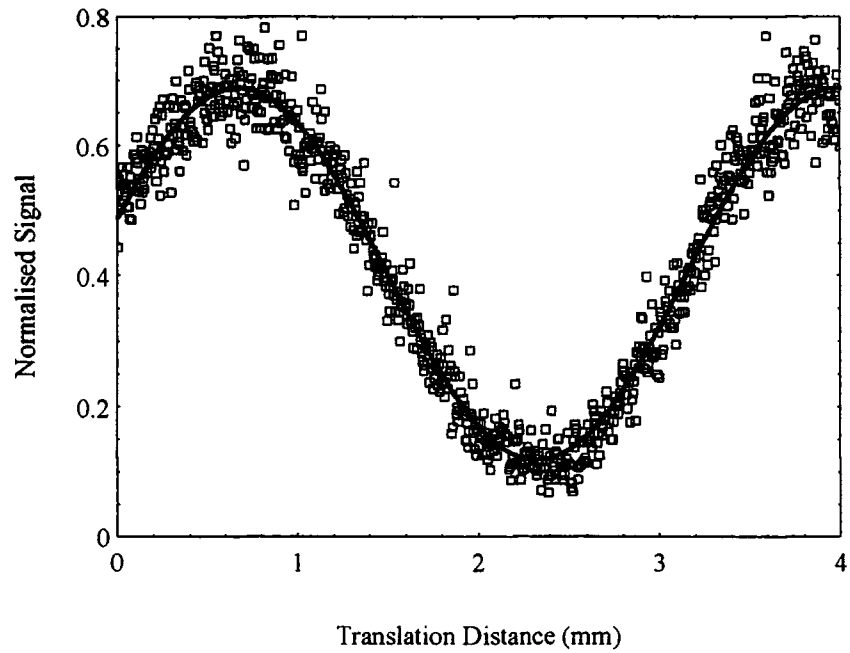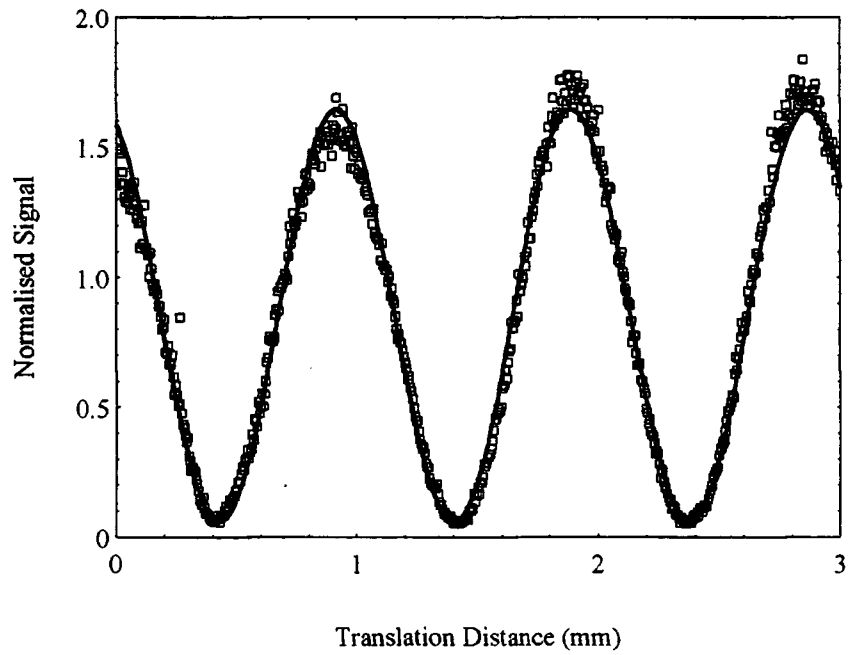
Figure 5.4-5: The Maker fringes obtained for DCM at 1.064 μm (top, θ_w = 2.72°) and 1.907 μm (bottom, θ_w = 4.55°). The squares are data points and the solid lines are fits to the data.
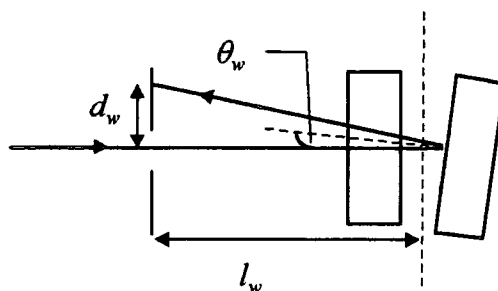
Figure 5.4-6: The set-up used to determine the solution wedge angle.

This method enables the measurement of the wedge angle to two decimal places for angles less than 3° and one decimal place for angles between 3° and 10°. The coherence lengths for the solvents were obtained by averaging over several sets of data. A fairly large variation in l_c is found between data sets due to errors in the measurement of θ_w, small movement of the solution wedge during experimentation, and errors incurred by the fitting program. However, the average coherence lengths for chloroform were found to be 22.8 ± 1.0 μm at 1.064 μm and 105 ± 5 μm at 1.907 μm which agree well with literature values [200, 207, 212]. For DCM, the average coherence lengths were found to be 24.0 ± 1.0 μm at 1.064 μm and 121 ± 12 μm at 1.907 μm.

Various values of Γ for chloroform are provided in the literature. Oudar's measurements [200], at 1.064 μm are slightly higher than the above results but are within experimental error. According to Oudar the sign of the non-linearity is positive which shall be taken to be correct. This also agrees with the measurements conducted by Kajzar *et al* [212]. At 1.907 μm the measurements conducted by Flipse *et al* [207] appear to be far lower than the above results, *circa* 1.5 × 10⁻¹⁴ esu [213]. There may be several reasons for this disagreement: Firstly, as with both experiments the absolute numbers rely on accurate referencing to quartz and either experiment may be erroneous. Thus, this may account for the slight increase observed at 1.907 μm, where a small decrease might be expected. Secondly, it is unlikely that the dispersion of chloroform will reduce the third order non-linearity by so much, unless either the fundamental and second harmonic frequencies for both experiments are close to

resonance. From the absorption spectrum of chloroform at 1.907 μm, this looks unlikely. Therefore for future calculations, the experimental results presented in this chapter will be used. In addition, it will be assumed that the sign of the non-linearity remains positive for both experiments.

For DCM, an extensive literature search revealed no previous experimental observations of either Γ_1 or l_c. Therefore, the sign of the non-linearity for DCM must be determined before measurements of unknown compounds in this solvent can be made. This is done by comparing the response of a known material in DCM (in this case NPP) to its response in chloroform.

§5.4.5 The Experimental Procedure to Determine the Gradient $\partial \Gamma / \partial w$ and Subsequent Determination of the Sign of Γ_1 for DCM.

The experimental procedure to obtain Γ_L versus weight fraction for NPP is as follows and was used with all EFISH experiments. The cell and pot were cleaned thoroughly and the glass windows inserted into the cell such that the appropriate solution wedge angle was made. The cell was then clamped tightly such that the windows did not move, placed in the pot, and the lid clamped into place. Precisely 6 ml of solvent was filtered and added to the pot such that the cell windows were covered completely by the solvent. Care was taken to ensure that any trapped air was removed from the solution wedge. The entire apparatus was then clamped onto the translation stage and an experimental run conducted with the appropriate static electric field applied. In the meantime, a solution of material of weight fraction 10^{-3} - 10^{-2} was made using a 10 ml volumetric flask. The solution was treated in an ultra-sonic bath for 15 minutes and if necessary heated. This was usually sufficient to dissolve the solute completely, after which the solution was subsequently filtered. When the experimental run for the solvent was completed, a small volume of solution, of size depending on the stock concentration, was added to the pot. The solution was then

allowed to mix, by gently shaking the pot, and the experimental run repeated. The weight fraction, w for each run was calculated using the equation

$$w = \frac{m_s}{m_s + V_T d},$$

where m_s is the mass of the solute, V_T is the total volume of solution in the cell and d is the density of the solution which is usually approximated to the density of the solvent for small weight fractions. The experiment was repeated for increasing concentrations such that approximately two orders of magnitude in w are traversed. Typically, the entire experiment was also repeated two to four times to obtain an average gradient and an indication of the errors involved with the procedure.

The graphs obtained for NPP in chloroform and DCM at both wavelengths are shown in Figure 5.5-1 and Figure 5.5-2. As is shown, Γ_L increases linearly with weight fraction in all four cases. The positive slope measured in DCM indicates that the macroscopic non-linearity of NPP in DCM is of the same sign to that of NPP in chloroform. Since the sign of Γ for chloroform is taken positive and the sign of β for NPP is known also to be positive, then DCM must also possess a positive Γ, and the sign of Γ for DCM has been determined.

The gradients obtained from these graphs are shown in Table 5.5-1. Two points to note about these results are that firstly, in either solvent the gradients are lower at 1.907 μm than at 1.064 μm. This is to be expected since at 1.907 μm both the fundamental and second harmonic frequencies are further away from resonance than at 1.064 μm. Secondly, the gradients measured in DCM are lower than the gradients observed in chloroform. This is surprising since the absorption band for NPP in DCM ($\lambda_{max.}$ = 396 nm) is closer to the second harmonic than that in chloroform ($\lambda_{max.}$ = 393 nm). Thus it would be logical for the measured gradient in DCM to higher than that in chloroform. Further analysis of these results will be undertaken in §5.5 and §5.6.

§5.4.6 The Experimental Procedure used to Measure the Absorption Coefficient.

Occasionally it is necessary to measure the absorption coefficient, $\alpha(\omega)$ of a material at ω or 2ω. A double beam, ultra-violet (UV) / visible spectrometer (Perkin-Elmer, Lambda19) is used for this purpose. A solution of material, typically of a concentration around 10^{-6} to 10^{-5} mol l^{-1} is placed in a 2 mm or 1 cm glass cell and the absorption spectrum is then recorded, referenced to the pure solvent. From this, the absorption coefficient, $\alpha(\omega)$ at the concentration of measurement, and the extinction coefficient, $\xi(\omega)$ may be found using the equation

$$\alpha(\omega) = \frac{I_\alpha(\omega)}{l_\alpha} = \xi(\omega)C,$$

(5.4-7)

where $I_\alpha(\omega)$ is the absorbance measured by the spectrometer, C is the solute concentration and l_α is the path length in the solution cell. Upon calculating the concentration for each EFISH run, $\alpha(\omega)$ is subsequently known, through multiplication of the extinction coefficient at the appropriate wavelength. This may then be used in the analysis of the experimental data using equation (5.3-17).

§5.5 Measurements of NLO Chromophores.

As explained in §5.4, EFISH measurements have been conducted on NPP which shall be compared to the results obtained for unknown materials. The graphs of Γ_L versus weight fraction, w in Figure 5.5-1 and Figure 5.5-2 produce positive slopes in both DCM and chloroform, suggesting a positive β which agrees with other measurements of NPP [201, 214, 215].
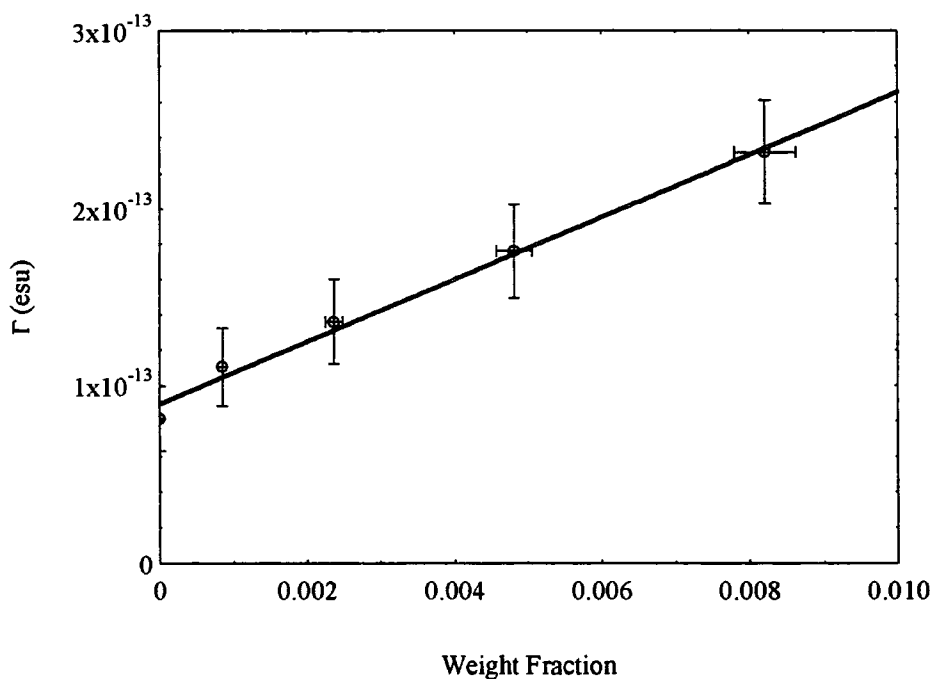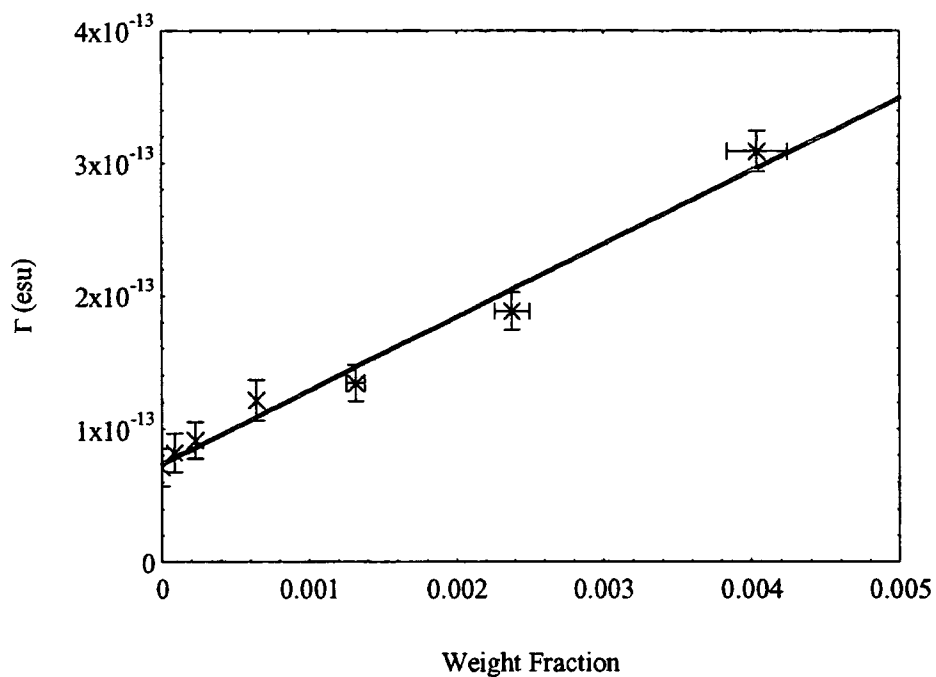
Figure 5.5-1: Typical graphs of Γ_L as a function of solute weight fraction for NPP in chloroform at 1.064 µm (top) and 1.907 µm (bottom). Circles are data points and the solid lines are straight line fits to the data.
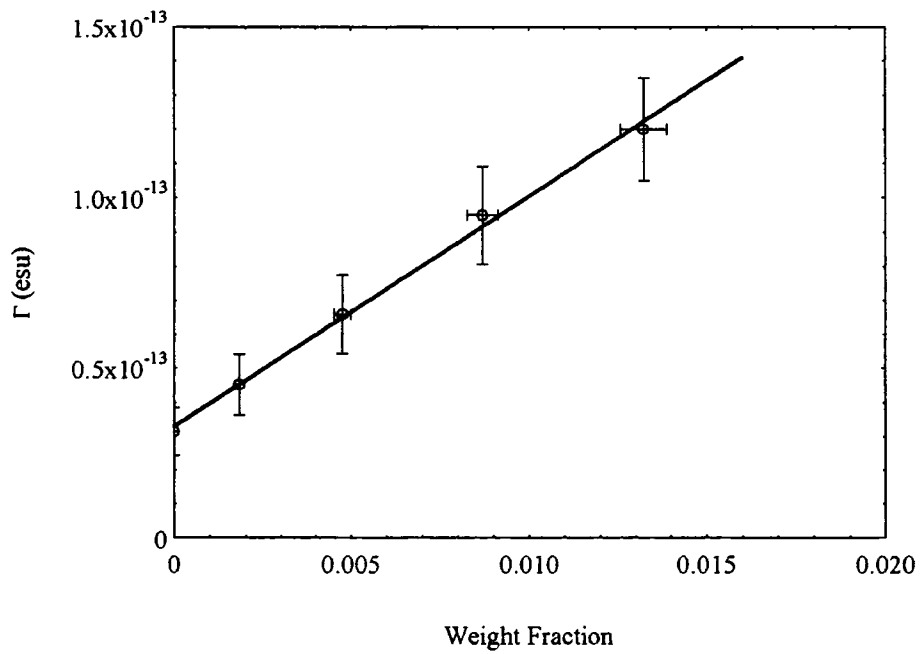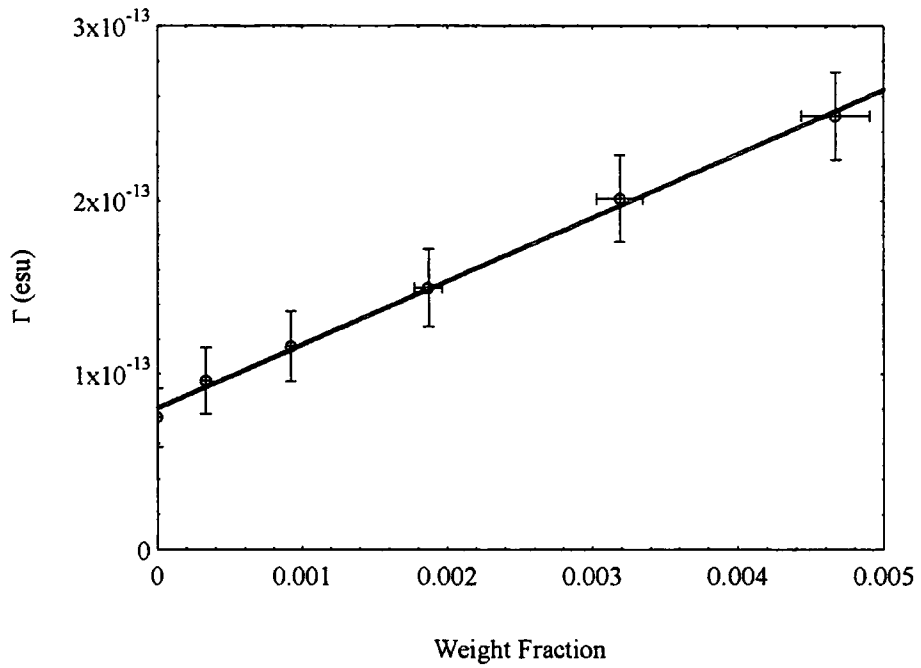
Figure 5.5-2: Typical graphs of Γ_L as a function of solute weight fraction for NPP in DCM at 1.064 μm (top) and 1.907 μm (bottom). Circles are data points and the solid lines are straight line fits to the data
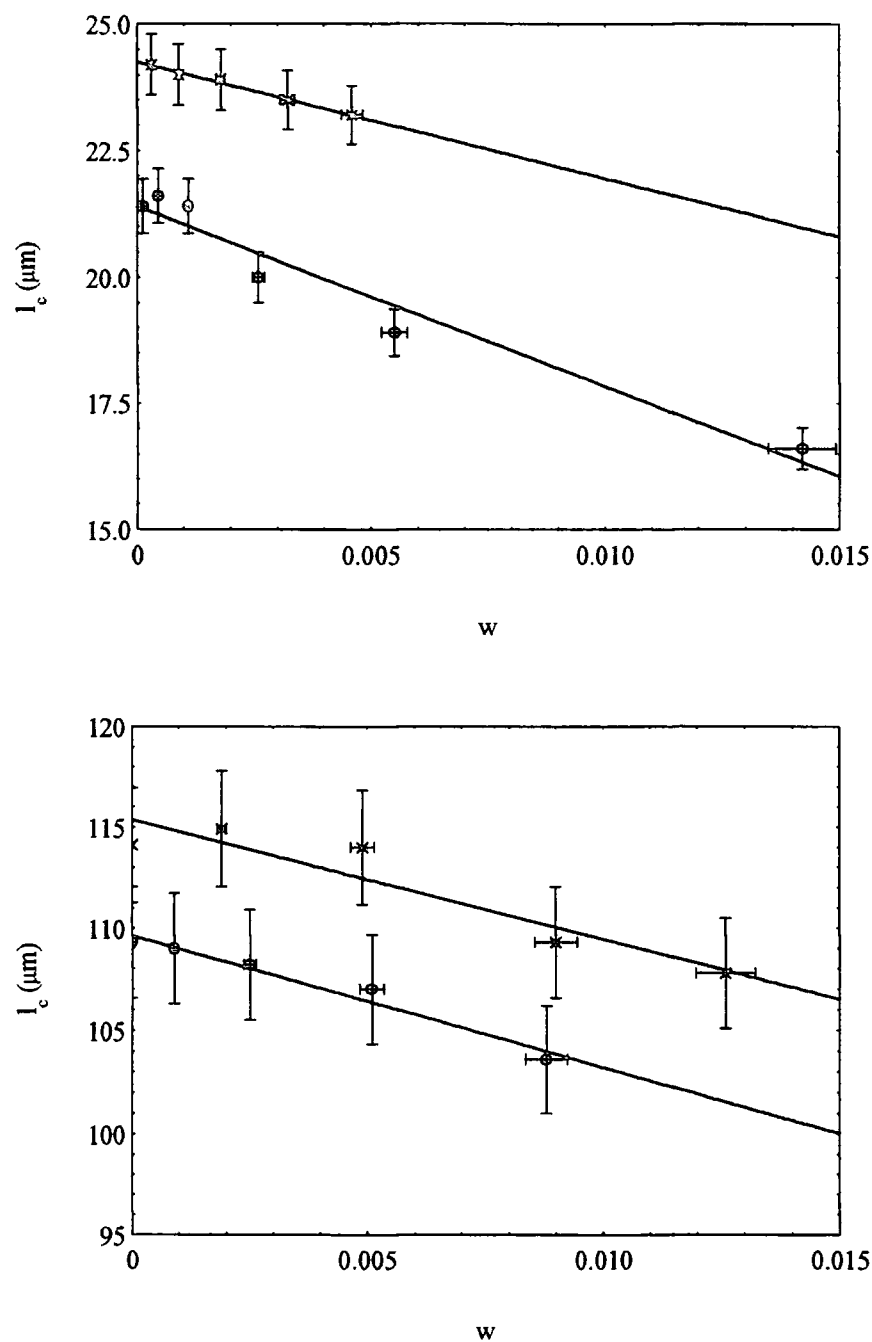
Figure 5.5-3: Typical variation of the coherence length, l_c with weight fraction of NPP. Top graph: at 1.064 μm, in DCM (crosses) and in chloroform (circles). Bottom graph: at 1.907 μm, in DCM (crosses) and in chloroform (circles). The solid lines are straight line fits to the data.

In addition to this data, the variation in coherence length with weight fraction can be used to study the variation of the difference in refractive index at ω and 2ω, Δn. The two can be related in the infinite dilution limit, via the relationship

$$\left.\frac{\partial \Delta n}{\partial w}\right|_0 = \frac{-\lambda}{4\left(l_c^0\right)^2}\left.\frac{\partial l_c}{\partial w}\right|_0,$$

(5.5-1)

where l_c^0 is the coherence length of the pure solvent and $\left.\partial l_c/\partial w\right|_0$ is the gradient of the l_c versus w graphs shown in Figure 5.5-3. The gradients of these graphs and the corresponding values of $\left.\partial \Delta n/\partial w\right|_0$ are shown in Table 5.5-1. As would be expected, the inclusion of a more dispersive element, i.e. the solute in the solution increases the difference between the refractive indices at ω and 2ω, resulting in a decrease of coherence length. In most cases, the change in coherence length over the concentration range is quite small. It should be noted that the gradients, $\left.\partial \Delta n/\partial w\right|_0$ for NPP are larger at both wavelengths in chloroform than in DCM. Also the respective gradients at 1.907 μm are smaller than at 1.064 μm, demonstrating the dispersion of the refractive indices of the solution.

The following sections provide comments on the results obtained for the unknown materials.

§5.5.1 DED.

The position of the longest wavelength electronic absorption band, λ_{max} for DED was found to be 474 nm in chloroform and 458 nm in DCM. In both cases this band extended to around 530 nm. Therefore, for 1.064 μm experiments there is negligible or no absorption at either ω or 2ω, but such experiments may benefit from the electronic resonance enhancement of β at 532 nm. Thus it was for this reason that experiments on DED were only conducted at 1.064 μm.

The graphs of Γ_L and l_c versus weight fraction are shown in Figure 5.5-4, and there are several points to note. Firstly, the non-linearity of the DED is opposite in sign to that of the solvents. This is demonstrated by a reduction in signal strength at weak solute concentrations followed by an increase in signal strength at strong concentrations, occurring when the macroscopic non-linearity of the solute is greater than the macroscopic non-linearity of the solvent, as is shown in DCM. Unfortunately, the low solubility of DED in chloroform inhibits the measurement of such an increase at larger weight fractions.

Secondly, at higher concentrations of DED in DCM, there is a deviation from linearity and a reduction in the gradient, $\partial \Gamma / \partial w$. There may be several reason for this, such as dimerisation of the solute at higher concentrations, drift in the power of the laser which is not accounted for by referencing, an increase of the conductivity of the solutions, or an increase in the absorption at 532 nm not accounted for. It is likely that the latter is the case. Closer inspection of the absorption spectrum of DED in DCM reveals that there may be a significant absorption at strong concentrations. The presence of an absorption at 532 nm will be a significant problem at the concentrations needed for EFISH which are typically about 100 times that needed for an absorption spectrum. Thus it may be that the gradient, $\partial \Gamma / \partial w$ is larger than indicated in Table 5.5-1. There are indications however that the gradient obtained in chloroform is larger than that in DCM.

Finally, Δn increases as expected, but the gradient, $\partial \Delta n / \partial w \big|_0$ is larger than that of NPP. This indicates that the wavelengths used in the experiment are closer to resonance as is clearly evident from the position of λ_{max}, thus there is a larger difference between $n_{2\omega}$ and n_{ω}. In addition to this, the respective gradient in chloroform is significantly higher than that in DCM which is in agreement with the general trend exhibited by the other materials. This is expected, since λ_{max}, is closer to the second harmonic in chloroform than in DCM. One should be aware however that it is difficult to facilitate a definite trend with the coherence length since the concentration of the solute is extremely weak and that Γ passes through zero, i.e.
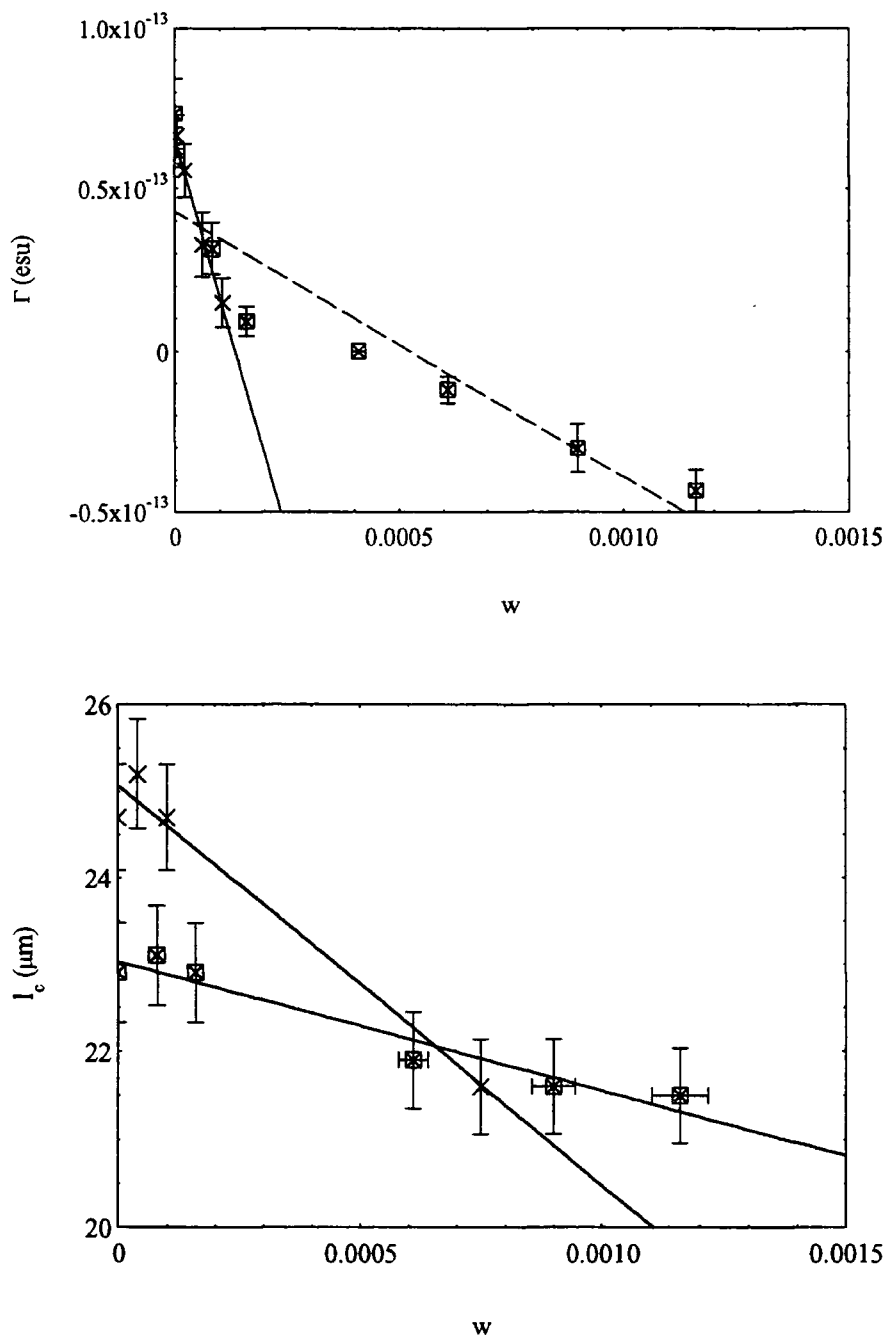
Figure 5.5-4: Typical variation of Γ_L (top) and l_c (bottom) with weight fraction of DED at 1.064 μm. Squares represent data taken in DCM and crosses represent data taken in chloroform. The solid lines are straight line fits to the data.

129

$l_c \rightarrow \infty$ for several points on the graph. In addition, there is a large error associated with the coherence lengths of the pure solvent due to temperature and compositional variations of the solvent, movement of the solution wedge angle, and errors induced by the fitting procedure. For this reason it is difficult to come to any definite conclusions about the coherence length.

§5.5.2 ULTRA.

The position of the absorption band for ULTRA was found to be 721 nm in chloroform and 719 nm in DCM. The band extends from approximately 500 nm to 850 nm. For ULTRA, as with the other tertiary amino TCNQ adducts, experiments were conducted at 1.064 μm in DCM only, and at 1.907 μm in chloroform and DCM. At 532 nm there is an appreciable absorption, though this is fairly small in comparison to the maximum intensity. However, this means that for the 1.064 μm experiments, the absorption coefficient, $\alpha(\omega)$ at 532 nm must be measured. This was done by transferring 1 ml of the stock solution which is added to the EFISH pot (see §5.4.5) to a 25 ml volumetric flask and diluting. A small proportion of the resulting solution was then transferred to a 2 mm path length spectroscopic cell, and the absorption spectrum, which is referenced to the solvent, measured. The 1.907 μm experiments were conducted in the usual manner as there is no absorption at either ω or 2ω.

The graphs of Γ_L and l_c versus w are shown in Figure 5.5-5. Like DED, the sign of the non-linearity is opposite to that of the solvent, suggesting a negative β. At 1.907 μm the gradient is steeper in chloroform than in DCM. At 1.064 μm, the gradient in DCM is again steeper than the corresponding 1.907 μm curve which might be expected due to resonance enhancement of β. However, care must be taken with the interpretation of the 1.064 μm experiment as 2ω is resonant and lies after the main electronic absorption band. This means that the sign of the zero frequency hyperpolarisability, $\beta(0)$ will be opposite to that of $\beta(\omega)$ for the 1.064 μm experiments. For the 1.907 μm experiments, the sign of $\beta(0)$ will remain negative as both ω and 2ω

are non-resonant. Thus, there is a disagreement between the two experiments which shall be discussed later.

The variation of Δn at 1.064 μm is large and opposite to that at 1.907 μm experiments, i.e. Δn decreases with increasing w, instead of increasing as is normally the case. Careful consideration of the position of the absorption band with respect to ω and 2ω suggest that this is likely, since the second harmonic frequency is at a point where anomalous dispersion of the refractive index occurs. Anomalous dispersion phase matching with respect to solute concentration is entirely expected [216] and observed through the measurement of l_c. It would thus be possible by increasing the concentration accordingly, to obtain a perfectly phase matched solution, providing the solubility and NLO response of the chromophore is large enough to observe such an effect.

§5.5.3 DCH.

The λ_{max} for DCH was found to be similar to that of ULTRA, 726 nm in chloroform and 725 nm in DCM. This time the absorption band extends from around 500 nm to only 800 nm (concentration $\approx 10^{-5}$ mol l^{-1}), however there is still an absorption at 532 nm. Thus, as with ULTRA, experiments are conducted in DCM at 1.064 μm and in both solvents at 1.907 μm.

The graphs of Γ_L and l_c versus w are shown in Figure 5.5-6. At 1.907 μm, the non-linear response in DCM is negative, however in chloroform the response is positive. However, the magnitude of the gradient is similar to that of ULTRA in either solvent. There may be several reasons for this which will be discussed later. The other behavioural properties of the DCH are similar to that of ULTRA. At 1.064 μm there is a sharp decrease in the signal at weak concentrations. Correspondingly, $\partial\Delta n/\partial w|_0$ decreases again exhibiting anomalous dispersion phase matching. At 1.907 μm, $\partial\Delta n/\partial w|_0$ increases as usual, however this time the gradient is larger in DCM than in chloroform which is opposite to the behaviour we have seen so far.
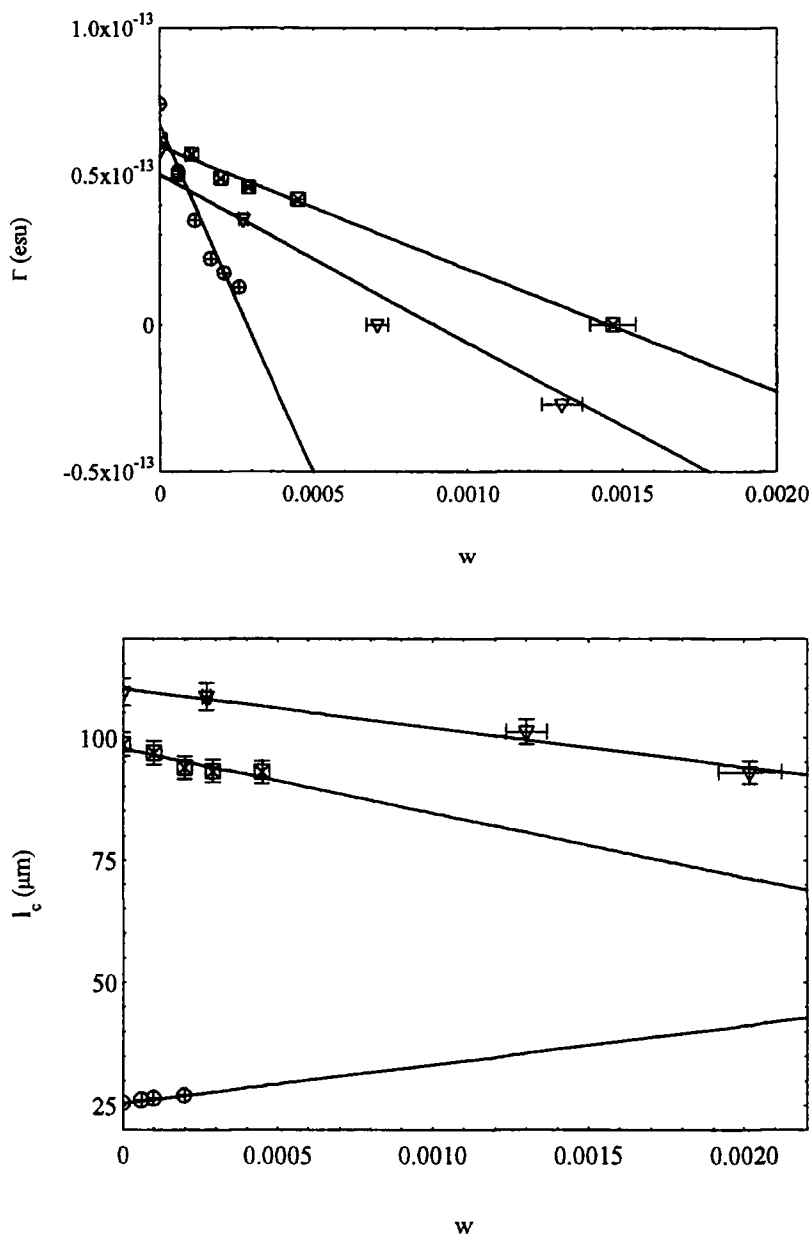
Figure 5.5-5: Typical variation of Γ_L (top) and l_c (bottom) with weight fraction of ULTRA at 1.064 μm and 1.907 μm. Circles represent data taken in DCM at 1.064 μm, squares represent data taken in chloroform at 1.907 μm and triangles represent the data taken in DCM at 1.907 μm. The solid lines are straight line fits to the data.
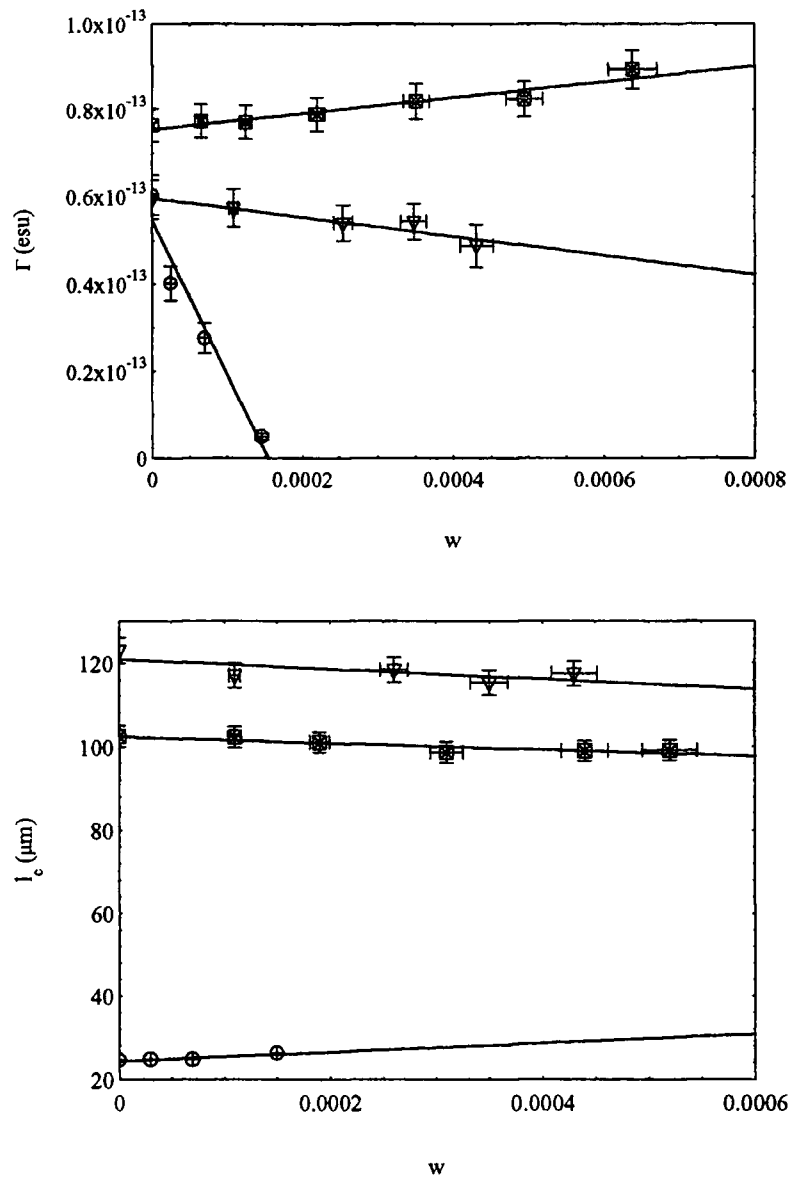
Figure 5.5-6: Typical variation of Γ_L (top) and l_c (bottom) with weight fraction of DCH at 1.064 μm and 1.907 μm. Circles represent data taken in DCM at 1.064 μm, squares represent data taken in chloroform at 1.907 μm and triangles represent the data taken in DCM at 1.907 μm. The solid lines are straight line fits to the data.
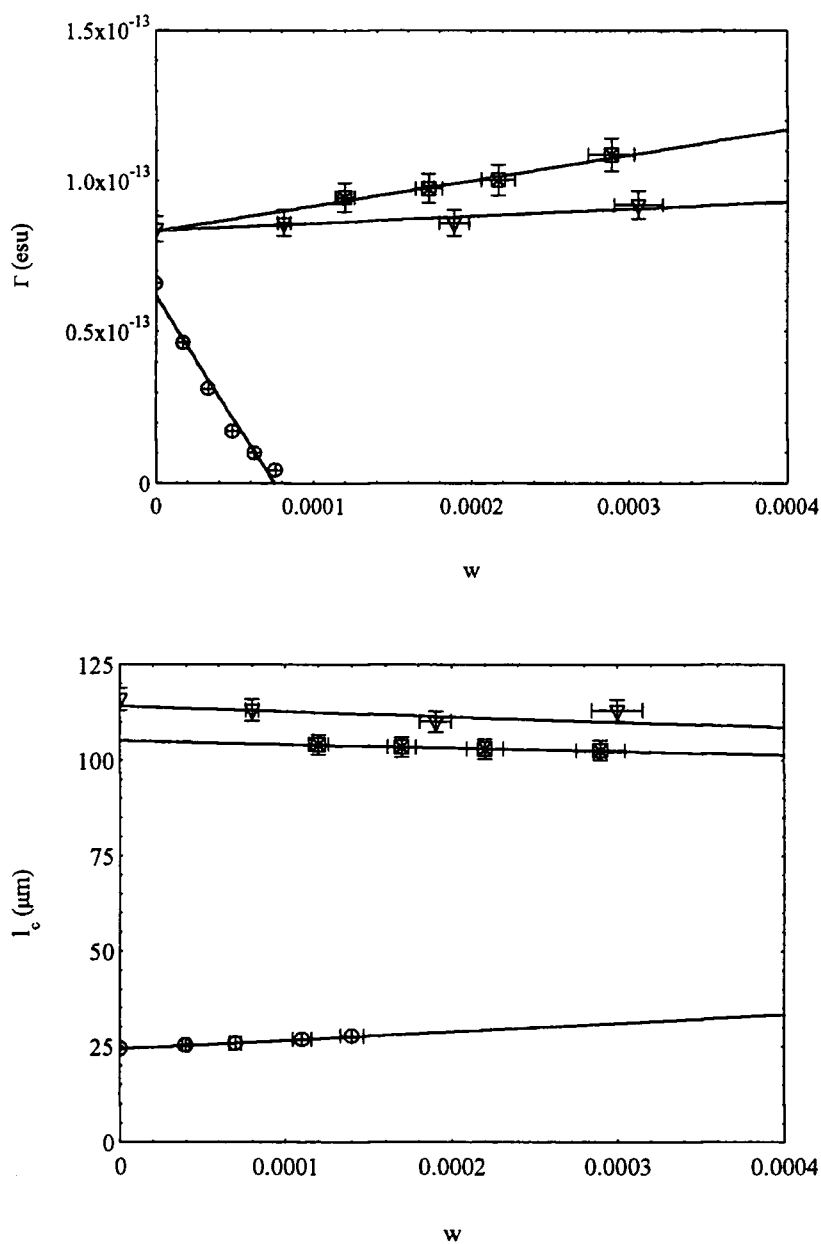
Figure 5.5-7: Typical variation of Γ_L (top) and l_c (bottom) with weight fraction of DEMI at 1.064 μm and 1.907 μm. Circles represent data taken in DCM at 1.064 μm, squares represent data taken in chloroform at 1.907 μm and triangles represent the data taken in DCM at 1.907 μm. The solid lines are straight line fits to the data.

Material	Solvent	Wavelength (μm)	$\partial\Gamma/\partial w$ ($\times 10^{-11}$ esu)	$\partial\ell_c/\partial w\big|_0$ (μm)	$\partial\Delta n/\partial w\big|_0$
NPP[d]	Chloroform	1.064	+4.5	-357	0.183
DED	Chloroform	1.064	-38[a]	-4591	2.12
NPP[d]	DCM	1.064	+3.5	-230	0.106
DED	DCM	1.064	-9.0	-1254	0.689
ULTRA	DCM	1.064	-19	+1300	-0.600
DCH[b]	DCM	1.064	-33	+12,000	-5.5
DEMI[c]	DCM	1.064	-75	+25,000	-11.5
NPP[d]	Chloroform	1.907	+1.7	-627	0.027
ULTRA	Chloroform	1.907	-9.0	-10,000	0.432
DCH[b]	Chloroform	1.907	+2.1	-8,000	0.346
DEMI[c]	Chloroform	1.907	+8.4	-9,300	0.402
NPP[d]	DCM	1.907	+0.67	-589	0.019
ULTRA	DCM	1.907	-2.1	-7,800	0.254
DCH	DCM	1.907	-5.7	-12,500	0.407
DEMI[c]	DCM	1.907	+2.7	-15,000	0.488

Table 5.5-1: The gradients obtained from EFISH experiments on NLO chromophores at 1.064 μm and 1.907 μm in DCM and chloroform. Errors are ± 10 % unless otherwise stated. a: ± 20 %, b: ± 15 %, c: ± 25 %, d: ± 5 %.

§5.5.4 DEMI.

The tertiary amino TCNQ adducts are all sparingly soluble in DCM and chloroform of which DEMI is the least soluble. Thus, the experimental uncertainty for DEMI is larger than that of the previous materials. $\lambda_{max.}$ for DEMI was found to be 717 nm in chloroform and 720 nm in DCM. Once again the absorption band extends from around 500 nm to 800 nm (concentration $\approx 10^{-5}$ mol l^{-1}), imposing the same conditions as with the previous two materials.

The graphs of Γ_L and l_c versus w are shown in Figure 5.5-7. This time, at 1.907 μm a positive non-linear response is shown for both solvents, the larger gradient being obtained in chloroform. However, this is contrary to the trends found with $\partial \Delta n / \partial w|_0$ where the gradient measured in DCM is marginally larger than that measured in chloroform. At 1.064 μm, once again a large negative non-linear response and a negative change in Δn with weight fraction is found.

§5.6 Calculations of $\mu\beta(\omega)$ and $\mu\beta(0)$.

The results obtained in §5.5 and presented in Table 5.5-1 can now be used to calculate the product $\mu\beta(\omega)$, as described in Chapter 2. We recall that in the infinite dilution limit for a two component solution, several equations may be used to obtain $\mu\beta(\omega)$, depending on the local field model used. In an attempt to compare results using spherical and ellipsoidal local fields, two equations, given previously by equations (2.4-8) and (2.4-9) in Chapter 2, shall be used

$$\gamma' = \frac{27M_2(n^2+2\varepsilon)}{N_a\varepsilon(n^2+2)^3(n_2^2+2)}\left[v_1\frac{\partial\Gamma}{\partial w}\bigg|_0 + \Gamma_1\frac{\partial v}{\partial w}\bigg|_0 + v_1\Gamma_1 - v_1\Gamma_1\left\{\left(\frac{1}{\varepsilon} - \frac{2}{2\varepsilon+n^2}\right)\frac{\partial\varepsilon}{\partial w}\bigg|_0 + \frac{3}{n^2+2}\frac{dn^2}{dw}\bigg|_0\right\}\right]$$

(5.6-1)

$$\gamma' = \frac{M_2\left(\varepsilon + \left(n_2^2 - \varepsilon\right)A_a\right)}{N_a\varepsilon\left(1 + \left(n^2 - 1\right)A_a\right)^3\left(1 + \left(n_2^2 - 1\right)A_a\right)}\left[v_1\frac{\partial T}{\partial w}\bigg|_0 + \Gamma_1\frac{\partial v}{\partial w}\bigg|_0 + v_1\Gamma_1 - \right.$$

$$\left. v_1\Gamma_1\left\{\left(\frac{1}{\varepsilon} - \frac{2}{2\varepsilon + n^2}\right)\frac{\partial \varepsilon}{\partial w}\bigg|_0 + \frac{3}{n^2 + 2}\frac{\partial n^2}{dw}\bigg|_0\right\}\right]$$

,

$$(5.6\text{-}2)$$

where γ' is given by equation (2.2-11) in Chapter 2.

Several parameters are needed in addition to $\partial T/\partial w$ for the calculation of $\mu\beta(0)$. The gradients $\partial\varepsilon/\partial w|_0$, $\partial v/\partial w|_0$ and $\partial n^2/\partial w$ can all be obtained experimentally, of which $\partial\varepsilon/\partial w|_0$ is obtained in Chapter 4. With $\partial v/\partial w|_0$ and $\partial n^2/\partial w$, the low solubility of the materials (with perhaps the exception of NPP) inhibits their direct measurement. Thus, these will be set to zero. Closer inspection of (5.6-1) and (5.6-2) reveals that the neglect of $\partial n^2/\partial w$ and $\partial v/\partial w|_0$ incurs no more than a 5 % error on $\mu\beta(\omega)$ [202]. In addition to this, since the refractive index of the solute is not known, n_2 is approximated to $n_{2\omega}$, resulting in a possible 10 % error.

We recall from Chapter 2, that the $\mu\beta$ product at zero frequency, $\mu\beta(0)$ may be calculated using the two level model [217, 218]

$$\mu\beta(0) = \mu\beta(\omega)\left(1 - \frac{\omega^2}{\omega_{eg}^2}\right)\left(1 - \frac{4\omega^2}{\omega_{eg}^2}\right),$$

$$(5.6\text{-}3)$$

where ω_{eg} is the frequency of the longest wavelength absorption band. Thus, to remove dispersion effects for each material, $\mu\beta(0)$ is presented in Table 5.6-1 for the different local field models described by equations (5.6-1) and (5.6-2).

Finally, using the dipole moments which were calculated from experimental measurements in Chapter 4, $\beta(0)$ values may be calculated and are presented in Table 5.6-2 for the two local field variants. Here, the results obtained using equation (5.6-1) have been divided by the appropriate spherical model dipole moments, and the

results obtained using equation (5.6-2) are divided by the corresponding ellipsoidal model dipole moments. As is indicated in Chapter 4, measurements of the dipole moment were conducted in DCM for ULTRA, DCH, and DEMI. Therefore, the dipole moments in chloroform must be calculated from the gas phase dipole moments (obtained from the experiments in DCM) using only the dielectric constant as an indication of the reaction field on the solute. With NPP and DED, dipole moment experiments were conducted in chloroform so, conversely the dipole moment in DCM must be calculated in the same manner.

Due to the enhanced reaction field associated with the ellipsoidal equation, the values of $\mu\beta(0)$ are higher than that of the spherical. The ellipsoidal $\beta(0)$ is also slightly higher than the spherical $\beta(0)$, despite dividing by a higher dipole moment, but in most cases only within experimental error. Thus, at first glance it appears there is little benefit from the use of ellipsoidal field factors in the calculation of β.

Comparing the data for NPP with that obtained earlier and discussed in Chapter 3, we see that the spherical values of $\beta(0)$ presented in Table 5.6-2 in all cases are lower than the EFISH values obtained in the literature (42×10^{-30} esu in acetone [215]). However, they are higher than that obtained in 1,4-dioxane (12×10^{-30} esu [201]). This perhaps demonstrates the effect of the solvent on the hyperpolarisability of a molecule. Since 1,4-dioxane is less polar than chloroform/DCM which in turn are less polar than acetone, it is possible that the hyperpolarisability increases with higher solvent dielectric constant. Discrepancies may also be due to wrong estimates of the dipole moment, wrong evaluation of the electric field applied to solutions, or erroneous referencing to quartz. These may also account for the differences in $\beta(0)$ for NPP which are measured in the same solvent but at different wavelengths. The same values of $\mu\beta(0)$ and $\beta(0)$ for a solute in a particular solvent should be obtained regardless of the wavelength used. However for NPP, the values of $\mu\beta$ obtained at 1.907 μm are smaller than the corresponding 1.064 μm experiments. Often, the two level model has

Material	Solvent	λ / μm	$\mu\beta(0)$ / $\times$ 10^{-48} esu	
			(5.6-1)	(5.6-2)
NPP[d]	Chloroform	1.064	209	375
DED[a]	Chloroform	1.064	-1017	-1861
NPP[d]	DCM	1.064	182	342
DED	DCM	1.064	-343	-642
ULTRA	DCM	1.064	1947	3625
DCH[b]	DCM	1.064	3544	6600
DEMI[c]	DCM	1.064	5684	10556
NPP[d]	Chloroform	1.907	167	300
ULTRA	Chloroform	1.907	-698	-1255
DCH[b]	Chloroform	1.907	158	278
DEMI[c]	Chloroform	1.907	467	827
NPP[d]	DCM	1.907	73	135
ULTRA	DCM	1.907	-175	-325
DCH	DCM	1.907	-485	-895
DEMI[c]	DCM	1.907	166	306

Table 5.6-1: Values of $\mu\beta(0)$ calculated from results presented in Table 5.5-1 using equations (5.6-1) and (5.6-2). Errors are ± 20 % unless otherwise stated. a: 30 %, b: 25 %, c: 40 %, d: ± 15 %.

Material	Solvent	λ / μm	μ_{sph} / D	μ_{ell} / D	$\beta(0)$ / × 10^{-30} esu	
					(5.6-1)	(5.6-2)
NPP[d]	Chloroform	1.064	6.9	8.3	30.3	45.2
DED[a]	Chloroform	1.064	18.2	20.3	-55.9	-93.0
NPP[d]	DCM	1.064	7.6	8.9	23.9	38.4
DED	DCM	1.064	21.9	24.8	-15.7	-25.9
ULTRA	DCM	1.064	13.5	19.0	144.2	190.8
DCH[b]	DCM	1.064	15.6	22.8	227.2	289.5
DEMI[c]	DCM	1.064	22.4	33.0	253.8	319.9
NPP[d]	Chloroform	1.907	6.9	8.3	24.2	36.1
ULTRA	Chloroform	1.907	11.6	18.2	-60.2	-69.0
DCH[b]	Chloroform	1.907	10.7	22.4	14.8	12.4
DEMI[c]	Chloroform	1.907	15.7	29.6	29.9	27.9
NPP[d]	DCM	1.907	7.6	8.9	9.6	15.1
ULTRA	DCM	1.907	113.5	19.0	-13.0	-17.1
DCH	DCM	1.907	15.6	22.8	-31.0	-39.3
DEMI[c]	DCM	1.907	22.4	33.0	7.7	9.3

Table 5.6-2: Values of β(0) obtained from EFISH experiments. Errors on β are ± 40 % unless otherwise stated. a: 50 %, b: 45 %, c: 55 %, d: ± 35 %. Errors on dipole moments are ± 20 %.

been demonstrated to be inadequate in modelling the dispersion of β for novel materials [198, 217, 218, 219], thus care must be taken with the interpretation of the zero frequency results. However, it is unlikely that this can account for such large discrepancies between the values of $\beta(0)$ measured in this study and the literature values. Since the signals obtained at 1.907 μm are weak and given the above possible errors, there is, thus a suggestion that the gradients may be underestimated slightly.

DED is found to possess a moderate $\beta(0)$ in chloroform, but this is considerably smaller in DCM. One must be cautious with the latter result, however as a deviation in linearity between Γ and w was observed which was attributed to an increase in absorption at 532 nm only at strong concentrations. Since the measured gradient was an average gradient, then it is possible that this is underestimated. For weak concentrations, the gradient (and therefore β) is similar to that in chloroform. In comparison to the MOPAC calculations of $\beta(0)$ presented in Chapter 3 ($\approx 10 \times 10^{-30}$ esu), we see that the magnitude of $\beta(0)$ in chloroform is larger than that predicted, and it is also of opposite sign. Assuming that the evolution of $\beta(0)$ for DED is similar to that predicted with the tertiary amino TCNQ adducts, the measurement of a negative β indicates that the molecule resides in an aromatic state and not the quinoidal state which is assumed with MOPAC calculations. The aromaticity of DED in the solution phase can be confirmed by considering the dipole moment. We recall that in the crystal phase DED exhibits a highly aromatic geometry where the dipole moment is only slightly larger than that obtained in chloroform, and thus the geometry must be similar. If a molecule was to posses a high dipole moment in the ground state, it is likely that the excited state geometry would be such that the dipole moment will be lower. Hence, a negative β would be observed as β is proportional to the difference between the ground and excited state dipole moments.

The values of $\mu\beta(0)$ and $\beta(0)$ obtained for the tertiary amino TCNQ adducts in DCM at 1.064 μm possess the opposite sign to some of those obtained at 1.907 μm, and the magnitudes are considerably larger. The reason for this is not clear, but there are two possible reason for the discrepancies. Firstly the two level model close to resonance is unlikely to be valid. The presence of several absorption peaks across the

absorption band means that it is necessary to include several more excited states to obtain a true resonant description of β. It is also likely, despite the correction for the absorption being included in the signal analysis, that the absorption at 532 nm is too large to observe any non-linearity in the system. If the non-linearity of these materials is small, as is indicated by the experiments at 1.907 μm, the absorption at the concentrations used will be dominant. Closer inspection of Figure 5.5-5 shows that the largest weight fraction is *circa* 5×10^{-4}. At this weight fraction the absorption coefficient at 532 nm is already around 2 cm^{-1}. Thus, the non-linearity due to the solute is swamped by the solvent contribution and a signal reduction is seen with increasing weight fraction. The low solubility of the materials in DCM however, prevents measurements at strong enough concentrations to confirm this hypothesis.

The magnitudes of *β(0)* for the tertiary amino TCNQ adducts at 1.907 μm are small (with the exception of ULTRA) or of a similar magnitude to that of NPP. This is contrary to that of the previous experiments discussed in Chapter 3 [201, 220]. There may be several reasons for this. The previous experiments have been conducted in different media. For NPP, we have already seen a marked dependence of the hyperpolarisability on the solvent in which it is dissolved. The tertiary amino TCNQ adducts are predicted to have an even larger solvent dependency through the SOS calculations. Thus a low value of $\beta(0)$ might indicate that the molecular geometries of the molecules are such that they reside close to the cyanine limit ($\beta = 0$). A comparison of the results in this chapter with such calculations will be made in Chapters 6 and 7.

There is a major disagreement, however with the results obtained here and those of the hyper-Rayleigh scattering experiments, conducted in chloroform at 1.064 μm and also discussed in Chapter 3 ($|\beta(0)| = 320 \times 10^{-30}$ esu). Once again there may be several reasons for this. Firstly, at strong or limiting concentrations dimerisation may occur. All of the TCNQ materials have a tendency to dimerise which is adequately demonstrated through the crystallographic structures [221, 221, 222]. A possible further indication that this occurs in DCM and chloroform is that the TCNQ

materials are all sparingly soluble in these solvents. Secondly, it might be possible that the conductivity of the solution increases upon the addition of the solute, resulting in a decrease of the static electric field and, thus a reduction in the alignment of the molecular dipoles. However, this would result in a non-linear relationship between Γ_L and w which is not seen with the tertiary amino TCNQ adducts. It is possible that the electric field has been erroneously estimated, but this would result in wrong estimates of Γ_1 which again has not been observed. This disagreement is obviously puzzling, therefore some attention will be paid to this in Chapters 6 and 7 where comparisons will be made to theoretical calculations and solvatochromism data.

Finally, one must note that the magnitudes of $\mu\beta$ products for the TCNQ materials are larger than NPP, up to five times larger for the case of DED in chloroform at 1.064 μm. However, the TCNQ materials have unusually large dipole moments, so the value of $\beta(0)$ is consequently small.

§5.7 Conclusions.

In this chapter the experimental technique and set-up associated with Electric Field Induced Second Harmonic generation (EFISH) has been described. The calibration measurements conducted on quartz, BK7 glass and chloroform have produced coherence lengths and Γ's close to those of literature values. As a result, further measurements of Γ and l_c for DCM are presented where the sign of the non-linearity was determined by conducting experiments on NPP in both chloroform and DCM. The results indicate that the sign of the non-linearity was the same as that of NPP and chloroform, and this was taken to be positive.

The results of experiments conducted at 1.064 μm and 1.907 μm on NPP and on four other materials in chloroform and DCM are also presented. It was found that generally the magnitude of β was smaller in DCM than in chloroform though results are at times difficult to interpret. The results for the tertiary amino TCNQ adducts are small which is possibly contrary to theoretical predictions, and contrary to those

obtained from hyper-Raleigh scattering measurements. In Chapter 6 solvatochromism experiments conducted on all of the materials to ascertain the position of the cyanine limit as a function of reaction field will be presented. This is followed by a discussion as to why the above results are small in DCM and chloroform, in Chapter 7.

Finally, the use of ellipsoidal local field factors has brought little or no change to the value of β. However, values of β are small, so it is difficult to distinguish between the two formalisms. There is a significant enhancement of the $\mu\beta$ product when using the ellipsoidal local field formalism however, since this includes an orientational component of the dipole moment. In addition, it is noted that $\mu\beta$ for the TCNQ derivatives is about three to five times that of NPP.

References to Chapter 5.

[196] P. D. Maker, R. W. Terhune, M. Nisenoff, C. M. Savage, *Phys. Rev. Lett.*, **8**, 21, (1961).

[197] J. Jerphagnon, S. K. Kurtz, *J. Appl. Phys.*, **41** *(4)*, 1667, (1970).

[198] C. C. Teng, A. F. Garito, *Phys. Rev. B.*, **28** *(12)*, 6766, (1983).

[199] B. F. Levine, C. G. Bethea, *J. Chem. Phys.*, **63** *(6)*, 2666, (1975).

[200] J. L. Oudar, *J. Chem. Phys.*, **67** *(2)*, 446, (1977).

[201] D. Gray, Ph.D. Thesis, **University of Durham**; *Molecular Organic Photonics.*, (1994).

[202] K. D. Singer, Ph.D. Thesis, **University of Pennsylvania**; *Experimental Studies of Second Order Non-Linear Optical Susceptibilities in Organic Systems.*, (1981).

[203] E. Hecht, *Optics*, **2nd ed.**, Addison - Wesley Publishing, Wokingham, England, (1987).

[204] J. L. Oudar, *J. Chem. Phys.*, **67** *(2)*, 446, (1977); Equation A9.

[205] J. L. Oudar, *J. Chem. Phys.*, **67** *(2)*, 446, (1977): *Appendix A, Equation A14.*

[206] *Mathematica*, Version **2.2**, Wolfram Research Inc., (1993).

[207] M. C. Flipse, R. de Jonge, R. H. Woudenberg, A. W. Marsman, C. A. van Walree, L. W. Jenneskens., *Chem. Phys. Lett.*, **245**, 297, (1995).

[208] Schott Glass, *Optical Glass Data Catalogue.*, (1987).

[209] J. E. Bertie, Z. Lan, R. N. Jones, Y. Apleblat, *Appl. Spectroscopy.*, **49 (6)**, 840, (1995).

[210] A. J. Riddick, W. B. Bunger, T. K. Sakano, *Organic Solvents., Physical Properties and Methods of Purification.*, **4th ed.**, John Wiley and Son Inc., New York, (1986).

[211] B. F. Levine, C. G. Bethea, *J. Chem. Phys.*, **63 (6)**, 2666, (1975).

[212] F. Kajzar, I. Ledoux, J. Zyss, *Phys. Rev. A*, **36 (5)**, 2210, (1987).

[213] M. C. Flipse, R. de Jonge, R. H. Woudenberg, A. W. Marsman, C. A. van Walree, L. W. Jenneskens., *Chem. Phys. Lett.*, **245**, 297, (1995): *Figure 2: EFISH Liquid Non-Linearities Versus Concentration in CHCl₃ for Various NLO Chromophores.*

[214] A. Fkyerat, A. Guelzim, F. Baert, J. Zyss, A Périgaud, *Phys. Rev. B*, **53 (24)**, 16236, (1996).

[215] M. Barzoukas, D. Josse, P. Fremaux, J. Zyss, J.-F. Nicoud, J. O. Morley, *J. Opt. Soc. Am. B*, **4 (6)**, 977, (1987).

[216] P. A. Cahill, K. D. Singer, *Chemistry of Anomalous Dispersion Phase-Matched Second Harmonic Generation*, Chapter 4, *ACS Symposium Series*, S. R. Marder, J. E. Sohn, G. D. Stucky, *Materials of NLO, Chemical Perspectives*, Washington DC, (1991).

[217] D. S. Chemla, J. Zyss, *Non-Linear Optical properties of Organic Molecules and Crystals.*, Volume 1, Academic Press Ltd., London, (1987).

[218] R. W. Boyd, *Non-Linear Optics.*, Academic Press Inc., London, (1992).

[219] Ch. Bosshard, G. Knöpfle, P. Prêtre, P. Günter, *J. Appl. Phys.*, **71 (4)**, 1594, (1992).

[220] M. Szablewski, P. R. Thomas, A. Thornton, D. Bloor, G. H. Cross, J. M. Cole, J. A. K. Howard, M. Malagoli, F. Meyers, J.-L. Brédas, W. Wenseleers, E. Goovaerts, *J. Am. Chem. Soc.*, **119 (13)**, 3144, (1997).

[221] J. C. Cole, J. A. K. Howard, G. H. Cross, M. Szablewski, *Acta Cryst. C.*, **C51**, 715, (1995).

[222] J. C. Cole, J. M. Cole, G. H. Cross, M. Farsari, J. A. K. Howard, M. Szablewski, *Acta Cryst B.*, **B53**, 812, (1997).

Chapter 6.

Solvatochromism of NLO Chromophores.

§6.1 Introduction.

It has been shown in Chapter 2 that the transition frequency of a molecule will change from a value in the gas phase to a new value in the solution phase. The degree of shift depends on the polarity of the solvent environment, i.e. the extent of the reaction field experienced by a molecule. However, the use of the reaction field for the purpose of a scale of solvent polarity, has its limitations in that it cannot describe adequately specific molecular interactions such as hydrogen bonding, and dipole-dipole interactions [223]. Therefore, it is often difficult to relate the transition frequency of a molecule to the reaction field it experiences in a particular solvent.

Molecules that exhibit large solvatochromic shifts have been used as probes in an attempt to develop a linear solvent polarity scale, thus eliminating the effect of these specific interactions on the position of the absorption band. Since their initial use [224, 225, 226, 227], one of the most widely used scales has been the $E_N^T(30)$ scale developed by Reichardt [226, 228, 229]. This scale is based on the absorption of the dye pyridinium-N-phenoxide (Figure 6.1-1) which shows one of the largest hypsochromic shifts (shift to higher frequencies) of the absorption band over a range of solvents of varying polarity. An improvement in estimating the polarity of a solvent was obtained using this scale, but it is based only on one indicator and thus anomalies with other materials were found to be common. Other polarity scales have since been developed, such as the π^*-scale [226, 227, 230, 231] and similar scales [232, 233] which are based on the solvatochromism of several dyes. However, such scales
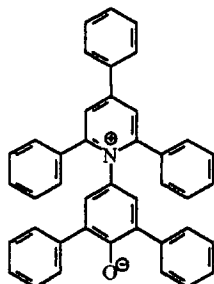
Figure 6.1-1: The pyridinium-N-phenoxide dye used as a reference for the $E_N^T(30)$ solvent polarity scale.

involve a more complicated analysis with only a limited benefit in accuracy. The simplicity of the Reichardt scale, coupled with the large amount of collected data, allows us thus to study the solvatochromism of the materials relatively easily, where the use of the reaction field as a polarity scale inhibits quantitative analysis. However, the α-scale (representing hydrogen bond donor acidities (HBD) [226, 230, 231]) and β-scale (representing hydrogen bond acceptor basicities (HBA) [226, 230, 231]) which are associated with Kamlet and Taft's π^*-scale [230, 231] can be used to account for a number of solute-solvent effects observed through the measurement of the transition frequency. Thus, these will also be referred to on occasion.

In this chapter, the absorption spectra of NPP, DED and the tertiary amino TCNQ adducts will be described. The positions of the longest wavelength absorption band for these materials have been measured in various solvents and are compared to Reichardt's polarity scale. In addition, the extinction coefficient of ULTRA has also been measured in a number of solvents and compared to this scale. Furthermore, a quantitative analysis of the solvatochromic shift is conducted in an attempt to estimate and compare values of the first hyperpolarisability in the gas phase.

In an attempt to eliminate the majority solute-solvent interactions which are observed through the measurement of the transition frequency of a chromophore dissolved in a number of solvents, solvatochromism experiments are also conducted in binary mixtures of toluene and acetonitrile. Any solute-solvent interactions which subsequently change the transition energy of the chromophore are therefore only due

to toluene or acetonitrile, thus allowing a more accurate determination of the transition energy with respect to solvent polarity. A quantitative analysis of the shift observed for the TCNQ materials obtained from these experiments is also conducted.

§6.2 Experimental.

The absorption spectra of NPP, DED and the three tertiary amino TCNQ adducts have been measured in seventeen different solvents using a double beam UV / visible spectrometer (Lambda19, Perkin-Elmer). Each spectrum was referenced to the solvent using two, 1 cm path length, quartz cuvettes, each filled with the solvent and placed in each beam of the spectrometer. When this was complete, the sample cuvette was filled with a solution of chromophore of concentration, typically 10^{-6} - 10^{-5} mol l^{-1}. The spectrum recorded usually ranged between 300 nm and 1000 nm. All solvents used were HPLC grade (Aldrich - Sigma Co.) but were not dried before use. As a result, an error in the estimate of the polarity of the solvent may be induced due to water absorption. The values for the $E_N^T(30)$ scale have been obtained from reference [226]. α, β and π*-scale values are obtained from references [226] and [231]. These may also be found in Appendix IV.

The Beer-Lambert law is utilised to measure the extinction coefficient of the materials [234]. A stock solution of the chromophore of concentration around 10^{-6} to 10^{-5} mol l^{-1} is made in a 50 ml volumetric flask and successively diluted (also using 50 ml volumetric flasks) such that at least one order of magnitude in concentration is traversed during the experiment. The maximum absorption intensity of the longest wavelength absorption band is measured for each concentration. The extinction coefficient at frequency ω, ξ(ω) may then be related to the absorbance, $I_\alpha(ω)$ via the equation

$$I_\alpha(\omega) = \xi(\omega)Cl$$

(6.2-1)

where C is the concentration of the solution and l is the absorption path length. Thus a graph of I_α over the path length versus concentration yields a straight line graph where the gradient is equal to $\xi(\lambda_{max.})$.

Binary mixture experiments were conducted on the three tertiary amino TCNQ adducts using toluene and acetonitrile mixtures which were found to be suitably miscible. A stock solution was initially made with a mass of material dissolved in a known volume of toluene and the absorption spectrum measured. An equal volume of toluene was also prepared for referencing purposes. Using a 50 ml burette, aliquots of acetonitrile were added to both the test and background samples, and the referenced absorption spectrum measured each time. The volume fraction, V^f of acetonitrile in each of the samples was found to be

$$V_{MeCN}^f (\%) = \frac{V_{MeCN}}{V_{tol.} + V_{MeCN}} \times 100$$

(6.2-2)

where V_{MeCN} and $V_{tol.}$ are the volume of acetonitrile and toluene respectively. The concentration of the solute is found by using the equation

$$C = \frac{m_s}{M(V_{tol} + V_{MeCN})}$$

(6.2-3)

where m_s is the mass of the solute and M is the molecular weight. The absorption spectra are then normalised to their respective concentrations. Experiments were conducted from 0 - 50% and 100 - 50% acetonitrile. The second experiment, therefore starts with an initial volume of acetonitrile and toluene is subsequently added to the samples. In addition to the absorption spectra, the dielectric constant, refractive index, and density of the pure solvent mixtures were also measured. The experimental set-up used to measure the dielectric constant is described in Chapter 4, and the refractive indices of the mixtures were measured using an Abbé refractometer at the sodium-D line. The density was obtained by measuring the mass of a known volume of

liquid placed in a volumetric flask to four decimal places, accounting for the mass of the flask. All parameters were measured at room temperature.

§6.3 Solvatochromic Behaviour Compared to the $E_N^T(30)$ Polarity Scale.

§6.3.1 NPP and DED.

The absorption spectra for NPP and DED consist of a single absorption peak centred approximately around 390 nm and 460 nm respectively. As mentioned in Chapter 3, the band for NPP is fairly narrow and extends from around 320 nm to 450 nm (concentration of measurement $\approx 10^{-5}$ mol l^{-1}). Similarly, the band for DED is approximately the same width and extends between 380 nm and 530 nm (concentration of measurement $\approx 10^{-5}$ mol l^{-1}). The position of these bands ($v_{max.}$) for NPP and DED in various solvents are presented in Figure 6.3-1 using the $E_N^T(30)$ scale as an indicator of the polarity of the solvent.

With NPP there is a reduction in the frequency of the transition with increasing solvent polarity, i.e. a bathochromic shift is exhibited. As is evident from equation (2.5-1), this indicates that $\Delta\mu$ and $\beta(0)$ are positive. The shift is quite small (no more than 25 nm over the entire range of solvents) and the fit to a straight line is not particularly good ($r^2 \approx 0.78$ for the straight line shown for NPP in Figure 6.3-1). Large deviations from the straight line are shown with 4 (diethylether), 12 (ethanol), and 13 (methanol). Even without the inclusion of these solvents in the data fit, deviations become larger as the polarity of the solvent increases. We can however, rationalise the largest errors, i.e. that of 12 and 13, by referring to the π^* and associated scales of polarity (Appendix IV). We see that the majority of solvents used in this set are HBA solvents where the value of β increases with the polarity of the
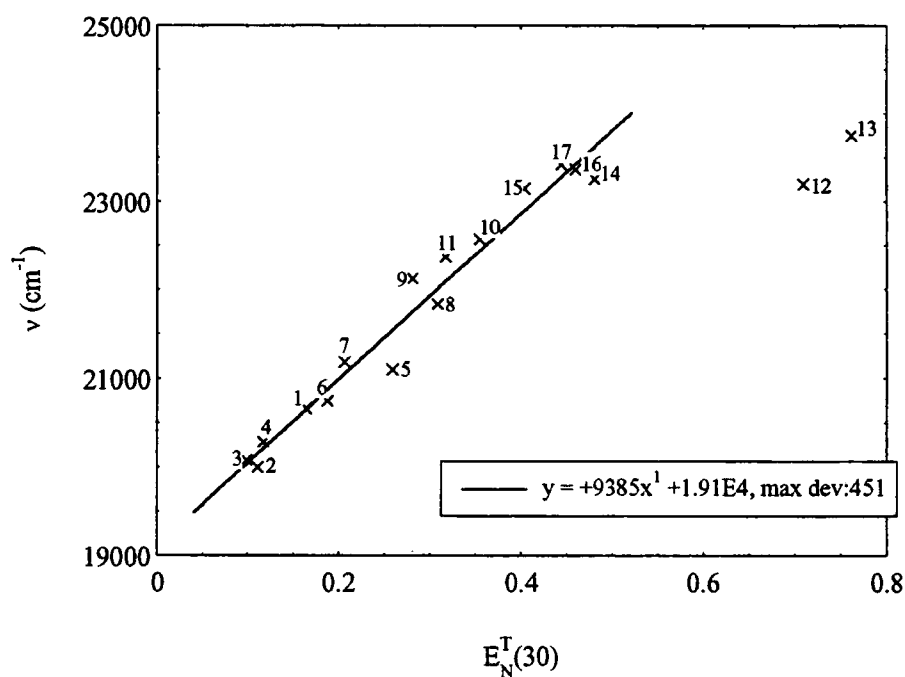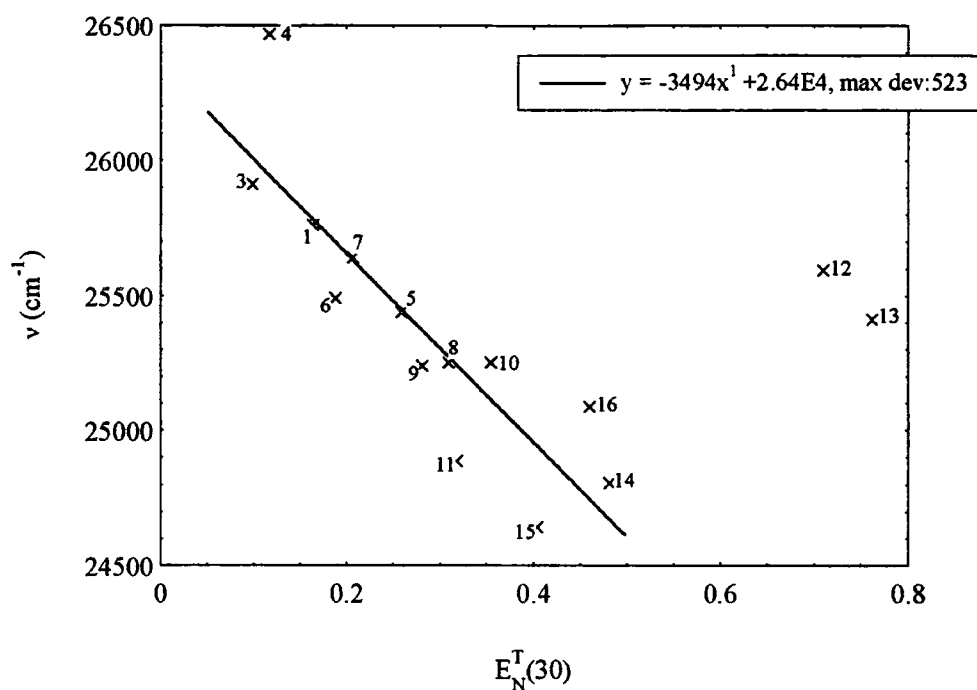
Figure 6.3-1: The position of the longest wavelength absorption band for NPP (top) and DED (bottom) in seventeen different solvents. The solid line is a straight line fit to the data, with the exception of 12 and 13. 1: 1,4-dioxane, 2: benzene, 3: toluene, 4: diethylether, 5: chloroform, 6: chlorobenzene, 7: tetrahydrofuran (THF), 8: dichloromethane (DCM), 9: cyclohexanone, 10: acetone, 11: tetramethylurea (TMU), 12: ethanol, 13: methanol, 14: nitromethane, 15: dimethylformamide (DMF), 16: acetonitrile, 17: dimethylsulfoxide (DMSO).

solvent. Ethanol and methanol have high HBD tendencies as well as high HBA tendencies, thus it is possible that ethanol may seem highly polar with one solute but only moderately polar with another solute. Since the $E_N^T(30)$ scale is based on the properties of just one dye, the value of $E_N^T(30)$ could be over or under-estimated for these solutions and this is clearly shown with the solvatochromism graph for NPP. Similar rationales may be applied to any of the other solvents in the data set.

With DED, an opposite solvatochromic shift, i.e. hypsochromic shift is observed. This indicates that $\beta(0)$ is negative for DED. The shift is larger over the range of solvents (around 70 nm), and this time, with the exception, again of 12 and 13, an extremely good linear relationship is observed with $E_N^T(30)$ ($r^2 \approx 0.96$ for the straight line shown for DED in Figure 6.3-1).

Further analysis of the solvatochromic data for DED and NPP will be conducted in §6.4. Nonetheless, it can be said that the solvatochromic data predicts a positive and negative $\beta(0)$ for NPP and DED, respectively, which is in agreement with the measurements obtained in Chapter 5.

Finally, one should also note for future reference, that the positions of DCM and chloroform on the $E_N^T(30)$ scale are close, indicating that the polarity of the respective solute in either solvent is similar, as expected. However, one would expect from this observation that $\beta(0)$ for NPP or DED would be larger in DCM than that in chloroform. This is contrary to the observed behaviour, and it is perhaps an indication that the EFISH result in DCM are under-estimated slightly.

§6.3.2 The Tertiary Amino TCNQ Adducts.

As indicated in Chapter 3 and subsequently shown in Figure 6.5-1, the absorption spectra for the tertiary amino TCNQ adducts are more complicated. They consist of multiple absorption bands between 500 and 800 nm which are dominated by two absorption peaks centred approximately around 700 nm (A) and 650 nm (B) (concentration $\approx 10^{-5}$ mol l^{-1}). The two bands merge in higher polarity solvents, and in

some cases, merge completely into one. Band A has been attributed to intra-molecular charge-transfer transitions [235] but the origin of band B is as yet unknown, despite various attempts to account for the additional band [236, 237]. The presence of this band complicates the issue of solvatochromism, since it may induce an apparent shift upon A due to the addition of the absorption intensities of the two bands. Furthermore, in polar solvents where the two bands merge, additional errors may also be incurred. Nevertheless, the position of band A is plotted for DEMI, DCH and ULTRA in Figure 6.3-2 and Figure 6.3-3 versus the $E_N^T(30)$ scale.

It is obvious from Figure 6.3-2 and Figure 6.3-3 that a linear relationship is not observed with the tertiary amino TCNQ adducts. The data is fitted to two straight lines, but in view of the errors involved with such a process, they are intended only as a guide to the eye. There are two regions of interest: In very low polar solvents a bathochromic shift is observed and which is around 10 nm or less. This is followed by a switch to a hypsochromic shift around the point where $E_N^T(30) \approx 0.25$. Once again with extremely polar solvents the ability of the $E_N^T(30)$ polarity scale to estimate the polarity of the solvent begins to break down, where we see that 12 and 13 deviate from the general trend with all of the molecules. As already indicated, other deviations may be due to errors in the measurement of the position of the absorption band or due to the specific effects of the solvent. Even so, the hypsochromic shift for all of the materials is either similar, or larger than the bathochromic shift.

The solvatochromic behaviour of the tertiary amino TCNQ adducts is not unlike that of merocyanine dyes [238, 239, 240, 241, 242, 243, 244] where a reversal in the transition energy shift is observed in very low polarity solvents. A literature search has revealed that there are only a few other materials in addition to merocyanine dyes that exhibit this behaviour [245, 246, 247, 248]. It is interesting to note however, that the position of the reversal point for the tertiary amino TCNQ adducts is observed in higher polarity solvents ($E_N^T(30) \approx 2.0 - 2.5$) that that associated with merocyanine dyes ($E_N^T(30) \approx 0.5 - 1.0$ [238]).
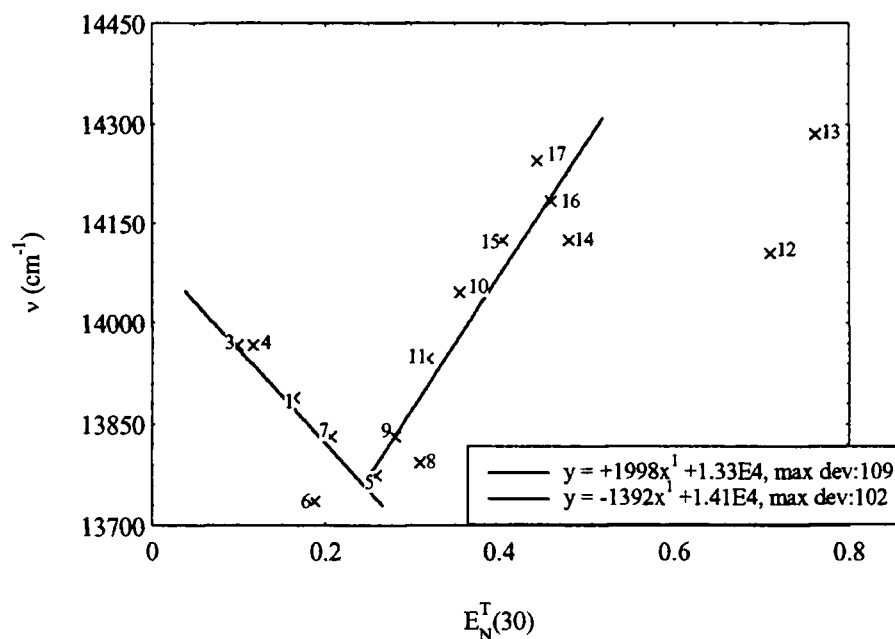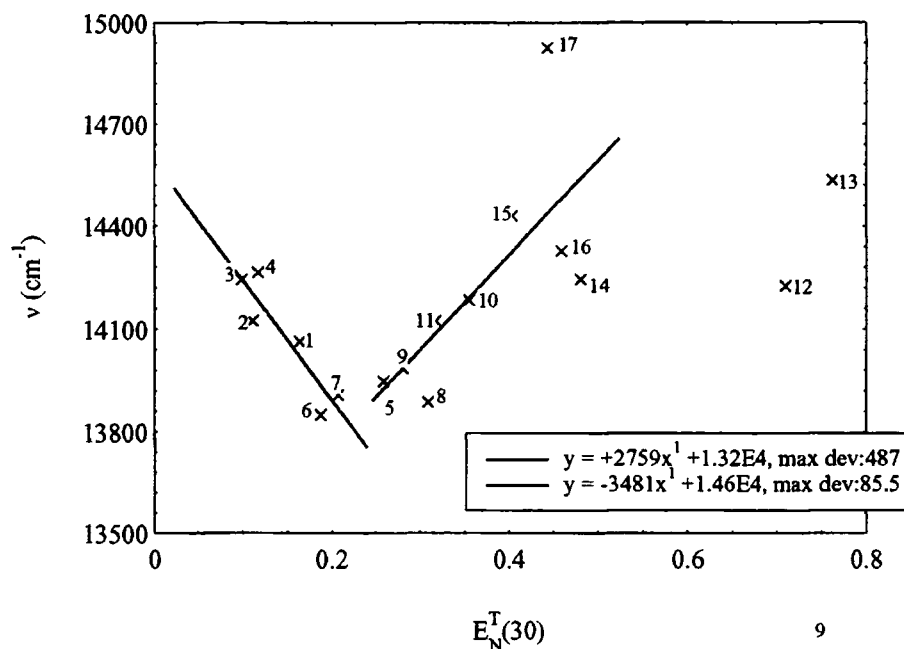
Figure 6.3-2: The position of the longest wavelength absorption band for DEMI (top) and DCH (bottom) in various solvents. For DEMI, the negative slope is produced by fitting 1 - 4, 6, and 7 to a straight line and the positive slope is produced by fitting 5, 9 - 11, and 14 - 16 to a straight line. Similarly for DCH, the negative line is produced by fitting 1, and 3 -7, where as the positive line is produced by fitting 5, 8 - 11, and 14 - 17. The solvents are the same as with Figure 6.3-1.

154
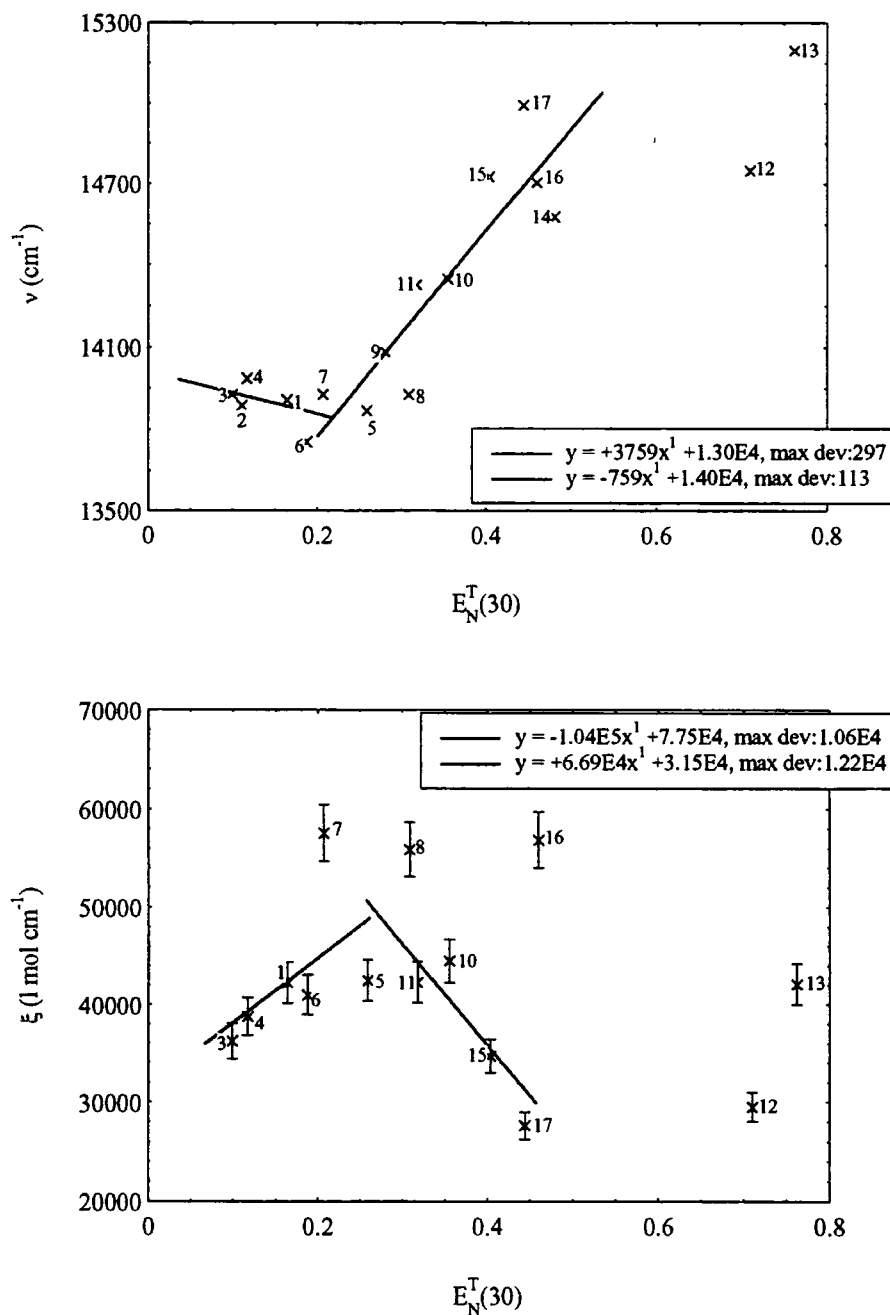
Figure 6.3-3: The position of the longest wavelength absorption band for ULTRA (top) in various solvents. In addition the extinction coefficient for ULTRA measured also in various solvents (bottom). With the top graph the negative line is produced by fitting 1 - 4, and 6 to a straight line and the positive slope is produced by fitting 5, 7 - 11, and 14 - 17. With the bottom graph the positive and negative slope are fitted to 1, 3 - 6 and 5, 8, 10, 11, 15, and 17 respectively.

The solvatochromic behaviour of DEMI is also in excellent agreement with the 40-state SOS calculations discussed in Chapter 3, where a reversal in shift of the transition frequency is predicted. This serves to indicate that the geometry of DEMI will evolve such that it exhibits quinoidal characteristics in low reaction field media (i.e. in low polarity solvents), and aromatic tendencies in high reaction field media. Thus it is highly likely that the dipole moment, polarisability, and hyperpolarisability will evolve with solvent polarity in a similar manner to that predicted by the SOS calculations. The solvatochromic evidence therefore intuitively shows that the sign of $\beta(0)$ for charge-transfer molecules, such as those discussed here, reverses as the polarity of the environment increases.

The position of the cyanine limit for the materials relative to each other is unclear due to the large errors associated with the data fitting. The magnitudes of the gradients for DEMI are similar on both sides of the cyanine limit whereas DCH and ULTRA both exhibit smaller bathochromic shifts compared to the hypsochromic shifts. This might indicate a slight increase in the aromaticity with DCH and ULTRA but this is difficult to confirm.

Also presented in Figure 6.3-3 is the measured extinction coefficient, $\varsigma(\nu_{max})$ for ULTRA in a number of the solvents, which is also plotted versus $E_N^T(30)$. Again there are large deviations from the general trend, so the straight lines are only intended as a guide to the eye. It appears that the extinction coefficient increases in lower polarity solvents, then decreases in higher polarity solvents. The maximum point is once again around $E_N^T(30) \approx 0.25$. The extinction coefficient, as subsequently shown, can be related to the transition dipole moment, which in turn can be related to the polarisability. It has also been shown that the polarisability exhibits exactly this kind of relationship where the peak of the polarisability coincides with the minimum in transition energy (see Chapter 3). Obviously, theoretical calculations on ULTRA would need to be conducted for any comparisons to be made, and in view of the errors involved with this graph, a more accurate determination of the extinction coefficient

with respect to solvent polarity is also needed. As will be seen this has been attempted with the results obtained from binary mixture experiments.

Again it is interesting to note the positions of chloroform (5) and DCM (8) on the graphs. With DEMI they are very close to the reversal point, both slightly to the right, but we note that DEMI in DCM has a lower transition frequency than in chloroform. Referring to Table 5.6-2 and the values of $\beta(0)$ obtained at 1.907 μm for DEMI, we see that DEMI in DCM is $+8 \times 10^{-30}$ esu which is lower than that in chloroform, $+30 \times 10^{-30}$ esu. From the lower observed transition energy, this is to be expected since it would indicate DEMI is closer to the cyanine limit in DCM and that the value of β is closer to zero. However, it would also appear from the positions of chloroform and DCM on the solvatochromism graph with respect to $E_N^T(30)$ that the value of β in these solvents should be negative, which is clearly not the case. Such differences can only be attributed to the error in the estimate of $E_N^T(30)$. With DCH, chloroform appears to be very close to the cyanine limit, and DCM is again just to the right, though the transition frequency of DCH in DCM is higher than that in chloroform. Again referring to Table 5.6-2, we find that $\beta(0)$ for DCH in DCM is -31×10^{-30} esu, and in chloroform, $\beta(0)$ is $+15 \times 10^{-30}$ esu. The higher observed transition frequency for DCH in DCM, serves to indicate again that DCH possesses a more negative β in DCM than that in chloroform. In fact β for DCH undergoes a reversal in sign between the two solvents. With ULTRA, both DCM and chloroform are to the right of the cyanine limit, and the transition frequencies relative to each other are similar to that of DCH. From Table 5.6-2, $\beta(0)$ for ULTRA in chloroform is -60×10^{-30} esu, and in DCM, $\beta(0)$ is -13×10^{-30} esu. This appears to be contrary to that predicted by the solvatochromism data. It is likely that this is due to erroneous measurement of μ, β or ν_{max}. Nonetheless, in general there appears to be a good agreement between the solvatochromism data and the measured EFISH values of $\beta(0)$ in that β is expected to be close to zero due to the fact that the tertiary amino TCNQ adducts possess geometries that are close to the cyanine limit in chloroform and DCM.

It is worth noting at this stage, since the EFISH measurements are in agreement with the solvatochromism data, the order of aromaticity for the tertiary amino TCNQ adducts. The aromaticity may be defined as the degree to which the chromophores tend to an aromatic state, where the BLA of a molecule is negative[1]. From the EFISH data in chloroform it appears that ULTRA is the most aromatic, followed by DCH then DEMI. This is nearly the conclusion made from measurements of the average BLA of the chromophores in the crystal phase, where the order of increasing aromaticity is DCH<DEMI<ULTRA [249].

In addition, the necessity of the third cyano-group to retain the quinoidal nature of the TCNQ derivative [249, 250] is further confirmed in view of the fact that DED, which lacks this cyano-group, exhibits purely a hypsochromic shift compared to the tertiary amino TCNQ adducts. This therefore indicates that DED is in a predominately aromatic state near the gas phase, whereas the tertiary amino TCNQ adducts near the gas phase reside in a predominately quinoidal state.

§6.4 An Attempt to obtain β from Solvatochromism.

Analysis of the extent of the solvatochromic shift has often been used to estimate the sign and magnitude of the hyperpolarisability, $\beta(0)$ [251, 252], where comparisons between solvatochromic results and that of EFISH experiments are made in two prominent papers [253, 254]. In this study, we follow the method used by Bosshard *et al* [253] with a few modifications to account for the use of the $E_N^T(30)$ scale to estimate the hyperpolarisability of NPP and DED.

Referring to §2.5 and utilising equation (2.5-2), the shift in frequency between the gas and solution phases may be described as

---

[1] Note: This should not be confused with the polarity of a molecule, i.e. the dipole moment of a molecule. This will vary with respect to aromaticity due to differing donor and acceptor strengths and differing charge-separation distances.

$$hc\left(v_{eg}^{sol} - v_{eg}^0\right) = -\frac{1}{4\pi\varepsilon_0 \bar{r}^3}\left[2\left(\mu^e - \mu^0\right)\mu^0\left(\frac{\varepsilon-1}{\varepsilon+2} - \frac{n^2-1}{n^2+2}\right) + \left\{\left(\mu^e\right)^2 - \left(\mu^0\right)^2\right\}\left(\frac{n^2-1}{n^2+2}\right)\right],$$

(6.4-1)

where μ^0 and μ^e are the dipole moments in the ground and excited state respectively, measured in the gas phase, ε and n are the dielectric constant and refractive index of the solvent respectively, and $\bar{r}$ is the average Onsager cavity radius. The additional effect to the evolution of the transition frequency due to the second term of (6.4-1) will be small for small or moderate changes in the ground and excited state dipole moments since the variation of the term involving n is small. Therefore the second term is sometimes excluded from the calculations. This then makes the estimate of the excited state dipole moment far easier. If μ^0 and $\bar{r}$ are known, it is possible to plot the position of the absorption band in various solvents versus the first term in (6.4-1), i.e. the terms involving ε and n^2. This will yield a straight line graph where the gradient can be used to find the excited state dipole moment in the gas phase. Thus (6.4-1) becomes

$$\frac{\partial v_{eg}}{\partial x} = \frac{2\left(\mu^e - \mu^0\right)\mu^0}{4\pi hc\varepsilon_0 \bar{r}^3},$$

(6.4-2)

where

$$x = \frac{\varepsilon-1}{\varepsilon+2} - \frac{n^2-1}{n^2+2}.$$

(6.4-3)

To relate the $E_N^T(30)$ polarity scale to (6.4-2), values of $E_N^T(30)$ have been plotted versus x (Figure 6.4-1). A near linear variation is exhibited and a gradient obtained by fitting a straight line to the data can be used to obtain the following equation

$$\frac{\partial v_{eg}}{\partial E_N^T(30)}\frac{\partial E_N^T(30)}{\partial x} \approx \frac{2(\mu^e - \mu^0)\mu^0}{4\pi hc\varepsilon_0 \bar{r}^3}.$$

<div align="right">(6.4-4)</div>

Considering the two-level model again (see §1.7, (1.7-5)), β may be obtained at zero frequency by using the following expression [253]

$$\beta_{zzz}(0) = \frac{3\mu_{eg}^2(\mu^e - \mu^0)}{2\varepsilon_0 \hbar^2 \omega_{eg}^2},$$

<div align="right">(6.4-5)</div>

where μ_{eg} is the transition dipole moment between the ground and excited state. μ_{eg} is obtained by estimating the oscillator strength (see equation (1.7-3)). The oscillator strength is calculated using the following expression [234, 253]

$$\int_{Band} \xi(\omega)d\omega = \frac{N_a e^2 (f^L)^2}{4m_e \ln 10 \varepsilon_0 c} f_{osc.}$$
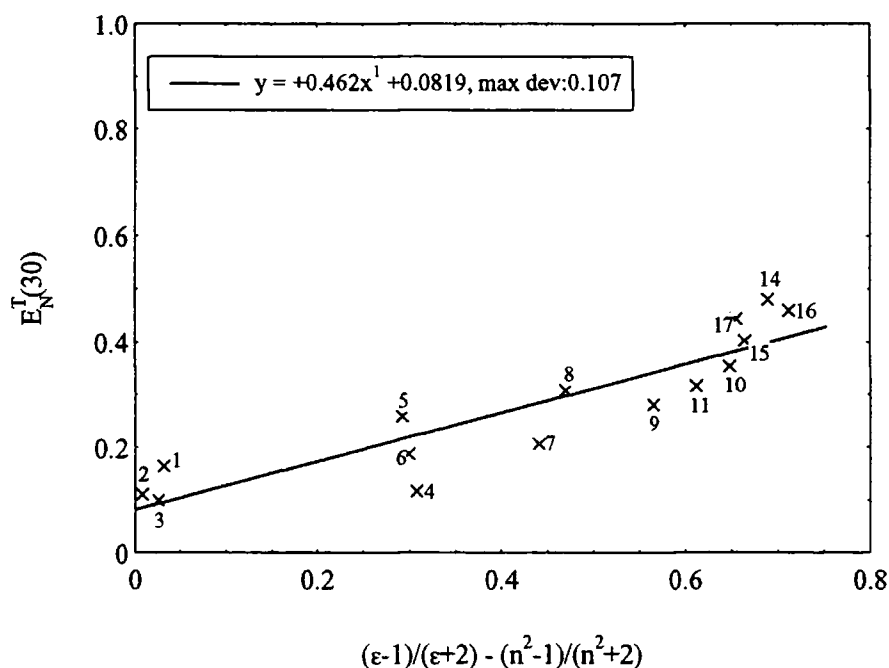
<div align="right">(6.4-6)</div>

Figure 6.4-1: $E_N^T(30)$ plotted versus functions of the dielectric constant and refractive index of solvents. The solid line is a straight line fit to the data.

where f_ω^L is the Lorentz-Lorenz local field given by equation (2.3-11) in Chapter 2 then utilising equation (1.7-3) to obtain μ_{eg}. Here Bosshard *et al* [253] are explicitly followed where they include the term f^L/n which accounts for local field variations on the electronic absorption band. It should also be noted that equation (6.4-6) estimates the absolute value of the transition dipole, but equation (6.4-5) requires only the component of the transition dipole in the z-direction. Thus, the use of these equations provide an upper limit to the value of β_{zzz} [253]

The area of the absorption band has been obtained for NPP and DED which are presented in Table 6.4-1 alongside the estimates of $f_{osc.}$ (see equation (1.7-4)), μ^e, μ_{eg} and β. Also presented are the cavity radius and ground state dipole moments for the two materials as calculated in Chapter 4 using SAS cavity radii. The estimates of the oscillator strength and transition dipole for NPP agree with estimates made elsewhere for NPP and similar materials [253, 254, 255], in that NPP possesses a moderately strong optical transition. The optical transition for DED is slightly stronger which is indicative of a larger polarisability due to the conjugated part of the molecule.

However, β for NPP and DED appears to be severely under-estimated in comparison to the EFISH values presented in this study and the corresponding values of β obtained from the literature, discussed in Chapter 3. Comparing values of β for NPP to that of the MOPAC calculations, also discussed in Chapter 3, we see that the above value is about ten times less than that predicted. The value of β for DED calculated here is also extremely low, and in comparison to the MOPAC value, it is also of opposite sign. Furthermore, it is far lower than the value of β measured in chloroform though there is at least an agreement as to the sign of β, which is to be expected. There are several reasons for these low estimated values. Firstly the neglect of the second term in equation (6.4-1) incurs a considerable error for molecules which

Material	$\int_{Band} \xi(\omega)d\omega$ $(\times 10^{18} \text{ m}^2 \text{ mol}^{-1} \text{ s}^{-1})$	μ_{eg} (D)	$f_{osc.}$	μ^0 (D)	μ^e (D)	$\bar{r}$ (Å^3)	β $(\times 10^{-30} \text{ esu})$
NPP [a]	0.86	3.62	0.46	3.9	5.3	3.2	1.0
DED [a]	1.09	4.38	0.59	7.9	5.4	3.6	-3.9

Table 6.4-1: Molecular parameters of NPP and DED obtained from solvatochromism experiments. Calculated using a: SAS radii, b: Crystal structure radii.

possess high dipole moments. Since DED has an extremely large dipole moment, the neglect of the second term may not be valid. However, the gas phase dipole moment for NPP is only moderate and it is surprising to see such a small value of β estimated for this molecule. Thus, a second reason for the low values might be attributed to the estimate of the cavity radius involved with the above calculations. It is noted that Bosshard *et al* [253] use typical cavity radii around 6 - 7 Å for molecules which are approximately the same size as NPP and DED. Furthermore, the same procedure is employed in the study conducted by Paley *et al* [254] where they use radii which are 0.7 times the length of the molecule under study and acknowledge that the choice of cavity radius is purely arbitrary. Suffice to say these radii are extremely large in comparison to the estimates used in this study and it is possibly the under-estimation of the cavity radius which causes an under-estimate of β.

In general this method of estimating β used here is poor since large errors are associated with the measurement of μ^0, r, the estimate of the gradient, $\partial v/\partial x$, and the theoretical approach to the calculation. Suffice to say however, that though it is difficult to estimate a magnitude of β, solvatochromism experiments are still extremely useful for determining the sign of β, since there is a very good agreement between the sign predicted from solvatochromism experiments and that obtained from EFISH measurements. In addition, and in view of the nature of the $E_N^T(30)$ scale in that specific solvent effects can mask considerably the trends exhibited by the solute, a quantitative analysis of the graphs for the tertiary amino TCNQ adducts would be futile. Indeed, the straight lines fitted to the data are intended only as a guide to the

eye. Obviously, a great error would be associated with any curve fitting to these graphs and the gradients would change depending of the selective nature of the data analysis. Furthermore, the validity of the two-level model when applied to the transition energy is also brought into question since it cannot fully account for a reversal in the ground and excited state dipole moments. In an attempt to obtain a more accurate evolution of the solvatochromism of the tertiary amino TCNQ adducts, our attention thus turns to the following binary mixture experiments.

§6.5 The Solvatochromism of Tertiary Amino TCNQ Adducts in Binary Mixtures of Toluene and Acetonitrile.

The experimental procedure for measuring the position of the absorption band in binary mixtures has been described in §6.2. Initially, several experiments were conducted in 1,4-dioxane - acetonitrile mixtures, but the polarity of 1,4-dioxane was high enough so that the cyanine limit was almost missed. Therefore, experiments were conducted in toluene - acetonitrile mixtures. Referring to Figure 6.3-2 and Figure 6.3-3, toluene (3) is the furthest solvent to the left of the graphs. Acetonitrile (16) on the other hand, is positioned to the far right of the graphs and does not exhibit any significant deviation from the fitted lines. Thus, it is hoped that the majority of solvent effects, such as hydrogen bonding, are removed by the use of toluene and acetonitrile.

The absorption spectra of DEMI, DCH, and ULTRA in a variety of volume fractions of acetonitrile are shown in Figure 6.5-1 to Figure 6.5-3, respectively. The spectra are all concentration normalised from a single value of the concentration of a stock solution, accounting for the additional volume of solvent mixture added. As a result the accuracy on the extinction coefficient is not very good, and errors are thus incurred as is evident from Figure 6.5-1 to Figure 6.5-3 with the erroneous extinction coefficient measurements. All three materials exhibit large increases in the intensity of the absorption band for over 0 - 35 % acetonitrile. The reason for this is not clear, but,

Figure 6.5-1: Evolution of the absorption spectrum of DEMI in mixtures of toluene and acetonitrile. Top: 0 - 50 %, bottom 50 - 100 % acetonitrile.

Figure 6.5-2: Evolution of the absorption spectrum of DCH in mixtures of toluene and acetonitrile. Top: 0 - 50 %, bottom: 50 - 100 % acetonitrile

Top chart legend:

—1.96	—3.85	—5.66	—7.41	—9.09	—18.03
—23.08	—28.57	—33.33	—37.50	—44.40	—50.00

Bottom chart legend:

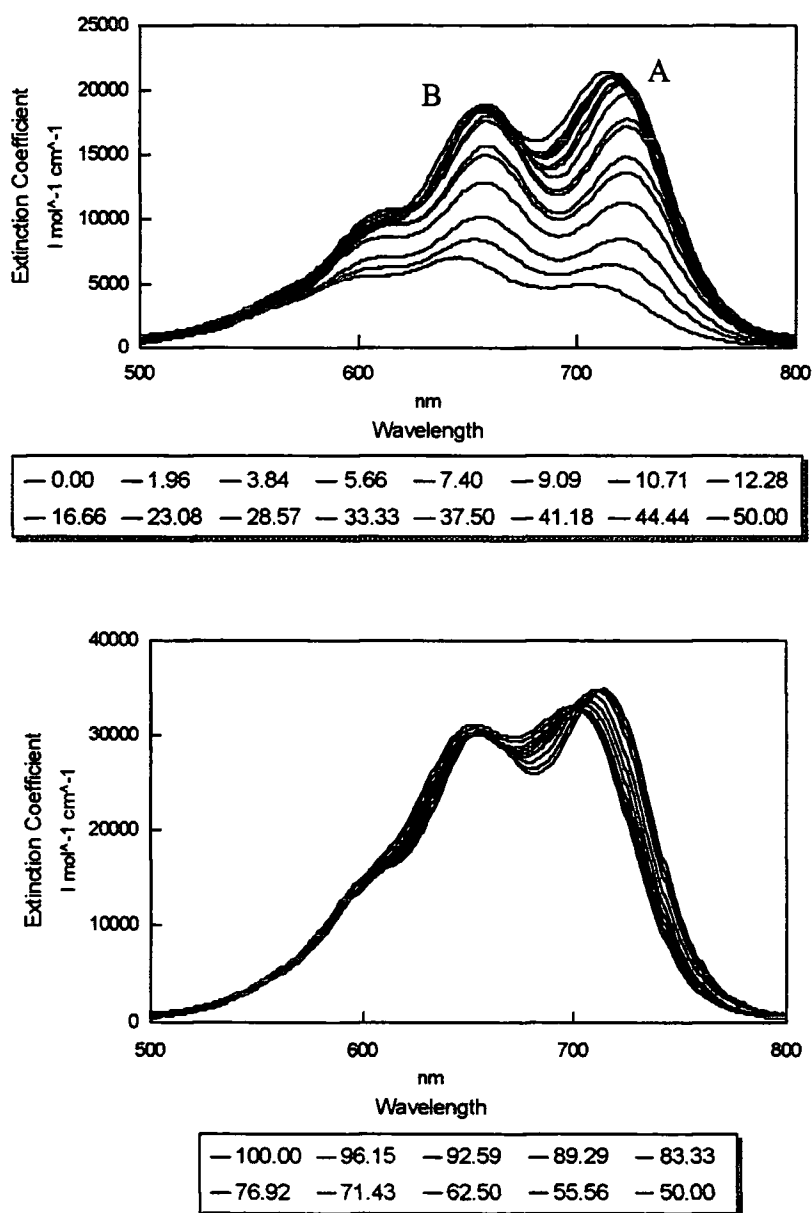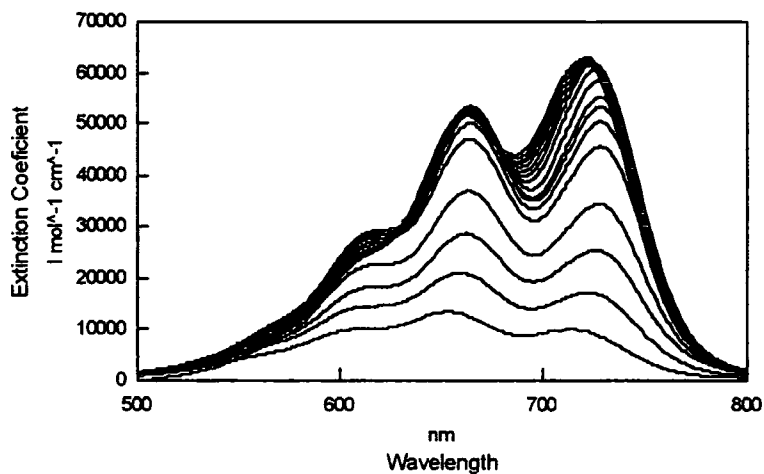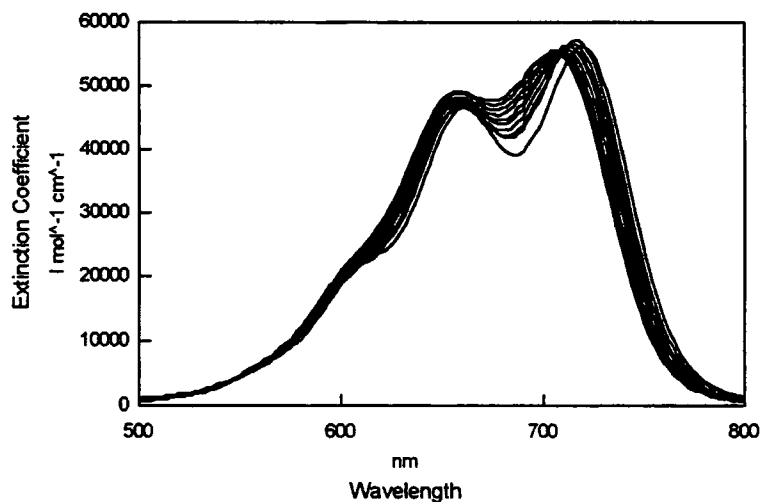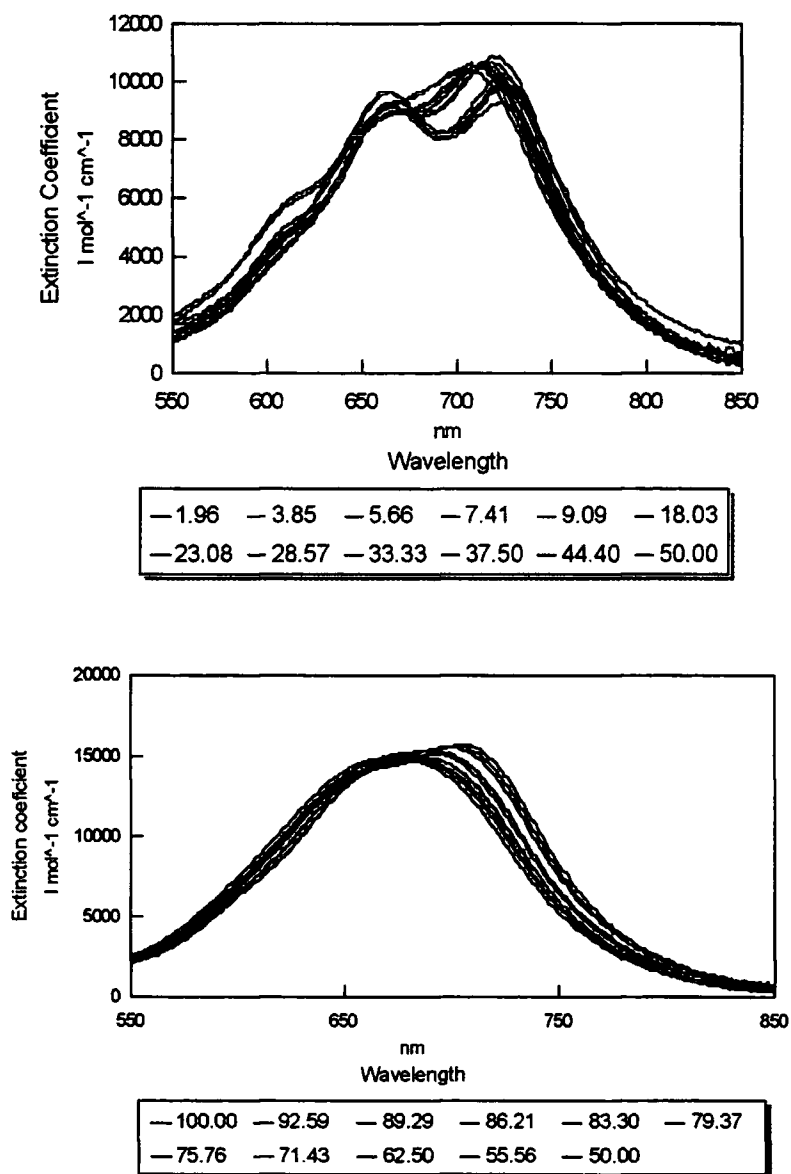|					
—100.00	—92.59	—89.29	—86.21	—83.30	—79.37
—75.76	—71.43	—62.50	—55.56	—50.00	

Figure 6.5-3: Evolution of the absorption spectrum of ULTRA in mixtures of toluene and acetonitrile. Top: 0 - 50 %, bottom: 50 - 100 % acetonitrile

despite great care to ensure that the solute was fully dissolved, it is likely that in all cases they have not, resulting in the loss of the absorption intensity. The effect is less prominent with ULTRA since it is far more soluble than DEMI or DCH. As already discussed, at low volume fractions DEMI and DCH exhibit two prominent absorption bands which gradually merge as more acetonitrile is added. With ULTRA on the other hand, the two absorption bands are already close together and almost merge completely when dissolved in pure acetonitrile. This indicates further that ULTRA is in a more aromatic state than DCH and DEMI, and serves to confirm the conclusions made with the preceding solvatochromism experiments and EFISH experiments on the tertiary amino TCNQ adducts. Finally, it should be noted that there is little evidence of an isosbestic point associated with the absorption bands of any of the tertiary amino TCNQ adducts which would indicate the presence of intermolecular complexes or isomer formation [223]. However, the bands A and B are generally too close to each other to confirm this fully.

The presence of the second band (B) as already mentioned, complicates the issue of the position of band A and severely hampers the measurement of the area under the peak. In an attempt to circumvent this problem, a spectral curve fitting program is employed which is commercially available [256]. The overall absorption band is fitted to four absorption peaks using a Gaussian and Lorentzian summation lineshape (see Appendix V). The first two bands correspond to peaks A and B, and the second two correspond to the respective vibronic bands associated with A and B [236]. This method was found to reproduce all absorption spectra extremely accurately ($r^2 > 0.999$). The error on the position of the band is approximately 1 %. The error on the area under the curve is uncertain, but it was found that it did not vary greater than 5 % over a number of fits using different initial positions for the bands. However, this error became larger (up to 20 %) when fitting the spectra at higher volume fractions where the bands merge.

The evolution of bands A and B for the tertiary amino TCNQ adducts, as estimated from the fitting procedure are shown in Figure 6.5-4 - Figure 6.5-10, where the error induced by the fitting procedure is adequately shown. It is difficult to
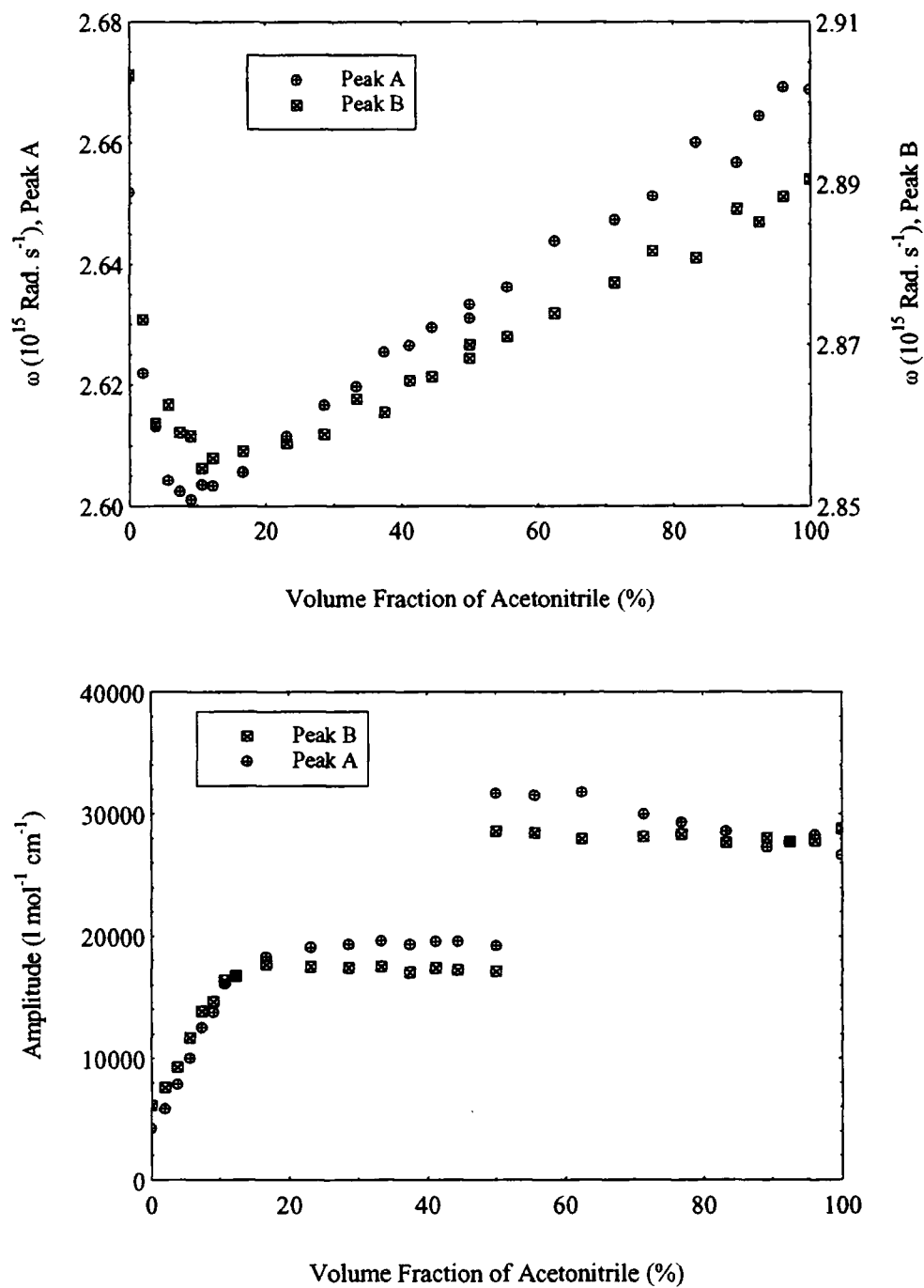
Figure 6.5-4: Evolution of various parameters of the absorption spectrum of DEMI with volume fraction of acetonitrile in toluene. Top: Frequency of bands A and B. Bottom: Peak intensities of bands A and B.
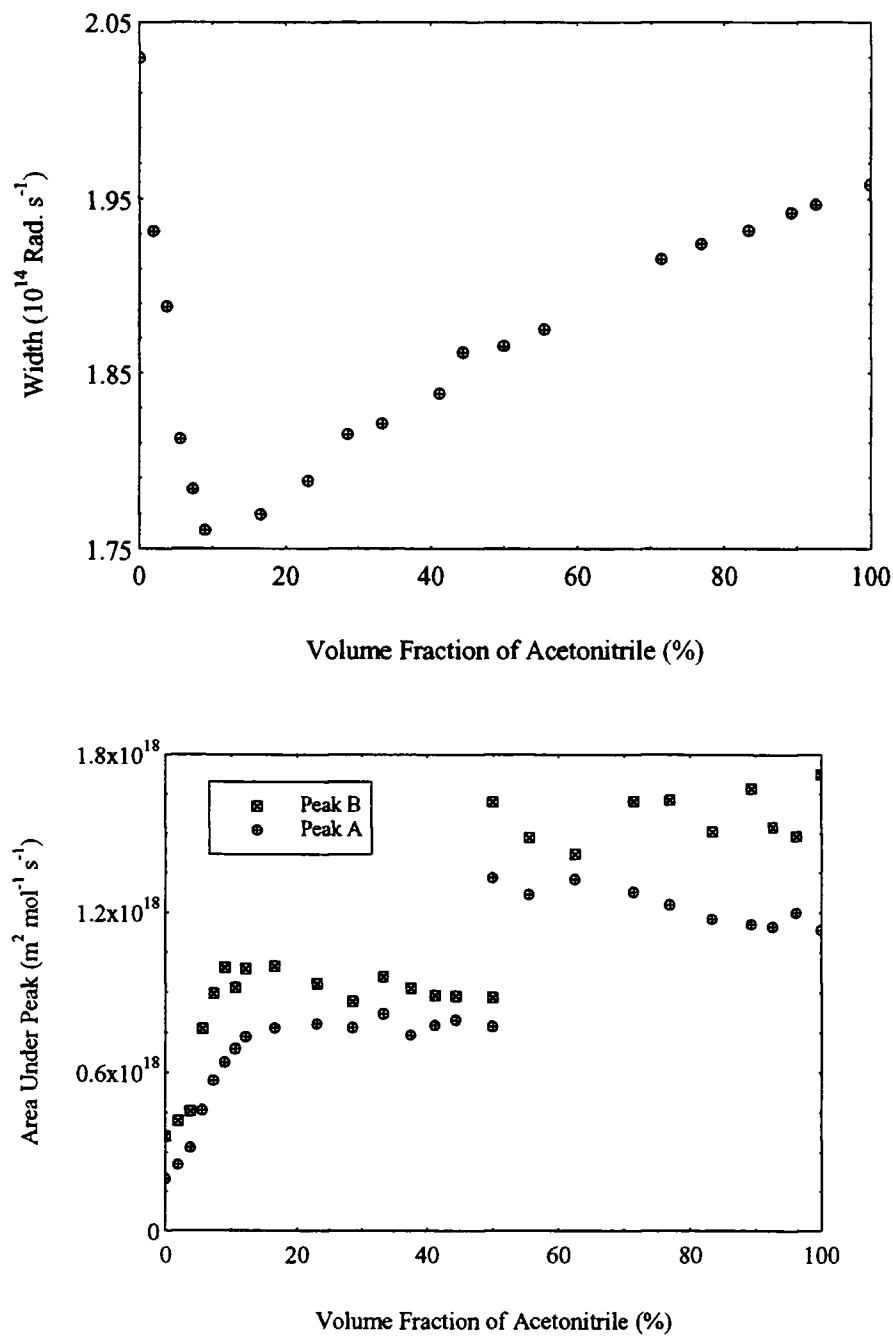
Figure 6.5-5: Evolution of various parameters the absorption spectrum of DEMI with volume fraction of acetonitrile in toluene continued. Top: Width of band A. Bottom: Area of bands A and B.
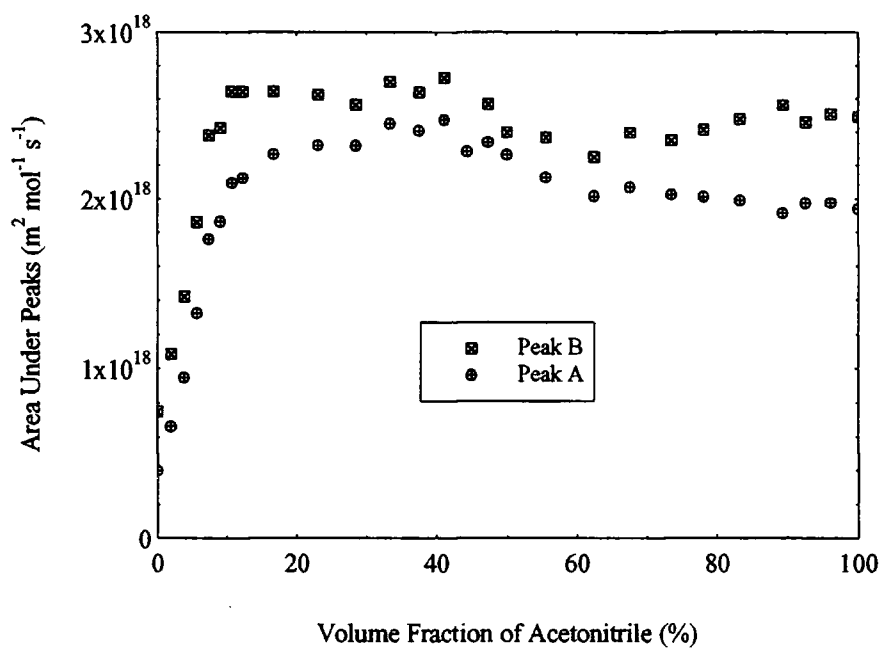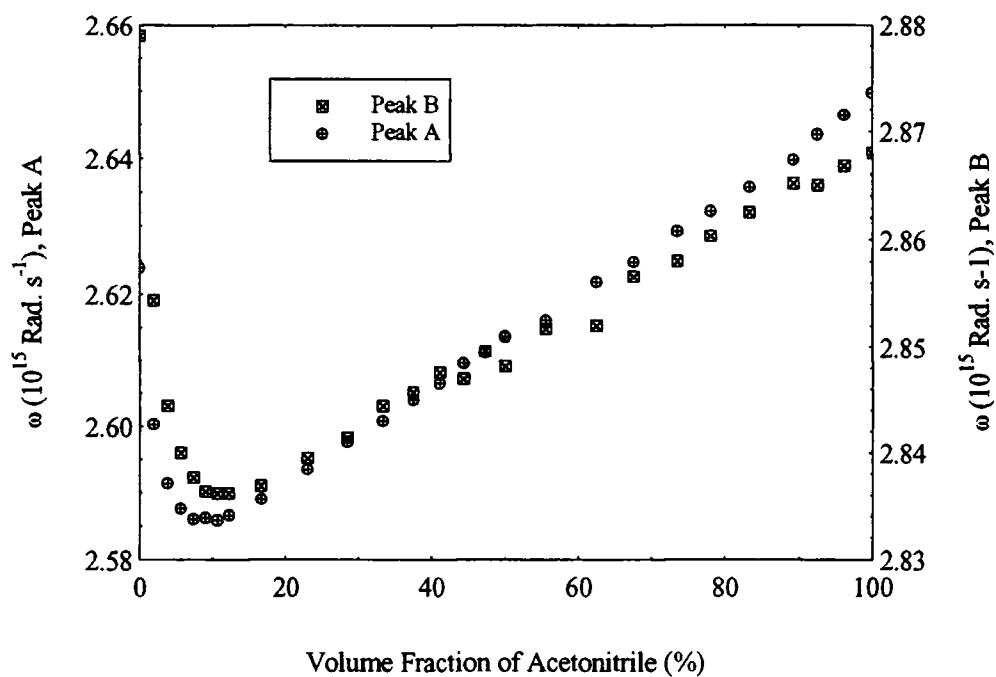
Figure 6.5-6: Evolution of various parameters of the absorption spectrum of DCH with volume fraction of acetonitrile in toluene. Top: Transition frequencies of bands A and B. Bottom: Area of bands A and B.
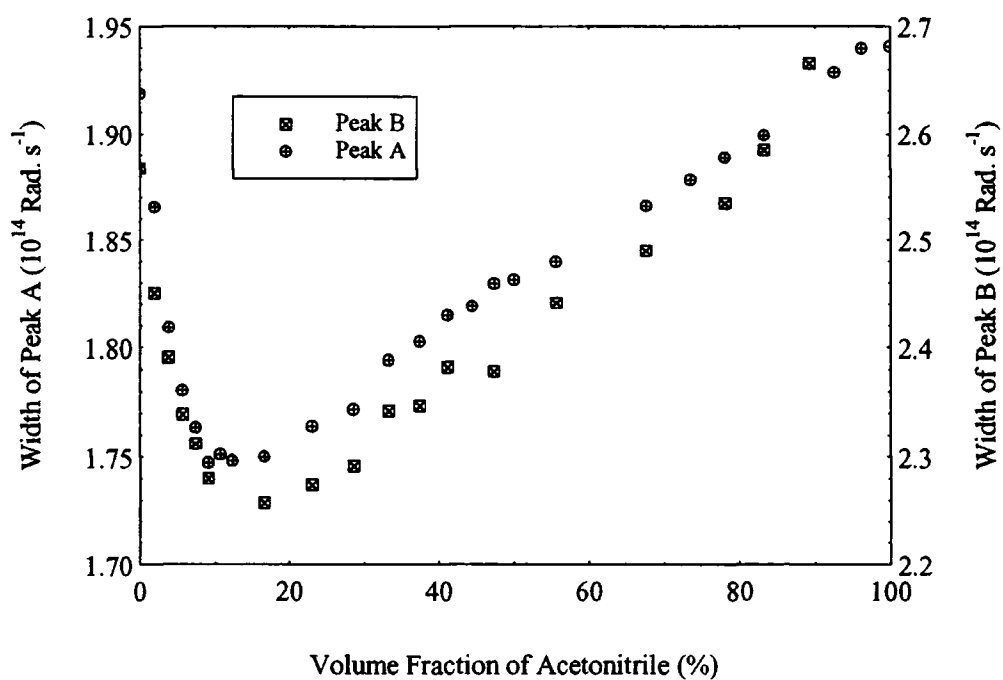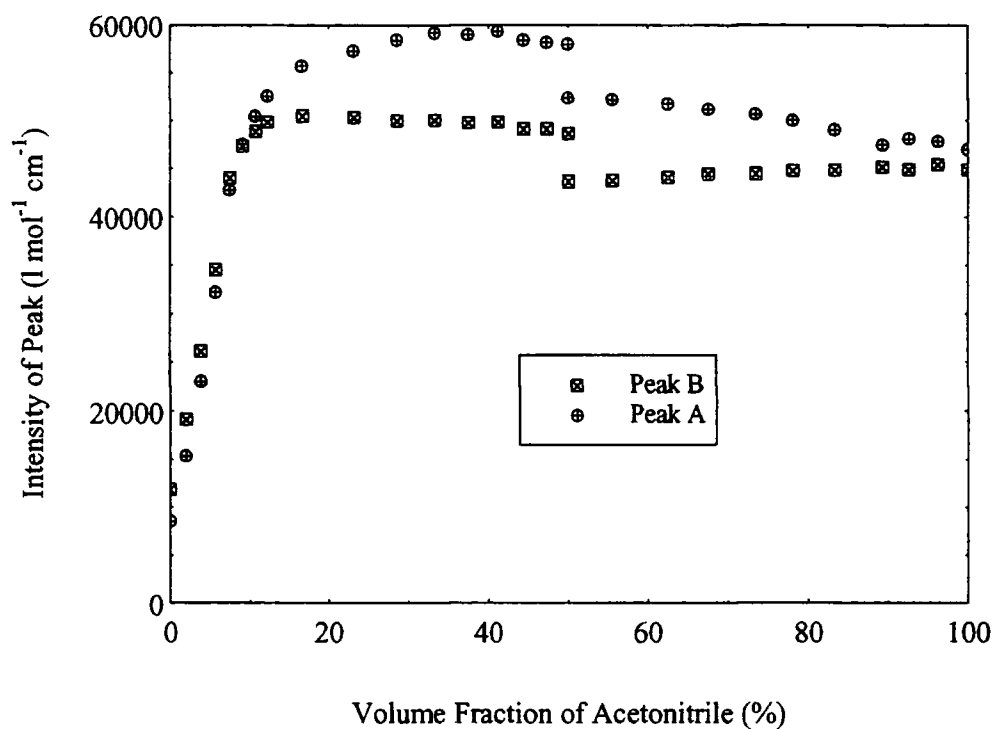
Figure 6.5-7: Evolution of various parameters of the absorption spectrum of DCH with volume fraction of acetonitrile in toluene continued. Top: Intensities of bands A and B. Bottom: Widths of bands A and B.
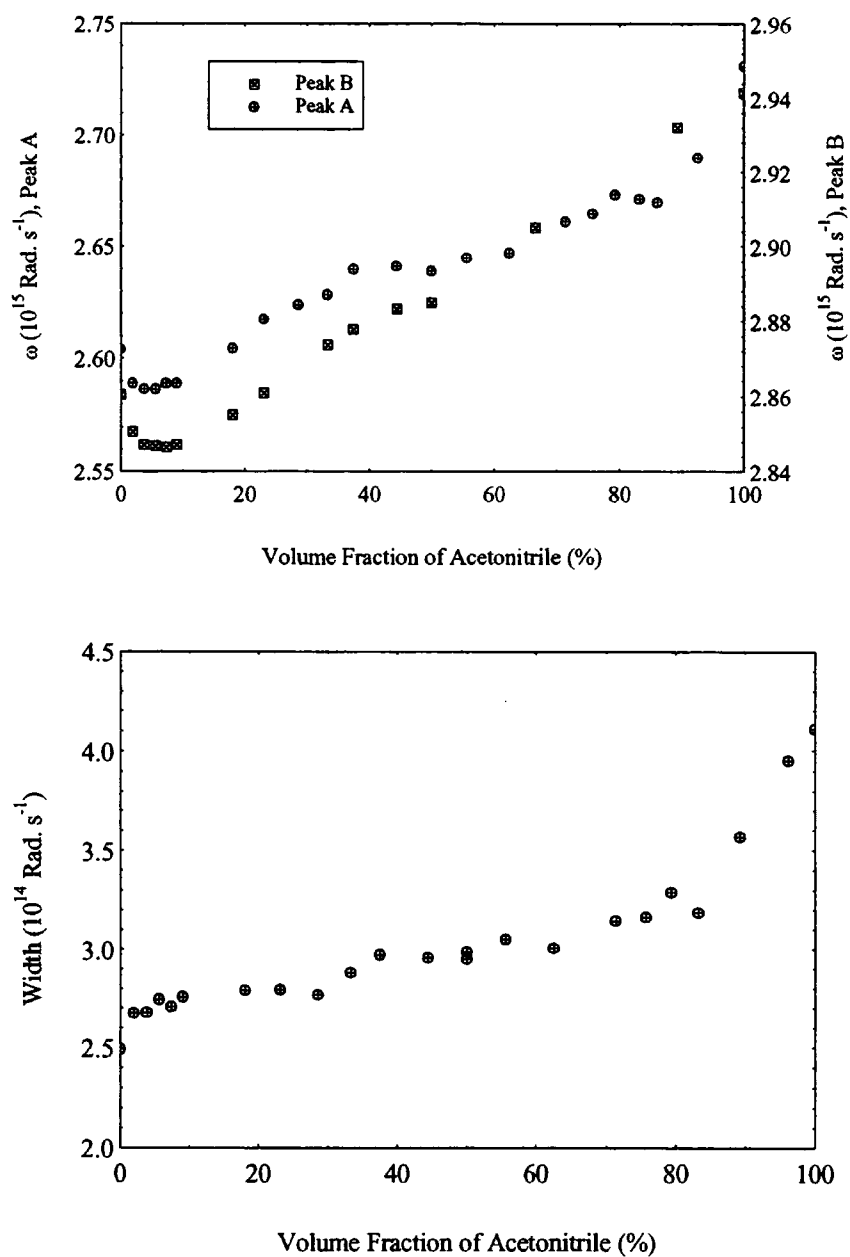
Figure 6.5-8: Variation of the absorption spectrum of ULTRA with volume fraction of acetonitrile in toluene. Top: Transition frequencies of bands A and B. Bottom: Width of band A only.
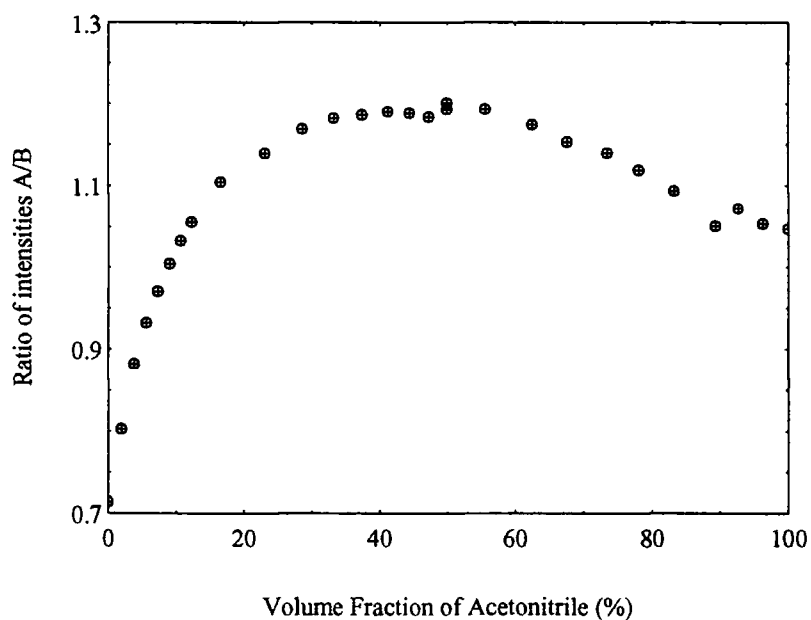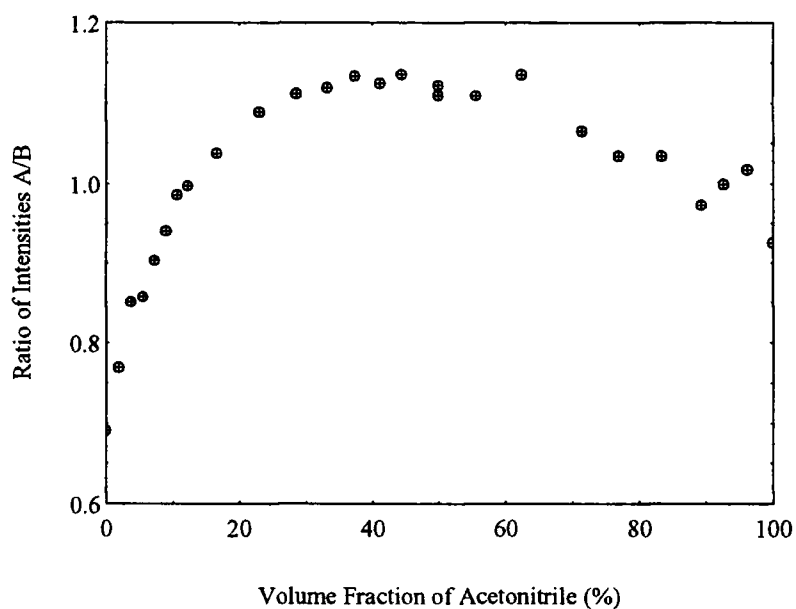
Figure 6.5-9: Variation of the ratio of intensities of band A over band B in the absorption spectrum of DEMI (top) and DCH (bottom).

173
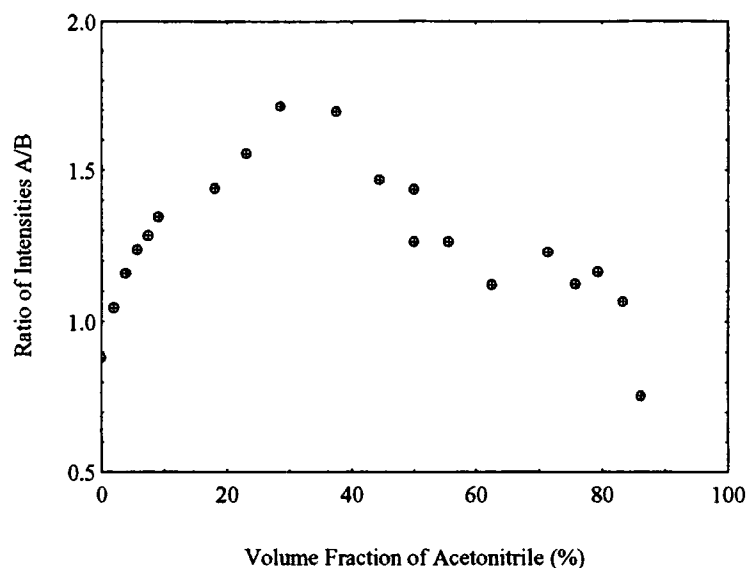
*Figure 6.5-10: Variation of the ratio of intensities of band
A over band B in the absorption spectrum of ULTRA.*

estimate the oscillator strength since this involves the calculation of the area under the absorption band, which is ultimately dependent on the intensity of the band. As already discussed, due to the possibility that the solute has not dissolved fully in toluene, the intensity follows an anomalous evolution with volume fraction. Secondly, it is difficult to match the absorption intensities between the separate halves of the experiments which accounts for the sudden jump in intensity at 50 % acetonitrile (see Figure 6.5-4 and Figure 6.5-7). Thus, the observation of any real trends in the evolution of the area is extremely difficult (see Figure 6.5-5 and Figure 6.5-6). For ULTRA the error on the width of the peak is extremely large since the absorption bands merge quickly, and it is almost impossible to identify any evolution of the width of the band with increasing volume fraction. As a result of these errors in combination with those involved with the concentration of the solute, the area under the absorption bands for ULTRA is not presented. For an analysis of the oscillator strength to be conducted, the experiments should be repeated with greater care with the above points in mind. However, there are indications from the experiments on DCH and DEMI that the area of the absorption bands remain constant. If this is the case, then the oscillator strength will increase and decrease due to the dependence upon the inverse of the transition frequency. Since the oscillator strength is related to the polarisability [257], the results

174

pertaining to the polarisability calculated by the 40-state SOS method appears to be confirmed further.

The evolution of the transition frequencies for all three materials are similar and show a reversal in the solvatochromic shift at low volume fractions. The point at which this occurs is found to be 8.9 %, 9.3 %, and 4.7 % acetonitrile for band A of DEMI, DCH and ULTRA respectively. A similar behaviour is exhibited with band B. There are indications that the reversal point occurs at a slightly higher volume fraction than band A. It is unclear however, if this is actually the evolution of B or an artefact of the fitting procedure. The widths of the absorption bands for DEMI and DCH follow a similar evolution to that of the transition energy, but no reversal is observed with ULTRA. The bands for DEMI and DCH first narrow rapidly, then widen, and the reversal point is similar to that of the transition energy which is why the area remains constant, but, as already indicated, care must be observed with this since the calculation of the width of the band may again be an artefact of the fitting procedure. Finally, it is interesting to note the evolution of the ratio of the intensities of band A and B with respect to volume fraction of acetonitrile. This is shown in Figure 6.5-9 and Figure 6.5-10 for the three materials. Band A is initially less intense than B. However, the intensity of A rapidly increases with respect to B where it soon becomes larger. The point where bands A and B are of equal intensity appears to occur roughly around the cyanine limit. At present, it is difficult to attribute a reason for this behaviour so it is left purely as a point of interest.

In addition, the positions of the cyanine limit with respect to volume fraction of acetonitrile immediately confirms the conclusion made earlier, that ULTRA is more aromatic than DEMI or DCH, and it appears from these measurements that DEMI and DCH are equally aromatic. This is in excellent agreement with the conclusions obtained with the EFISH results.

It is interesting to estimate the reaction fields and dipole moments of the material at the cyanine limit. The evolution of the density, dielectric constant, and refractive index (see Figure 6.5-11 and Figure 6.5-12) of the pure solvent mixture has been measured. All the graphs exhibit a linear variation with volume fraction (though
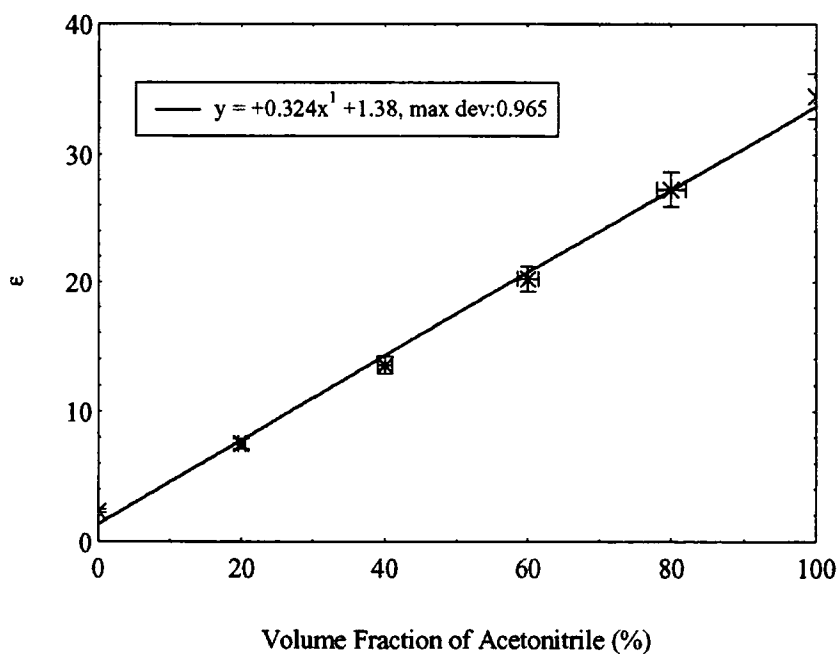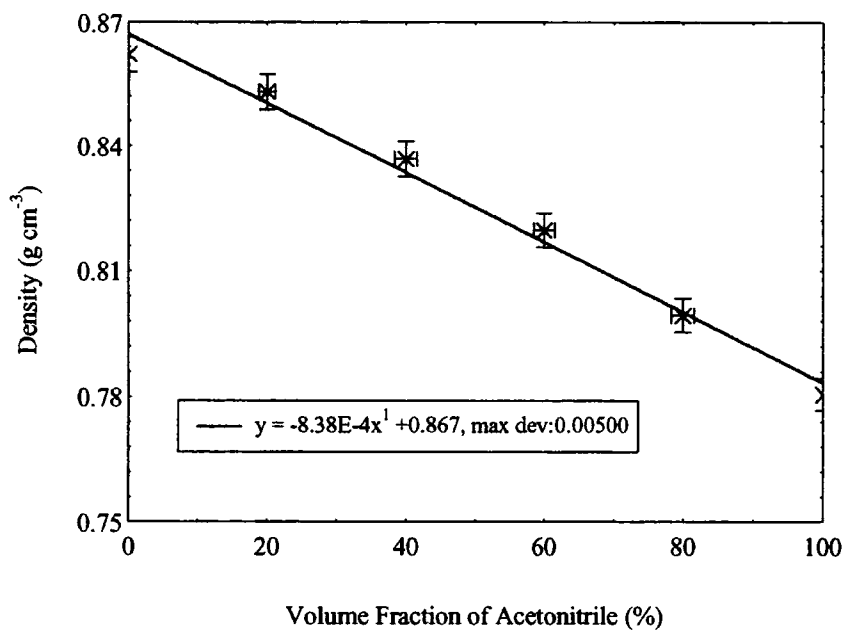
Figure 6.5-11: Variation of the density (top) and dielectric constant (bottom) of mixtures of acetonitrile and toluene.
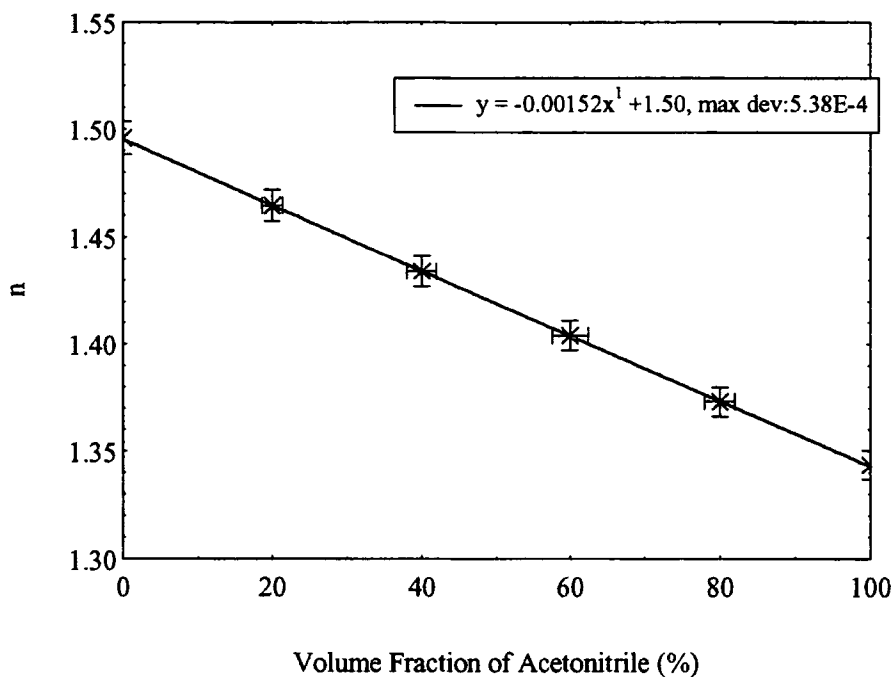
*Figure 6.5-12: Variation of the refractive index of mixtures of
acetonitrile and toluene.*

there is the slightest of deviations shown with the density), thus the medium is ideal in
which to study the variation of the transition frequency with reaction field. The
reaction field, R may be calculated by using equation (2.3-13) for ellipsoidal and
spherical local fields. Using the volume fractions obtained at the reversal point for
each material and using Figure 6.5-11, the dielectric constant at the reversal point may
be estimated for DEMI, DCH and ULTRA. Then, the reaction field, R_{ε} and dipole
moment, μ_{ε} at the cyanine limit may be calculated using the estimates of the dipole
moment, and polarisability presented in Chapter 4 for both local field formalisms.
These are presented in Table 6.4-1. It is noted that the dipole moment at the cyanine
limit is higher using an ellipsoidal local field formalism than the corresponding spherical
dipole moment in accordance with the findings in Chapter 4. Conversely the respective
reaction field is lower than the spherical reaction field. The reaction field at this point
for DEMI will be compared to the 40-state calculations in the next chapter in an
attempt to ascertain which local field is the better approximation to the SOS
calculations. It should be noted that at the cyanine limit, the change in dipole moment

177

upon excitation, $\Delta\mu$ is equal to zero so the excited state and ground state dipole moments are equal. This means that the estimates of μ in Table 6.5-1 are also estimates of the excited state dipole moment. Calculations of the excited state dipole moment of D-π-A polyenes have revealed an almost constant variation with reaction field where the variation is only 10 - 20 % between the gas phase and the cyanine limit [257]. Such a variation means it is possible to estimate $\Delta\mu$ *in the gas phase* and thus $\beta(0)$ may also be estimated in the gas phase using the two level model. The results are presented in Table 6.5-2 alongside estimates of the oscillator strength, $f_{osc.}$ and the transition dipole moment, μ_{eg} which has been measured in DCM. $f_{osc.}$ and μ_{eg} have been estimated from the area under absorption band A in DCM, utilising the fitting program [256] to estimate the size and shape of the band. As shown, the estimates appear to be reasonable. $\beta(0)$ is calculated using equation (6.4-5) using the transition frequency for DCM. The use of the transition frequency for DCM instead of the gas phase value may result in a small over-estimate of $\beta(0)$. Given the errors involved with such estimates, the values of $\beta(0)$ presented here are in good agreement with the MOPAC values of $\beta(0)$ presented in Chapter 3, though the values are less than that predicted by the 40-state SOS calculation. Nonetheless, this method appears to be valid to a first approximation.

Material	V_f(%)	ε	μ_g^{sph} (D)	μ_g^{ell} (D)	μ_ε^{sph} (D)	R_{sph} $\times 10^{-3}$ au	μ_ε^{ell} (D)	R_{ell} $\times 10^{-3}$ au
DEMI	8.9	4.2	6.8	15.2	15.6	11.3	28.8	7.0
DCH	9.3	4.4	5.0	13.1	11.6	6.8	21.9	4.6
ULTRA	4.7	2.9	6.4	14.1	9.8	4.3	17.3	2.9

Table 6.5-1: Estimates of the dipole moment and reaction field at the cyanine limit for the three tertiary amino TCNQ adducts, obtained from the measured values of volume fraction of acetonitrile and corresponding dielectric constant, using the spherical and ellipsoidal gas phase dipole moments estimated in Chapter 4.

Material	$f_{osc.}$	μ_{eg} (D)	$\Delta\mu^{sph}$ (D)	$\Delta\mu^{ell}$ (D)	β_{sph} $\times$ 10^{-30} esu	β_{ell} x 10^{-30} esu
DEMI	0.74	6.14	8.8	11.9	65	88
DCH	0.50	5.04	6.6	8.8	33	45
ULTRA	0.92	6.84	3.4	3.2	31	29

Table 6.5-2: The oscillator strength and transition dipole moment estimated in DCM. Also presented are estimates of the change in dipole moment upon excitation in the gas phase and corresponding values of β(0) for both local field formalisms. The error on Δμ and β is ± 35 %.

§6.6 Conclusions.

The position of the absorption band for the five materials discussed in this thesis have been measured and compared to Reichardt's $E_N^T(30)$ polarity scale. Both NPP and DED were found to exhibit standard solvatochromic behaviour where a bathochromic shift was found for NPP and a hypsochromic shift was found for DED. Attempts to estimate β from an analysis of the degree of solvatochromic shift yielded a lower β value than that suggested by MOPAC calculations or EFISH experiments. The solvatochromic behaviour of the tertiary amino TCNQ adducts was found to be similar to that of the merocyanines in that a reversal in the direction of shift is observed and that there is now direct evidence of a change in sign in β. Closer inspection of the position of specific solvents such as DCM and chloroform reveal that small values of β would be expected since the tertiary amino TCNQ adducts are close to the cyanine limit in these solvents. Such experiments have confirmed also that ULTRA lies further to the right of the BLA diagram than DEMI or DCH.

In an attempt to obtain a more accurate evolution of the transition frequency with respect to solvent polarity, experiments have been conducted in binary mixtures of toluene and acetonitrile. This has served to confirm the order of aromaticity of the materials which is in agreement with studies conducted in the crystal phase. Analysis

of the evolution of the oscillator strength proves difficult due to experimental error in the estimate of the concentration of the solutions. Nonetheless, estimates of the oscillator strength in conjunction with estimates of the dipole moment in the gas phase and at the cyanine limit have proved useful to estimate $\beta(0)$ in the gas phase. These were found to agree reasonably well with MOPAC calculations.

Comparisons of the evolution of the transition energy with reaction field for DEMI with the SOS calculations will be made in the next chapter.

References to Chapter 6.

[223] N. Mataga, T. Kubota, *Molecular Interactions and Electronic Spectra.*, Marcel Dekker Inc., New York, (1970).

[224] E. M. Kosower, *J. Am. Chem. Soc.*, **80**, 3253, (1958).

[225] S. Ehrenson, *J. Am. Chem. Soc.*, **103**, 6036, (1981).

[226] C. Reichardt, *Solvents and Solvent Effects in Organic Chemistry.*, **2nd Ed.**, VCH (UK) Ltd., Cambridge, (1990).

[227] E. Buncel, S. Rajagopal, *Acc. Chem. Res.*, **23**, 226, (1990).

[228] C. Reichardt, *Chem. Rev.*, **94**, 2319, (1994).

[229] C. Reichardt, *Chem. Soc. Rev.*, 147, (1992).

[230] M. J. Taft, J. L. Abboud, R. W. Taft, *J. Am. Chem. Soc.*, **99 (18)**, 6027, (1977).

[231] M. J. Kamlet, J. L. M. Abboud, R. W. Taft, *Prog. Phys. Org. Chem.*, **13**, 485, (1981).

[232] J. E. Brady, P. W. Carr, *J. Phys. Chem.*, **86 (16)**, 8053, (1982).

[233] E. Buncel, S. Rajagopal, *J. Org. Chem.*, **54**, 798, (1989).

[234] P. W. Atkins, *Physical Chemistry.*, **3rd Ed.**, Oxford University Press, Oxford, (1986).

[235] M. Szablewski, G. H. Cross, D. Bloor, Private Communication, (1994).

[236] D. Bloor, Private Communication, (1996).

[237] M. Malagoli, G. H. Cross, Private Communication, (1995).

[238] F. J. Kampas, *Chem. Phys. Lett.*, **26 (3)**, 334, (1973).

[239] A. Botrel, A. Le Beuze, P. Jacques, H. Strub, *J. Chem. Soc. Farad. Trans.*, **80**, 1235, (1984).

[240] P. Jacques, *J. Phys. Chem.*, **90**, 5535, (1986).

[241] H. G. Benson, J. N. Murrell, *J. Chem. Soc. Farad. Trans. 2*, **68 (1)**, 137, (1972).

[242] E. Buncel, S. Rajagopal, *J. Org. Chem.*, **54**, 798, (1989).

[243] L. G. S. Brooker, A. C. Craig, D. W. Hesaltine, P. W. Jenkins, L. L. Lincoln, J. Am. Chem. Soc., 87 (11), 2443, 2443, (1965).

[244] A. Botrel, A. Le Beuze, P. Jacques, H. Strub, *J. Chem. Soc. Farad. Trans. 2*, **80**, 1235, (1984).

[245] J. Figueras, *J. Am. Chem. Soc.*, **93 (13)**, 3255, (1971).

[246] B. K. Mishra, M. Kuaner, A. Mishra, G. B. Behera, *Bull. Chem. Soc. Jpn.*, **69**, 2581, (1996).

[247] J. Aihara, *Bull. Chem. Soc. Jpn.*, **54**, 1561, (1981).

[248] J. A. Soroka, K. B. Soroka, *J. Phys. Org. Chem.*, **4**, 592, (1991).

[249] J. M. Cole, Ph.D. Thesis, **University of Durham.**; *Structural Studies of Organic and Organometallic Compounds Using X-Ray and Neutron Techniques.*, (1997).

[250] J. C. Cole, J. M. Cole, G. H. Cross, M. Farsari, J. A. K. Howard, M. Szablewski, *Acta Crystallographer B*, **B53**, 812, (1997).

[251] J. Sworakowski, J. Lipinski, L. Ziølek, K. Palewska, S. Nespurek, *J. Phys. Chem.*, **100**, 12288, (1996).

[252] M. Barzoukas. A. Fort, P. Boy, C. Combellas, A. Thiebault, *Non-Linear Optics*, 7, 41, (1994).

[253] Ch. Bosshard, G. Knöpfle, P. Prêtre, P. Günter, *J. Appl. Phys.*, **71 (4)**, 1594, (1992).

[254] M. S. Paley, J. M. Harris, H. Looser, J. C. Baumert, G. C. Bjorklund, D. Jundt, R. J. Tweig, *J. Org. Chem.*, **54**, 3774, (1989).

[255] J. Zyss, F. Nicoud, M. Coquillay, *J. Chem. Phys.*, **81 (9)**, 4160, (1984).

[256] Peakfit, Version 4.0, AISN. Software Inc., (1991 -1995).

[257] F. Meyers, S. R. Marder, B. M. Pierce, J.-L. Brédas, *Chem. Phys. Lett.*, **228**, 171, (1994); *Figure 3, p173*.

Chapter 7

A Comparison of Experimental and Theoretical Data for DEMI.

§7.1 Introduction.

In the previous chapters, a large amount of experimental data has been collected for DEMI, namely the dipole moment, μ, first hyperpolarisability, $\beta(0)$, and transition energies, v_{eg} in various solvent media. Since μ is known, the evolution of the dipole moment can be calculated as a function of reaction field, R and compared to the 40-state SOS calculations on DEMI, which are discussed in Chapter 3 [258]. Furthermore, if the reaction field of DEMI is known, the evolution of v_{eg} as a function of R may be compared to the SOS calculations utilising the results discussed in Chapter 6. The reaction field of DEMI in chloroform and DCM can also be estimated allowing comparisons of $\beta(0)$ to be made. Since DEMI has been observed to lie close to the cyanine limit in chloroform and DCM, we can see whether such calculations conclude the same result.

Such comparisons will also attempt to ascertain which of the local field formalisms provide a better match to the theoretical calculations. The results of the hyper-Rayleigh scattering experiments conducted elsewhere will also be discussed and compared to the data presented in this study.

§7.2 The Dipole Moment.

Values of the dipole moment in DCM, μ_s and in the gas phase, μ_g, calculated in Chapter 4 using the ellipsoidal and spherical local field formalisms, are summarised in Table 7.2-1 alongside some of the parameters used to estimate these, namely the polarisability, α, the cavity radius, $\bar{r}$, and the shape factor A_z. The variation with $\bar{r}$ has already been discussed (see for example Figure 4.5-1, Chapter 4) where large increases in the dipole moment are seen for moderate increases in cavity radius. We recall, through calculations of the refractive index and the dipole moment, that there are indications that the "actual" cavity radius may lie somewhere between the estimated SAS and crystal structure radii. Thus, both the SAS and crystal structure radii and their corresponding dipole moments are presented below.

Obviously from these results, uncertainty remains over which estimated value of the dipole moment represents more closely the "real" dipole moment of the molecule. Given that the evolution of the transition frequency of DEMI in various solvents is novel, it is crucial that an accurate estimate of the reaction field acting upon the molecule is made so that the position of the cyanine limit with respect to reaction field is found. The gas phase dipole moment, estimated from the experiments in DCM, is at the point where the reaction field, R is zero. Thus, we can immediately compare this with both sets of SOS calculations. Furthermore, from this value and by varying

Parameter	$\mu_s^{Sph.}$	$\mu_g^{Sph.}$	$\mu_s^{Sph.}$	$\mu_g^{Sph.}$	$\mu_s^{ell.}$	$\mu_g^{ell.}$	$\mu_s^{ell.}$	$\mu_g^{ell.}$
μ (D)	22.4	6.8	30.6	17.3	33.0	15.2	38.1	26.0
$\bar{r}$ (Å)	3.8	3.8	4.4	4.4	3.8	3.8	4.4	4.4
$\bar{\alpha}$ / α_z (Å³)	45.4	45.4	45.4	45.4	99.0	99.0	99.0	99.0
A_z	0.3333	0.3333	0.3333	0.3333	0.1027	0.1027	0.1027	0.1027

Table 7.2-1: Various dipole moments estimated for DEMI and the parameters used in their estimation.

the value of the dielectric constant, the dipole moment and reaction field may be estimated and plotted as a function of each other. Recalling equations (2.4-5) and (2.3-14),

$$\mu_s = (1 - f\alpha)\mu_g \text{ and } R = \frac{f\mu_g}{(1 - f\alpha)},$$

(7.2-1)

it is possible to plot μ_s as a function of R (shown in Figure 7.2-1) for both the spherical and ellipsoidal local field formalisms which are estimated using the SAS cavity radius. These are plotted for dielectric constants ranging between 0 (i.e. the gas phase value) and 80 (the dielectric constant for water), thus representing nearly the entire range of reaction fields experienced by DEMI in the gas and solution phases, neglecting specific solvent effects. It is easy to see that a straight line is produced due to the proportionality of μ_s with R. Also plotted in Figure 7.2-1 are the two sets of SOS calculations using the SCI (Single Configuration excitation Interactions) and SD-CI (Single and Double excitation Interactions) methods. As discussed in Chapter 3, the evolution of μ for both sets of calculations are similar and there is little difference between the values of μ at any value of reaction field. In comparison, there is a far better correlation between the experimental estimates of μ_s calculated using the ellipsoidal formalisms and the SOS calculations than that obtained with the spherical formalisms. For similar solution state dipole moments, a larger reaction field is experienced if a spherical cavity was used than if an ellipsoidal cavity is used. This is primarily due to the larger polarisability, α_z associated with the ellipsoidal local field model compared to that used with the spherical local field model, thus intuitively an agreement with an ellipsoidal field model is likely since the theoretical calculations also utilise the larger polarisability, α_z instead of the average polarisability.

Before any conclusions can be made however, the polarisability and cavity radius used in such calculations must be considered. Obviously, the evolution of the dipole moment with reaction field will differ depending on the value of these two parameters. Reproducing Figure 7.2-1, Figure 7.2-2 shows the variation of the
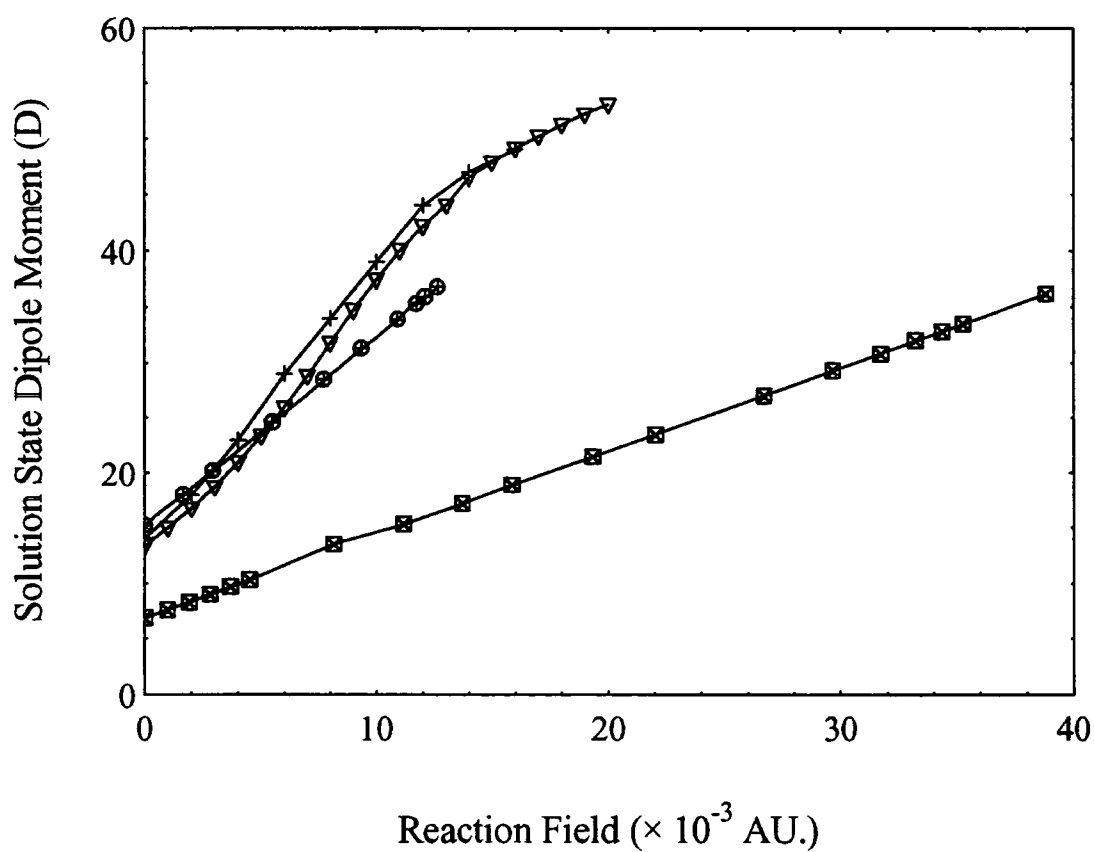
Figure 7.2-1: Variation of the dipole moment with reaction field, as estimated from experiment using the spherical (squares) and ellipsoidal (circles) local field formalisms. These are compared to the results of 40-state SOS calculations using SCI (crosses) and SD-CI (triangles) methods.
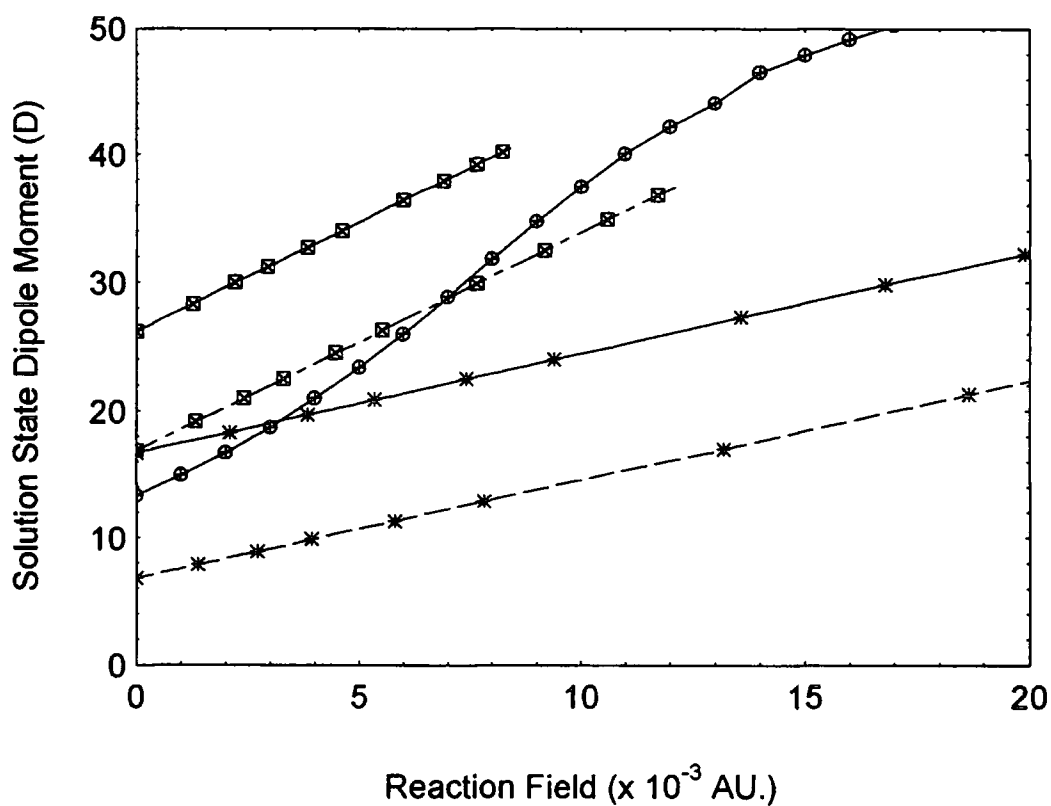
Figure 7.2-2: Variation of the dipole moment with reaction field, as estimated from experiment using the spherical (stars) and ellipsoidal (squares) local field formalisms, calculated using the SAS cavity radius (dotted lines) and crystal structure radius (solid lines). These are compared to the results of 40-state SOS calculations using the SD-CI (circles) method.

spherical and ellipsoidal dipole moments with reaction field if the cavity radius is changed to the crystal structure radius. With the ellipsoidal curves it is assumed that the ratios of the principal axes remain the same and therefore, A_z remains unchanged. In this case, the increase in cavity radius increases the value of the dipole moment, but the gradient of each curve remains unchanged. Therefore, there is still a better correlation between the ellipsoidal dipole moments and the SOS calculations, compared to that of the spherical dipole moments.

A change in the gradient, $\partial\mu/\partial R$ is induced by a change in the polarisability. Comparing the average polarisability calculated by MOPAC and used for the experiments in this study (45.4 Å^3) to the average polarisabilities estimated by the 40-state SOS calculations, the SCI method (44.5 Å^3 in the gas phase [258]) agrees well with the MOPAC calculations but the SD-CI method predicts far lower polarisabilities (26 Å^3 in the gas phase [258]). Similar comparisons are observed for α_z (100 Å^3 (MOPAC), 121.2 Å^3 in the gas phase (SCI), 64.6 Å^3 in the gas phase (SD-CI)), and it is noted that the SCI estimate of the α_z is higher than the MOPAC estimate, but the SD-CI α_z is again lower. The effect of a change of the polarisability on the curves produced in Figure 7.2-1 is simple. If the polarisability is higher than the value used in experiments, from the experimental solution state dipole moment the value of the gas phase dipole moment will be lower than estimated in Figure 7.2-1, perhaps providing a better initial correlation with the SCI calculations and the ellipsoidal values. However, as the dielectric constant of the medium increases, the dipole moment will increase faster with reaction field than is seen with Figure 7.2-1. Thus, a larger gradient is observed. If on the other hand, the polarisability is smaller than that used experimentally, a higher gas phase dipole moment will be predicted, but the gradient will be lower since a larger change in reaction field is needed to produce the same change in dipole moment. If the SD-CI polarisabilities were used, both the ellipsoidal and spherical curves would not correlate with the SOS calculations. However, if the SCI polarisabilities were used, there would still be a good correlation with the ellipsoidal formalism and not the spherical formalism. We must recall however, the comment made in Chapter 3, that the gradient, $\partial\mu/\partial R$ pertaining to the

SD-CI calculations should be lower as is confirmed by the above argument. As this is not exhibited with the SD-CI calculations, some inconsistency is associated with these results. With the above points in mind, one is led to the conclusion that the use of an ellipsoidal local field when estimating dipole moments, provides a better estimate (in accordance with the SCI calculations at any rate) than the use of a spherical local field, and that the method used in Chapter 4 provides a satisfactory correlation, given the experimental error. Furthermore, one should note that SOS $\overline{\alpha}$ and α_z also vary with reaction field, which accounts for the changes in gradient with the SOS dipole moment curves. Obviously it is difficult to incorporate such a change into the experimental estimates of the dipole moment, thus only a linear correlation with reaction field is observed with the experimental curves. It is therefore possible that a poor correlation of the dipole moment is found with the SOS calculations for specific values of reaction field.

A comparison of the evolution of ν_{eg} with R can now be made to the SOS calculations, and the position of the cyanine limit with respect to R, estimated in the following section.

§7.3 The Transition Energy.

The evolution of the dielectric constant with volume fraction of acetonitrile, (Figure 6.5-8) can be used in conjunction with the dipole moment measurements discussed above, to estimate the reaction field for DEMI as a function of volume fraction of acetonitrile. Then, the transition energy of the absorption band for DEMI may be plotted versus reaction field and compared to the SOS calculations (SCI data only, since SD-CI data is unavailable). This is shown in Figure 7.3-1 for both spherical and ellipsoidal local field formalisms.

Unfortunately the magnitude of the transition energies do not agree, and the theoretical calculations predict a larger variation of the transition energy than is clearly the case from the experimental results. Nonetheless, there is excellent agreement with
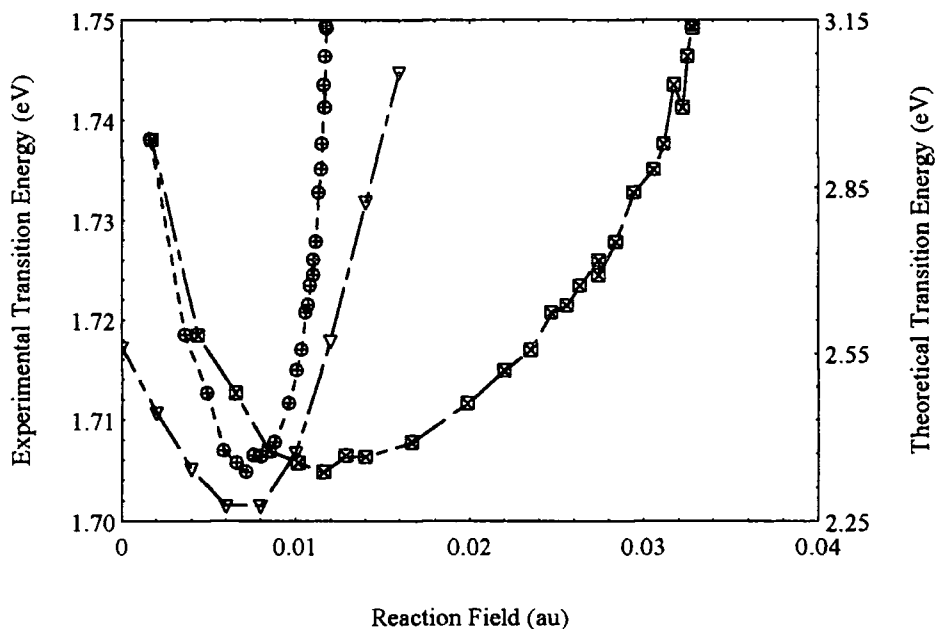
Figure 7.3-1: Evolution of the transition energy of DEMI versus reaction field. Experimental estimates of the reaction field are made using the ellipsoidal (circles) and spherical (squares) formalisms. These are compared to 40 state SOS SCI calculations (triangles).
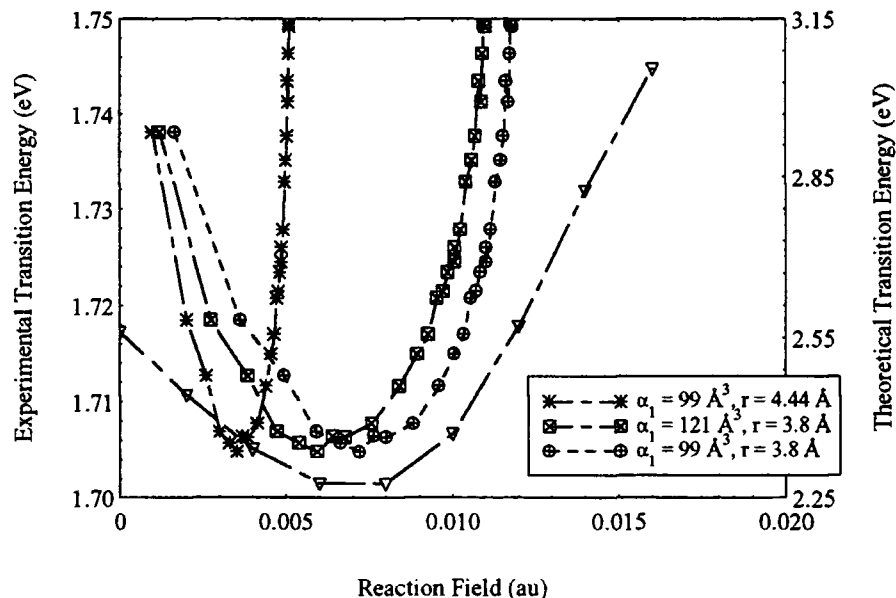
Figure 7.3-3: Variation of the transition energy of DEMI with reaction field which is estimated using various polarisabilities and cavity radii and compared to theoretical results.

the position of the minimum as estimated using the ellipsoidal dipole moments and the theoretical calculations. This is not surprising since there is already a good correlation between the theory and the ellipsoidal dipole moments. Therefore, it is logical that the estimate of the reaction field which is obtained from the dipole moment would appear to agree well with theory. As a result it is seen, once again, that the estimated reaction field for the spherical data is too large and does not agree with the theoretical data.

The effect of varying the polarisability and cavity radius for the estimate of the reaction field is seen in Figure 7.3-3. Increasing the polarisability to that of the SCI value (121 Å^3), shifts the entire curve to smaller reaction fields, but the "width" of the curve remains relatively unchanged (squares and dashed line). Increasing the radius however, has the effect of decreasing the "width" as well as shifting the entire curve to smaller reaction fields (stars and dashed line). Thus, for there to be a better correlation with the SCI calculations, the SCI polarisability and a smaller radius should be used which would have the effect of "widening" the curve while ensuring that the minimum still correlates. In view of the fact that the magnitude of the transition energies do not agree it would be a futile gesture to try to do this.

Finally, recalling Table 6.6-1, it is found that the minimum energy is found when the ground state dipole moment is 29 ± 6 D, as calculated using the ellipsoidal formalism. This is also in agreement with the theoretical data (32 D for the SCI calculations and 29 D for the SD-CI calculations). It is noted that this is approximately the estimated value of the ellipsoidal dipole moment for DEMI in chloroform and DCM (33 ± 7 D in DCM and 30 ± 6 D in chloroform). Once again, the experimental evidence appears to agree with the theoretical results since the observed transition energy of DEMI in chloroform and DCM is close to the minimum transition energy, i.e. the cyanine limit.

§7.4 The First Hyperpolarisability.

In Chapter 5 it was found that though the dipole moment depended a great deal on the geometrical nature of the local field, there was only a small increase in the value

of β when ellipsoidal local fields are used, though this was only for small values of β.

In Table 7.4-1, values of $\beta(0)$ for DEMI obtained from the EFISH experiments at 1.907 μm are thus summarised for the ellipsoidal local field formalism only. Also presented are the corresponding values of $\beta(0)$ found from the SCI and SD-CI calculations (see Figure 3.3-2, Chapter 3 and the figures below) by correlating the estimated reaction field of DEMI in chloroform and DCM. Inspection of the results reveal that $\beta(0)_{EFISH}$ does not agree with the SCI theory in either solvent. Recalling Figure 3.3-2 which is reproduced below (Figure 7.4-1), it is evident that the point where $\beta(0)$ is zero is not at the point where the minimum transition energy occurs. The minimum transition energy nearly coincides with the maximum (in a negative sense) $\beta(0)$. Thus a large negative value is calculated for DEMI in both solvents. However, the SD-CI data produces a lower result because; generally the magnitude of $\beta(0)$ is lower, $\beta(0)$ first increases to a maximum before decreasing to zero, and the variation of $\beta(0)$ is less sensitive to the reaction field. Therefore in the case of chloroform there is quite a good agreement (given the experimental error involved) with the SD-CI theory. It is also noted that confusingly the SD-CI cyanine limit ($\beta = 0$) coincides with the SCI transition energy minima which suggest further inconsistencies between the two sets of calculations.

The sensitivity of the $\beta(0)$ response to the reaction field as calculated by the SOS method is very large. Inspection of Figure 7.4-2 shows that relatively small changes in dipole moment produce very large changes of $\beta(0)$. For example, the

Solvent	$\beta(0)_{EFISH}$	$\beta(0)_{SCI}$	$\beta(0)_{SD-CI}$
Chloroform	+28	-376	-20
DCM	+9	-484	-212

Table 7.4-1: Summary of EFISH results for DEMI compared to theoretical calculations estimated from a correlation of reaction fields. Units of 10^{-30} esu.
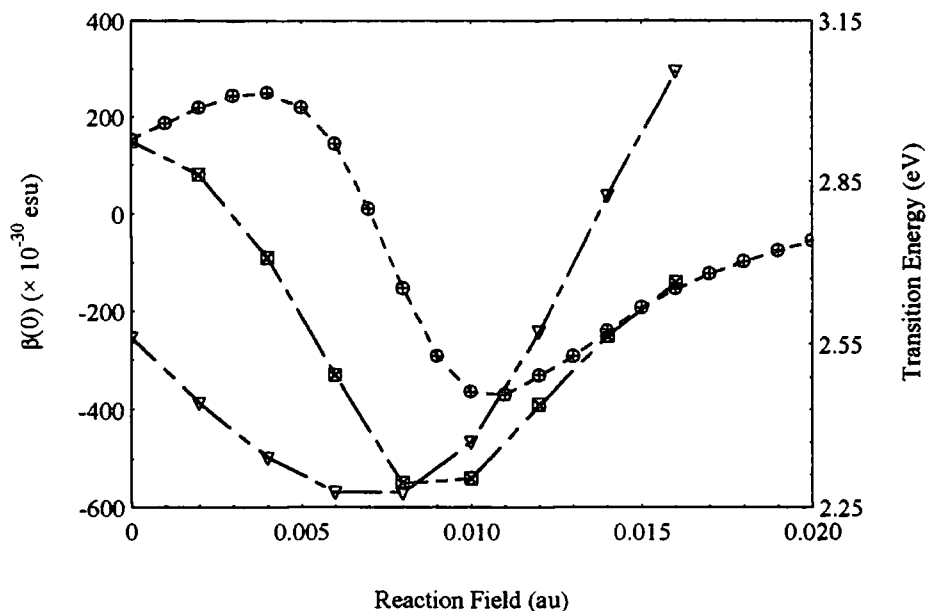
Figure 7.4-1: Evolution of β(0) for DEMI as estimated using 40-state SOS SCI (Squares) and SD-CI (circles) calculations. Also presented is the theoretical evolution of the transition energy estimated using the SCI method.
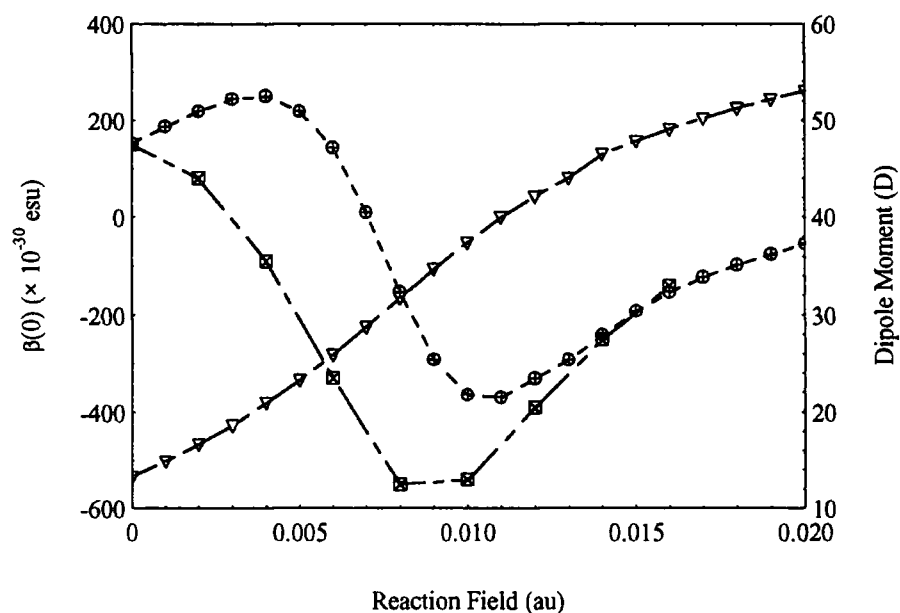
Figure 7.4-2: Evolution of β(0) for DEMI as estimated using 40-state SOS SCI (Squares) and SD-CI (circles) calculations. Also presented is the theoretical evolution of the dipole moment estimated using the SD-CI method.

difference between the dipole moments of DEMI in chloroform and DCM (29 - 33 D) induces a change of -190 × 10^{-30} esu in $\beta(0)$ with the SD-CI calculations. A similar change is observed with the SCI results. Therefore, any error in the estimate of μ or R would result in a grave error in the correlation of the values of $\beta(0)$. This is a possible reason as to why the results in DCM do not correlate. Also, in view of the fact that the calculations (at least the SCI calculations) over-estimate the response of the transition energy to reaction field, the $\beta(0)$ response with respect to reaction field may also be erroneous. Thus, relatively small changes in dipole moment, in reality may not result in a large change in $\beta(0)$. Indeed, it is unfortunate that the evolution of the transition energy with respect to reaction field is unavailable for the SD-CI calculations, and it is suggested that this is obtained as soon as possible.

Independent measurements on DEMI, as discussed in Chapter 3 are confusing to say the least, and attempts to correlate them are hindered also by the choice of local field factor [259, 260, 261]. However, there is further evidence that the measured value of $\beta(0)$ correlates well with the SD-CI calculations. Recalling Chapter 3, -85 × 10^{-30} esu was measured for DEMI in DMF using a dipole moment of 45 D to extract $\beta(0)$ (which agrees moderately well with the dipole moment measurements presented in this study) [259]. Comparing the $\beta(0)$ values in Figure 7.4-2, the corresponding dipole moment according to the SD-CI calculations is around 50 D. Considering that the predicted value is equivalent to an ellipsoidal dipole moment, which should be larger than the experimental spherical value, it appears there is also a good correlation between measurement and calculation. $\beta(0)$ was also found to be approximately -200 × 10^{-30} esu in a PMMA thin film, and the corresponding dipole moment was found to be 46 D, estimated using ellipsoidal local fields [261]. Again referring to the SD-CI calculations and given the possible errors involved, there is an excellent agreement with experiment where $\beta(0)$ is predicted to be -250 × 10^{-30} esu. However, at these high reaction fields, the two sets of calculations converge, i.e. similar values of $\beta(0)$ are obtained for similar dipole moments so there is also a degree of agreement here with the SCI calculations. It appears that the confusion over the

correlation of experimental results with these calculations has thus arisen due to the sensitivity of the calculated $\beta(0)$ to the reaction field.

However, one must be careful with the above correlations. The experimental estimates of the dipole moment are calculated on the basis of polarisabilities which are similar to that of the SCI theory, which clearly do not agree with the SD-CI polarisabilities. If the SD-CI polarisabilities were used, then there would be a poor correlation between the evolution of the dipole moments and transition energies, as well as the hyperpolarisabilities. Estimates of the polarisability using MOPAC (in conjunction with the average radius, $\bar{r}$ admittedly) provide reasonable estimates of the refractive index when using the Clausius-Mossotti equation. Thus, there is a tendency to "believe" the SCI polarisabilities rather than the SD-CI polarisabilities, even though it would be logical for the polarisability to reduce if a second electronic excitation is take into account during transitions, as is done with the SD-CI data. On the other hand with the SCI calculations, even though there is a good correlation between dipole moments and the evolution of the transition energies, the hyperpolarisabilities do not match at lower reaction fields which is perhaps due to the over-estimation of the sensitivity of the transition energy to reaction field. In fact, there is an excellent correlation between the SD-CI $\beta(0)$ values and experimental measurements. Clearly there are further inconsistencies here.

There is an extremely poor correlation between the magnitude of $\beta(0)$ measured for DEMI in chloroform using EFISH ($\approx 30 \times 10^{-30}$ esu) and the magnitude of $\beta(0)$ measured for DEMI in chloroform using hyper-Rayleigh scattering techniques (350×10^{-30} esu) [262, 263]. There are arguments for and against the EFISH values being reasonable. It is possible that, due to the high polarity of the solute, conduction may occur in the cell resulting in a reduction of the signal which could be mistaken as a non-linear optical response of opposite sign to the solvent. However, if this was the case, at higher concentrations no up-turn in signal would be seen as the non-linearity of the solute overcomes the non-linearity of the solvent. The up-turn has been observed at least in the case of ULTRA and DED in DCM. If the conduction was

a function of the concentration, then a non-linear behaviour would be observed with Γ and w, and this has not been seen. True, the concentrations are weak and large errors are associated with the values of $\beta(0)$, so it is possible that the actual NLO response is not seen and the increase in signal could be due to slowly varying fluctuations in laser power. However, experiments were conducted extremely carefully and repeated several times where similar gradients of Γ versus w were found each time. Furthermore, it seems unlikely, given the good correlation with the solvatochromic experimental evidence, that the EFISH experiments provide erroneous results. Measurements of the evolution of $\beta(0)$ with reaction field (as is conducted with the binary mixture experiment on the transition energy in toluene and acetonitrile) via hyper-Rayleigh scattering experiments are currently underway [263], and the initial results yield some interesting questions. Figure 7.4-2 shows that $\left|\beta(0)\right|$ for DEMI falls to about half the value in toluene, at around about 30 % acetonitrile, which is then followed by a rise to the acetonitrile value. The results are not yet conclusive, but this does show that a minimum in $\left|\beta(0)\right|$ is observed. Furthermore, and perhaps crucially, Figure 7.4-2 shows that $\left|\beta(0)\right|$ does not fall to zero; a phenomenon which has been
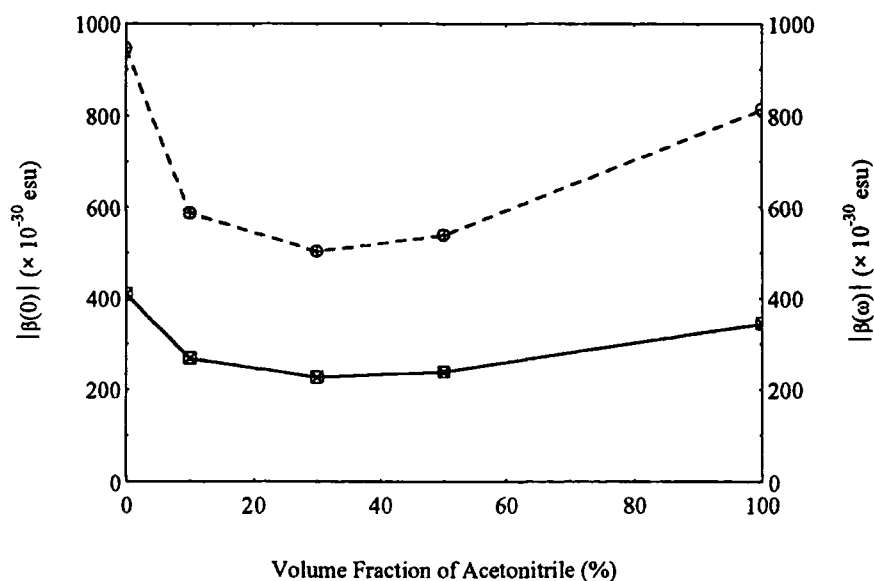
Figure 7.4-2: Evolution of the magnitude of β for DEMI in volume fractions of acetonitrile and toluene.

attributed to incoherent summation of the second harmonic scattered signal due to fluctuations of the reaction field of DEMI in solution [263]. Therefore, the hyper-Rayleigh scattering experiments may provide an over-estimation of $\beta(0)$ when a polar molecule such as DEMI resides close to the cyanine limit. However as indicated, the results are new and are as yet inconclusive, thus it would be difficult to use this for the reason for the discrepancy. Further experimentation is also being conducted to ascertain whether ULTRA evolves in a similar manner.

§7.5 Conclusions

A comparison has been made between experimental measurements of μ, v_{eg} and $\beta(0)$ as a function of reaction field for DEMI to that of SOS calculations. A good correlation has been found with μ which has been calculated using ellipsoidal local fields. However, this is only found if the polarisabilities in such calculations are similar to the SCI variation of the SOS method. If the SD-CI polarisability is used a poor correlation is found with the dipole moment. However, this also intuitively suggests a degree of inconsistency between the two sets of calculations, since they predict similar dipole moments.

On the basis of calculations of the dipole moment using the SCI polarisabilities, the position of the minimum transition energy (i.e. at the cyanine limit) with respect to reaction field agrees well with the SCI calculations. However, the sensitivity of the transition energy to the reaction field is clearly over-estimated, and the magnitude of this energy is also clearly over-estimated. SD-CI data is presently unavailable and it is suggested that such calculations should be obtained.

The SCI estimate of the evolution of $\beta(0)$ does not agree with that of EFISH experiments. However, the SD-CI estimate of $\beta(0)$ does agree with experimental results, though it is acknowledged this agreement is based on different values of polarisabilities used for the calculation of the dipole moment and reaction field. There is also a fairly good correlation with results obtained elsewhere and the SD-CI calculations. It is also noted that the sensitivity of the SOS values of $\beta(0)$ to the

reaction field is large, thus providing a possible reason as to why there are often poor correlations between theory and experiment.

Attempts to correlate results from hyper-Rayleigh scattering experiments have proved unsuccessful. However, there is evidence that the hyperpolarisability is over-estimated at the cyanine limit, due to the fact that the measurement of the evolution of $|\beta(0)|$ for DEMI with reaction field, produces data that does not fall to zero.

Such attempts to compare data have proven to be difficult in the light of local field problems. However, these suggest consistently, that the use of ellipsoidal local field formalisms for the measurement of the dipole moment and reaction field on a molecule, produces a better correlation with the SOS calculations, as would be expected since similar polarisabilities are used in the estimate of the dipole moment.

The presence of two sets of calculations confuses comparisons further due to apparent inconsistencies with the polarisabilities and the position of the cyanine limit. Though it is logical that the SD-CI calculations are more accurate, it would be useful to ascertain if this is true before further comparisons can be made. As indicated, attempts to do this are currently underway, with hyper-Rayleigh scattering experiments on the evolution of $|\beta(0)|$ of DEMI and ULTRA, and it would be useful, despite experimental difficulties, if this could be conducted with EFISH experiments. Then it could be ascertained, quite readily, if any of the theoretical models are correct.

References to Chapter 7.

[258] T. Kogej, M. Malagoli, J.-L. Brédas, G. H. Cross, Private Communications, (1995 - 1997).

[259] D. Gray, Ph.D. Thesis, **University of Durham.**; *Molecular Organic Photonics.*, (1994).

[260] G. H. Cross, M. Szablewski, P. Thomas, Private communications (1994 - 1998).

[261] D. Healy, Ph.D. Thesis, **University of Durham.**; *Solid Solution Studies of the Molecular Non-Linear Optical Properties of Organic Chromophores.*, (1996).

[262] M. Szablewski, P. R. Thomas, A. Thornton, D. Bloor, G. H. Cross, J. M. Cole, J. A. K. Howard, M. Malagoli, F. Meyers, J.-L. Brédas, W Wenseleers, E. Goovaerts, *J. Am. Chem. Soc.*, **119 (13)**, 3144, (1997).

[263] W. Wenseleers, Université of Antwerp-UIA, Belgium, Private Communications, (1997 - 1998).

Summary.

In this thesis, the measurement of the dipole moment, hyperpolarisability and transition frequency of a number of highly polar and polarisable NLO organic chromophores in various solvents, is discussed and compared to similar measurements conducted on NPP. A summary of the results obtained for these materials is given here with indications as to possible avenues for future work.

As discussed in Chapter 3, NPP is a well known material and has been studied extensively. Literature values of the dipole moment, μ (7 to 8 D) and hyperpolarisability, $\beta(0)$ ($\approx 40 \times 10^{-30}$ esu in acetone, 12×10^{-30} esu in 1,4-dioxane) have been obtained. These compare well to the values obtained in this study (μ = 6.9 / 8.3 D, β = 30.3 / 45.2 $\times 10^{-30}$ esu (1.064 μm) in chloroform for spherical and ellipsoidal formalisms respectively). Furthermore, indications of the sign of β for NPP, derived from solvatochromism experiments, agree well with the results obtained from the EFISH experiments in that a positive β is predicted and observed. However, attempts to estimate the value of β for NPP using the solvatochromic data, yielded values that were too low.

The dipole moments of four materials, synthesised at Sheffield Hallam University, were measured in chloroform. The dipole moments of three of the "Sheffield" materials were found to be extremely large (11-18 D (spherical local field)) which serves to confirm the zwitterionic nature of the molecules. In addition, the dipole moment of SHEF D was found to be moderate in chloroform (4.4 D). This is however, large compared to that of a solvent molecule ($\mu \approx 1$ D for chloroform), which has a similar charge-separation distance to that of SHEF D. This further confirms that SHEF D is indeed zwitterionic.

The dipole moments for DED (measured in chloroform) and the three tertiary amino TCNQ adducts (measured in DCM) were also obtained. The dipole moments

for these chromophores were also found to be extremely large (14 - 23 D (spherical formalism), 19 - 33 D (ellipsoidal formalism)). These were far higher than that obtained for NPP (up to five times higher for DEMI) and slightly higher than those possessed by three of the "Sheffield" materials. Once again, the high dipole moments serve to indicate the zwitterionic nature of the tertiary amino TCNQ adducts. It was noted that the dipole moment calculated using the ellipsoidal local field formalism for DEMI (15 D gas phase) agreed remarkably well with the results of 40-state SOS calculations for DEMI, which predicts a dipole moment in the gas phase of 14 D. The dipole moment for DED, measured in solution (20 D ellipsoidal formalism), is also in agreement with experimental measurements conducted on DED in the crystal phase (26 D).

With EFISH experiments, calibration of the solvents, and the glass windows involved with the experiment, yielded good agreements with the results obtained from the literature. One is thus lead to believe that the experiment works reasonably well. This is further confirmed by the good agreement of $\beta(0)$ for NPP, measured here, with that obtained from the literature.

Measurements of $\mu\beta(0)$ for DED yielded a $\beta(0)$ value which was only slightly higher than that of NPP ($-55 / -93 \times 10^{-30}$ esu (spherical / ellipsoidal) in chloroform at 1.064 μm), but it was noted that the magnitude of $\mu\beta(0)$ was five times higher than the magnitude of $\mu\beta(0)$ obtained for NPP. Measurements of $\beta(0)$ for DED in DCM yielded lower values than those in chloroform, but it was noted that a deviation in linearity with the Γ versus w graph was evident. This was attributed to the fact that at stronger concentrations a finite absorption at 532 nm reduces the second harmonic signal produced. Thus, the $\beta(0)$ value for DED in DCM is erroneous. However, the sign of $\beta(0)$ obtained for DED in both chloroform and DCM again agrees with the sign predicted by solvatochromism experiments where a hypsochromic (negative) shift in transition energy was observed. Once again, attempts to measure the value of $\beta(0)$ from the solvatochromic data proved unsuccessful where the calculated $\beta(0)$ is far lower than the EFISH value.

The values of $\beta(0)$ for the tertiary amino TCNQ adducts measured at 1.064 µm were found to be erroneous, since the sign of $\beta(0)$ at 1.064 µm did not agree with the sign of $\beta(0)$ obtained at 1.907 µm. This was attributed to the fact that the absorption intensity at 532 nm is large, thus the second harmonic signal is overcome by the absorption at the concentration of measurement. Nonetheless, the 1.064 µm EFISH experiments on the tertiary amino TCNQ adducts served to demonstrate anomalous dispersion phase matching. The coherence length was found not to decrease, as is usually found with EFISH experiments conducted away from resonance, but to increase with increasing solute concentration. This was attributed to the fact that at 532 nm the refractive index of the solution at 2ω is increasing slower than the refractive index of the solution at ω, due to the anomalous dispersion of the refractive index at 2ω. Thus, it would be possible, by increasing the concentration of the solute accordingly, to obtain a perfectly phase matched solution, providing the solubility and NLO response of the chromophore is large enough to observe such an effect.

The hyperpolarisabilities for the tertiary amino TCNQ adducts measured at 1.907 µm in chloroform or DCM were all found to be extremely low, though again it is noted that the magnitude of the $\mu\beta(0)$ products were equivalent or higher than the magnitude of $\mu\beta(0)$ for NPP (see Tables 5.6-1 and 5.6-2). Furthermore, the sign of $\beta(0)$ varied for the same chromophore, depending on the solvent of measurement. The low values of $\beta(0)$ for the tertiary amino TCNQ adducts were attributed to the fact that the geometry of the tertiary amino TCNQ adducts are such that they reside close to the cyanine limit in chloroform and DCM. The results of solvatochromism experimentation produces encouraging signs for this hypothesis. Reversals in the shift of the transition frequencies of the tertiary amino TCNQ adducts were found when plotted versus the $E_N^T(30)$ solvent polarity scale. Furthermore, similar behaviour is exhibited through the measurement of the extinction coefficient of the absorption band for ULTRA in various solvent media. This reversal is similar to that exhibited by merocyanine dyes, and it is indicative that the geometry of the tertiary amino TCNQ adducts crosses the cyanine limit as the polarity of the molecular environment increases. This agrees well with the results of theoretical calculations on the tertiary

amino TCNQ adducts (see Chapter 3). Furthermore, the transition frequencies of the tertiary amino TCNQ adducts in chloroform and DCM are such that they lie close to the minimum transition frequency, i.e. the geometries of the tertiary amino TCNQ adducts are close to the cyanine limit in these solvents. Therefore the low value of $\beta(0)$ measured through EFISH is confirmed through solvatochromic analysis since β is expected to be zero at the cyanine limit.

From the positions of the cyanine limit with respect to each other, and the values of $\beta(0)$ with respect to each other, the order of aromaticity for the tertiary amino TCNQ adducts could be confirmed (DCH<DEMI<ULTRA). Furthermore it is also postulated that DED is more aromatic than any of the tertiary amino TCNQ adducts since no reversal of the transition energy shift is observed for DED and that it is negative. This agrees with the conclusions made from studies of these materials in the crystal phase.

Attempts to accurately estimate the position of the cyanine limit with respect to the reaction field of the tertiary amino TCNQ adducts have been made via solvatochromism experiments conducted with binary mixtures of toluene and acetonitrile. The minimum in transition frequency was found to occur at low volume fractions of acetonitrile (8-10 % acetonitrile), and the order of aromaticity predicted from these results agrees with the conclusions made earlier. It is noted that at the cyanine limit, the excited state dipole moment is equal to the ground state dipole moment, since β, and subsequently $\Delta\mu$, is zero. Thus, attempts to measure the excited state dipole moment were made by estimating the value of the dipole moment at the cyanine limit via the measurements of the ground state gas phase dipole moments conducted earlier. The subsequent excited state dipole moments of the tertiary amino TCNQ adducts were found to be similar in magnitude to the ground state solution phase dipole moments measured in DCM, further confirming that the geometry of the tertiary amino TCNQ adducts lies close to the cyanine limit in these solvents. It was further postulated that $\Delta\mu$ and consequently $\beta(0)$ could be estimated in the gas phase, providing the excited state dipole moment stays constant. It was further postulated that the error due to changes in the value of the excited state dipole moment is only

around 10 - 20 %. Subsequent calculations of $\beta(0)$ for the tertiary amino TCNQ adducts yielded positive values that were not unlikely for these molecules in the gas phase. The $\beta(0)$ values were lower than the values of $\beta(0)$ predicted by 40-state SOS calculations on the tertiary amino TCNQ adducts, but nonetheless these served as a good first approximation to obtaining a value of β.

Comparisons of the experimentally determined dipole moment of DEMI to the 40-state SOS calculated dipole moment reveal that measurements of the dipole moment, calculated using ellipsoidal formalisms allow for better correlations than if spherical formalisms were used to calculate the dipole moment. This was to be expected to a degree, since both the theoretical calculations and the ellipsoidal formalisms utilise the polarisability tensor which is higher than the average polarisability utilised for the spherical formalisms. Further comparisons revealed a good agreement between the values of the ground state dipole moment for DEMI, measured in this study, and the theoretical calculations. Furthermore, this meant that an agreement was also made with respect to the positions of the cyanine limit as a function of the reaction field for DEMI. Correlations with the hyperpolarisability, measured in this study, and that of the theoretical calculations, revealed that the theoretical evolution of β is extremely sensitive to reaction field. This allows for poor correlations obtained previously elsewhere. In addition, inconsistencies between sets of theoretical calculations and between different molecular parameters (for example the point where $\beta = 0$ does not coincide with the transition frequency minima) inhibits comparisons further. Nonetheless, there appears to be a good agreement between the EFISH results presented here, and the SD-CI SOS calculations (see Chapters 3 and 7).

It was also noted that $|\beta(0)|$ for DEMI obtained from EFISH experiments in chloroform at 1.907 μm (30×10^{-30} esu) does not agree with $|\beta(0)|$ obtained from hyper-Rayleigh scattering (HRS) experiments conducted on DEMI also in chloroform (350×10^{-30} esu). In view of the above arguments for the position of the cyanine limit of the tertiary amino TCNQ adducts and the subsequent low values of $\beta(0)$ measured, the HRS result appears to be over-estimated. This is perhaps further confirmed by

additional HRS experimentation which has been conducted elsewhere on DEMI in binary mixtures of toluene and acetonitrile. Though $|\beta(0)|$ was found to fall significantly and then rise with higher volume fractions of acetonitrile as expected, $|\beta(0)|$ did not fall to zero, which was extremely surprising. The experiments are yet to be fully confirmed and are still ongoing, however this significantly explains the discrepancy between the EFISH results and the HRS measurement. Further HRS experimentation is being conducted upon ULTRA and it will be interesting to see if similar results are yielded.

Comparisons should therefore be made between HRS experiments and EFISH experiments. Experimental difficulties are significant with EFISH, such as low solubility and degradation of high dielectric constant solvents under the influence of high intensity static electric fields, which is why such experiments using higher dielectric solvents have not been conducted thus far. However, the enhanced solubility of ULTRA at least lends itself to the possibility that EFISH experiments could be conducted on ULTRA in mixed media, and it is possible for other experimental difficulties to be overcome, by pacifying electrodes. The reason why $|\beta(0)|$ for DEMI does not reduce to zero with the HRS experiments has been attributed to random fluctuations of the solvent media inducing fluctuations in the reaction field of DEMI which are subsequently measured by the HRS technique. These fluctuations would not be measured using EFISH since the signal from EFISH experiments is coherently summed. Comparisons of the two experiments in the same media would confirm this hypothesis conclusively.

The molecular properties of the tertiary amino TCNQ adducts and their subsequent evolution are extremely novel. Extensive literature searches have revealed only a few materials that exhibit similar reversals in the shift of the transition frequency, thus exhibiting a crossover from quinoidal tendencies to aromatic tendencies. Furthermore, the dipole moment is extremely large in comparison to organic molecules of similar size. As a result the tertiary amino TCNQ adducts have the potential to enhance our understanding of how such highly dipolar molecules behave under the

influence of electric fields in various media. It is suggested that further solvatochromic experiments utilising a number of different binary mixtures should therefore be conducted.

Finally, such experiments may tell us how the solvents interact with the solute molecules as well as how the geometry of the solute evolves with increasing solvent polarity. The origin of the second absorption band associated with the absorption spectra of the tertiary amino TCNQ adducts has not been attributed, and attempts to associate the band to various phenomena pertaining to the chromophores, have as yet proved inconclusive. Solvatochromic experiments conducted in binary mixtures of associating solvents may reveal a possible answer. The presence or lack of an isosbestic point on the absorption band may infer or eliminate the possibility that the band is a consequence of inter-molecular interactions.

Appendix I

Computer Programs.

Several computer programs have been developed to allow relatively easy collection and analysis of experimental data obtained from EFISH and dipole moment experiments. In this appendix these computer programs are described.

A1.1 EFISH Experiments.

The programs used to collect the data and write it to a file have previously been developed [264] and will not be shown here. The resulting experimental data is left in the form of a text file consisting of three columns of data representing the translation distance, the second harmonic signal, and the normalised signal. The analysis only requires the use of the normalised signal (the last column) thus the middle column may be discarded by inserting the program into various spreadsheet packages [265] and re-saving as a text file ensuring that any text headers are removed.

To analyse the fringes, a non-linear regressional analysis program [266] is employed in conjunction with a small control program shown below. The control program was developed using a standard text editor and saved in text format:

Title "Maker Fringe Fitting Program";

// This program finds the amplitude, offset, frequency and phase of the maker fringes;

Angletype Radians;

Variables l, Intensity;

Parameter Offset, Amplitude, Frequency, Phase;

Sweep Frequency=1.0,2.6,0.2;

Function Intensity=Offset+Amplitude*(Sin(Frequency*l+Phase))^2;

Plot Grid, Title="Maker Fringes", Xlabel="Distance (mm)", Ylabel="Normalised Intensity";
Rplot;
Nplot;
Poutput "c:/dir1/dir2/..../file.dat";
Output To "c:/dir1/dir2/..../file.out" l, Intensity, Predicted;

Data "c:/dir1/dir2/...../file.txt";

The control program is designed to fit the function which is described by (5.4-1) in §5 using the "Function" command in the program. To ensure that the best fit is found, several initial frequencies are tried through the "Sweep" function. Upon convergence, the "Amplitude", "Frequency", "Phase" and "Offset" "Parameters" are calculated and stored in a data file (file.dat) via the "Poutput" command. The "Plot" command allows a graph of the fit to be displayed on screen. This is also sent to a file (file.out) via the "Output" command. Finally, the "Data" command specifies where the data file (file.txt) can be found.

Once the Maker fringe fitting is complete, the amplitude, frequency and offset of the fringes may then be used to calculate Γ_L, and the coherence length, l_c. For this purpose a dedicated mathematical analysis program has been utilised [267] in conjunction with several subprograms shown below.

First the coherence length and the average height of the fringes must be calculated, taking into account any neutral density filters in the signal arm and the ratio of the boxcar sensitivities between the solution experiment and the corresponding quartz experiment:

(*This part of the program finds the average intensity, a_m and the coherence length, l_c from the Amplitude, Offset, and Frequency obtained from the fitting program*)

```
nd=0;                      (*Neutral density value in signal arm*)
angle=2.5*3.14159/180;     (*Wedge angle (radians)*)
a1=0.59529;                (*Amplitude*)
a2=0.05424;                (*Offset*)
frequency=1.29744;         (*Frequency*)
r=5/5;                     (*Ratio of sensitivities quartz/solution*)

a3=3.1459/(2*frequency);
lc=a3*Tan[angle];          (*Coherence length*)
am=(a1/2+a2)*(10^nd)*r;    (*Average intensity*)

Print["*****************************************"]
Print["Coherence Length = ",lc*10^3, " microns"]
Print["Average Intensity = ",am]
Print["*****************************************"]
```

Once this is completed, the coherence lengths and average intensities for glass, quartz and each solution may be used in the next program to calculate the corresponding Γ_L's. The appropriate optical and electrical constants are provided in §5.4:

(*This part of the program calculates Γ from the average intensities and coherence lengths calculated above.*)

```
eps0=8.85 10^-12;          (*Permittivity of free space, F m^-1*)
wlngth=1.064;              (*Wavlength (μm)*)
e0=2.5*10^3/(299.8*0.2);   (*Electric field (statvolts cm^-1)*)
x1=0.3;                    (*Path length before wedge (cm)*)
x2=0.2;                    (*Path length across wedge (cm)*)
x3=0.3;                    (*Path length after wedge (cm)*)
```

(*Glass parameters*)

lcg=20.56;   (*Glass coherence length (μm)*)

ng2w=1.519;   (*Refractive index, 2ω*)

ngw=1.50699;   (*Refractive index, ω*)

gammag=3.8*10^-14;   (*Γ of BK7 Glass (esu)*)

(*Quartz parameters*)

lcq=20.9;   (*Coherence length for quartz (μm)*)

amq=5230;   (Average fringe height for Quartz*)

nq2w=1.54702;   (*Refractive index, 2ω*)

nqw=1.53413;   (*Refractive index, ω*)

d11=1.2*10^-9;   (*d_{11} coefficient for quartz (esu)*)

(*Fresnel factors for quartz*)

q1=(2*nq2w/(nq2w+1))*((nqw+1)/(nq2w+1))*(1/(nq2w+nqw))*((2/(nqw+1))^2);
q2=((nq2w+nqw)/(nq2w+1))*(1/(nq2w+nqw))*((2/(nqw+1))^2);

(*Solution parameters*)

lcl=22.2;   (*Coherence length (μm)*)

aml=.1102;   (*Average intensity*)

nl2w=1.447;   (*Refractive index, 2ω*)

nlw=nl2w-wlngth/(4*lcl);   (*Refractive index, ω*)

alphw=0.0;   (*Absorption at ω (cm^{-1})*)

alph2w=0.0;   (*Absorption at 2ω (cm^{-1})*)

(*Fresnel factors for solution*)

tpw=2*ngw/(ngw+nlw);

tw=2/(1+ngw);

ta2w=2*ng2w/(1+ng2w);

t1=ta2w*tw^2*(1/(ng2w+ngw))*((ngw+nl2w)/(ng2w+nl2w));

t2=ta2w*tw^2*tpw^2*(1/(nl2w+nlw))*((nlw+nl2w)/(ng2w+nl2w));

(*Calculation of Γ_L*)

fx=(Exp[-2*alphw*x2]+Exp[-alph2w*x2])*Exp[-alph2w*x3]*Exp[-2*alphw*x1];
gammal=1/(t2*lcl)*Sqrt[((-t1*gammag*lcg+
((aml/amq)*((q1^2)+(q2^2))*(d11^2)*(lcq)^2/((e0^2)*fx))^(0.5)))^2];

Print["**"]
Print["gamma = ", gammal," esu"]
Print["**"]

This program may modified for the calculation of Γ_G by inserting equation (5.4-4) and the related Fresnel factors shown in §5.4 into the appropriate sections above.

To calculate $\mu\beta(\omega)$ from the gradient of Γ_L versus weight fraction, another program was developed as shown below. For this part, the gradients of the graphs obtained from the dipole moment experiments and the corresponding dipole moments are required. In addition if available, the change in refractive index with weight fraction and change in specific volume should also be used, but these are not essential as their neglect produces only a small error in the final calculation. Several local field variations are possible and are obtained by inter-changing the equations under the reaction field factor section:

(*This part of the equation calculates the final gamma for the solute by knowing the solvent Γ, and the gradient, $\partial\Gamma/\partial w$ from the Γ - weight fraction graph, and $\partial\varepsilon/\partial w$ from the dielectric data*)

na=6.022045 10^23;   (*Avogadro's number (mol^{-1})*)
lcl=24.0;   (*Coherence length of the solvent*)
wlngth=1.064;   (*Wavelength (μm)*)
nw=n2w-wlngth/(4*lcl);   (*Refractive index at frequency ω*)
n2w=1.447;   (*Refractive index at frequency 2ω*)

e1=4.3;	(*Dielectric constant of solvent*)
gamma1=6.0*10^-14;	(*Γ of the solvent (esu)*)
mw=296.4;	(*Molecular weight of solute (g mol^{-1})*)
d=1.31678;	(*Density of solvent (g cm^{-3})*)
mu=18.2*10^-18;	(*Dipole moment (esu)*)
k=1.38*10^-16;	(*Boltzmans constant (esu)*)
t=296;	(*Temperature (K)*)

(*Solution gradients*)

dgamdw=-1.34*10^-11;	(*Gradient from EFISH graph (esu)*)
dedc=64100;	(*Dielectric constant with concentration (cm^3 mol^{-1})*)
dedw=d/mw*dedc;	(*Dielectric constant with weight fraction*)
vol1=1/d;	(*The specific volume (cm^3 g^{-1}*)
dvoldw=0;	(*Change in specific volume*)
dn2dw=0;	(*Change in square of refractive index*)

(*The reaction field factors*)

f1sph=81*mw/((e1+2)*(nw^2+2)^3);

f2sph=(2*e1+nw^2)*(2*nw^2+n2w^2)^3*mw/((n2w^2+2)^4*nw^6*e1);

f3sph=27*mw*(nw^2+2*e1)/(e1*(nw^2+2)^3*(n2w^2+2));

fell=27*mw*(e1+(n2w^2-e1)*along)/(e1*(1-(n2w^2-1)*along)*(nw^2+2)^3);

along=0.1027;

nfac1=3/(nw^2+2);

epsfac1=1/(e1+2);

nfac2=1/(nw^2);

epsfac2=1/e1-2/(2*e1+nw^2);

(*Calculation of $\mu\beta$*)

(*For Debye factors use; f1sph, nfac1, and epsfac1*)

(*For pure Onsager factors; use f2sph, nfac2 and epsfac2*)

(*For mixed Lorentz/Onsager factors; use f3sph, nfac1, and epsfac2*)

(*For ellipsoidal factors; use fell, nfac1 and epsfac2*)

```
a=EngineeringForm[
gamma2=f3sph*((vol1*dgamdw)+(gamma1*dvoldw)+(vol1*gamma1)
-vol1*gamma1*(nfac1*dn2dw+epsfac2*dedw))/na];


b=EngineeringForm[mubeta=gamma2*5*k*t];


c=EngineeringForm[beta=mubeta/mu];


Print["***************************************"]
Print["mu*beta = ", b," esu"]
Print["***************************************"]
Print["beta = ", c," esu"]
Print["***************************************"]
```

Finally, to calculate the value of β at zero frequency using the two-level model described in §5.6, the following program may be used:

(*This part of the program calculates $\beta(0)$*)

```
v=2.998*10^8;               (*Speed of light (m s^{-1})*)
lambdamax=474*10^-9;        (*$\lambda_{max}$ (m)*)
wavelength=1.064*10^-6;     (*Wavelength (m)*)
betaw=-389.6*10^-30;        (*$\beta(\omega)$ (esu)*)
mu=33*10^-18;               (*$\mu$ (esu)*)
```

(*Conversion to angular frequencies*)

```
w=v/(2*3.1415*wavelength);
weg=v/(2*3.1415*lambdamax);
```

(*Calculation of $\beta(0)$*)

```
a=EngineeringForm[beta0=betaw*(1-(w^2/(weg^2)))*((1-4*(w^2)/(weg^2)))];
```

```
b=EngineeringForm[mu*beta0];

Print["****************************************"]
Print["beta0 = ", a," esu"]
Print["****************************************"]
Print["mu*beta = ", b," esu"]
Print["****************************************"]
```

A1.2 Dipole Moment Experiments.

The following programs are used in conjunction with Mathematica [267] to calculate dipole moments using various local fields. First using Debye local fields:

(*Guggenhiems equation for dipole moment*)

```
k=1.38 10^-16;              (*Boltzmans constant (*ergs K⁻¹*)
t=295;                      (*Temperature (K)*)
e1=4.8;                     (*Dielectric constant of solvent*)
n1=1.436;                   (*Refractive index of solvent*)
grad=31400;                 (*Gradient ∂ε/∂C (mols cm⁻³)*)
na=6.022 10^23;             (*Avogadro's number*)
```

(*Calculation of the μ*)

```
u=(10^36*9*k*t/(na*4*Pi)*3/((e1+2)*(n1^2+2))*grad)^0.5;

Print["guggenhiems dipole moment = ",u," Debyes"]
```

Secondly, using Onsager's local fields. As is explained in §4.4, the average polarisability and molecular semi-axes are needed for this calculation in conjunction with the experimental results.

(*Programme to determine dipole moments using Onsager local fields.*)

Slope=38000;   (*Gradient $\partial\varepsilon/\partial C$ (mols cm^{-3})*)

eps1=4.8;   (*Dielectric constant of solvent*)

aav=45;   (* Average Polarisability *)

kT=4.1*10^-21;   (*Boltzmans constant times Temperature (J)*)

slo=Slope*10^-6/(6.023*10^23);   (* Convert Slope to SI Units (m^{-3})*)

a=9.5;   (*1/2 molecule length (Å)*)

b=3.1;   (*1/2 molecule width (Å)*)

c=2.2;   (*1/2 molecule thickness (Å)*)

r=(a*b*c)^(1/3);

Print["r= ",r]

(* Reaction Field Factors *)

fsph=(1/(r^3))*(2*eps1-2)/(2*eps1+1);

(* Spherical Cavity Field correction factor *)

Gsph=((3*eps1)/(2*eps1+1))*(1/(1-fsph*aav));

(*Calculation of Dipole Moments*)

musol=Sqrt[(slo-Gsph*aav*10^-30)3*kT*8.854*10^-12/Gsph]/(3.336*10^-30);

Print["usol = ", musol, " D"]

mugas=(1-fsph*aav)*musol;

Print["ug =", mugas, " D"]

(*Calculation of reaction field*)

react=fsph*musol*0.0583;

Print["reation field = ",react]

Finally, for the calculation of dipole moments using ellipsoidal local fields, the next computer program is utilised. This time the polarisability along the major axis and the molecular semi-axes lengths are required:

(*Programme to Determine Solution State Dipole Moments *)

```
Slope=38000; `              (*Gradient ∂ε/∂C (mols cm⁻³)*)

eps1=4.8;                   (*Dielectric constant of solvent*)

kT=4.07295*10^-21;          (*Boltzmans constant times Temperature (J)*)

a1=100;                     (* Dipole axis polarisability (Å³)*)

aav=45;                     (* Average Polarisability (Å³)*)

slo=Slope*10^-6/(6.023*10^23);  (* Convert Slope to Correct Units *)
```

(* Determine Scholte Ellipsoidal Integrals *)

```
a=8.0;                      (*1/2 molecule length (Å)*)

b=3.6;                      (*1/2 molecule width (Å)*)

c=1.9;                      (*1/2 molecule thickness (Å)*)

r=(a*b*c)^(1/3);

Print["r= ",r," Angstroms"]


x2=(s+a^2)^(3/2);

y1=(s+b^2)^(1/2);

z1=(s+c^2)^(1/2);

m1=x2*y1*z1;

Along=((a*b*c)/2)*NIntegrate[1/m1, {s,0,Infinity}];

Print["Along = ", Along]
```

(* Reaction Field Factors *)

```
flong=(3/(r^3))*Along*(1-Along)*(eps1-1)/(eps1+(1-eps1)*Along);

fsph=(1/(r^3))*(2*eps1-2)/(2*eps1+1);
```

(* Ellipsoidal Cavity Field Correction Factor*)

Gell=(eps1/(eps1+(1-eps1)*Along))*(1/(1-flong*a1));

(* Spherical Cavity Field correction factor *)

Gsph=((3*eps1)/(2*eps1+1))*(1/(1-fsph*aav));

(*Calculate dipole moments*)

musol=Sqrt[(slo-Gell*a1*10^-30)*3*kT*8.854*10^(-12)/Gell]/(3.336*10^-30);
Print["usol = ", musol, " D"]

mugas=(1-flong*a1)*musol;
Print["ug =", mugas, " D"]

(*Calculate reaction field*)

react=flong*musol*0.0583;
Print["reation field = ",react," AU"]

References to Appendix I.

[264] D. Gray, Ph.D. Thesis, **University of Durham**; *Molecular Organic Photonics.*, (1994).

[265] *Lotus 123*, Release **4.01**, Lotus Development Corporation, 1993; *EasyPlot*, Version **3.00 - 5**, Spiral Software and MIT., 1989 - 1995.

[266] *NLREG*, Version **3.0** (Shareware Version), P. H. Sherrod, 1992 - 1995.

[267] *Mathematica*, Version **2.2**, Wolfram Research Inc., 1993.

Appendix II

Description of the Second Harmonic Waves and Boundary Conditions in Non-Linear Media.

In the following sections, the equations describing the second harmonic, bound and free wave field amplitudes (Chapter 5, (5.3-6) and (5.3-7)) will be derived, where a description of the boundary conditions in the EFISH cell is also given [268, 269, 270]. The derivations of the bound and free wave amplitudes for the specific case of the solution wedge in the EFISH cell the are also given.

AII.1 The Bound Wave.

The non-linear wave equation, defined in §1.3, may be written for the spatially varying second harmonic electric field, $E^{2\omega}(z)$ as [269, 271]

$$\frac{\partial^2 E^{2\omega}}{\partial z^2} + \alpha_{2\omega}\frac{\partial E^{2\omega}}{\partial z} + k_f^2 E^{2\omega} = -\frac{16\pi\omega^2}{c^2}d_{\mathit{eff}}(z)\left[E^{\omega}(z)\right]^2 e^{ik_b z},$$

AII- 1

where $k_f = 2\omega n_{2\omega}/c$, and $k_b = 2\omega n_{\omega}/c$ are the free wave vectors of the second harmonic free and bound waves, respectively, $\alpha_{2\omega}$ is the absorption coefficient at the second harmonic frequency, and $d_{\mathit{eff}}(z)$ is the spatially varying induced non-linear coefficient of the medium. The solution of AII- 1 is the sum of the free wave

217

amplitude, E_f and bound wave amplitude, $E_b(z)$ which will vary because of the spatial variation of the non-linear polarisation;

$$E^{2\omega}(z) = E_f e^{-\alpha_{2\omega}/2} e^{ik_f z} + E_b(z) e^{ik_b z}.$$

<div align="right">AII- 2</div>

Assuming no initial free wave, substitution of AII- 2 into AII- 1 yields the equation for $E_b(z)$

$$\frac{\partial^2 E_b(z)}{\partial z^2} + (\alpha_{2\omega} + 2ik_b)\frac{\partial E_b(z)}{\partial z} + (k_f^2 - k_b^2 + ik_b\alpha_{2\omega})E_b(z) = -\frac{16\pi\omega^2}{c^2}d_{e\!f\!f}(z)[E^\omega(z)]^2.$$

<div align="right">AII- 3</div>

The inter-electrode distance is far larger than the coherence length $(l_c = \pi/|k_f - k_b| = \pi/\Delta k)$, thus the fringing of the static electric field induces a smooth variation in $d_{e\!f\!f}(z)$. The slowly varying amplitude approximation may then be considered so that [269]

$$\left|\frac{\partial^2 E_b(z)}{\partial z^2}\right| << \left|(\alpha_{2\omega} + 2ik_b)\frac{\partial E_b(z)}{\partial z}\right| << \left|(k_f^2 - k_b^2 + ik_b\alpha_{2\omega})E_b(z)\right|,$$

<div align="right">AII- 4</div>

then

$$E_b(z) = \frac{-16\pi\omega^2}{c^2(k_f^2 - k_b^2 + ik_b\alpha_{2\omega})}d_{e\!f\!f}(z)[E^\omega(z)]^2.$$

<div align="right">AII- 5</div>

Equation AII- 5 may be simplified further if $\alpha_{2\omega}$ is small compared to Δk, which is always the case for absorption coefficients less than 100 cm^{-1} [268]

$$E_b(z) = \frac{-4\pi}{n_{2\omega}^2 - n_\omega^2}d_{e\!f\!f}(z)[E^\omega(z)]^2,$$

<div align="right">AII- 6</div>

so (5.3-6) in Chapter 5 is thus obtained.

AII.2 Boundary Conditions.

In each part of the cell where second harmonic light is generated, the fundamental wave is accompanied by a second harmonic bound wave which is proportional to the non-linear polarisation as described in AII-1. At each boundary, a transmitted and reflected second harmonic free wave will be created, where the amplitudes may be calculated by considering the boundary conditions for the second harmonic electric and magnetic fields, $E_{2\omega}$ and $H_{2\omega}$ respectively.

Considering the general case of a boundary between two media, 1 and 2 respectively, in medium 1 the second harmonic waves are a free wave, $E_f^{(1)}$, a bound wave, $E_b^{(1)}$ and a reflected free wave, E_R so that

$$E^{2\omega}(z) = E_f^{(1)} e^{i\theta_f} + E_b^{(1)} e^{i\theta_b} + E_R e^{i\theta_f},$$

AII- 7

where

$$\theta_f = \left(k_f + i\frac{\alpha_{2\omega}}{2}\right)z, \quad \theta_b = (k_b + i\alpha_\omega)z,$$

AII- 8

and α_ω, $\alpha_{2\omega}$, k_f and k_b refer to medium 1. Note for completeness, the absorption at ω is also included. Since the wedge angle is small (no more than 10°), continuity relations of the E and H field parallel to the interface can be observed, thus leading to [270]

$$E_f^{(1)} e^{i\theta_f} + E_b^{(1)}(z)e^{i\theta_b} + E_R^{(1)} e^{-i\theta_f} = E_f^{(2)} e^{i\theta_f} + E_b^{(2)}(z)e^{i\theta_b} + E_R^{(2)} e^{-i\theta_f}$$

$$n_{2\omega}^{(1)} E_f^{(1)} e^{i\theta_f} + n_\omega^{(1)} E_b^{(1)}(z)e^{i\theta_b} - n_{2\omega}^{(1)} E_R e^{-i\theta_f} = n_{2\omega}^{(2)} E_f^{(2)} e^{i\theta_f} + n_\omega^{(2)} E_b^{(2)}(z)e^{i\theta_b} - n_{2\omega}^{(2)} E_R^{(2)} e^{-i\theta_f}$$

AII- 9

where $z = z_0$ at the interface. It is assumed that $E_R^{(2)}$ can be omitted from the two equations in AII- 9 since multiple reflections are neglected for a finite wedge angle [268, 270]. Also, the assumption that θ_f and θ_b are identical in media 1 and 2 is in error with the physical situation, though the final results remain unchanged with the specific case [270]. Eliminating $E_R^{(2)}$ from AII- 9 yields

$$E_f^{(2)}e^{i\theta_f} = t_{2\omega}E_f^{(1)}e^{i\theta_f} + \left[T_1 E_b^{(1)} - T_2 E_b^{(2)}\right]e^{i\theta_b},$$

AII- 10

thus obtaining (5.5-7) in Chapter 5, where

$$T_1 = \frac{n_\omega^{(1)} + n_{2\omega}^{(1)}}{n_{2\omega}^{(1)} + n_{2\omega}^{(2)}}, \quad T_2 = \frac{n_{2\omega}^{(1)} + n_\omega^{(2)}}{n_{2\omega}^{(1)} + n_{2\omega}^{(2)}},$$

AII- 11

and [272]

$$t_{2\omega} = \frac{2n_{2\omega}^{(1)}}{\left(n_{2\omega}^{(1)} + n_{2\omega}^{(2)}\right)}.$$

AII- 12

AII.3 The Second Harmonic Wave in an EFISH Cell.

As mentioned in Chapter 5, the analysis of the second harmonic wave throughout the region concerning the electrodes is identical to that of Oudar's [270]. Considering Figure 5.3-1 in Chapter 5, at position 3 there is no incident free wave and the two bound waves for the glass (G) and solution media (L) are

$$E_b^{G'} = \frac{4\pi}{\left(n_{2\omega}^G\right)^2 - \left(n_\omega^G\right)^2}\Gamma_G E_0\left(E^\omega(3)\right)^2 = \left(t_L^\omega t_G^\omega\right)^2 e^{-\alpha_\omega x_1}E_b^G$$

$$E_b^{L'} = \frac{4\pi}{\left(n_{2\omega}^L\right)^2 - \left(n_\omega^L\right)^2}\Gamma_L E_0\left(t_G^\omega E^\omega(3)\right)^2 = \left(t_L^\omega t_G^\omega\right)^2 e^{-\alpha_\omega x_1}E_b^L$$

AII- 13

as described by the equations in (5.3-10), Chapter 5. Using AII- 10 the free wave created at position 3 is thus

$$E_f^L = T_1 E_b^{G'} - T_2 E_b^{L'},$$

<div align="right">AII- 14</div>

where T_1 and T_2 are described by AII- 11 for the glass (1) and solution (2) media respectively. Just before position 4 in Figure 5.3-1, the free wave is

$$E_f(4) = E_f^L e^{i(k_f + i(\alpha_{2\omega}/2))x_2},$$

<div align="right">AII- 15</div>

where x_2 is the path length between the glass windows. The two bound waves created at position 4 are now

$$E_b^{(1)}(4) = E_b^{L'}$$
$$E_b^{(2)}(4) = \left(t_G^\omega t_L^\omega\right)^2 E_b^{G''}$$

<div align="right">AII- 16</div>

where t_L^ω is given by equation (5.3-5) in Chapter 5. Therefore, the total free wave after position 4 is thus

$$E_f^G e^{i\theta_f} = t_L^{2\omega} E_f^L e^{i\theta_f} + \left[T_L E_b^{L'} - T_G \left(t_G^\omega t_L^\omega\right)^2 E_b^{G'} \right] e^{i\theta_b}$$

<div align="right">AII- 17</div>

where $t_L^{2\omega}$ is the same as (5.3-5) except that the refractive indices are measured at 2ω, and T_L and T_G are described by AII- 11 for the solution (1) and glass (2) media respectively.

As already indicated in Chapter 5, the product of the Fresnel factor, $t_G^\omega t_L^\omega$ is close to unity, so these factors may be dropped. Furthermore, since the refractive index of the liquid and glass media differ by no more than 15 %, the same argument may be applied to some of the other coefficients, namely

<div align="center">221</div>

$$T_1 t_L^{2\omega} \approx T_G$$
$$T_2 t_L^{2\omega} \approx T_L$$

AII- 18

Thus, with the aid of these assumptions and AII- 14, after transmission through interface 5, AII- 17 becomes

$$E_f^{2\omega} = t_G^{2\omega} \left[T_G E_b^{G'} - T_L E_b^{L'} \right] \left(e^{i\theta_f} + e^{i\theta_b} \right)$$

AII- 19

as is given by equations (5.3-9) and (5.3-10) in Chapter 5.

References for Appendix II.

[268] J. L. Oudar, *J. Chem. Phys.*, **67 (2)**, 446, (1977).

[269] R. W. Boyd, *Non-Linear Optics*, Academic Press Inc., London, (1992).

[270] F. Kajzar, I Ledoux, J. Zyss, *Phys. Rev. A*, **36 (5)**, 2210, (1987).

[271] J. Jerphagnon, S. K. Kurtz, *J. Appl. Phys.*, **41 (4)**, 1667, (1970).

[272] E. Hecht, *Optics*, **2nd Ed.**, Addison-Wesley Publishing, Wokingham, England, (1987)

Appendix III

Systems of Units and Conversion Factors.

Throughout this study a variety of different unit systems are used for non-linear optical and other parameters. This appendix is intended to remove any confusion over the magnitude of these parameters by converting them to the MKS system and using the numerical factors below.

In the Gaussian system of units (CGS), the polarisation of a bulk media, $\mathbf{P}(t)$ is related to the electric field strength, $\mathbf{E}(t)$ by [273]

$$\mathbf{P}(t) = \mathbf{P}_0 + \chi^{(1)}\mathbf{E}(t) + \chi^{(2)}\mathbf{E}^2(t) + \chi^{(3)}\mathbf{E}^3(t) + \ldots,$$

AIII- 1

where the units of $\mathbf{P}(t)$, $\mathbf{P}_0$ and $\mathbf{E}(t)$ are statvolts cm^{-1} $\equiv$ statcoulomb cm^{-2}. Thus $\chi^{(1)}$ is dimensionless, $\chi^{(2)}$ has units of cm statvolt^{-1}, and $\chi^{(3)}$ has units of cm^2 statvolt^2. Similarly for the polarisation of an individual molecule, $\mathbf{p}(t)$, the relationship to the local field, $\mathbf{E}_{loc}(t)$ is as follows

$$\mathbf{p}(t) = \mu + \alpha\mathbf{E}_{loc}(t) + \beta\mathbf{E}_{loc}^2(t) + \gamma\mathbf{E}_{loc}^3(t) + \ldots,$$

AIII- 2

where $\mathbf{p}(t)$, and μ, this time have units of statvolts cm^2 $\equiv$ statcoulomb cm, and $\mathbf{E}_{loc}(t)$ still has units of statvolts cm^{-1}. Thus, the units of α, β and γ are cm^3, cm^4 statvolt^{-1} and cm^5 statvolt^{-2} respectively. Usually, the units in the Gaussian system are just quoted as electro-static units (esu).

Similarly in the MKS system, $\mathbf{P}(t)$ and $\mathbf{p}(t)$ are related to $\mathbf{E}(t)$ and $\mathbf{E}_{loc}(t)$ via the equations

$$\mathbf{P}(t) = \mathbf{P}_0 + \varepsilon_0 \left[\chi^{(1)}\mathbf{E}(t) + \chi^{(2)}\mathbf{E}^2(t) + \chi^{(3)}\mathbf{E}^3(t) \right]$$
$$\mathbf{p}(t) = \mu + \varepsilon_0 \left[\alpha\mathbf{E}_{loc}(t) + \beta\mathbf{E}_{loc}^2(t) + \gamma\mathbf{E}_{loc}^3(t) \right]$$

AIII- 3

where the units of $\mathbf{P}(t)$ and $\mathbf{P}_0$ are C m^{-2}, $\mathbf{p}(t)$ and μ are C m, $\mathbf{E}(t)$ and $\mathbf{E}_{loc}(t)$ are V m^{-1}, and ε_0 is 8.85 $\times$ 10^{-12} F m^{-1}. Since [F] = C V^{-1}, $\chi^{(1)}$ is still dimensionless, $\chi^{(2)}$ has units of m V^{-1}, and $\chi^{(3)}$ has units of m^2 V^{-2}. Also, α, β and γ have units of m^3, m^4 V^{-1}, and m^5 V^{-2}, respectively.

To convert from one unit system to another, various conversion factors need to be considered which are also presented in Table AIII- 1. The most notable inclusion to these is the 4π factor. In a Gaussian system for a linear medium, the displacement, $\mathbf{D}$ is given by

$$\mathbf{D} = \mathbf{E} + 4\pi\mathbf{P} = \mathbf{E}\left(1 + 4\pi\chi^{(1)}\right).$$

AIII- 4

However, in the MKS system the same equation is given by

$$\mathbf{D} = \varepsilon_0\mathbf{E} + \mathbf{P} = \varepsilon_0\mathbf{E}\left(1 + \chi^{(1)}\right),$$

AIII- 5

thus it is easy to see that a multiplicative factor of 4π is involved when converting to MKS units from Gaussian units. A similar factor is involved with the microscopic displacement.

Occasionally a slightly different convention is used with the MKS system in the placement of ε_0

$$P(t) = P_0 + \varepsilon_0 \chi^{(1)} E(t) + \chi^{(2)} E^2(t) + \chi^{(3)} E^3(t)$$
$$p(t) = \mu + \varepsilon_0 \alpha E_{loc}(t) + \beta E_{loc}^2(t) + \gamma E_{loc}^3(t)$$

AIII- 6

If this is the case, $\chi^{(2)}$, $\chi^{(3)}$, β, and γ are simply multiplied by ε_0 to convert to this MKS system from the previous MKS system.

Finally, the atomic unit may be derived from the solution to Schrödingers equation for a one electron atom (i.e. Hydrogen). The Rydberg unit of energy is defined as (MKS units) [274]

$$Ryd = \frac{me^4}{32\pi^2 \varepsilon_0^2 \hbar^2} = 13.605 \, eV,$$

where m is the mass of an electron, e is the electronic charge, and $\hbar$ is Planck's constant divided by 2π. The atomic unit of energy is defined as 1 au = 2 × Ryd, and the atomic unit of length is the first Bohr radius,

$$a_0 = \frac{4\pi\varepsilon_0 \hbar^2}{me^2} = 0.52892 \, \text{Å}.$$

Thus 1 Ryd = $e^2/16\pi\varepsilon_0 a_0$, and 1 au = $e^2/4\pi\varepsilon_0 a_0$. The electric field produced by an oscillating dipole the size of the first Bohr radius is $E = E_{n=1}/ea_0$, thus the atomic unit of electric field is (note capitals here denote the atomic unit of electric field)

$$AU = \frac{e}{4\pi\varepsilon_0 a_0^2}.$$

Conversions to the MKS system for miscellaneous units are presented in Table AIII- 2 below. Values of the numerical constants used in the MKS and CGS systems are also presented in Table AIII- 3 [273].

Parameter	Units (MKS)	Units (esu)	Conversion Factor, x (1 (MKS) = x (esu))
Q	C	statC	2.998×10^9
V	V	statV	$1/299.8$
ε_0	F m^{-1}	—	—
$[F]$	C V^{-1}	statC statV^{-1}	9×10^9
$\mathbf{E}(t)$, $\mathbf{E}_{loc}(t)$	V m^{-1}	statV cm^{-1}	$1/(3 \times 10^4)$
$\mathbf{P}(t)$	C m^{-2}	statC cm^{-2}	3×10^5
$\mathbf{P}_0$	C m^{-2}	statC cm^{-2}	3×10^5
$\chi^{(1)}$	None	None	1
$\chi^{(2)}$	m V^{-1}	cm statV^{-1}	$(3 \times 10^4)/4\pi$
$\chi^{(3)}$ ($\equiv \Gamma$)	m^2 V^{-2}	cm statV^{-2}	$(3 \times 10^4)^2/4\pi$
$\mathbf{p}(t)$	C m	statC cm	3×10^{11}
μ	C m	statC cm	3×10^{11}
α	m^3	cm^3	10^6
β	m^4 V^{-1}	cm^4 statV^{-1}	$(3 \times 10^{10})/4\pi$
γ	m^5 V^{-2}	cm^5 statV^{-2}	$10^6(3 \times 10^4)^2/4\pi$

Table AIII- 1: Units and Conversion factors between the MKS and CGS systems. e.g.
$1\ m^3 = 10^6\ cm^3$.

Parameter	Units (X)	Units (Y)	Conversion Factor, x $(1\,X = x\,Y)$
$\bar{r}$	m	Angstroms (Å)	10^{10}
μ	esu	Debyes (D)	10^{18}
μ	C m	Debyes (D)	3×10^{29}
$\tilde{E}(t)$, $\mathbf{E}_{loc}(t)$	V m^{-1}	Atomic units (au)	1.948×10^{-12}

Table AIII- 2: Miscellaneous unit systems and conversion to the MKS system. e.g. 1 m = 10^{10} Å.

Constant	Symbol	MKS Units	CGS Units
Speed of light.	c	2.998×10^{8} m s^{-1}	2.998×10^{10} cm s^{-1}
Charge of electron.	e	1.602×10^{-19} C	4.803×10^{-10} esu
Avogadro number.	N_a	6.023×10^{23} mol^{-1}	6.023×10^{23} mol^{-1}
Electron rest mass.	m_e	9.109×10^{-31} Kg	9.109×10^{-28} g
Boltzman constant.	k_B	1.381×10^{-23} J K^{-1}	1.381×10^{-16} erg K^{-1}
Planck constant.	h	6.626×10^{-34} J s	6.626×10^{-27} erg s
Electron volt.	eV	1.602×10^{-19} J	1.602×10^{-12} erg

Table AIII- 3: Numerical constants presented in both MKS and CGS systems.

References to Appendix III

[273] R. W. Boyd, *Non-Linear Optics*, Academic Press Inc., London, (1992).

[274] N. Mataga, T. Kubota, *Molecular Interactions and Electronic Spectra*, Marcel Dekker Inc., New York, (1970), p 25.

Appendix IV

Tables of the $E_N^T(30)$ and π^* Scales of Solvent Polarity.

The following table shows values of various indicators of solvent polarity. Solvents are in order of increasing dielectric constant [275] and are compared to the $E_N^T(30)$ polarity scale and the π^*-scale with it's associated HBA (β) and HBD (α) parameters [276].

Solvent	ε	$E_N^T(30)$	π^*	β	α
1,4 Dioxane	2.2	0.164	0.553	0.37	0.00
Benzene	2.3	0.111	0.588	0.10	0.00
Toluene	2.4	0.099	0.535	0.11	0.00
Diethylether	4.3	0.117	0.273	0.47	0.00
Chloroform	4.8	0.259	0.580	0.00	0.44
Chlorobenzene	5.6	0.188	0.709	0.07	0.00
THF	7.6	0.207	0.576	0.55	0.00
DCM	8.9	0.309	0.82	0.00	0.30
Cyclohexanone	16.1	0.281	0.755	0.53	—

Acetone	20.7	0.355	0.683	0.48	0.08
TMU	23.1	0.318	—	—	—
Ethanol	24.6	0.710[†]	0.540	0.77	0.83
Methanol	32.7	0.762	0.586	0.62	0.93
Nitromethane	35.9	0.481	0.848	—	0.85
DMF	36.7	0.404	0.875	0.69	0.00
Acetonitrile	37.5	0.460	0.713	0.31	0.19
DMSO	46.7	0.444	1.000	0.76	0.00

Table AIV-1: Scales of solvent polarity.

References to Appendix IV

[275] A. J. Riddick, W. B. Bunger, T. K. Sakano, *Organic Solvents., Physical Properties and Methods of Purification.*, **4th ed.**, John Wiley and Son Inc., New York, (1986).

[276] C. Reichardt, *Solvents and Solvent Effects in Organic Chemistry.*, **2nd Ed.**, VCH (UK) Ltd., Cambridge, (1990).

Appendix V

The Gaussian-Lorentz Summation Lineshape Used for Spectral Curve Fitting.

The lineshape used to fit the absorption spectrum of the tertiary amino TCNQ adducts is as follows [277]

$$
y_i = a_0 \left[\frac{\dfrac{a_3 \sqrt{\ln 2}}{a_2 \sqrt{\pi}} \exp\left(-4 \ln 2 \left\{ \dfrac{x - a_1}{a_2} \right\}^2 \right) + \dfrac{1 - a_3}{\pi a_2 \left\{ 1 + 4\left(\dfrac{x - a_1}{a_2} \right) \right\}}}{\dfrac{a_3 \sqrt{\ln 2}}{a_2 \sqrt{\pi}} + \dfrac{1 - a_3}{\pi a_2}} \right],
$$

where a_0, a_1, a_2, and a_3 are the peak amplitude, centre, width, and lineshape factor respectively. The fitting program finds the parameters a_0 - a_3 and the area, a_4 may be found by using the following equation

$$
a_4 = \frac{a_0}{\dfrac{a_3 \sqrt{\ln 2}}{a_2 \sqrt{\pi}} + \dfrac{1 - a_3}{\pi a_2}} .
$$

As explained in Chapter 6, four peaks are fitted to the total absorption band and the area and position of the first two bands estimated. An example of an absorption fit is shown in the graph below. r^2 was found to be better than 0.999 each time and it is estimated that the error on the position and area is no more than 1 % and 5 % respectively.
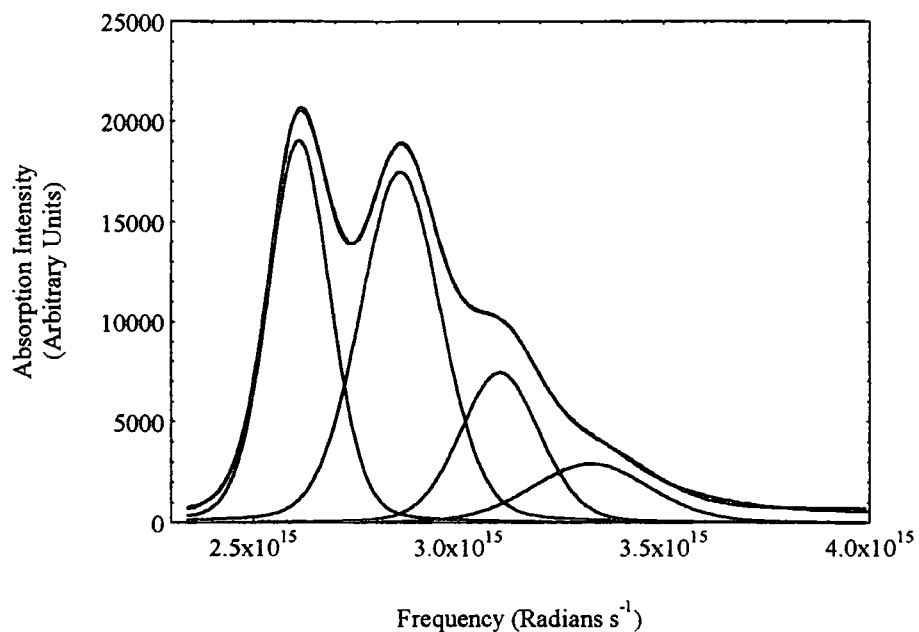
Figure AV- 1: The absorption spectrum for DEMI with a typical fit from four Gaussian - Lorentz summation lineshapes.

References to Appendix V.

[277] Peakfit, Version **4.0**, AISN Software Inc., (1991 -1995): *Help files.*

Appendix VI

Derivation of the Reaction Field.

The derivation of Onsager's reaction field is well known and is reproduced in many texts [278, 279, 280]. Considering a spherical cavity of radius a which is surrounded by a medium of dielectric constant, ε, at the centre of which is a non-polarisable, ideal, point dipole oriented in the z-direction (see Figure 2.3-1), the potential outside and inside the sphere, defined by ϕ_1 and ϕ_2, respectively must be found. The solution to Laplace's equation, $\nabla^2\phi = 0$ is the usual manifestation of ϕ_1 and ϕ_2 [278]. In spherical co-ordinates, Laplace's equation becomes

$$\nabla^2\phi = \frac{\partial^2}{\partial r^2}(r\phi) + \frac{1}{r^2\sin\theta}\frac{\partial}{\partial\theta}\left(\sin\theta\frac{\partial\phi}{\partial\theta}\right) = 0$$

AVI- 1

where r and θ are spherical co-ordinates. The general solution to AVI- 1 is given by Böttcher [278], and is found to be

$$\phi(r,\theta) = \sum_{n=0}^{\infty}\left(a_n r^n + b_n r^{-(n+1)}\right)P_n(\cos\theta)$$

AVI- 2

where a_n and b_n are determined from the potentials at the boundary or from the asymptotic behaviour at infinity, and $P_n(\cos\theta)$ is the Legendre polynomial defined by the generating function [278]

$$F(\cos\theta, z) = \frac{1}{\sqrt{1 - 2(\cos\theta)z + z^2}} = \sum_{n=0}^{n} P_n(\cos\theta)z^n.$$

<div align="right">*AVI- 3*</div>

Thus, ϕ_1 and ϕ_2 are obtained using AVI- 2, yielding the coefficients a_n, b_n, c_n, and d_n, respectively for the potentials outside and inside the cavity. The boundary conditions in this case are

$$(\phi_1)_{r\to\infty} = 0,$$
$$(\phi_1)_{r=a} = (\phi_2)_{r=a},$$
$$\varepsilon\left(\frac{\partial\phi_1}{\partial r}\right)_{r=a} = \left(\frac{\partial\phi_2}{\partial r}\right)_{r=a}.$$

<div align="right">*AVI- 4*</div>

The term represented by the coefficient d_n in ϕ_2 is due to charges inside the cavity, which, for an ideal dipole, may be represented by the potential [278, 279]

$$\phi = \frac{\mu}{r^2}\cos\theta.$$

<div align="right">*AVI- 5*</div>

In addition, using the boundary conditions, we find that $a_n = 0$ and, for values of $n \neq 1$, b_n and c_n are also zero. For $n = 1$, using the boundary conditions and AVI- 5, we find that

$$b_1 = \frac{3}{2\varepsilon+1}\mu,$$
$$c_1 = -\frac{2(\varepsilon-1)}{2\varepsilon+1}\frac{\mu}{a^3}$$

<div align="right">*AVI- 6*</div>

so that

$$\phi_1 = \frac{3\varepsilon}{2\varepsilon+1}\frac{\mu}{r^2}\cos\theta,$$

$$\phi_2 = \frac{\mu}{r^2}\cos\theta - \frac{2(\varepsilon-1)}{2\varepsilon+1}\frac{\mu}{a^3}\cos\theta.$$

AVI- 7

The potential inside the cavity is, thus a superposition of the dipole field in vacuo and a uniform reaction field **R**, given by [278, 279, 280]

$$\mathbf{R} = \frac{1}{\bar{r}^3}\frac{2(\varepsilon-1)}{2\varepsilon+2}\mu = f\mu .$$

AVI- 8

For a polarisable point dipole, the above calculations may be extended with the inclusion of a polarisability, α [280]. The reaction field may then be defined as [278]

$$\mathbf{R} = \frac{f}{1-f\alpha}\mu .$$

AVI- 9

The calculation of the ellipsoidal reaction field is far more intricate, so only the result is presented here. Scholte [281] was the first to derive an expression for the ellipsoidal reaction field, and a number of similar calculations have since been made, essentially arriving at the same result [278, 282, 283]. With the case of a homogeneous dipole density, with it's direction not along one of the major axes of the ellipsoid, the reaction field for a non-polarisable ideal point dipole is

$$\mathbf{R} = \mathbf{F}\cdot\mu$$

AVI- 10

where the tensor **F** is defined as

$$\mathbf{F}_\lambda = \frac{3}{abc}\frac{A_\lambda(1-A_\lambda)(\varepsilon-1)}{\varepsilon+(1-\varepsilon)A_\lambda}$$

AVI- 11

where A_λ is the shape factor, given previously by equation (2.3-20), in the λ direction, where $\lambda = x, y, z$ and a, b, and c are the principle semi-axes of the ellipsoid in the z, y, and x direction respectively. A similar relationship for the reaction field to AVI- 9 is then found for the case of a polarisable dipole, substituting AVI- 11 for f.

References to Appendix VI

[278] C. J. F. Böttcher, *Theory of Electric Polarisation.*, **2nd ed.**; O. C. Van Belle, P. Bordewick, A. Rip., Volume **1**; *Dielectrics in Static Fields.*, Elsevier, London, (1993).

[279] B. K. P. Scaife, *Principles of Dielectrics*, Clarendon Press, Oxford, (1989).

[280] L. Onsager, *J. Am. Chem. Soc.*, **58**, 1486, (1936).

[281] Th. G. Scholte, *Recueil*, **70**, 50, (1951).

[282] R. J. W. E. Le Fèvre, D. A. A. S. Narayana Rao, *Aust. J. Chem.*, **8**, 330, (1955).

[283] J. A. Abbott, H. C. Bolton, *Trans. Farad. Soc.*, **48**, 422, (1952).